Paleoclimate and Hydrology of Bermuda from the Last Interglacial to Today Using Oxygen and Clumped Isotope Geochemistry

by

Jade Ziqiu Zhang

A dissertation submitted in partial fulfillment
of the requirements for the degree of
Doctor of Philosophy
(Earth and Environmental Sciences)
in the University of Michigan
2023

Doctoral Committee:

Assistant Professor Sierra V. Petersen, Chair
Associate Professor Andrew Gronewold
Associate Professor Naomi Levin
Professor Kyger C. Lohmann

Jade Ziqiu Zhang

jadezz@umich.edu

ORCID iD: 0000-0002-9967-5029

Dedication

To mom, to whom I owe everything

Acknowledgements

First, to my advisor Sierra Petersen: thank you for your guidance, patience, constant encouragement and support. Thank you for all of your insightful feedback over the years and thank you for always challenging me to think about the results in different ways. Thank you for allowing me so much independence to pursue my research projects and for that extra dash of optimism carrying me through the ups and downs of life. I owe you a tremendous debt of gratitude.

To my committee members, Kacey Lohmann, thank you for teaching me about mass spectrometers and for teaching me how to prepare water samples on a manual extraction line. You are always available to help me with anything in the lab, thank you for always sharing your expertise on all things isotope related. Thank you to Naomi Levin, for your feedback, advice and time and for always reminding me to think about the big-picture. I also appreciate your enthusiasm and admire your awareness on effective science communication. Thank you to Drew Gronewold, for your expertise on hydrology and all your feedback, ideas and advise.

I would like to acknowledge the support of many individuals and collaborators, none of the work would have been possible without their involvement. Thank you to Ian Winkelstern, for all the field adventures and scientific conversations. Thank you to Shaun Lavis, Bruce Williams, Ricardo Anderson and Maria Marcano. Thank you for collecting water samples in Bermuda during the Pandemic, your enthusiasm and dedication are beyond appreciated! And thank you to

everyone in the Earth Department who collected numerous water and mollusk samples during your family vacations.

Thank you to the funding agencies for supporting this dissertation work. This dissertation research was supported by National Science Foundation Graduate Research Fellowship, University of Michigan Rackham Merit Fellowship, Rackham Research Grant, and Scott Turner Awards.

Thank you to all the current and former SCIPP lab members for being a source of support and encouragement over the years. Thank you to Alex Quizon, Lucas Gomes, and Allison Curley for all the fun SCIPP outings and brunch hangouts and for lending an ear. You help strengthen the sense of community I felt throughout graduate school. Thank you to Julia Kelson and Matt Jones for constantly inspiring me and providing critical feedback throughout my time here. Thank you to Steve Wedel, Sabrina Lanker, Lora Wingate, Ashling Neary and Justin VanDeVelde for all your lab assistance.

Thank you to all of the friends I have made while at Michigan, for listening to my struggles, for your smiles, and for supporting me through the highs and lows. Lastly, a huge thank you to my family. Thank you mom, stepdad, grandparents, for your love, unwavering support and constant encouragement. Thank you for providing a different perspective on life when I am tired or stressed. Thank you for always believing in me.

Table of Contents

List of Tables

List of Figures

Abstract

The Last Interglacial (LIG), also known as Marine Isotope Stage 5e (MIS 5e), was an interval with climate as warm or slightly warmer than today. Global mean sea surface temperatures were reconstructed to be ~2°C warmer than present, accompanied by a ~6-9m increase in the sea level. At the regional scale, this warming was non-uniform. The North Atlantic/Greenland/Iceland/Nordic Seas were reconstructed to be warmer than today, whereas the Central Atlantic/Caribbean Seas were reconstructed to be cooler than modern. Situated at the boundary between these two regions, Bermuda can provide a unique record of Last Interglacial climate. In this dissertation, I conduct and optimize isotopic analyses of modern waters and fossil invertebrates from Bermuda to reconstruct modern hydrology and Last Interglacial climate, respectively.

First, I determine the most accurate approach for estimating seasonality by comparing multiple isotopic sampling techniques. Validation of these techniques in the modern, where true seasonality and annual mean temperatures are known, improves our ability to accurately apply these methods toward paleoseasonality reconstruction. This study showed high resolution paleoseasonality reconstruction of temperature and $\delta^{18}O_w$ is possible with multiple isotopic sampling techniques, especially when a sampling and analysis framework is chosen that balances resolution and growth rate, a finding which can be extrapolated to other species and time periods.

Second, I evaluate modern variability in salinity and the oxygen isotopic composition of water ($\delta^{18}O_w$) across various types of modern water samples collected from Bermuda. Well water

samples tapping Bermuda's main freshwater aquifer show the aquifer has changed shape over recent decades and demonstrate linear mixing of seawater and freshwater underground. Seawater samples from the South Shore show variability in $\delta^{18}O_w$ on the order of ~2.4‰ on monthly timescales and up to 1.4‰ on hourly timescales. We propose that this significantly greater variability in $\delta^{18}O_w$ compared to seawater samples from elsewhere around the island is the result of variable freshwater discharge from the underground aquifer. This is the first detailed study of Bermudan hydrology using $\delta^{18}O_w$. Studies like this set an important benchmark for long-term sustainable extraction of freshwater on the island.

Lastly, MIS 5e seasonality in temperature and $\delta^{18}O_w$ were reconstructed via oxygen and clumped isotope measurements of multiple fossil invertebrate species collected from both the Great Sound and South Shore. Combined with previously published data, our new data captures a decreasing trend in temperature and $\delta^{18}O_w$ through MIS 5e, from close-to-modern conditions to cooler or more depleted conditions relative to today. Previous paleoceanographic studies have regarded MIS 5e as a single time slice, classified as either warmer or cooler than today for a given location. These findings illustrate that MIS 5e-aged outcrops like those in Bermuda can't all be viewed as representing the same moment in time, but rather subsample a ~10-15 kyr interval of time during which local climate changed measurably. The reconstructed trends in temperature and $\delta^{18}O_w$ have implications for ice melt histories and past ocean circulation patterns.

Together, this dissertation demonstrates effective application of the novel clumped isotope methods to estimate temperature seasonality, documents the current state of freshwater-saltwater interaction in modern Bermudan waters, and emphasizes that the interval of time

known as MIS 5e contains changes in climate that should not be treated as a single moment in time.

Chapter 1 Introduction

1.1 Overview and motivation

The Last Interglacial (Marine Isotope Stage 5e, or MIS 5e) began approximately 130,000 years ago and ended about 116,000 years ago at the onset of the Last Glacial period (Kukla et al., 2002). Changes in the orbital configuration resulted in an increase in global mean temperatures of up to 2 °C compared to the pre-industrial conditions (Harrison et al., 1995; Kukla et al., 1997; Otto-Bliesner et al., 2013). Further evidence from proxy records suggests even more pronounced warming at high latitudes (CLIMAP, 1984; Capron et al., 2014; Pedersen et al., 2016). This increase in global mean temperatures led to significant ice losses from the Greenland and Antarctic ice sheets as well as from other high-latitude ice masses. The combination of ice loss and thermal expansion of seawater led to an increase in global sea level of around 6-9m (Cuffey and Marshall, 2000; Kopp et al., 2009; Turney and Jones, 2010; Stone et al., 2013). Even though the Last Interglacial may not be a perfect analogue for future greenhouse gas driven warming, it is still the most recent time in which global temperatures exceeded modern values and can therefore serve as a comparison to a future warmer climate state (Guarino et al., 2020). As climate changes of this magnitude have not occurred in recorded human history, understanding of the impact of such warming and rise in sea level on particular regions is of great value.

While overall Last Interglacial climate is often considered to be warm, ocean conditions were not uniformly warmer during this time (CLIMAP, 1984; Turney and Jones, 2010). For example, in the Atlantic ocean, a regional scale temperature pattern existed dividing the Central

Atlantic/Caribbean from the North Atlantic/Greenland/Iceland/Nordic Sea. Specifically, cooler-than-modern temperatures were reconstructed in the Central Atlantic while warm temperatures were reconstructed in the North Atlantic region (CLIMAP, 1984; Turney and Jones, 2010). This temperature dichotomy between ocean areas is not fully understood due to the lack of data from the Central Atlantic region between 20 °N to 40 °N. Situated around this paleo-interface, with cooler-than-modern regions to the south and warmer-than-modern regions to the north, Bermuda (32.4°N, 64.8°W) can provide a unique record of Last Interglacial climate in this dynamic region.

Largely owing to the warm Gulf Stream Current, Bermuda has a subtropical climate in the western North Atlantic. The open water around Bermuda has an annual sea surface temperature range from 19 to 29 °C and an annual average temperature of 24 °C (Coates et al., 2013). Bermuda contains raised beach and marine deposits representing deglacial sea level rise and interglacial sea level high stands, dated to the past four interglacial periods (Marine Isotope Stages 5e, 7, 9 and 11). Marine deposits, or more specifically the marine invertebrate fossil they contain, can preserve information about sea surface temperatures in and around Bermuda during prior interglacial intervals, and during MIS 5e in particular.

The overall motivation and goal of this dissertation is to move the scientific community towards a fuller understanding of climate and ocean conditions in and around Bermuda during the Last Interglacial period. We present new isotopic data describing paleoseasonality in temperature and the isotopic composition of coastal seawater, estimated from multiple species of mollusk collected at multiple sites across the island of Bermuda. In order to obtain a better understanding of hydrologic conditions affecting this coastal seawater, we present new oxygen isotope measurements of modern surface, sea, and ground waters from around Bermuda. We also

evaluate multiple isotope sampling techniques to establish the best approaches of extracting paleoseasonality information from mollusk shells. Taken together, the four content chapters in this dissertation offer new insights on the evolution of climate in Bermuda over the Last Interglacial, as well as modern hydrologic conditions, and novel approaches to use of isotope measurements at subannual scale.

1.2 Geochemical Methods

1.2.1 Stable Isotopes of Oxygen

All oxygen atoms have eight protons but the nucleus might contain eight, nine or ten neutrons. ^{16}O, with eight protons and eight neutrons makes up 99.76% of the oxygen atoms, and is the most common isotope found in nature. ^{18}O, with eight protons and ten neutrons, only makes up 0.2% of oxygen atoms. The even more rare ^{17}O, with eight protons and nine neutrons, only makes up 0.04% of oxygen atoms. The ratio between the light isotope ^{16}O and the heavy isotope ^{18}O ($R^{18} = {}^{18}O/{}^{16}O$) in water differs in natural materials. The ratio between the heavy-to-light isotope from an unknown sample to the known universally accepted standards is expressed with delta (δ) notation:

$$\delta = \left(\frac{R_{sample}}{R_{standard}} - 1\right) * 1000 \qquad \text{Eqn. 1.1}$$

where R is the ratio of heavy-to-light isotopes in a sample or international standard. The two most common standards for oxygen isotope measurements are Vienna Standard Mean Ocean Water (VSMOW) and Vienna Pee Dee Belemnite (VPDB). The oxygen isotopic composition of

water is usually reported relative to VSMOW whereas the oxygen isotopic composition of carbonates can be reported relative to either but to VPDB is more common.

1.2.2 Oxygen Isotope Thermometry

Urey (1947) suggested that the amount of ^{18}O, preferentially concentrated in calcium carbonate ($\delta^{18}O_{carb}$) relative to the water from which the carbonate is precipitated from ($\delta^{18}O_w$), is temperature dependent. This temperature relationship between $\delta^{18}O_{carb}$ and $\delta^{18}O_w$ could be used to determine past oceanic temperatures, and an example of this relationship can be expressed as

$$1000 * \ln\left(\alpha_{aragonite-H_2O}\right) = 17.88 * (10^3 T^{-1}) - 31.14 \qquad \text{Eqn. 1.2}$$

Where $\alpha_{aragonite-H_2O}$ is the fractionation factor between aragonite and water and T is temperature in Kelvin (Kim et al., 2007). The relationship between temperature, $\delta^{18}O_{carb}$ and $\delta^{18}O_w$ has been redefined over the years and this thermometry method has been extended to many areas of earth science. Another example of this relationship is expressed below

$$T = 21.8 - 4.69 * (\delta^{18}O_{aragonite} - \delta^{18}O_w) \qquad \text{Eqn. 1.3}$$

Where T is temperature in Celsius (Grossman and Ku, 1986). Regardless of which expression, this thermometry method presents a conundrum, of which only one variable is known ($\delta^{18}O_{carb}$), and two are unknown ($\delta^{18}O_w$ and temperature). Paleotemperatures estimated from $\delta^{18}O_{carb}$ require either the knowledge on the formation $\delta^{18}O_w$ value or an assumption of the $\delta^{18}O_w$ value,

which are equally difficult in deep time. $\delta^{18}O_w$ can be affected by local precipitation/evaporation, freshwater runoff, coastal upwelling, etc. This makes it difficult to quantify in the past, and in many modern environments.

1.2.3 Carbonate Clumped Isotopes

The carbonate clumped isotope thermometry is a novel method based on the temperature dependent ordering of the heavy isotopes ^{13}C and ^{18}O within the carbonate lattice (Ghosh et al., 2006; Eiler, 2007). This innovative method has advanced rapidly since its infancy and quickly diversified its field of application, including but not limited to the field of paleoclimate, paleontology, diagenesis and metamorphism (Eiler, 2011). The carbonate clumped isotopic composition, denoted as Δ_{47}, is defined as the excess amount of mass 47 CO_2 relative to the amount expected for stochastic distribution:

$$\Delta_{47} = \left(\frac{R_{47}}{R_{47*}} - 1\right) * 1000 \qquad \text{Eqn. 1.4}$$

Where R_{47} is the abundance ratio between isotopologues of CO_2 with mass 47 primarily ($^{13}C^{18}O^{16}O$) and the most common isotopologues of CO_2 with no heavy isotope substitutes ($^{12}C^{16}O^{16}O$). R_{47}* is that same ratio but the distribution of heavy isotopes among the isotopologues is dictated by stochastic (random) distribution (Eiler, 2007). Δ_{47} enables direct estimation of the formation temperature of a carbonate material, independent of the surrounding water composition. The original clumped isotope thermometer is expressed as

$$\Delta_{47} = \frac{56200}{T^2} - 0.02 \qquad \text{Eqn. 1.5}$$

Where T is temperature in Kelvin (Ghosh et al., 2006). This resolves the long-standing issue from the traditional carbonate $\delta^{18}O$ paleothermometry, and eliminates the need for prior knowledge of $\delta^{18}O_w$. Since the original Δ_{47}-to-Temperature equation, numerous studies have produced other empirical equations through increased sample replications using natural, biogenic and synthetic carbonates, improved calibration schemes and standardizations to better relate Δ_{47}-values to known temperatures. The most widely accepted equations are described in Petersen et al. (2019) and Anderson et al. (2021). In addition to direct estimation of temperatures, Δ_{47} also allows simultaneous estimation of $\delta^{18}O_{carb}$, $\delta^{18}O_w$ and $\delta^{13}C_{carb}$.

1.2.4 Oxygen Isotope Sclerochronology

The measurement of $\delta^{18}O$ along the growth axis of mollusk shells, corals or sponges is a widely used technique in paleoclimate studies known as sclerochronology (Shackleton, 1973; Corrège, 2006; Rosenheim et al., 2004). Given the appropriate balance of sampling resolution and growth rate, sclerochronology can reveal subannual changes in temperature. However, the accurate reconstruction of environmental/ocean temperatures relies on the knowledge of the oxygen isotopic composition of the surrounding fluid ($\delta^{18}O_w$) at every point throughout the year. In most paleoclimate studies, $\delta^{18}O_w$ is unknown and assumed to be constant in time. This may be an acceptable assumption for open-ocean conditions, but becomes more problematic in coastal settings where many studied mollusks live. If, in fact, $\delta^{18}O_w$ is changing throughout the year, this could lead to inaccurate estimates of the absolute maximum and minimum temperatures and annual range, with errors occurring in either the over or underestimation direction. The lack of

direct knowledge of seasonal variability of $\delta^{18}O_w$ in ancient waters has limited the accurate application of the oxygen isotope sclerochronology.

1.2.5 Subannual and High Resolution Clumped Isotope Sclerochronology

As mentioned above, $\delta^{18}O$ sclerochronology suffers from an issue of unknown fluid $\delta^{18}O$. In situations where oxygen isotope composition of water could be independently determined, $\delta^{18}O$-based thermometry could still be a reliable method. Clumped isotope paleothermometry can independently constrain $\delta^{18}O_w$ and pair with oxygen isotope sclerochronology to more accurately reconstruct past salinity.

One limitation hindering the broad usage of clumped isotope thermometry at subannual scales is its large sample size requirement. $\delta^{18}O$-based paleoseasonality studies drill sequential microscopic samples using tools like a micromill to extract ~50μg of material per sample point. Typical recommended sample size for a single clumped isotope data point, on the other hand, is ~9-20mg (covering 3+ replicates of a homogenous powder). This great mismatch in sample material requirements, not to mention the vastly greater machine time required to measure one Δ_{47} data point, has prevented much application of Δ_{47} sclerochronology.

Due to this widely recognized concern and desire to apply Δ_{47} to limited sample materials like foraminifera, Schmid and Bernasconi (2010) attempted to design a new measurement scheme using a Kiel sample prep device to allow smaller samples to be analyzed. Even though the measurement scheme was not firmly established at the time, it prompted a rapid future development in major mechanical modifications as well as measurement protocol and data treatment. Subsequent developments in instrumentation (Petersen and Schrag, 2014), sampling and data treatment (Caldarescu et al., 2021; de Winter et al., 2021) have now made this possible.

Until recently, due to this large sample requirement, paleoclimate reconstruction studies often apply Δ_{47} to a single bulk sample in order to maximize the sample material. This often results in averaging multiple months or years of growth depending on the species, further contributes ambiguity to the results. More recently, Δ_{47} thermometry applied at the subannual scale is often paired with $\delta^{18}O$ sclerochronology. In this approach, summers ($\delta^{18}O$ minima) and winters ($\delta^{18}O$ maxima) are first identified based on the $\delta^{18}O$ sclerochronology results. These identified seasonal extremes are then resampled to acquire one large homogenized sample, replicated 3-4 times. In addition to the large sample size requirement, this approach also heavily relies on the correctly identified seasonal extremes from $\delta^{18}O$ sclerochronology.

Recent mass spectrometric development allows clumped isotope analysis using a much smaller amount of material, reducing the single replicate amount from 3-5mg to 150-450μg. Now, instead of requiring the 3-4 replicates for each sample point, individual aliquots of sample (150-450μg) is analyzed once for high resolution Δ_{47} and the resultant data could be combined in different ways to achieve a similar accuracy outcome (de Winter et al., 2021; Caldarescu et al., 2021; Zhang and Petersen, 2023). This greatly expands the possibility of Δ_{47} paleoseasonality, and as Δ_{47} sclerochronology reconstructs high resolution temperature records, a high resolution record of the water composition is simultaneously reconstructed, making this an extremely valuable tool for both paleoclimatology and paleohydrology.

1.3 Research Questions and Outline of the Dissertation Chapters

The overall goal of the four dissertation chapters is to improve knowledge of paleoseasonality in Bermuda during the Last Interglacial and of modern hydrology. This is achieved through new subannual scale paleoclimate data as well as further exploration in

clumped isotope methods development, and modern hydrologic observations. The four content chapters are summarized by questions below:

1.3.1 How accurately does H.R. Δ_{47} thermometry reconstruct seasonal temperatures compared to other isotopic sampling approaches? (Chapter 2)

$\delta^{18}O$ sclerochronology is a widely used technique to reconstruct carbonate formation temperatures, but the required a priori knowledge of $\delta^{18}O_w$ and the inherent assumption of $\delta^{18}O_w$ being constant present problems for paleoseasonality reconstruction. Although Δ_{47} thermometry resolves these issues in principle, the typical sample size requirement for this method is still a restriction for many studies and sample types. Recent advancements in mass spectrometry have allowed smaller sample sizes to be analyzed, making high resolution sampling possible. However, these new methods have not yet been widely tested.

Chapter 2 evaluates the performance of multiple isotope sampling techniques in a modern setting where seasonality and mean annual temperatures were known. This study was carried out on the common mid-sized bivalve *Lucina pensylvanica* (*L. pensylvanica*). Chapter 2 assesses the ability of multiple isotope techniques to correctly reconstruct both mean annual temperature and seasonality. "Seasonally-targeted" and "continuous high resolution" Δ_{47} sampling methods were compared to each other and to the known modern seasonality to determine the best sampling approach. Sampling and analysis approaches were proposed that balance sample size and growth rate, which can be applied to future paleotemperature and paleoseasonality reconstruction.

Chapter 2 was published in *Chemical Geology* (Zhang and Petersen, 2023).

1.3.2 What was the seasonality in temperature in Bermuda during MIS 5e? (Chapter 3)

A previous paleoclimate study began the effort of understanding the Last Interglacial climate in Bermuda through $\delta^{18}O$ sclerochronology and bulk clumped isotope analyses of the marine gastropod *Cittarium pica* (Winkelstern et al., 2017). This initial study reconstructed cooler-than-modern sea surface temperatures during MIS 5e, but also found temperature differences between two closely located study sites of similar age.

Chapter 3 expands upon the above study and further explores paleoseasonality through subannual-scale clumped isotope measurements. This chapter aims to determine whether the cooler-than-modern temperatures and the observed temperature differences between the two study sites presented from the previous study (Winkelstern et al., 2017) persist with higher resolution sampling. A subset of the shells from the original study were resampled for Δ_{47} analysis at subannual resolution, targeting high and lows in the $\delta^{18}O_{carb}$ record across multiple years of growth. Variation in Δ_{47} temperatures were compared to modern seasonality and used, in conjunction with $\delta^{18}O_{carb}$, to calculate subannual variation in $\delta^{18}O_w$.

It is difficult to interpret reconstructed paleo-$\delta^{18}O_w$ values without knowledge of $\delta^{18}O_w$ values and variability in the modern setting and understanding of the processes driving change. $\delta^{18}O_w$ values around Bermuda had only been previously analyzed in one other study containing a couple of measurements (Epstein and Mayeda, 1953). In this study, modern seawaters were collected from 16 locations around the island of Bermuda and analyzed for $\delta^{18}O_w$ to improve understanding on the modern $\delta^{18}O_w$ variability and allow better interpretation of paleo $\delta^{18}O_w$ values reconstructed from Δ_{47}.

Chapter 3 was published in *Paleoceanography and Paleoclimatology* (Zhang et al., 2021).

1.3.3 What are the magnitudes of $\delta^{18}O_w$ variability in different types of water in modern Bermuda? (Chapter 4)

Subannual clumped isotope analyses of the rocky shore dwelling gastropod *Cittarium pica* and measurements of oxygen isotopes in modern waters from Chapter 3 suggested submarine groundwater discharged from the Devonshire freshwater lens may be affecting the seawater $\delta^{18}O$ values along South Shore today and during MIS 5e. Aquifer water is sourced from local precipitation, which is isotopically depleted relative to surrounding seawater. Discharge of fresh, isotopically depleted groundwater would reduce surrounding seawater salinity and $\delta^{18}O_w$. However, the limited data from Chapter 3 and one other previous study containing a couple of samples from Bermuda (Epstein and Mayeda, 1953) did not sufficiently quantify the spatial and temporal variability of $\delta^{18}O_w$ in Bermudan seawater and processes driving that variability.

Chapter 4 evaluates the variability in salinity and $\delta^{18}O_w$ from seawater samples collected along South Shore and elsewhere across the island of Bermuda. Seawater values are then compared to values representing other water types including well, tap, marsh, and rain waters. Variability in salinity and $\delta^{18}O_w$ are investigated on different time scales, including bi-weekly over a period of months and hourly over a full tidal cycle.

This chapter is in preparation for submission to *Journal of Hydrology: Regional Studies*.

1.3.4 Was seasonality in temperature and $\delta^{18}O_w$ in the Great Sound similar to or different from variability along the South Shore? (Chapter 5)

In Chapter 3, Last Interglacial seasonality was reconstructed through subannual-scale clumped isotope analysis of marine gastropods living on the rocky South Shore of Bermuda. Cooler-than-modern temperatures were estimated from two study sites along the South Shore

(Zhang et al, 2021). However, a recent study by our collaborators found warm, close-to-modern-conditions from Last Interglacial deposits on an island in the Great Sound of Bermuda, a protected bay on the north side of the island (Minnebo et al., in prep). New amino acid racemization (AAR) dates accompanying the temperature estimates suggest the age of the sites in the Great Sound and along the South Shore may slightly differ. Additionally, the environment represented by the two areas are also different, both today and in the past, as indicated by sedimentology and taxa present. The South Shore is a rocky coastline exposed to the open Atlantic Ocean, inhabited by the rock-dwelling gastropod *C. pica*, whereas the Great Sound is a semi-protected harbor containing many small islands today, opening out to the shallowly submerged portion of the Bermuda Platform, containing many other bivalves that prefer sandy bottoms, such as *L. pensylvanica*. Chapter 5 aims to resolve the temperature differences previously reconstructed between the South Shore and the Great Sound and determine whether the age difference or paleoenvironmental difference was more important.

Seasonality in temperature and $\delta^{18}O_w$ were estimated from fossil *L. pensylvanica* collected from multiple Great Sound sites, all dated to MIS 5e. New data from these additional Great Sound sites were compared with previously published data from the Great Sound and South Shore (Winkelstern et al., 2017; Zhang et al., 2021; Minnebo et al., in prep). All of the isotope data was synthesized with stratigraphy, sedimentology, and AAR dating to create a full picture of climate and paleoenvironmental evolution through the Last Interglacial in Bermuda.

1.4 Summary

Overall, the four content chapters presented here build and improve upon previous insights on the Last Interglacial climate and modern hydrology in Bermuda. The ideal isotope

geochemical sampling approach and analysis protocol is first refined and tested in the modern setting in order to optimize sampling resolution and precision (Chapter 2). Modern $\delta^{18}O_w$ variability is then reconstructed across the island to increase understanding of submarine groundwater discharge processes both in the modern setting and in the past (Chapter 4). Through oxygen and refined clumped isotope measurements targeting different fossil species and multiple sites on the island, paleoseasonality and $\delta^{18}O_w$ variability delineated here offer a new perspective on the evolution of paleoclimate and paleoenvironment in Bermuda over the Last Interglacial (Chapter 3 and Chapter 5).

1.5 References

Anderson, N.T. et al., 2021, A unified clumped isotope thermometer calibration (0.5–1,100°C) using carbonate-based standardization: Geophysical Research Letters, v. 48, doi:10.1029/2020GL092069.

Caldarescu, D.E., Sadatzki, H., Andersson, C., Schäfer, P., Fortunato, H., and Meckler, A.N., 2021, Clumped isotope thermometry in bivalve shells: A tool for reconstructing seasonal upwelling: Geochimica et Cosmochimica Acta, v. 294, p. 174–191, doi:10.1016/j.gca.2020.11.019.

Capron, E., Govin, A., Stone, E.J., Masson-Delmotte, V., Mulitza, S., Otto-Bliesner, B., Rasmussen, T.L., Sime, L.C., Waelbroeck, C., and Wolff, E.W., 2014, Temporal and spatial structure of multi-millennial temperature changes at high latitudes during the Last interglacial: Quaternary Science Reviews, v. 103, p. 116–133, doi:10.1016/j.quascirev.2014.08.018.

CLIMAP (1984), The Last Interglacial Ocean, Quaternary Research, v. 21, 123–224.

Coates, K.A., Fourqurean, J.W., Kenworthy, W.J., Logan, A., Manuel, S.A., and Smith, S.R., 2013, Introduction to Bermuda: Geology, Oceanography and Climate, p. 115–133, doi:10.1007/978-94-007-5965-7_10.

Corrège, T., 2006, Sea surface temperature and salinity reconstruction from coral geochemical tracers: Palaeogeography, Palaeoclimatology, Palaeoecology, v. 232, p. 408–428, doi:10.1016/j.palaeo.2005.10.014.

Cuffey, K.M., and Marshall[23], S.J., 2000, Substantial contribution to sea-level rise during the last interglacial from the Greenland ice sheet: Nature, v. 404.

Eiler, J.M., 2007, "Clumped-isotope" geochemistry-The study of naturally-occurring, multiply-substituted isotopologues: Earth and Planetary Science Letters, v. 262, p. 309–327, doi:10.1016/j.epsl.2007.08.020.

Eiler, J.M., 2011, Paleoclimate reconstruction using carbonate clumped isotope thermometry: Quaternary Science Reviews, v. 30, p. 3575–3588, doi:10.1016/j.quascirev.2011.09.001.

Epstein, S., and Mayeda, T., 1953, variation of O^{18} content of waters from natural sources: Geochimica et Cosmochimica Acta , v. 4, p. 213–224.

Ghosh, P., Adkins, J., Affek, H., Balta, B., Guo, W., Schauble, E.A., Schrag, D., and Eiler, J.M., 2006, ^{13}C-^{18}O bonds in carbonate minerals: A new kind of paleothermometer: Geochimica et Cosmochimica Acta, v. 70, p. 1439–1456, doi:10.1016/j.gca.2005.11.014.

Grossman, E.L., and Ku, T.-L., 1986, Oxygen and carbon isotope fractionation in biogenic aragonite: temperature effects: Chemical Geology (Isotope Geoscience Section), v. 59, p. 59.

Guarino, M.V. et al., 2020, Sea-ice-free Arctic during the Last Interglacial supports fast future loss: Nature Climate Change, v. 10, p. 928–932, doi:10.1038/s41558-020-0865-2.

Harrison, S.P., Kutzbach, J.E., Prentice, I.C., Behling, P.J., and Sykes, M.T., 1995, The response of northern hemisphere extratropical climate and vegetation to orbitally induced changes in insolation during the Last Interglacial: Quaternary Research, v. 43, p. 174–184.

Kim, S.T., Mucci, A., and Taylor, B.E., 2007, Phosphoric acid fractionation factors for calcite and aragonite between 25 and 75 °C: Revisited: Chemical Geology, v. 246, p. 135–146, doi:10.1016/j.chemgeo.2007.08.005.

Kopp, R.E., Simons, F.J., Mitrovica, J.X., Maloof, A.C., and Oppenheimer, M., 2009, Probabilistic assessment of sea level during the last interglacial stage: Nature, v. 462, p. 863–867, doi:10.1038/nature08686.

Kukla, G., Mcmanus, J.F., Rousseau, D.-D., Chuine~, I., and Doherty, L.-, 1997, How long and how stable was the Last Interglacial? Quaternary Science Reviews, v. 16, p. 605–612.

Kukla, G.J. et al., 2002, Last interglacial climates: Quaternary Research, v. 58, p. 2–13, doi:10.1006/qres.2001.2316.

Minnebo, L., Winkelstern, I. Z., Zhang, J. Z., Petersen, S. V., Highly local variability in coastal last interglacial temperature and seawater $\delta^{18}O$ in Bermuda revealed by clumped isotope sclerochronology. Manuscript in preparation.

Otto-Bliesner, B.L., Rosenbloom, N., Stone, E.J., Mckay, N.P., Lunt, D.J., Brady, E.C., and Overpeck, J.T., 2013, How warm was the last interglacial? new model-data comparisons: Philosophical Transactions of the Royal Society A: Mathematical, Physical and Engineering Sciences, v. 371, doi:10.1098/rsta.2013.0097.

Pedersen, R.A., Langen, P.L., and Vinther, B.M., 2016, The last interglacial climate: comparing direct and indirect impacts of insolation changes: Climate Dynamics, v. 48, p. 3391–3407, doi:10.1007/s00382-016-3274-5.

Petersen, S. V. et al., 2019, Effects of improved ^{17}O correction on interlaboratory agreement in clumped isotope calibrations, estimates of mineral-specific offsets, and temperature dependence of acid digestion fractionation: Geochemistry, Geophysics, Geosystems, v. 20, p. 3495–3519, doi:10.1029/2018GC008127.

Petersen, S. V., and Schrag, D.P., 2014, Clumped isotope measurements of small carbonate samples using a high-efficiency dual-reservoir technique: Rapid Communications in Mass Spectrometry, v. 28, p. 2371–2381, doi:10.1002/rcm.7022.

Rosenheim, B.E., Swart, P.K., Thorrold, S.R., Willenz, P., Berry, L., and Latkoczy, C., 2004, High-resolution Sr/Ca records in sclerosponges calibrated to temperature in situ: Geology, v. 32, p. 145–148, doi:10.1130/G20117.1.

Schmid, T.W., and Bernasconi, S.M., 2010, An automated method for “clumped-isotope” measurements on small carbonate samples: Rapid Communications in Mass Spectrometry, v. 24, p. 1955–1963, doi:10.1002/rcm.4598.

Shackleton, N.J., 1973, Oxygen isotope analysis as a means of determining season of occupation of prehistoric midden sites: Archaeometry, v. 15, p. 133–141.

Stone, E.J., Lunt, D.J., Annan, J.D., and Hargreaves, J.C., 2013, Quantification of the Greenland ice sheet contribution to Last Interglacial sea level rise: Climate of the Past, v. 9, p. 621–639, doi:10.5194/cp-9-621-2013.

Turney, C.S.M., and Jones, R.T., 2010, Does the Agulhas Current amplify global temperatures during super-interglacials? Journal of Quaternary Science, v. 25, p. 839–843, doi:10.1002/jqs.1423.

Urey, H., 1947, The thermodynamic properties of isotopic substances: Journal of the Chemical Society (Resumed), p. 562–581.

Winkelstern, I.Z., Rowe, M.P., Lohmann, K.C., Defliese, W.F., Petersen, S. V., and Brewer, A.W., 2017, Meltwater pulse recorded in Last Interglacial mollusk shells from Bermuda: Paleoceanography, v. 32, p. 132–145, doi:10.1002/2016PA003014.

de Winter, N., Agterhuis, T., and Ziegler, M., 2021, Optimizing sampling strategies in high-resolution paleoclimate records: Climate of the Past , p. 1–52, doi:10.5194/cp-2020-118.

Zhang, J.Z., and Petersen, S. V., 2023, Clumped and oxygen isotope sclerochronology methods tested in the bivalve *Lucina pensylvanica*: Chemical Geology, v. 620, p. 121346, doi:10.1016/j.chemgeo.2023.121346.

Zhang, J.Z., Petersen, S. V., Winkelstern, I.Z., and Lohmann, K.C., 2021, Seasonally variable aquifer discharge and cooler climate in Bermuda during the last interglacial revealed by subannual clumped isotope analysis: Paleoceanography and Paleoclimatology, v. 36, p. 1–19, doi:10.1029/2020PA004145.

Chapter 2 Clumped and Oxygen Isotope Sclerochronology Methods Tested in the Bivalve *Lucina pensylvanica*[1]

2.1 Abstract

Geochemical signatures preserved within the geologic record can be used to reconstruct past mean temperature and seasonality, but in order to accurately apply any geochemical proxy method in the past, a rigorous study of how the recorded proxy is related to temperature in the modern setting must be conducted. Here, we assess the ability of multiple isotope techniques to correctly record mean annual temperature and seasonality in the bivalve *Lucina pensylvanica*. We compare subannual-resolution $\delta^{18}O$-based, seasonally-targeted and continuous high-resolution (H.R.) clumped isotope (Δ_{47})-based thermometry methods, as well as multiple data treatment methods for each, to determine which approach best matches known modern temperatures (maximum and minimum absolute temperature and annual temperature range), with the goal of defining the ideal sampling scheme for use on fossil shells. In *L. pensylvanica* shells collected from 7 sites, we observe neither mean temperature nor seasonal biases. Mean annual temperature is best matched by averaging all seasonally-targeted Δ_{47}-temperatures. Seasonality is best matched by averaging $\delta^{18}O_{carb}$-based temperatures from all summers and all winters before taking the difference. Of two data treatment approaches applied to the continuous high-resolution

[1] Zhang, J. Z., & Petersen, S. V. (2023). Clumped and oxygen isotope sclerochronology methods tested in the bivalve *Lucina pensylvanica*. *Chemical Geology*, *620*, 121346.

Δ_{47}-based temperatures, "data optimization" is apparently better at resolving smaller seasonal temperature differences. In contrast, "data smoothing" produces a temperature record unbiased by prior assignment of seasonal extremes and has the simultaneous ability to detect subannual variability in $\delta^{18}O_{w.}$ However, accurate application of H.R. Δ_{47} methods must balance sampling resolution and growth rate. If sampling resolution is high enough relative to the growth rate (~1pt/month or better), we recommend continuous high-resolution Δ_{47}-thermometry with data smoothing. If this resolution cannot be achieved due to slow growth rates or insufficient shell size, we recommend pairing subannual $\delta^{18}O_{carb}$-based and seasonally-targeted Δ_{47}-based temperature reconstruction to acquire seasonal range in temperature and absolute temperature extremes.

2.2 Introduction

Small changes in seasonal temperature extremes can affect multiple elements of the Earth's climate system. For example, warming winters have increasing Colorado's mountain pine beetle infestation (Negron and Cain, 2019) and warming summers over the Greenland Ice Sheet have exceeded the melting point, triggering extensive surface melting (Nghiem et al., 2012). Determining how seasonality has changed in the past across different mean climate states can help predict which areas may be impacted by uneven seasonal warming in the future. Quantifying past changes in seasonality can also be used to validate climate model simulations at a finer scale (Tierney et al., 2020) and improve mean annual temperature reconstructions through identifying seasonal biases in time-averaged proxy records (Ivany, 2012). However, in most paleoclimate studies, reconstructed temperatures are often limited to long-term annual means, and paleoseasonality is overlooked. This is especially true in deep time, due to a variety of

obstacles with the resolution and preservation of different climate archives (Ivany and Judd, 2021).

A common approach to reconstructing seasonal climate cycles in the past is through high-resolution oxygen isotope analysis ($\delta^{18}O$) of fast-accumulating biogenic archives such as corals, mollusk shells or sponges (Shackleton, 1973; Correge et al., 2006; Rosenheim et al., 2004). The oxygen isotopic composition of carbonate materials like shells or coral skeletons is related to the temperature of formation, equivalent to ocean temperatures for marine organisms (Epstein et al., 1953). Given the correct balance of sampling resolution and growth rate, sclerochronology, or sequential sampling of a shell or coral along its growth axis, can therefore reveal subannual changes in environmental/ocean temperature (Schöne et al., 2004; Wanamaker et al., 2009; Wanamaker et al., 2011; Trofimova et al., 2018). However, this method also requires knowledge of the oxygen isotopic composition of the surrounding fluid ($\delta^{18}O_w$) to reconstruct absolute temperatures (Epstein et al., 1953).

In many studies, $\delta^{18}O_w$ is assumed to be seasonally constant, albeit unknown, thus allowing calculation of the seasonal range in temperature from the measured range in $\delta^{18}O$ without quantitative knowledge of $\delta^{18}O_w$. However, without knowledge of $\delta^{18}O_w$, absolute maximum and minimum temperatures cannot be determined. The lack of direct knowledge of both the mean value and seasonal variability of $\delta^{18}O_w$ in ancient waters has limited the accurate application of the oxygen isotope paleothermometer in the past, both for paleoseasonality and mean temperature reconstructions. Paired measurements of trace element ratios and $\delta^{18}O$ have attempted to separate the influence of changing temperature and $\delta^{18}O_w$, but appear to require species-specific trace element calibrations, limiting their applicability further back in time

(Gillikin et al., 2005). More recently, carbonate clumped isotope thermometry has risen as a tool to reconstruct past temperatures in the absence of prior knowledge of $\delta^{18}O_w$ (Eiler, 2007).

Carbonate clumped isotope (Δ_{47}) paleothermometry is a thermodynamically-based isotope proxy that leverages the temperature dependence of the internal ordering of the heavy isotopes ^{13}C and ^{18}O within the carbonate mineral lattice, specifically the abundance of carbonate ions containing both of these heavy isotopes bonded together (Ghosh et al., 2006, Eiler, 2011). This method enables direct estimation of the formation temperature of a carbonate material, independent of the surrounding water composition and is applicable to all types of carbonate materials, with no species-specific calibrations known to be needed for bivalves (Eiler, 2011; Henkes et al., 2013; Eagle et al., 2013; Wacker et al., 2014; Huyghe et al., 2022). When combined with traditional carbonate $\delta^{18}O$ paleothermometry, this technique also allows the simultaneous reconstruction of $\delta^{18}O_w$, providing valuable information about the formation environment (Eiler, 2007).

Until recently, large sample size requirements have limited application of clumped isotope paleothermometry to paleoseasonality reconstruction. Early measurements required 8-16mg of $CaCO_3$ powder per replicate for a total of 24-48 mg for the typical three replicates (Ghosh et al., 2006; Tripati et al., 2010). Subsequently, sample sizes for individual replicates decreased to 3-5mg on most machines, still requiring 12-20mg in total to achieve good precision (Defliese et al., 2015; Daëron et al., 2016; Kelson et al., 2017). Compared to the 20-200 μg typically needed for single $\delta^{18}O$ analyses, this larger sample size requirement for Δ_{47} and need for triple replication largely prohibited the acquisition of subannual and/or high-resolution Δ_{47}-based temperature records (Keating-Bitonti et al., 2011).

Engineer advances now allow clumped isotope analysis of much smaller amounts of material (~150-450μg per replicate) on certain instrumental set ups (Kiel device, Schmid and Bernasconi, 2010; NuCarb device, Mackey et al 2020), opening the possibility of subannual Δ_{47} records. In one approach (Δ_{47} sclerochronology), individual aliquots drilled sequentially along the direction of growth, as in typical $\delta^{18}O$-based sclerochronology, are each analyzed once for Δ_{47}, then data from multiple adjacent aliquots is combined in different ways in post-processing ("smoothing", "binning", or "optimization") to reduce uncertainty on calculated temperatures (deWinter et al., 2021; Caldarescu et al., 2021; Agterhuis et al., 2022). Another approach that addresses seasonal temperature fluctuations while working within sample material constraints (called seasonally-targeted Δ_{47}) combines high-resolution $\delta^{18}O$-based sclerochronology with a few, targeted bulk Δ_{47} analyses. In this method, summers and winters are assumed to correspond to $\delta^{18}O$ minima and maxima, respectively (Zhang et al., 2021). These intervals are then re-drilled to acquire one larger homogenized sample per seasonal extreme, which is replicated three times (Zhang et al., 2021). Assuming summers and winters are correctly identified, this method quantifies absolute temperature extremes and seasonal $\delta^{18}O_w$ variability but does not produce a continuous annual record of changing conditions. Depending on shell size, growth rate, sampling resolution, drill bit size, and geochemical reproducibility for a given instrument, one of these methods may be preferable over the other.

As these techniques are newly being applied at subannual scale, it is prudent to first validate these approaches using modern shells collected from sites where climate parameters (mean annual temperature, seasonality, $\delta^{18}O_{sw}$) are known. Validation in the modern can identify any biases in how these isotopic parameters are recorded in the shell or measured in the lab before the techniques are applied to fossil shells. For example, some calcifying organisms such

as shallow water corals do not precipitate their skeletons in isotopic equilibrium with seawater, instead creating a calcifying fluid with a pH elevated relative to the surrounding seawater (Thiagarajan et al., 2011; Spooner et al., 2016), leading to offsets in Δ_{47} from values predicted for the known growth temperature. The presence of chemical symbionts in many species of the family Lucinidae (Taylor and Glover, 2000) raises the possibility of symbiont-induced vital effects, which could manifest as offsets in Δ_{47}, as seen in corals.

In this study, we aim to determine whether *Lucina pensylvanica*, and by extension related species of this genus, can correctly record mean annual temperature (MAT), maximum and minimum seasonal temperatures (Tmax and Tmin) and mean annual range in temperature ("seasonality" or MART). We compare results from $\delta^{18}O$ sclerochronology, seasonally-targeted Δ_{47} and Δ_{47} sclerochronology and assess how best to combine data from multiple years of shell growth to match modern climate most closely. We compare the performance of these different paleothermometry methods in areas with moderate (Florida) to more muted seasonality (Caribbean). Lastly, we discuss how to choose the most reliable sampling approach and data interpretation for paleotemperature and paleoseasonality reconstruction.

2.3 Materials and Methods

2.3.1 Lucina pensylvanica

The bivalve *Lucina pensylvanica* belongs to the family Lucinidae. *L. pensylvanica* first appeared in the Pleistocene (Taylor and Glover, 2000; Yanes et al., 2012) and fossils in the family Lucinidae have been found dating back to the Silurian (Taylor and Glover, 2006). Species within this family are found today across a latitude range of 9° to 35°N, and members of the broader order Lucinida live over an even wider latitude range from 55°S to 60°N (Allen, 1958;

Yanes et al., 2012). *L. pensylvanica* occupies predominantly shallow-water habitats, with substrates ranging from fine, intertidal muds to coarse sandy seagrass beds to organic rich sediments (Allen 1958; Taylor and Glover, 2000; Yanes et al., 2012). In at least 30 species within Lucinidae (including *L. pensylvanica*), symbiotic sulfur-oxidizing bacteria have been detected in the gill filaments, acquired from and specialized for the specific surrounding environment (Taylor and Glover, 2000; Brissac et al., 2011). Shells of *L. pensylvanica* consist of three distinct aragonitic layers, identifiable in hand-sample and under scanning electron microscopy (SEM).

Numerous studies on the feeding, respiratory systems, physiology, morphology, and mode of life of Lucinidae have been conducted (e.g., Allen 1958; Taylor and Glover, 2000; Yanes et al., 2012). However, little attention has been paid to their potential as a recorder of past climate and seasonality. Previous studies of *L. pensylvanica* from the Florida Keys and Bahamas suggest that this species spawns in the warm season (Bigatti et al., 2004) and grows rapidly until sexual maturity is reached at a size of 25mm in the Florida Keys (Taylor et al., 2004) or 18mm in the Bahamas (Yanes et al., 2012), after which growth rates slow down. In the Florida Keys, shell size asymptotes around 38 mm at a maximum age of 5 years (Culotta, 1988; Bigatti et al., 2004; Taylor et al., 2004). Studies suggest that shell growth in *L. pensylvanica* occurs year-round, but growth rates may decrease during the warmest months due to heat stress or reproduction (Bigatti et al., 2004; Yanes et al., 2012).

2.3.2 Study Areas and Modern Climatology

Seven single valves of *L. pensylvanica* were collected from three beaches in Florida and four in the Caribbean. Florida sites include Cocoa Beach (CBFL; 28.3°N, 80.6°W); Hollywood

Beach (HBFL; 26.0°N, 80.1°W); and Miami (25.7°N, 80.2°W). Caribbean sites include Montego Bay, Jamaica (18°N, 77°W); Cartagena, Colombia (10.3°N, 75.4°W); San Blas Island, Panama (9.5°N, 78.8°W); and St. Thomas, U.S. Virgin Island (18°N, 64°W) (Figure 2.1). All shells were collected between 2018 and 2020. Although deceased, separated and lacking all fragile external lamellae due to wear (Taylor et al., 2004), collected valves show no signs of dissolution or more significant wear, so are assumed to have died within the past few years and thus record recent seawater temperatures in their shell geochemistry. Shell collection was completed by the crowdsource citizens science program, allowing us to easily sample from multiple sites, leveraging travel of others.

Modern seasonal patterns in temperature and precipitation were determined for each site from the NOAA NCDC ERSST v5 and CRU 3.25 Global Precipitation Data Set, respectively (https://iridl.ldeo.columbia.edu/SOURCES/.NOAA/.NCDC/.ERSST/.version5/.sst/), by averaging the past 60 years of data (1960-2022). Observed monthly mean sea surface temperatures (SSTs) from the Florida sites range from 21.6-23.5˚C in winter and up to 29-29.9˚C in summer, respectively (Figure 2.S1A, Table 2.S2), with a seasonal range of 7.4˚C in more northerly CBFL and 6.4˚C in the more southerly HBFL and Miami. All three of these sites experience two-peak rainy seasons with highest rainfall occurring in June and August/September, although the peaks are quite muted in CBFL. Seasonal Variance in Precipitation (SVP), calculated as the difference between the rainiest and driest monthly precipitation means (Figure 2.S1B), ranges from 133 mm in CBFL to 183 in Miami to 196mm in HBFL.

In contrast, seasonality at the Caribbean sites is much more muted, ranging from 26-27°C in winter to 28.6-29.4°C in summer (Figure 2.S1A, Table 2.S2), for a total seasonal range of 1.8-

2.9˚C. SVP in the Caribbean sites is greater compared to Florida sites, with the greatest SVP occurring in Panama (266mm) due to high monthly rainfalls in May and October/November and in Colombia (219mm) due to very dry months of January/February (Figure 2.S1B). A two-peak rainy season is also experienced in all Caribbean sites, but the timing is different than in Florida, with the first peak occurring earlier (May) and the second peak occurring later (September/October/November) with moderately high rainfall in between (Figure 2.S1). Mean annual temperature (MAT) was calculated as the mean of 12 monthly mean sea surface temperature. Mean annual range in temperature (MART) was calculated as the difference between the warmest and the coldest month. Season-to-season range in temperature (SRT) was calculated as the difference between the summertime (Jun-Jul-Aug) and wintertime (Dec-Jan-Feb) 3-month mean sea surface temperatures. SRT is always smaller than MART, and may be a better comparison point when growth rates are slower and seasonally-targeted sampling combines multiple warm/cold months into a single sample.

2.3.3 Physical Parameters

Morphometric measurements were made on each shell, including 1) maximum valve length, from umbo to ventral margin; 2) maximum valve width, perpendicular to valve length, across the widest part of the shell; 3) valve weight (Figure 2.2). These parameters were compared to each other and to mean annual temperature and shell age, as defined by stable isotope sclerochronology profiles (see below) (Figure 2.3). One shell (CBFL) was imaged under scanning electron microscopy to confirm the assumption of minimal post-depositional alteration and visualize shell microstructures. Documenting the appearance of shell microstructures in

modern, well-preserved shell valves is a valuable reference point for future studies on fossil shells, where preservation is uncertain.

2.3.4 Sampling for Isotopic Analysis

All *L. pensylvanica* valves were sampled serially from umbo to ventral margin for $\delta^{18}O$ (and $\delta^{13}C$) sclerochronology. Drilling was conducted along the axis of maximum growth using a dental drill operated at its lowest speed (1000 RPM) to prevent frictional heating that can alter Δ_{47} (Figure 2.2). A 0.8mm scriber point carbide tip was used for $\delta^{18}O$ sampling; and a 1.4mm inverted cone carbide tip was used for Δ_{47} sampling. Drill holes were kept shallow as to only penetrate the outer most shell layer (~0.5 mm depth) to avoid crossing growth lines, and were spaced every ~1.5 mm, resulting in a resolution of 10-15 points per year of growth. Drilling began 8mm from the umbo on the Miami shell due to the outer layer being broken off nearest the umbo. Similarly, the drill path deviated laterally from the axis of maximum growth on the CBFL shell due to roughly ¼ of the shell being broken off near the ventral margin (Figure 2.S3).

Maxima and minima from each $\delta^{18}O$ profile were resampled using the same low speed dental drill to collect a total of ~20 mg of homogenized calcium carbonate powder per drill location for seasonally-targeted Δ_{47} analysis (Figure 2.2). Drill zones were extended laterally from the midline (axis of maximum growth) to gather enough material while minimizing time averaging (Figure 2.2). Final drill zone sizes ranged from 10 to 30 mm wide and 1 to 3 mm along the growth axis and were roughly 0.5 mm deep. Depending on the size of the shell and number of years of growth, 2 to 6 points were analyzed per shell for seasonally-targeted Δ_{47}.

Two *L. pensylvanica* specimens (Miami, Colombia) were chosen for high resolution (H.R.) Δ_{47} sclerochronology to test the ability to quantify seasonal variability in temperature and

$\delta^{18}O_w$ in a lower- and higher-seasonality environment using continuous sampling approaches. New samples were drilled from umbo to ventral margin, following the same sampling path and resolution as for $\delta^{18}O$ sclerochronology (Figure 2.2). For the Miami shell, approximately 3-4mg of powder was collected at each point, enough for a single replicate in "bellows mode" (see below). In contrast, for the Colombia shell, aliquots of 350-450 μg were drilled at each position for analysis in "coldfinger mode" (see below).

2.3.5 Stable Oxygen and Carbon Isotope Analysis

Each carbonate powder was analyzed for $\delta^{13}C$ and $\delta^{18}O$ using a Kiel IV automated carbonate preparation device attached to a Thermo-Finnegan MAT 253 or Delta V dual inlet mass spectrometer at the University of Michigan Stable Isotope Lab. Data was standardized against NBS-18 and NBS-19 with units reported in per mille (‰), relative to the VPDB standard, with a typical uncertainty of ±0.1‰ or less in both $\delta^{13}C$ and $\delta^{18}O$.

Assuming a constant $\delta^{18}O_w$ value, each $\delta^{18}O_c$ value was converted to temperature using the water-aragonite fractionation factor of Kim et al. (2007). Temperatures were derived using two different $\delta^{18}O_w$ values: 1) instrumental $\delta^{18}O_w$ values taken from either the GISS $\delta^{18}O_w$ database or new measurement as part of this study (see below), or 2) shell mean $\delta^{18}O_w$ values calculated by averaging 2-6 seasonally-targeted Δ_{47} measurements (see below).

2.3.6 Clumped Isotope Analysis and Data Processing

Clumped isotope analyses were carried out on a Nu Instruments Perspective isotope ratio mass spectrometer connected to a NuCarb automated carbonate sample preparation device in the University of Michigan Stable Isotope SCIPP Lab in one of two different modes (O'Hora et al.,

2022; Jones et al., 2022). “Bellows mode” was used for all seasonally-targeted Δ_{47} and Δ_{47} sclerochronology on the Miami shell. “Coldfinger mode” was used for Δ_{47} sclerochronology on the Colombia shell. These two different modes were each used to be able to compare and test the accuracy and applicability of each analysis type.

In “bellows mode”, approximately 3-4 mg of powder was loaded into an individual sample vial, placed in a carousel within the Nu Carb device (maintained at 70°C). 150µl of 105 wt. % H_3PO_4 was injected into the sample vial and after being isolated for the first five minutes to prevent vigorous bubbling driving acid into the valves, the vial was opened to a liquid-nitrogen cooled trap where CO_2 was collected for a further 15 minutes. Collected CO_2 was separated from water via two variable-temperature traps and cleaned of contaminants by passing over silver wool and a cryo-cooled trap containing PorapaqQ material (-30 °C, 15 minutes). Lastly, purified CO_2 was expanded directly into the sample bellow for analysis on the mass spectrometer. Both the sample and reference bellows are compressed to achieve 8e-8nA current on the major ion beam and were continuously adjusted between each cycle to maintain consistent beam intensity for the full 4 blocks of 20 cycles with no depletion. All seasonally-targeted Δ_{47} samples were replicated three or more times (separate acid reactions), spread out over a period of months to accommodate long-term variation in mass spectrometer behavior. Δ_{47} sclerochronology samples from the Miami shell were each measured a single time in this mode.

In “coldfinger mode”, individual aliquots of $CaCO_3$ are much smaller 300-450 µg, but are otherwise treated similarly in the reaction and purification steps. Instead of the (much smaller amount of) pure CO_2 gas being expanded into the bellows, sample gas is frozen into a small coldfinger directly adjacent to the change-over block. Reference gas fills an identical dummy coldfinger on the reference side to a matching pressure, then both are closed and allowed to

bleed gradually into the source for 3 blocks of 20 cycles. Pressures (and beam intensities) remain balanced while depleting over the full analysis. Δ_{47} sclerochronology samples from the Colombia shell were each measured a single time in this mode.

Δ_{47} values were calculated from raw voltages using an R-code script and Brand/IUPAC ^{17}O parameters, as described in Petersen et al. (2019). Δ_{47} values were projected into the I-CDES90 reference frame by fitting one line through ETH 1 and ETH2 in δ47 vs Δ_{47} space with a +0.003‰ adjustment for the difference between ETH1/2, then using all four ETH standards and defined I-CDES90 Intercarb values (Bernasconi et al., 2021) to create the empirical transfer function. Five in-house standards (calcitic Carrara marble "CM", aragonitic ooids from Joulter's Cay Bahamas "Ooids", an aragonitic coral mixture "CORS", an aragonitic gastropod *Cittarium pica* "Pica", and a cold-water aragonitic bivalve *Arctica islandica* "Ice") were run periodically to monitor for drift in corrected values through time. Final Δ_{47} values were converted to temperature using the temperature relationship of Anderson et al. (2021) because it was also anchored to ETH standards. Long-term reproducibility of Δ_{47} is 0.0189‰ (1sd) in "bellows mode" and 0.024‰ (1sd) in "coldfinger mode", based on ETH and in-house carbonate standard performance over a two-year period.

Carbonate $\delta^{18}O$ values synchronously acquired during analysis of each clumped isotope replicate were combined with the Δ_{47}-derived temperature for the corresponding replicate to calculate replicate/aliquot-level $\delta^{18}O_w$ values using the water-aragonite fractionation factor of Kim et al. (2007). For seasonally-targeted samples, 3-5 replicates were averaged to get a mean $\delta^{18}O$, $\delta^{13}C$, Temperature, and $\delta^{18}O_w$ for each distinct powder. Sample mean values from 2-6 seasonally-targeted powders per shell were combined into a shell mean Δ_{47}-derived Temperature and $\delta^{18}O_w$ value. The former was compared to MAT and the later was used to convert subannual-

resolution $\delta^{18}O_{carb}$ profiles to temperature profiles assuming $\delta^{18}O_w$ was constant (Figure 2.4). The same number of apparent summer and winter points were sampled in most shells, meaning these shell means should not be biased towards one season, with the exception of the Panama shell which had 2 summer and 1 winter. Metrics like standard deviation on these shell averages do not represent uncertainty in the MAT calculation, but instead reflect the magnitude of the seasonal cycle.

For Δ_{47} sclerochronology, aliquot-level $\delta^{18}O$, $\delta^{13}C$, Temperature, and $\delta^{18}O_w$ were combined in two different ways to reduce uncertainty, analogous to the triple replication of homogenous powders employed in seasonally-targeted Δ_{47} samples. In the first method ("smoothing"), a moving window covering N adjacent points was incremented through the whole record to create a smoothed profile (Caldarescu et al 2021; de Winter et al., 2021), where N=3 or 4 for "bellows mode" (Miami) and N=4, 5, or 6 for "coldfinger mode" (Colombia) due to their different long-term precisions. In the second method ("optimization"), samples are sorted based on their $\delta^{18}O_c$ values and averages were taken from only the few with lowest $\delta^{18}O_c$ values (supposedly representing the warmest times) or highest $\delta^{18}O_c$ values (supposedly representing the coldest times) regardless of their position in the profile (de Winter et al., 2021). Variable thresholds defining how many points fall into the warm/cold categories were applied, resulting in an increasing number of datapoints being averaged as thresholds approached each other (n=3 or 4; n=6; n=8 or 9; n=10 or 13; Figure 2.S9-2.11). A third data treatment method called "binning" has been demonstrated previously for Δ_{47} sclerochronology, where groups of adjacent points are averaged together in bins of varying sizes, guided by the structure of the $\delta^{18}O$ profile (Caldarescu et al, 2021). In that study, a much higher sampling resolution was used. Given our sampling

method and the growth rate of *L. pensylvanica*, we determined that this method was unlikely to be successful in our samples and did not pursue it further.

2.3.7 Determination of Seasonal Extrema and Inferred Growth Rate

An age vs. size profile for each specimen was determined from the subannual-resolution $\delta^{18}O$ profile, assuming each oscillation from peak to trough represented one year of growth. Although previous studies suggest *L. pensylvanica* spawn in the warm season, 6 out of 7 shells (excluding Miami) show isotope profiles beginning with high $\delta^{18}O$ values, inferred to be a colder season. It is likely that if not for the missing exterior layer deferring sampling to 8mm beyond the umbo, the Miami shell would also show high $\delta^{18}O$ values closest to the umbo. Therefore, in all shells the first $\delta^{18}O$ minima was assumed to be the first summer and was assigned an age of 0.5 years old. The following $\delta^{18}O$ maxima was then assigned to be the first winter at an age of 1 year old. Because shells from different sites lived different lengths of time, growth rates were compared based on length at the second summer.

2.3.8 Determination of Modern Seawater $\delta^{18}O_w$

We gathered existing $\delta^{18}O_w$ measurements from the NASA Goddard Institute for Space Studies (GISS) $\delta^{18}O_{sw}$ database (Figure 2.1, Table 2.S1) for the study region (5-45°N, 93-42°W) (LeGrande and Schmidt (2006); Schmidt et al. (1999)) (Figure 2.1). From this, we selected the closest modern water measurement to each study site, which varied from 34km away (Miami) to 700km away (Panama) (Table 2.S1). We supplemented this database with 14 new $\delta^{18}O_w$ measurements from sites in Florida, Atlantic Coast, and Puerto Rico (Table 2.S3). In two cases,

newly analyzed water samples provided a closer modern comparison point than was available from the GISS database.

Newly collected seawater samples were analyzed for $\delta^{18}O_w$ in the University of Michigan Stable Isotope Laboratory using a CO_2-water equilibration method, followed by analysis on a gas-sourced dual inlet mass spectrometer. To prepare samples for equilibration, vials with sealed septa were first flushed and filled with dry tank CO_2 to a head-space pressure of 1 atm. A 4 ml aliquot of sample or standard water was injected into each vial, then left to equilibrate in a 25°C water bath for at least 48 hours. After the equilibration period, pure CO_2 was extracted and dehydrated through repeated stages of cryogenic separation at -95°C on a custom-built vacuum extraction line (Figure 2.S2). Each extracted CO_2 sample was dividing into 3-6 aliquots which were separately flame sealed into Pyrex tubes for storage until analysis. Purified CO_2 was analyzed on a Thermo-Finnegan MAT 253 dual inlet mass spectrometer for at least 3 acquisitions of 12 sample-reference cycles at an m/z 44 beam strength of 16V.

Samples were run alongside in-house liquid standards which, in turn, were calibrated using USGS standards (USGS 45, 46), which were also run occasionally for validation. At least two aliquots of each unknown sample were measured on the mass spectrometer, spread out over weeks to accommodate variation in mass spectrometer behavior, and remaining aliquots were archived in case a third measurement was needed in the future. All new $\delta^{18}O_w$ values are presented relative to SMOW and can be found in Table 2.S2. Results have a typical uncertainty of ± 0.1‰ based on recurrent analysis of our in-house deionised water standard.

2.4 Results

2.4.1 Physical Parameters, Growth Rate, and Shell Size

Shell structures previously documented by Taylor et al. (2004) were observed under scanning electron microscope (SEM), including crossed-lamellar structures in both the middle- and inner-layers and irregular prisms of the pallial myostracum, confirming assumption of negligible post-deposition alteration (Figure 2.S4).

According to the age determination based on $\delta^{18}O$ sclerochronology profiles, 1.5 to 4 years of growth were observed, consistent with a maximum documented lifespan of 5 years (Bigatti et al., 2004). *L. pensylvanica* from the Florida sites lived 3.5-4 years, while the Caribbean *L. pensylvanica* lived around 1.5-2 years (Figure 2.3). Generally, shell length, width, and weight all increase in proportion, with the exception of the CBFL shell; valve length ranged from 20mm to 45mm, width ranged from 25 to 50mm and weight ranged from 1g to 15g (Figure 2.3). A piece of the CBFL valve was missing, representing roughly a quarter of its shell area, leading to underestimations of true shell weight. Despite being broken, accurate length and width estimates were still possible (Figure 2.3D-E, 2.S4). Regardless of total lifespan, 6 out of 7 shells follow the same length-to-age profile (Figure 2.3A, 2.3B). The apparent exception here is the shell from Jamaica. This shell was the largest and heaviest of the assemblage, reaching a final length of 45mm, yet only living 2 years according to the $\delta^{18}O$ sclerochronology profile (Figure 2.3A, 2.3B).

2.4.2 $\delta^{18}O$-based Temperature Reconstructions assuming fixed $\delta^{18}O_{sw}$

$\delta^{18}O$ values varied from around -2.0‰ to 0.0‰ for FL shells, while three of four Caribbean shells varied within a smaller range of -2.0‰ to -1.0‰ (Figure 2.S5). The shell from Colombia had the lowest absolute $\delta^{18}O$ values, ranging from -3.0‰ to -1.5‰ and a range of

variability (~1.5‰) more in line with the Florida shells than the other Caribbean shells (Figure 2.S5).

Agreement with instrumental MAT values was the closest when using Δ_{47}-based $\delta^{18}O_w$ values, leading to 5 out of 7 shells with estimated temperatures within 0.5°C of instrumental MATs. The other two shells (HBFL and Colombia) showed a slight cold bias, with 1.7 and 1.5°C offsets from the instrumental MAT values, respectively (Figure 2.5). Using instrumental/database $\delta^{18}O_w$ values instead changed MAT values by as much as 5-6°C in some cases. The greatest discrepancies were seen in sites where the closest available instrumental/database $\delta^{18}O_w$ value was still quite far from the shell collection site (Colombia, Panama, >500 miles away – Table 2.S1). Similarly, estimates of absolute summer and winter temperatures were closer to instrumental values using Δ_{47}-based $\delta^{18}O_w$ values.

$\delta^{18}O$-based MART values, which are a function of the magnitude of variability in $\delta^{18}O$ and not the absolute values, are unaffected by choice of $\delta^{18}O_w$. Calculated MART values in our 7 shells overestimate true seasonality by ~1-2°C in most sites. This overestimation in $\delta^{18}O$-based MART differs from previous study (Yanes et al., 2012), which suffered from insufficient sampling resolution (Figure 2.4-5, 2.S8). MART is significantly overestimated in Colombia (7.4°C vs. 2.4/1.4°C MART/SRT) and Panama (5.2°C vs. 1.8/1.2°C MART/SRT), potentially indicating a role of seasonally variable $\delta^{18}O_w$ at these sites, amplifying the fluctuations in $\delta^{18}O$. Summer/winter averaging reduces the estimated MART by both decreasing summertime estimates and increasing wintertime estimates (Figure 2.5). This results in better agreement with instrumental seasonal extremes and MART, potentially due to reduced weighting of outliers or single season extremes.

2.4.3 Seasonally-Targeted Δ_{47}-based Temperature Reconstructions

Seasonally-targeted Δ_{47} samples generally show warm/cool oscillations in line with expectations based on $\delta^{18}O$, implying correct identification of the position of seasonal extremes (Figure 2.4). An exception to this is the shell from CBFL, which shows a 'stair-step' pattern of temperatures increasing through time, but individual winters still cooler than adjacent summers (see Supplement).

Seasonally-targeted Δ_{47}-based mean annual temperature estimations (averaging n=2-6 samples/shell) result in excellent agreement (within 0.5°C) with instrumental MAT in 5 of 7 shells, excluding HBFL and Colombia (Figure 2.5). Typical methods of determining uncertainty such as taking a standard deviation would reflect the magnitude of the seasonal cycle in a given location as opposed to uncertainty in the average and therefore are not plotted or considered.

Δ_{47}-based MART reconstructions match true MARTs for the FL sites very well (<0.5°C offset), but overestimate MART for the Caribbean sites (Figure 2.S8C). This overestimated MART is most prominent in the Panama shell which estimates a MART 7.1°C greater than the instrumental MART. When Δ_{47} values from multiple apparent summer or winter zones were averaged prior to calculating a difference, the resulting MART estimate was reduced for all sites except USVI (Figure 2.5, Table 2.S2). This improved alignment with instrumental MART for the Caribbean sites but worsened it for Florida sites, CBFL especially (Figure 2.S8C-D). In the Caribbean sites, MART estimates are reduced by up to 3.2°C due to summer-winter averaging, yet this is still not enough to match the extremely low MART in these tropical sites (Figure 2.S8D). Averaging over more summers/winters would likely reduce theses MART estimates further, if shells with longer lifespans could be found from these sites.

$\delta^{18}O_w$ calculated from Δ_{47} are ranged as follows: -0.1 to +1.4‰ (CBFL), -0.2 to +0.9‰ (HBFL), 0 to +1.1‰ (Miami), -0.5 to +0.2‰ (Colombia), +0.3 to +1.1‰ (Jamaica), -0.2 to

+1.0‰ (Panama), +0.5 to +1.5 ‰(USVI) (Figure 2.S13). Mean values are within 0.5‰ of instrumental/database values for 5 of 7 sites (Table 2.S1). Larger differences occur where the database value comes from >500 miles from the shell collection site (e.g., Colombia). Mismatch of Δ_{47}-derived and instrumental $\delta^{18}O_w$ values from HBFL, which were collected from the exact same site as the shell, may indicate that the few-day period in which the modern waters were collected was not representative of the annual average, or that the beach-collected shell lived during a period where local $\delta^{18}O_w$ values were much different than today. Absolute $\delta^{18}O_w$ values depend heavily on the choice of $\delta^{18}O_w$-Temp-$CaCO_3$ calibration, for which there remains uncertainty in the aragonite-water system sufficient to explain the rest of the observed offsets (Zhou and Zheng, 2003; Kim et al., 2007).

2.4.4 High Resolution Δ_{47} Temperature Reconstructions - Optimization

The "optimization" method of processing Δ_{47} sclerochronology data returned very different results in the two shells analyzed. In the Colombia shell, estimates of summer and winter temperature were consistently close to each other, in line with the small instrumental MART at this site. Absolute MART (and uncertainty) decreased as thresholds were brought closer together and more points were averaged on either extreme (Figure 2.7, Figures 2.S10-12). The best estimate of MART was achieved by averaging the top 13 points and the bottom 11 points, which corresponds roughly to the top and bottom halves of the data (n=5 points excluded in the middle) (Figure 2.7). However, selecting such a large fraction of the data goes against the idea of isolating seasonal extremes. Averaging a randomly selected 13 points and 11 points resulted in a MART of ~3°C.

In the Miami shell, estimates of summer and winter temperatures and MART were similar regardless of thresholds used (less than 3°C variation in either extreme). However, all ranges were reversed from expectation, with the low $\delta^{18}O$ points corresponding to the colder temperature and vice versa. $\delta^{18}O$ values for the first four points of the sclerochronology profile disagreed between original $\delta^{18}O$ sclerochronology and $\delta^{18}O$ values acquired during H.R. Δ_{47} analysis, potentially leading to mis-assignment into a seasonal average using the optimization method (Figure 2.S6). Removing these four points reduced the reconstructed MART, but all ranges remained reversed (Figure 2.S12).

2.4.5 High Resolution Δ_{47} Temperature Reconstructions - Smoothing

In the Miami shell, the smoothing method estimated Δ_{47} values from 0.57 to 0.60‰ using a window size of n=3, equivalent to a temperature range of 21.9 to 31.9°C. This range is greater and temperatures are warmer than those estimated based on seasonally-targeted Δ_{47} points of 0.59 to 0.61‰ (temperatures of 21.1 to 28.1°C) (Table 2.S2). This is also warmer than the instrumental MART of 23.2-29.8°C, although it is well-centered. The mean H.R. Δ_{47} temperatures for the Miami shell is estimated to be 27.2°C compared to the instrumental MAT of 25.0°C. This slight positive bias may be the result of preferential growth during warmer months, leading to a volumetric weighting towards warmer temperatures when all equally-spaced points are combined. Comparing the midpoints of the estimated ranges leads to an even closer agreement (26.9 for H.R. Δ_{47} range vs. 26.5 for the instrumental range).

The structure of the "smoothed" record appears to align with the $\delta^{18}O$ reconstructed record. Low $\delta^{18}O$ zones occurring around 15-17mm, 28-30mm and 35-40mm (Figure 2.4, Figure 2.S5, Figure 2.6A) roughly correspond to low Δ_{47} zones around 17mm, 28mm, and 35mm

(Figure 2.7B, Figure 2.S5), with similarly aligning high $\delta^{18}O$ and high Δ_{47} zones in between. Around 8-10mm, Δ_{47} values are also low, which aligns with another low $\delta^{18}O$ zone in the $\delta^{18}O$ reconstructed record (Figure 2.S5, Figure 2.4). Re-drilled powders from this early portion surprisingly showed higher $\delta^{18}O$ values during H.R. Δ_{47} analysis, potentially due to drilling into different layers (Figure 2.S6).

$\delta^{18}O_w$ values estimated from data smoothing range from -0.3 to +2.2‰, with a mean of 0.9‰, which matches closely to the instrumental/database value of 1.0‰ (Table 2.S1). This differs from the mean $\delta^{18}O_w$ value from seasonally targeted Δ_{47} of 0.5‰. No coherent seasonal signal is observed aligning variation in $\delta^{18}O_w$ with identified seasonality in temperature. The $\delta^{18}O_w$ record is particularly invariant across the last two years of growth.

In the Colombia shell, increasing the window size reduced the estimated MART from 15.6 to 11.6 (Table 2.S2). However, even with a window size of n=6, the calculated temperature range of 21.7 to 33.3°C is still much larger than the range estimated from seasonally-targeted Δ_{47} measurements (23.0 to 28.3°C) or from the instrumental record (26.5-28.9°C) (Figure 2.6, 2.8). Despite this large overestimation in temperature range, the mean H.R. Δ_{47} temperature is well centered.

The shape of the $\delta^{18}O$ reconstructed record suggests two years of growth indicated by two summer peaks occurring around 8-10mm and 20-22mm and two winter peaks around 12-15mm and 25mm. In contrast, the H.R. Δ_{47} smoothed temperature record suggests one year of growth, indicated by a single "plateaued" summer extreme peaking around 10mm and a single winter extreme occurring around 20-22mm (Figure 2.6, S6). Given the small Colombia shell size (25X25mm), the 1-year growth estimated from H.R. Δ_{47} may be more reasonable. Assuming one

year of growth, the adjusted growth rate of the Colombia shell would match those of the USVI shell, which lived for 1.5 years with a shell size of 21X25mm (Figure 2.3).

$\delta^{18}O_w$ values estimated from data smoothing range from -0.8 to +1.7‰ in the Colombia shell, with a mean of 0.5‰ (Figure 2.6F). This differs from the mean $\delta^{18}O_w$ value from seasonally targeted Δ_{47} of -0.3‰, which was used to convert $\delta^{18}O$ sclerochronology to temperature in Figures 2.4 and 2.5, and the instrumental/database value of 0.7‰. If $\delta^{18}O$ sclerochronology was converted to temperature using 0.5‰, this would result in absolute temperatures closer to those estimated using the instrumental value. This is complicated by the fact that we observed a 0-0.5‰ offset between $\delta^{18}O$ values measured during $\delta^{18}O$ sclerochronology and both H.R. Δ_{47} analysis (Figure 2.S6) and seasonally targeted Δ_{47} analysis. Depending on which of these is more accurate, this could shift estimated $\delta^{18}O_w$ values by a similar amount and the subsequent $\delta^{18}O$-based temperatures by 0-2°C.

2.5 Discussion

2.5.1 Consistent Growth Rates and Shell Morphology, With a Few Exceptions

L. pensylvanica shells from all sites appear to follow the same length-to-age growth curve, which is also consistent with previous studies (Bigatti et al., 2004) (Figure 2.3A). The sole exception is the shell from Jamaica, which grew bigger, faster (Figure 2.3A). Weight is also elevated in this specimen relative to length and width (Figure 2.3D, 2.3E), indicating a thicker shell relative to others. The Jamaica site has one of the warmest mean annual temperatures of any site from this study, which may explain this prolific growth, yet Panama and Colombia have similarly warm climates but demonstrate ‘regular’ growth. After revisiting the growth curve for the Colombia shell to reflect 1 year of growth instead of 2 based on the Δ_{47} sclerochronology

data (smoothing), the inferred higher growth rate is larger than most other shells but still less than Jamaica.

After accounting for the missing outer layer in the first 8mm of the Miami shell, all new $\delta^{18}O$ profiles begin with high $\delta^{18}O$ values, indicating a winter start to shell growth. At first, this seems to contradict the early studies that show warm season spawning (Bigatti et al., 2004, Taylor et al., 2004, Yanes et al., 2012). We interpret these new results to suggest that following spawning, a measurable thickness of shell does not accumulate until the first winter season. Sampling nearest the umbo is either not close enough to the peak of the umbo to sample the true start of growth, or drilled too deeply, combining shell accreted in the first warm months with subsequent cooler months.

Shells from our study show a roughly 1:1 ratio of length to width (Figure 2.3F). This is consistent with a *L. pensylvanica* population from the Bahamas (Yanes et al., 2012), but another population from FL Keys (Taylor et al., 2004) show greater length to width, or a more elongated as opposed to circular shell shape. It's possible that this discrepancy is due to different methods of measuring width, although the magnitude of the difference (~10mm) seems too great for this explanation, given the circularity of the shells. If real, this may suggest population-scale morphological change.

2.5.2 Temperature Reconstructions Assuming Fixed $\delta^{18}O_{sw}$

Typical studies employing $\delta^{18}O$-based paleothermometry usually assume a constant $\delta^{18}O_w$ value (Schöne et al., 2004, Jones et al., 2005). However, without accurate knowledge of $\delta^{18}O_w$, the converted maximum and minimum temperatures, and MATs can be skewed in either direction. This is demonstrated through $\delta^{18}O$-based temperature ranges calculated using the GISS

database $\delta^{18}O_w$ value, which is representative of a "best guess" modern estimate that might be used in a paleoclimate study. Temperatures estimated using database $\delta^{18}O_w$ values are both too high (Colombia) and too low (USVI). Best alignment with MAT and summer/winter temperatures was achieved when the selected $\delta^{18}O_w$ value was located close to the shell collection site. The agreement deteriorates as the selected $\delta^{18}O_w$ values were recorded farther away from shell collection site, like in Colombia and Panama (Figure 2.5, Table 2.S1).

Better agreement in MAT and MART estimates with instrumental values was achieved when using Δ_{47}-based shell mean $\delta^{18}O_w$ values, which should reflect a highly localized estimates of $\delta^{18}O_w$, therefore more accurate than database values. This indicates at least one method of estimating $\delta^{18}O_w$ using Δ_{47} analysis should be conducted in all paleoclimatology studies. In increasing order, a single bulk Δ_{47} analysis (drilled to average over a large portion of the shell), the mean of multiple seasonally-targeted Δ_{47} analysis, or the mean of continuous H.R. Δ_{47} analyses should be used to convert H.R. $\delta^{18}O$ values into a record of seasonal temperature variability.

However, all of these approaches still assume seasonally invariable $\delta^{18}O_w$, which may not be the reality in some environments. This is reflected through observation that $\delta^{18}O$-based MART estimates in Colombia, Panama and USVI that assume constant $\delta^{18}O_w$ overestimate instrumental MARTs by up to 5°C, likely indicating seasonally variable $\delta^{18}O_w$, which is amplifying the fluctuations in $\delta^{18}O$. In the sections below, we discuss two cases differently effected by seasonally variable $\delta^{18}O_w$ from this study.

2.5.3 Seasonally Variable $\delta^{18}O_w$ and Moderate Temperature Seasonality: Miami

Seasonally-targeted Δ_{47} measurements for the Miami shell follow the expected pattern of warm/cool oscillation, with apparent summer intervals ($\delta^{18}O$ minima) tending to produce warmer temperatures than those targeting apparent winter intervals ($\delta^{18}O$ maxima), implying correct identification of seasonal extremes and limited variability in $\delta^{18}O_w$. However, $\delta^{18}O$-based MART estimates slightly overestimate true MART, suggesting $\delta^{18}O_w$ is in fact varying and that variation amplifies the $\delta^{18}O$ range. To achieve amplification of the $\delta^{18}O$ range, the highest (lowest) $\delta^{18}Ow$ values must occur during the coldest (warmest) times.

H.R. Δ_{47} analysis with data smoothing, producing subannual temperature and $\delta^{18}O_w$ records, is independent of any assumptions about seasonal timing or magnitude of $\delta^{18}O_w$ variability, or *a priori* assignment of the position of summer/winter shell growth. This method does a very good job capturing true seasonality over multiple years (Figure 2.6). This appears worse in the absolute range (Figure 2.5) due to single-point extrema that lie outside of the true range. However, Figure 2.6 clearly shows that for three of four years of growth, the summers and winters align well with instrumental temperatures. This suggests that summer/winter averaging of the smoothed record would perhaps result in the best estimate of seasonal temperature extremes and MART.

Supporting above inferences that $\delta^{18}O_w$ is varying, the continuous $\delta^{18}O_w$ profile calculated from seasonally targeted Δ_{47} shows variation of ~1.1‰, although error bars are large. There is no coherent seasonal signal in this $\delta^{18}O_w$ profile. The first two years contain most of the variability, whereas the latter two years are relatively invariant. Variability of ~0.6‰ in $\delta^{18}O_w$ near Miami have been observed in a short 1.5-year-long record from 1989-1991 (Leder et al., 1996), and measured $\delta^{18}O_w$ extrema similarly did not show any coherent seasonal

pattern. This suggests that this record is accurately capturing real (highly variable) patterns of $\delta^{18}O_w$ variability around Miami.

Although H.R. Δ_{47} measurements with data optimization appears to capture the MART and absolute seasonal extremes well, the summers and winters are reversed (Figure 2.7-2.8). When $\delta^{18}O_w$ values are varying unpredictably at the subannual scale as suggested above by both instrumental measurements and H.R. Δ_{47} with data smoothing, using absolute thresholds for $\delta^{18}O$ values can be inaccurate because $\delta^{18}O$ values of seasonal extremes may not always be the same. This is particularly apparent in the wintertime $\delta^{18}O$ values in the Miami shell, which vary from 0 to -1.3‰.

Overall, in a situation with unpredictable, highly variable $\delta^{18}O_w$ patterns, H.R. Δ_{47} with data smoothing works very well. Both $\delta^{18}O$-based methods assuming fixed $\delta^{18}O_w$ and H.R. Δ_{47} with optimization which assumes correct identification of seasonal extremes perform worse and are not recommended.

2.5.4 Seasonally Variable $\delta^{18}O_w$ and Low Temperature Seasonality: Colombia

$\delta^{18}O$-based MART estimates assuming constant $\delta^{18}O_w$ significantly overestimate true MART in tropical Colombia (Figure 2.4), suggesting high variability in $\delta^{18}O_w$ throughout the year. This could possibly be occurring in-phase with temperature changes (highest $\delta^{18}O_w$ during coldest months and vice versa), amplifying the apparent seasonal cycle in $\delta^{18}O$. However, due to the extremely low true MART in Colombia, even moderate $\delta^{18}O_w$ variability could falsely create an apparent seasonality in $\delta^{18}O$ that would lead to misidentification of seasonal extremes. If $\delta^{18}O_w$ cycled from lower to higher values multiple times within a single year, this could result in a $\delta^{18}O$ record suggesting more years of growth than in fact occurred.

Misidentification of seasonal extremes in the $\delta^{18}O$ record is supported by multiple lines of evidence. Seasonally-targeted Δ_{47} show a confused pattern in the Colombia shell, with one of the most glaring mis-matches with expected seasonality occurring in the first "summer" sample (Figure 2.4). H.R. Δ_{47} with data smoothing suggests only one instead of two years of growth, with the summer aligning with a $\delta^{18}O$ minima (as precited), but the winter aligning with the second $\delta^{18}O$ minima (previously inferred to be a second summer). This divergence in the number of years of growth suggests $\delta^{18}O_w$ cycling more than once per year, but this is not reflected in the smoothed H.R. Δ_{47}-based $\delta^{18}O_w$ record, which shows highest values in the fall season and lowest in the winter season (-0.8 to +1.7‰).

There is substantial evidence supporting $\delta^{18}O_w$ variability in Colombia. Colombia has the second highest seasonal variation in precipitation (SVP) of any of our sites, experiencing 219mm difference in monthly rainfall between the wettest and driest month. The rainy season, which would deliver precipitation that was depleted in heavy isotopes compared to seawater, occurs during the warm season of May-October, with dual peaks in May and October and very dry conditions conducive to evaporative enrichment in January-March (Figure 2.S1). In addition to the local rainfall, the Dique Canal discharges 55-250 m^3/s freshwater from the greater Magdalena River watershed into Cartegena Bay, driving significant salinity gradients of ~30 psu between surface and bottom waters and ~10+ psu variations in surface waters between the rainy seasons and dry season (Tosic et al., 2019). The timing of discharge is slightly delayed from local rainfall, with two peaks in June-July and November-December, and lowest values in February-April. Taken together, this complicates predictions of the exact timing of $\delta^{18}O_w$ variability, but suggests a complex pattern of subannual $\delta^{18}O_w$ variability is highly plausible.

Surprisingly, despite the apparent inaccuracy of seasonal identification based on $\delta^{18}O$, it appears H.R. Δ_{47} measurements with data optimization achieved best agreement with observed seasonality for the Colombia shell. Particularly with an increased window size, averaging the top 13 points and the bottom 11 points, the calculated range becomes perfectly aligned with its small instrumental MART (Figure 2.7). This is the only method to result in such a low MART. However, this is likely due to larger number of datapoints being combined here rather than superior data combination strategy. When only averaging 3-4 datapoints, the optimized H.R. Δ_{47} MART estimated for the Colombia shell was much warmer than its instrumental MART. When true seasonality is low, averaging any half of the points will result in a value close to the MAT. The alignment of the summer, as inferred from smoothed H.R. Δ_{47}, with the first low $\delta^{18}O$ peak around 5-10mm likely kept the inferred summer temperature above the inferred winter temperature using any thresholds.

In a situation where $\delta^{18}O_w$ varies multiple times per year, using any method that requires assigning position of seasonal extremes using the $\delta^{18}O$ record is a poor choice. This is especially true in a location with low temperature seasonality. (If temperature seasonality was high, such as in a mid-latitude site, temperature seasonality could overprint low to moderate $\delta^{18}O_w$ variability and still result in correct seasonal identification.) Although the H.R. Δ_{47} with smoothing should have given us the best results, this method still overestimated MART significantly, perhaps due to increased uncertainty in coldfinger mode. Despite the overestimation in MART, the mean of all H.R. Δ_{47} points best matches MAT.

2.5.5 Choosing the Best Method: Sample Size vs. Growth Rate vs. Analytical Resolution

A single measurement of Δ_{47}, un-replicated, has a large uncertainty which is mostly a function of integration time. The two measurement modes on the Nu Perspective used in this study ("bellows mode" for 3-4mg aliquots and "coldfinger (CF) mode" for 300-400µg aliquots) have different single-replicate uncertainties due to different integration times (80 vs. 60 cycles, respectively), best quantified by the long-term standard deviation of carbonate standards (sd=0.018‰ for bellows mode, sd= 0.024‰ for CF mode). On a Kiel device (as used by de Winter et al., 2021), a single replicate of 80-250µg only runs for 20 cycles, resulting in larger single-replicate uncertainty (long-term 1sd = 0.04‰). These uncertainties are reduced in the ultimate sample mean through replication. Depending on which of these methods are used, a different number of replicates are needed to achieve a temperature estimate with a desirably low uncertainty of ~1-2ºC, equivalent to ~0.010‰ 1SE in Δ_{47} at Earth surface temperatures. In bellows mode, 3-4 replicates are needed, compared to 5-6 for CF mode and 15-18 for Kiel-based measurements. On average, temperature error on a sample with more than 3 replicates measured in bellows mode is about 2-3 ºC.

When sampling for H.R. $\delta^{18}O$ or Δ_{47} sclerochronology, the physical sampling resolution is limited by the size of the drill bit and the spacing between drilled points, regardless of the total shell size or annual growth rate. Assuming sampling is conducted with essentially no spacing between each sample point, the maximum number of points per unit distance along the growth axis is defined by the width of the drill bit alone (e.g. with a 1mm drill bit, you can achieve 1 point per mm). To go to even higher resolution, "trough sampling" can be used, where the drill bit shaves off a thin slice of material that is thinner than the drill bit width, leaving behind a trough. This trough sampling results in less powder per point as the distance along the growth axis is smaller, so widening of the trough from side to side, tracing growth bands, ("lateral

extension") is often needed to acquire enough material. This is often done with a micromill, which uses a computer-controlled drill to carefully drill out designated pathways. Lateral extension is only possible when sampling the top surface of the shell where growth bands are visible and is not possible when drilling on the interior surface of a cross sectioned shell (Figure 2.9). Lateral extension can also be used to acquire larger amounts of material for more material-intensive methods like bellows mode.

Growth rate, total lifespan and shell size should be considered when selecting the most effective clumped isotope sampling approach. Growth rate (mm along growth axis per year of life) translates points per unit distance into points per unit time (e.g. points/year of growth). More importantly for the purposes of seasonality estimation, the growth rate combined with the sampling resolution defines the number of points per seasonal extreme. In order to capture the full magnitude of seasonal variability, a resolution of >1 point per month must be achieved, whether for $\delta^{18}O$ or H.R. Δ_{47} analysis. If shell growth rates are too slow, a single drill hole will combine material from multiple months of growth and produce a seasonal average instead of a warmest or coldest month mean. Total shell size defines the ability to extend drill points laterally to acquire more sample powder from a similarly narrow unit of time/distance. Total lifespan determines the number of years of growth that can potentially be averaged together, such as in the summer-winter averaging method.

In the above study, we demonstrated that H.R. Δ_{47} with data smoothing produces the best estimates of absolute summer and winter temperatures and MART because this method 1) does not assume the position of seasonal extremes; 2) does not assume that $\delta^{18}O_w$ is constant throughout the year; and 3) does not require prior knowledge of the mean $\delta^{18}O_w$ value. However, in order to achieve robust temperature estimates for seasonal extremes and MART, enough

points per seasonal extreme must be sampled and averaged together. Depending on the analytical methods used, at least 3 replicates/aliquots and possibly as many as 20 replicates/aliquots must be averaged. This may not be achievable if growth rates are too slow, drill bit and/or point spacing is too large, or shell size is too small. Figure 2.9 describes the recommended oxygen and clumped isotope sampling approach for different shell growth rates.

In fast growing shells (>20mm/yr), sampling resolution of ~1mm between points (such as that achieved in this study using a hand drill) will easily result in 12-20 pts per year, 1-2 points per month, or 4-6 points per season. In this regime, we recommend H.R. Δ_{47} sampling for bellows mode with smoothing, acquiring 3-4mg single aliquots along the whole transect, using lateral extension and growth band tracing to acquire enough material per aliquot. In bellows mode, a smoothing window of n=3 is sufficient, which under this high growth rate scenario would combine material from at most 2 adjacent months, capturing seasonal extremes well. H.R. Δ_{47} with smoothing using CF mode would also be possible, as a smoothing window of n=6 would still likely be able to capture a single season average, but not the single warmest or coldest month by itself. This is demonstrated by the Colombia shell (Figure 2.6). CF mode becomes increasingly applicable as growth rates increase.

In a shell with an intermediate growth rate (10-15mm/yr), sampling resolutions of ~1 point per month, or ~3 points per seasonal extreme would still allow H.R. Δ_{47} with smoothing using bellows mode, where the window size of n=3 would capture a seasonal extreme but not quite the single warmest/coldest month. This is demonstrated by the Miami shell (Figure 2.9). H.R. Δ_{47} with smoothing using CF mode would not be a good choice for slower growing shells, as the larger window size would necessarily combine aliquots from shoulder seasons, resulting in

muted estimates of MART. If growth rates get slower than this, there are insufficient points per month or points per season for H.R. Δ_{47} methods.

When growth rates are intermediate (10-15mm/yr) or slow (<6mm/yr) and H.R. Δ_{47} methods are not possible, seasonally-targeted Δ_{47} approach combined with H.R. $\delta^{18}O$ sclerochronology can substitute. Although this method requires proper identification of seasonal extremes from $\delta^{18}O$ profiles, by averaging many replicated Δ_{47} samples from across the shell, mean $\delta^{18}O_w$ values and MAT estimates become more robust. Whether ~1-2 points per seasonal extreme (slow growth) or ~3-4 points per seasonal extreme (intermediate growth) are achieved in $\delta^{18}O$ sclerochronology, a single homogenous powder can be drilled from the appropriate growth interval, with lateral extension tracing the growth band if needed to increase material acquired. Depending on the thickness of the growth interval in question and limitations on lateral extension due to total shell size or preservation, this could be ~12-15mg replicated 3-4 times in bellows mode (as demonstrated in all 7 shells, Figure 2.9) or ~2mg replicated 5-6 times in CF mode. In smaller shells, tracing growth bands laterally without risking drilling into other layers may be more difficult, favoring CF mode.

If lateral sampling is too difficult due to small shell size or poor exterior preservation, seasonally-targeted Δ_{47} sampling can be replaced with a single bulk Δ_{47} sample. Preferably, this is done by drilling a long transect along the growth direction or a wide hole near the ventral margin, both intended to average multiple years of growth. Some organisms shut down growth during certain seasons, so this bulk measurement may not necessarily represent mean annual conditions. This can often be determined from $\delta^{18}O$ profiles.

Lastly, $\delta^{18}O$ sclerochronology is routinely conducted on a cross-sectioned shell because growth bands are most visible from this view. When sampling the exterior, we extended our drill

spots laterally, following a curved path delineated by growth bands to capture more material while limiting time averaging. However, when drilling into the cut face, lateral extension like this is impossible because curvature of growth bands from the center to the edge of the shell is hidden within the shell interior and the risk of drilling into adjacent growth intervals is great. In this case, HR Δ_{47} with CF mode can acquire both $\delta^{18}O$ and Δ_{47} sclerochronology (Figure 2.9). If growth rates are high enough, such as in the younger portion of some shells, data smoothing with CF mode may be able to estimate warmest/coldest month, or seasonal extremes. If growth rates are slower, overall or towards the ventral margin, H.R. Δ_{47} with smoothing will not work, as in the slow growing shells described above. Here, we suggest bulk Δ_{47} combined with $\delta^{18}O$ sclerochronology.

Kiel-derived Δ_{47} sclerochronology requires many more aliquots per season to work properly, but each aliquot can be smaller. This is conducive to "trough sampling" often drilled via micromill, where very small aliquots can be acquired with confidence. A recent study by Caldarescu et al (2021) conducted high resolution Δ_{47}-based sclerochronology with similar data averaging strategies, with very small aliquots analyzed using a Kiel device. The bivalve used (*Megapitaria aurantiaca*) was much larger and faster growing compared to *L. pensylvanica*, ranging from 50 to over 100mm in length, providing more surface area for higher resolution sampling (Lopez-Rocha et al., 2021). They averaged together anywhere from n=14 to n=61 points per season. As in our study, they were able to achieve good agreement with instrumental temperatures.

Taken together, any of the analytical methods can be used (bellows, CF mode, or Kiel-based Δ_{47}), but the variable precision of these methods must be balanced against sampling

resolution, growth rates, and shell size (Figure 2.9). In this way, our results from *L. pensylvanica* can be generalized for any bivalve species.

2.6 Conclusions

In this study, we applied multiple isotope techniques to modern *L. pensylvanica* collected from seven locations, spanning ~20° in latitude, to assess their ability to correctly record mean annual temperatures and seasonality and to establish the most reliable sampling approach and data treatment method for paleotemperature/paleoseasonality reconstruction. Altogether, we did not observe any seasonal, mean temperature, or biologically-induced (species-specific) biases in modern *L. pensylvanica*, suggesting species from within the same genus and/or family could serve as reliable paleotemperature/paleoseasonality recorders for future work.

$\delta^{18}O$-based reconstruction of MART best matched modern MART, especially after averaging multiple summers and winters. However, without knowing the regional $\delta^{18}O_w$ values, $\delta^{18}O$-based reconstructions do not accurately capture absolute summer and winter temperature extremes. This can be improved using a seasonally-targeted Δ_{47}-based sampling approach. Yielding sub-annual scale Δ_{47}-temperatures as well as $\delta^{18}O_w$ values, this approach allows for seasonal variations in $\delta^{18}O_w$ and produces more reasonable max-to-min ranges and the best estimates of MAT.

The best method for reconstructing MAT, MART and absolute seasonal temperature extremes while allowing for and directly quantifying variability in $\delta^{18}O_w$ is H.R. Δ_{47} with data smoothing. This method removes the need to assign the position of seasonal extremes based on the $\delta^{18}O$ profile. However, in order to effectively apply H.R. Δ_{47}-based reconstructions, a delicate balance must be struck between analytical method used, physical sampling resolution,

shell size and growth rate. Ideally a minimum of 3-4 Δ_{47} aliquots per season should be drilled for this approach and analyzed using bellows mode for best precision, as demonstrated in the Miami shell. Using the coldfinger mode can reduce the amount of total powder needed for analysis, but much higher sampling resolutions (6+ per season) are needed to overcome the lower reproducibility of this analytical mode. *L. pensylvanica* is not well suited for this type of approach due to its smaller size and slow growth rate, as demonstrated by the Colombia shell. Larger, faster growing shells should be selected for best estimation of subannual temperatures using H.R. Δ_{47}.

For species with slow to intermediate growth where H.R. Δ_{47} with data smoothing may not be possible, we suggest different sampling methods. Summer/winter averaged seasonally-targeted Δ_{47}-based reconstruction coupled with summer-winter averaged $\delta^{18}O$-based reconstruction using Δ_{47}-derived $\delta^{18}O_w$ values are recommended for estimating seasonality and MATs in this situation. Data optimization should only be applied when $\delta^{18}O_w$ is independently known to be constant. In the slowest growing shells, a single bulk Δ_{47} sample combined with $\delta^{18}O$ sclerochronology can provide a better constraint on $\delta^{18}O_w$ than database $\delta^{18}O_w$ values, and lead to better absolute seasonal temperature estimates derived from $\delta^{18}O$.

Our results on *L. pensylvanica* can thus be generalized to all bivalves to dictate ideal sampling approaches. This study, combined with other recent studies (de Winter et al., 2021; Caldarescu et al 2021; Agterhuis et al 2022) increasingly demonstrate the power of using clumped isotopes at the subannual scale. Subannual paleoclimate data can provide new insight into the more tangible effects of climate change beyond changes in mean annual temperature.

2.7 Acknowledgements

We thank Lora Wingate, Steven Wedel, Kyger C. Lohmann, Ashling Neary and Justin VanDeVelde for isotope laboratory assistance at the University of Michigan. We thank S.T. Petersen, S.Wedel, R. Dzombak, M. Mustafa and the University of Michigan department of Earth and Environmental Sciences for crowd-sourcing shell collection. This project was supported by National Science Foundation grant 1903237, Sloan Research Fellowship 2022 to S.V. Petersen, National Science Foundation GRFP, Rackham Graduate School Merit Fellowship and University of Michigan Turner Grant to J.Z. Zhang.

2.8 Appendices

2.8.1 CO_2 Seasonally-Targeted Δ_{47}-based Temperature Reconstructions: Cocoa Beach, FL Shell

Seasonally-targeted Δ_{47} samples generally show the expected pattern of warm/cool oscillation, with apparent summer intervals ($\delta^{18}O$ minima) tending to produce warmer temperatures than those targeting apparent winter intervals ($\delta^{18}O$ maxima). An exception to this is the shell from CBFL, which displays a "staircase" pattern where each paired summer is greater than the preceding winter temperature, but year-to-year variation exceeds within-year variation (Figure 4). In the Florida sites, summer/winter averaging reduced MART estimates by up to 6°C (CBFL), leading to a significant underestimation of true MART (Figure S8D). In the CBFL shell, the extreme reduction in MART to near zero is driven by the observed "staircase" pattern in Δ_{47}-based temperatures, with each following annual cycle appearing warmer than the previous one (Figure 4). When taking full max-to-min/MART on this shell, it appears to be capturing the overall annual variability, however, due to its "stepping up" pattern, when averaging the multiple

summers/winters together, the range becomes unreasonably low. We can think of no reasonable explanation for this ‘staircase’ pattern, and thus attribute it to an undiagnosed instrument issue with a few of the samples.

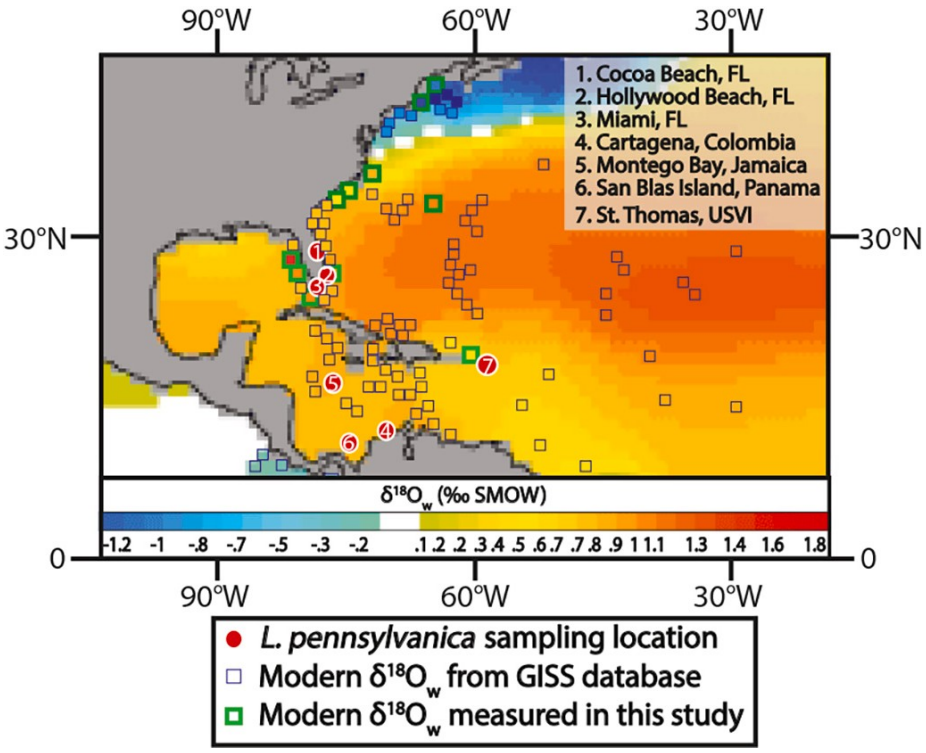

Figure 2.1. Location of study sites.

Background plotted using modified LeGrande and Schmidt (2006) global gridded data model. Detailed information on measured modern $\delta^{18}O_w$ values can be found in supplement. Color inside the $\delta^{18}O_w$ points are GISS/measured values overplotted onto the gridded model.

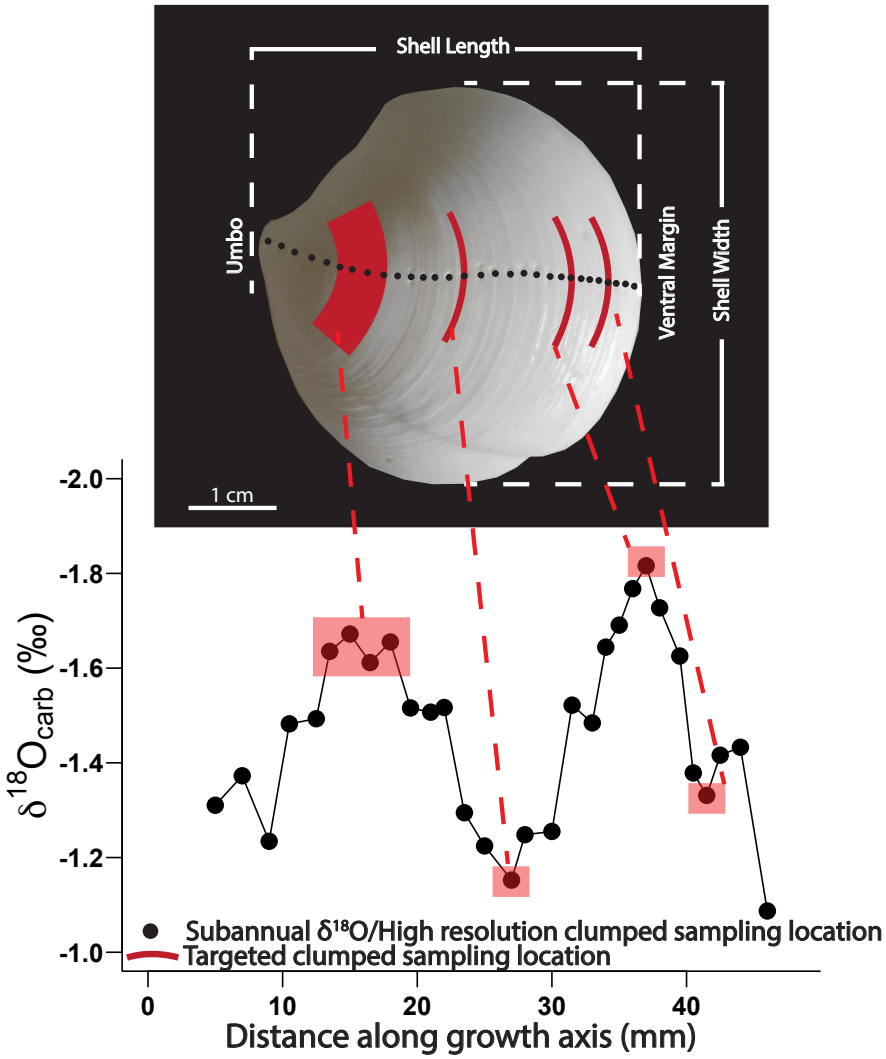

Figure 2.2. Annotated image of modern *L. pensylvanica* shell.

L. pensylvanica shell sampled from Jamaica, showing high resolution $\delta^{18}O/\Delta_{47}$ drilling spots (black) and larger seasonally-targeted Δ_{47} sampling locations (red) as well as morphometric measurements

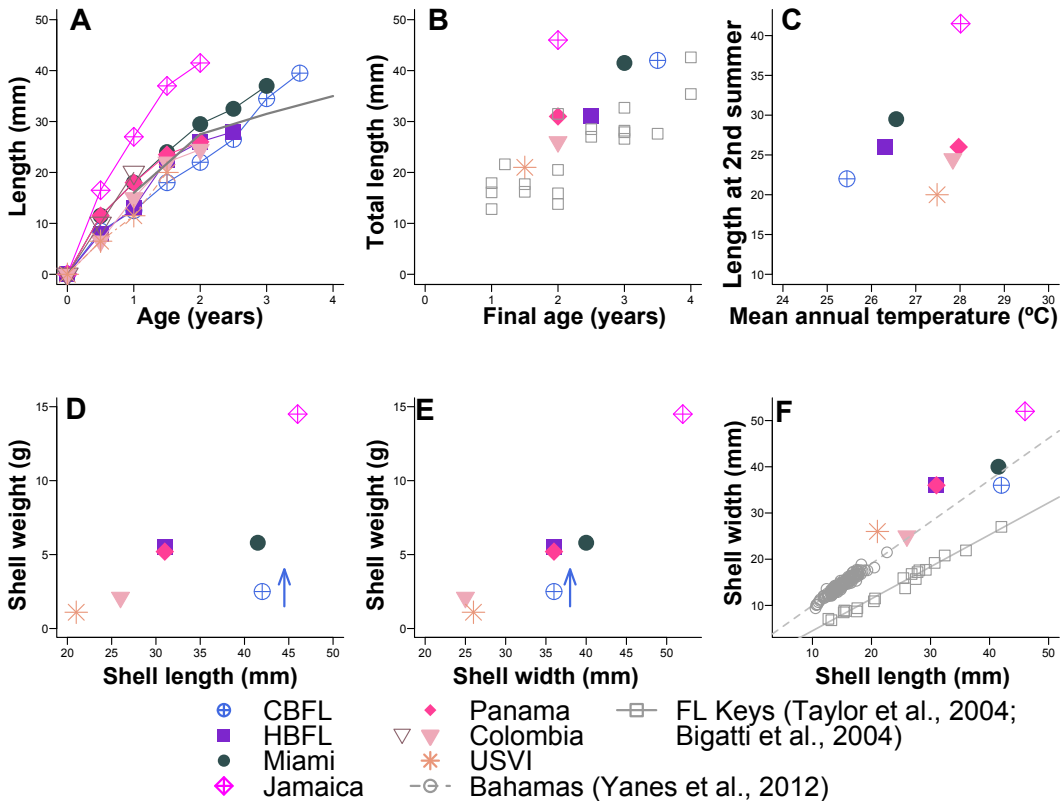

Figure 2.3. Linear morphometric measurements of seven *L. pensylvanica* shells

Physical parameter data from this study and two previous studies (Taylor et al., 2004; Bigatti et al., 2004; Yanes et al., 2012) are included here for comparison. Growth adjusted for the Colombia shell based on H.R. Clumped measurements (See discussion).

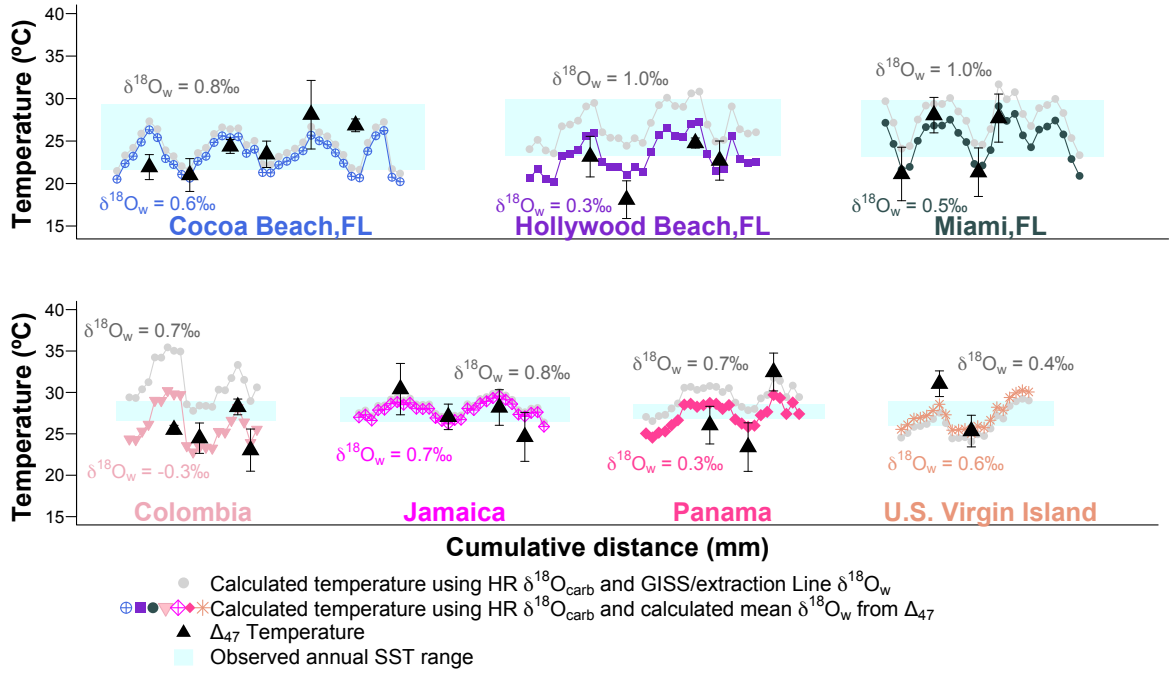

Figure 2.4. Reconstructed temperature profiles of seven *L. pensylvanica* shells via different isotope methods.

$\delta^{18}O$ sclerochronology converted to temperature assuming constant $\delta^{18}O_w$, using either the mean $\delta^{18}O_w$ calculated from the 2-6 Δ_{47} points shown (colored points) or $\delta^{18}O_w$ measured in modern seawater as part of this study or from the NASA GISS database, whichever was geographically closest (grey points) (Table 2.S1).

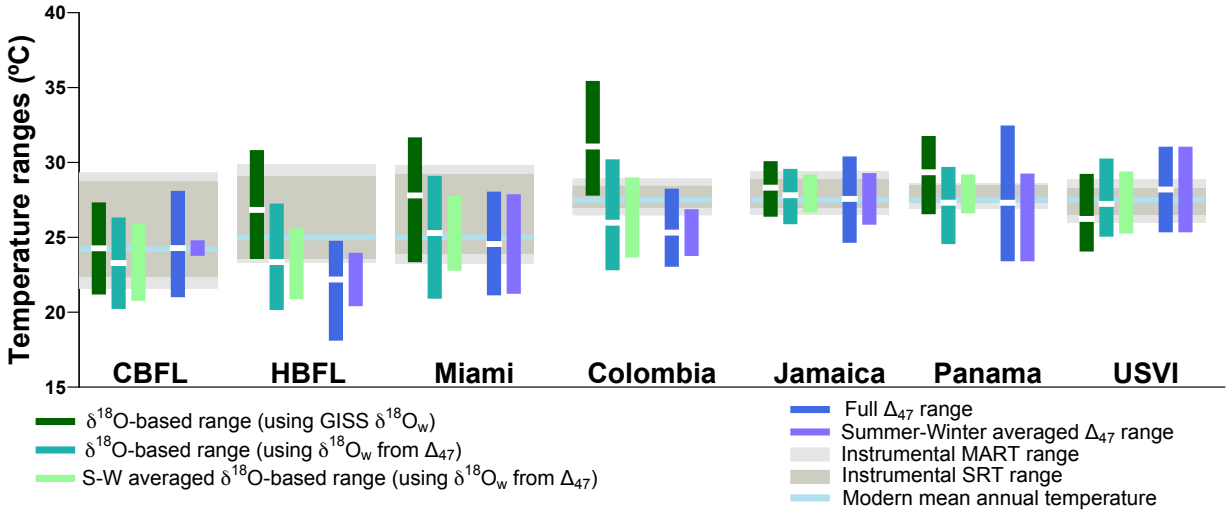

Figure 2.5. Range and mean value comparison of reconstructed temperatures via different isotope methods.

White bars indicate mean values, calculated as the mean of all temperatures in a given shell profile. S-W= Summer-winter. GISS=Goddard institute for space studies.

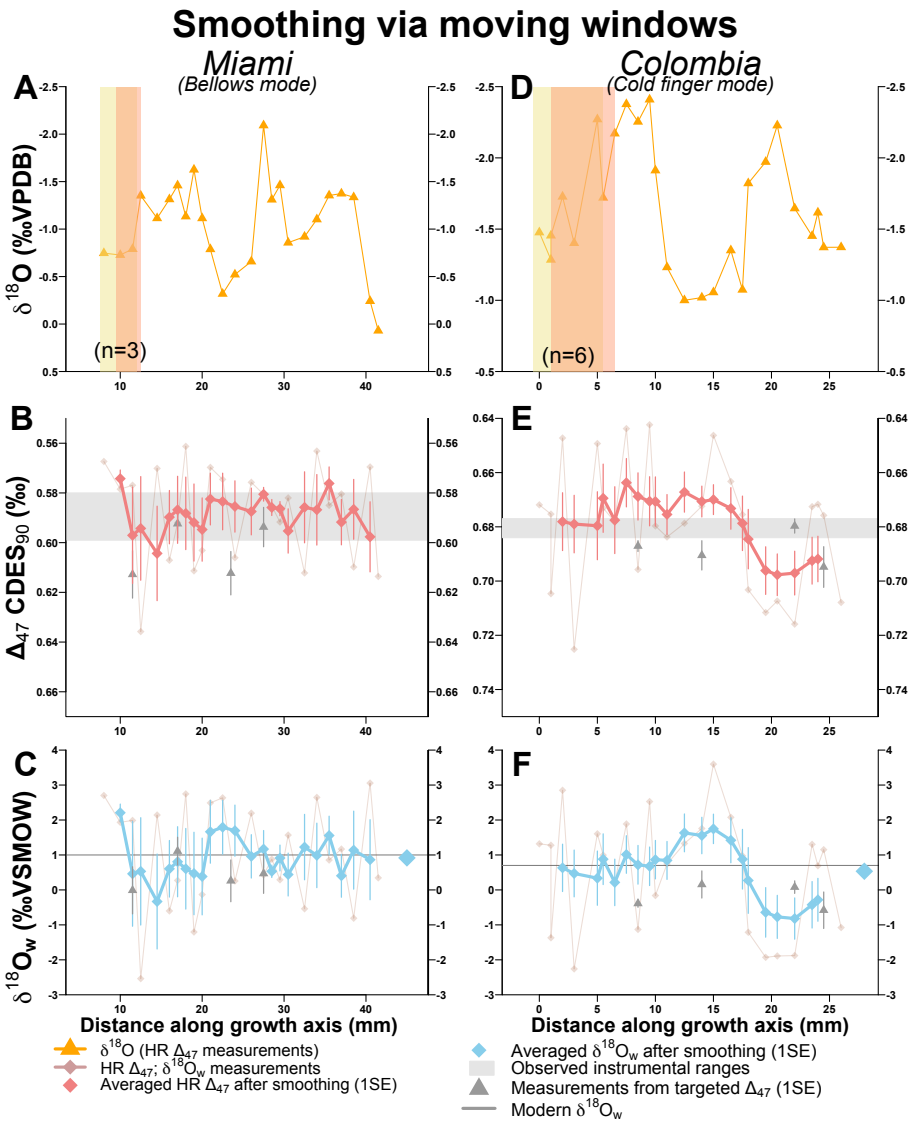

Figure 2.6. H.R. Δ_{47} measurements (smoothing) of shells from Miami and Colombia.

A, D. $\delta^{18}O$ measurements from stable isotope and H.R. Δ_{47}-based thermometry. B, E. H.R. Δ_{47} measurements and averaged datapoints after data smoothing via a moving window (1SE). Grey points show seasonally-targeted Δ_{47} measurements. C, F. $\delta^{18}O_w$ derived from H.R. Δ_{47} measurements and averaged datapoints after smoothing (1SE). Grey points show $\delta^{18}O_w$ derived from seasonally-targeted Δ_{47} measurements.

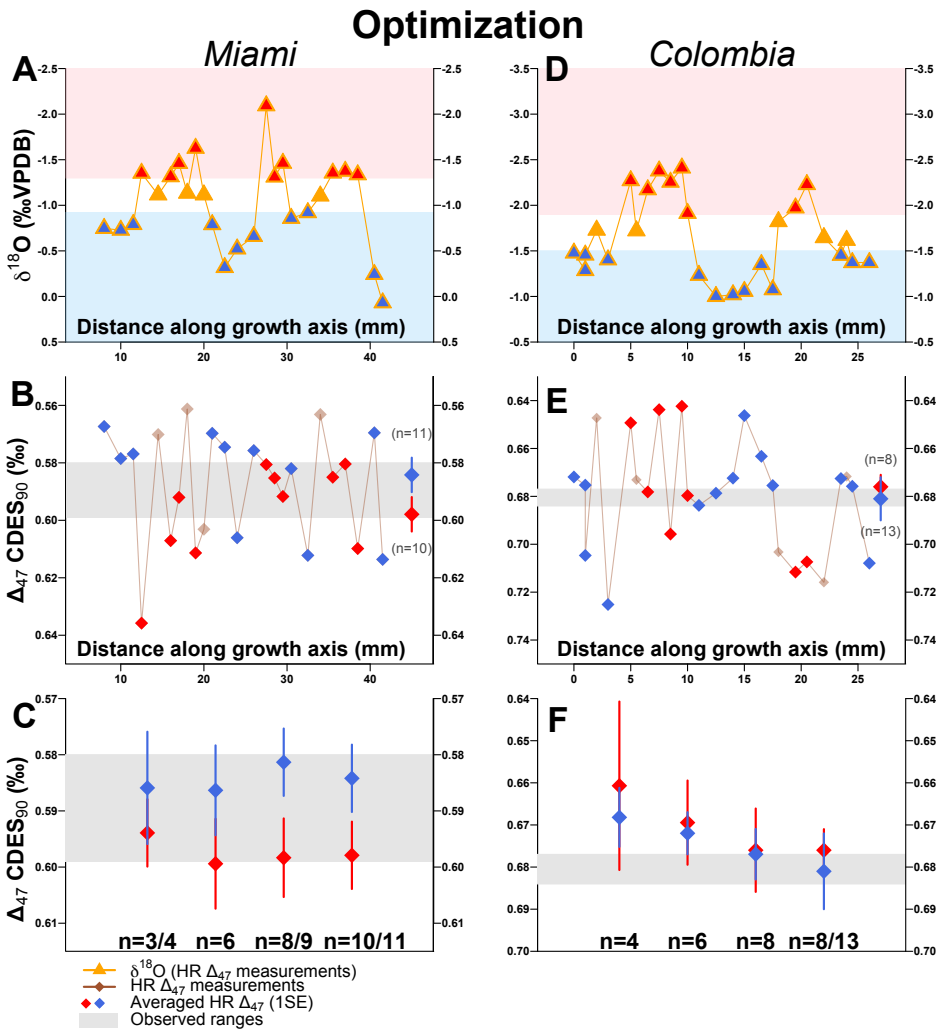

Figure 2.7. H.R. Δ_{47} measurements (optimization) of shells from Miami and Colombia.

A, D. $\delta^{18}O$ measurements from stable isotope and H.R. Δ_{47}-based thermometry. Pink and blue shading indicates warm and cold thresholds defined based on data optimization. B, E. H.R. Δ_{47} measurements with red and blue colored datapoints plotted based on thresholds selected using data optimization. C, F. Averaged Δ_{47} values from each of repeated optimization approaches with different numbers of datapoints combined.

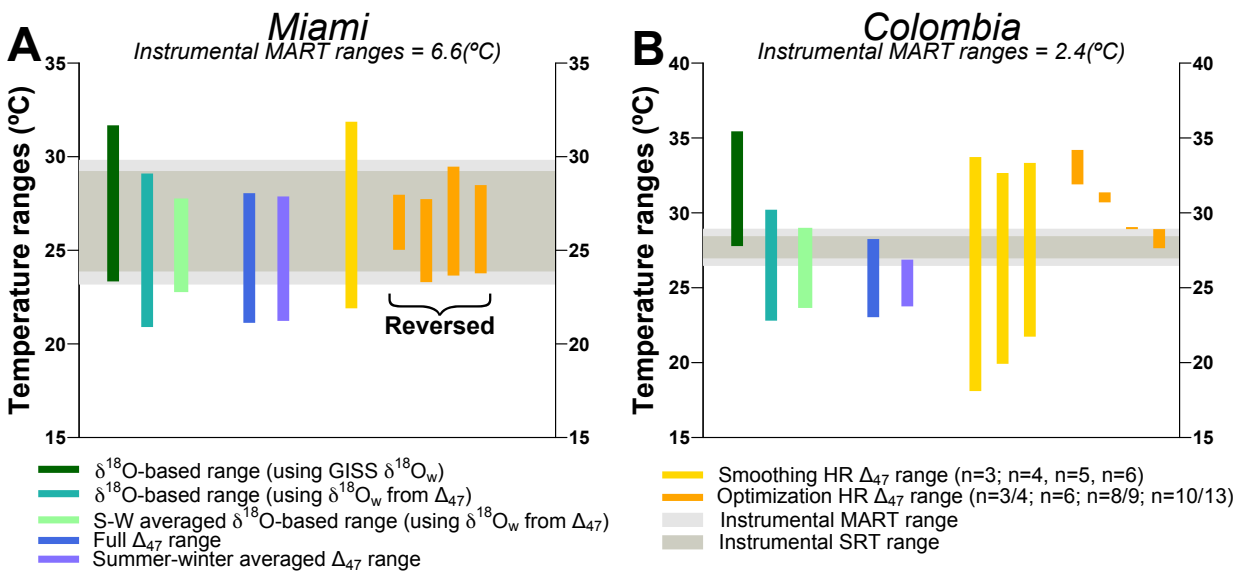

Figure 2.8. Summary of reconstructed temperature ranges using different approaches and comparison against observed seasonality.

Note that the Miami shell was analyzed under bellows mode while the Colombia shell was analyzed under coldfinger mode for H.R. Δ_{47} measurements.

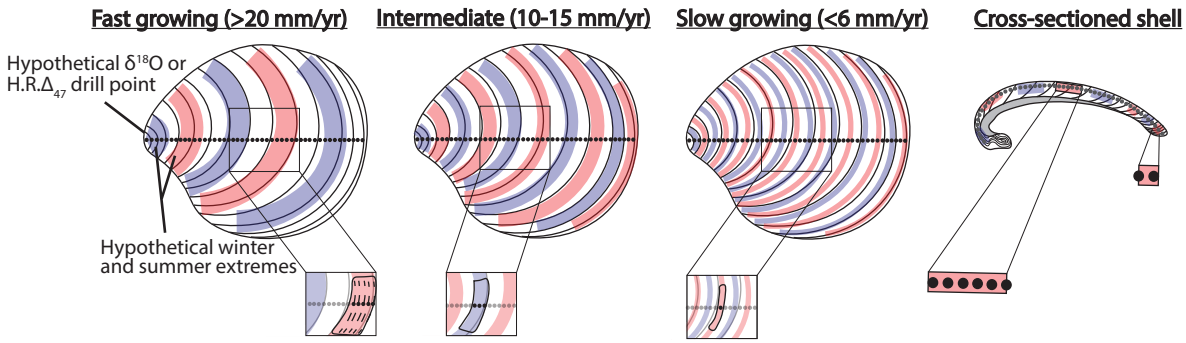

Number of points per seasonal extreme	5-6	3-4	1-2	5-6	1-2
Recommandation:					
H.R. $\delta^{18}O$		Yes	Yes		Yes
S.T. Δ_{47}		Yes (Bellows)	Yes (Coldfinger)		
H.R. Δ_{47} ($\delta^{18}O$ measured simultaneously)	Yes (Bellows (ideal) or Coldfinger, Kiel)			Yes (Coldfinger, Kiel)	
Bulk Δ_{47}			Yes (less ideal)		Yes

Figure 2.9. Diagram showing relation between growth rate and analytical resolution with recommended isotope techniques.

H.R.= High Resolution; S.T.= Seasonally Targeted.

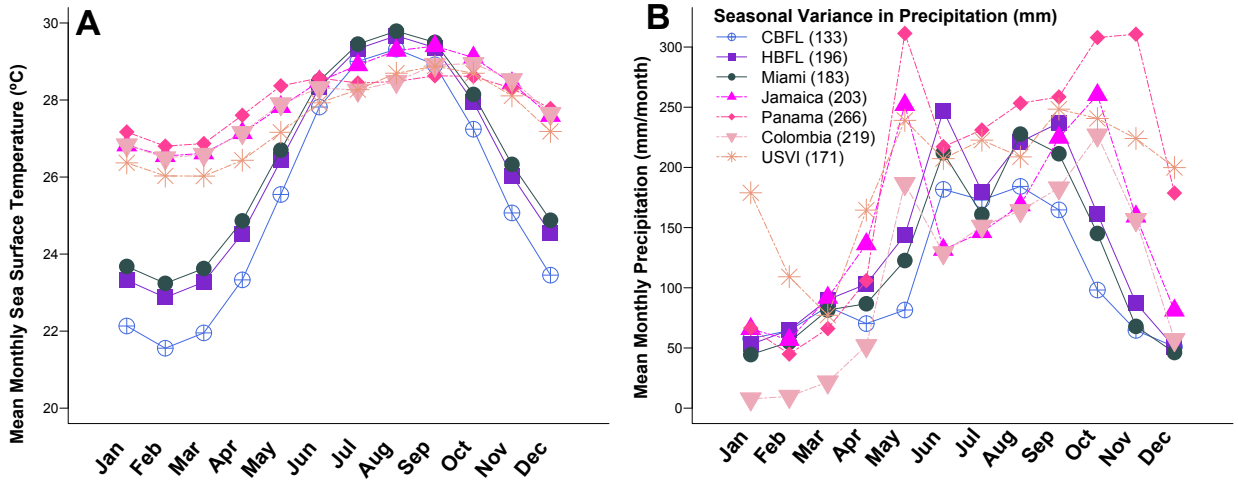

Figure 2.S1. Modern climate data of study sites.

A) Monthly mean sea surface temperature (ºC) for each study location (NOAA NCDC ERSST version 5). B) Monthly Precipitation (mm/month) for each study location (CRU 3.25 Global Precipitation Data Set). Shown data averages together records from the past 80 years.

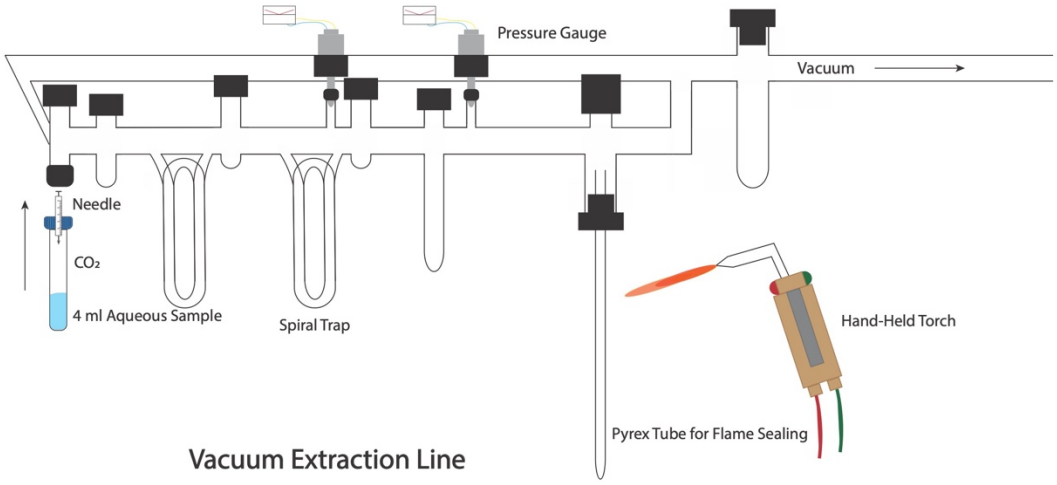

Figure 2.S2. Diagram showing the custom-built vacuum extraction line.

Figure 2.S3. **Photos of sampled *L. pensylvanica* valves, 1 shell from each location**.

Drill holes visible along growth axis (high resolution sclerochronology) and tracing individual growth bands (seasonally-targeted Δ_{47}).

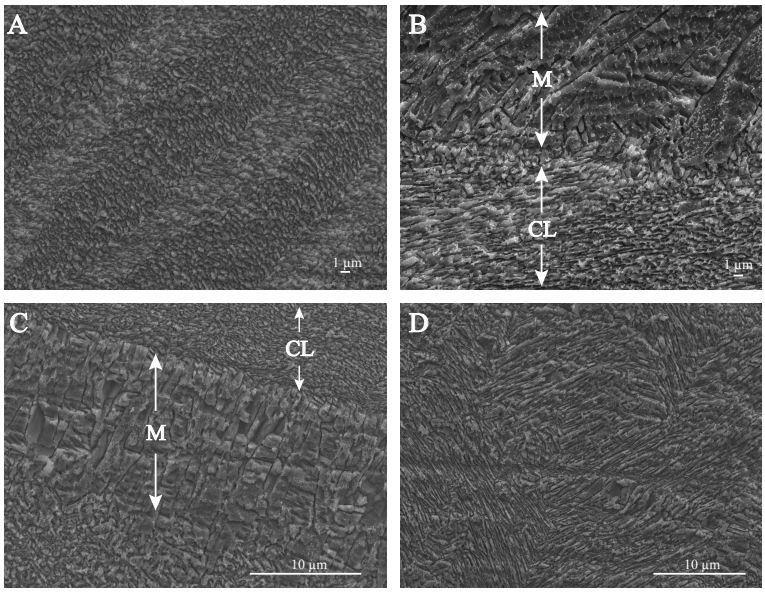

Figure 2.S4. **SEM images showing different aragonitic shell structures of the *L. pensylvanica* shell**

Imaged *L. pensylvanica* shell collected from Cocoa Beach, FL. (A) crossed-lamellar texture of the middle layer. (B) boundary between middle layer crossed-lamellar (CL) and myostracum (M). (C) finely organized irregular prisms in the pallial myostracum (M) with crossed-lamellar (CL) of the middle layer and inner layer on either side; and (D) inner layer showing complex crossed-lamellar structure.

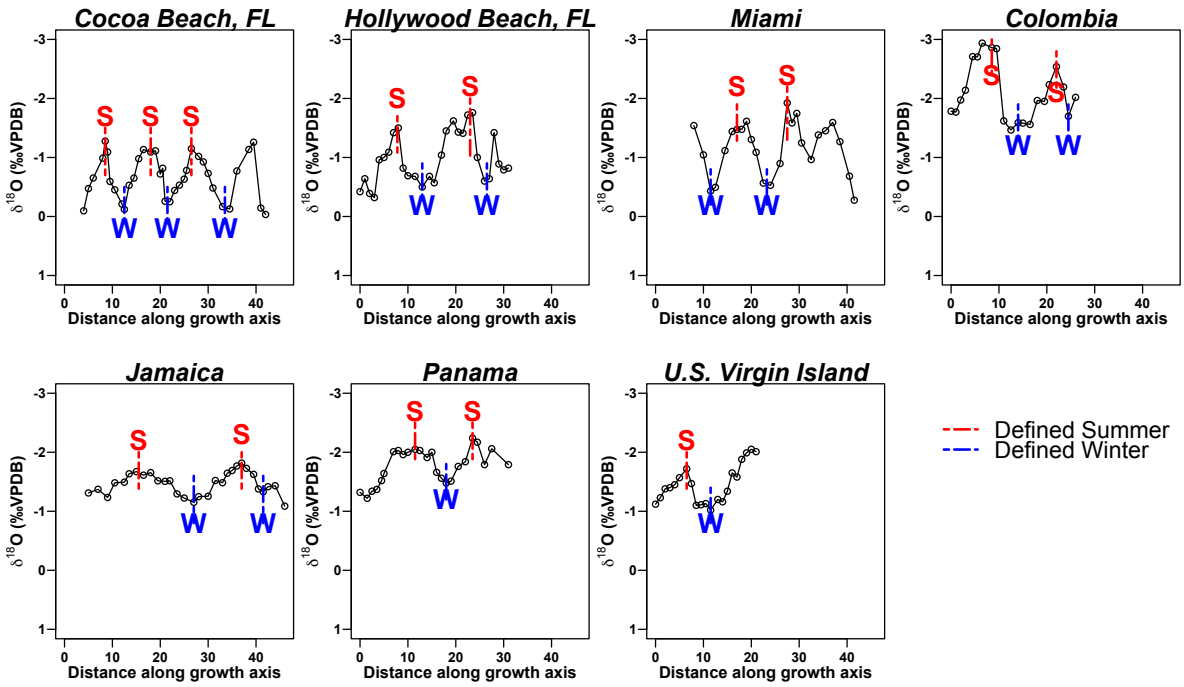

Figure 2.S5. $\delta^{18}O$ profiles of all modern *L. Pensylvanica* showing identified seasonal extremes used for growth rate determinations and targeted Δ_{47} re-sampling.

Y-axis is inverted, in alignment with typical assumption, with the lightest $\delta^{18}O_{carb}$ values correspond to warm-season (summer) extremes, although this may not be the case in all samples.

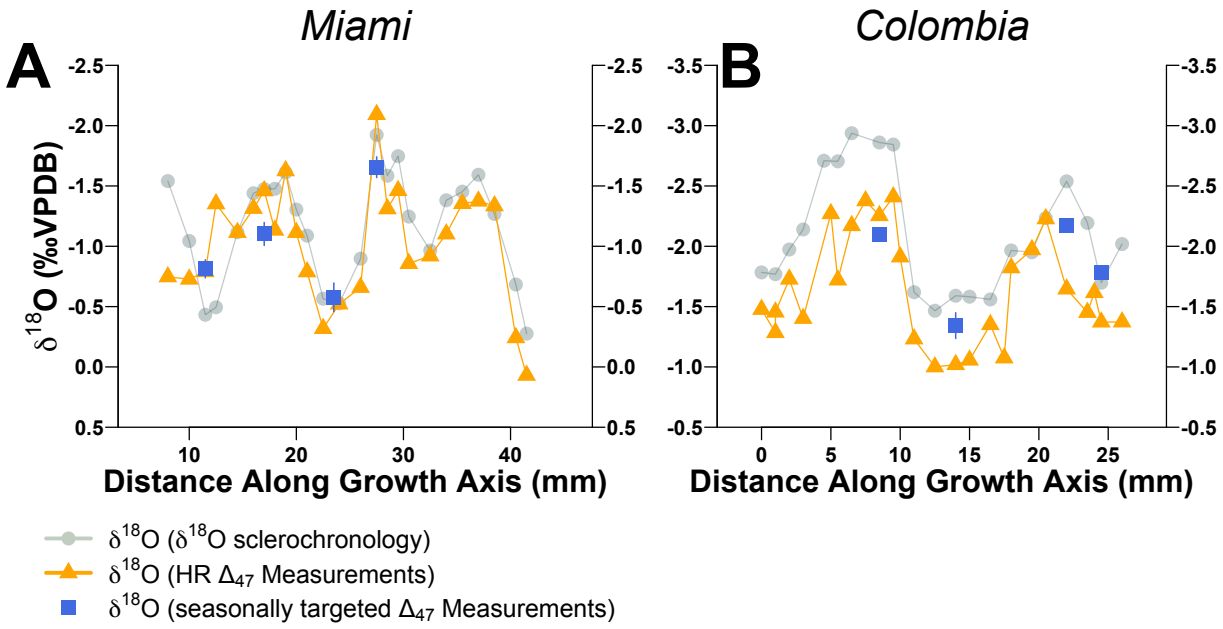

Figure 2.S6. $\delta^{18}O$ record comparison amongst $\delta^{18}O$ sclerochronology, seasonally-targeted Δ_{47} and the H.R. Δ_{47} data.

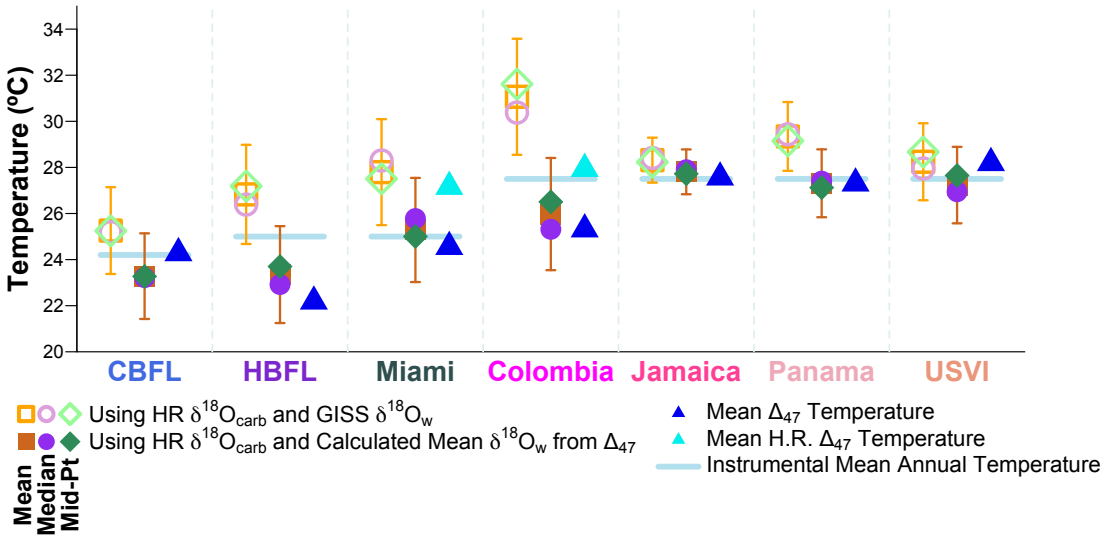

Figure 2.S7. Mean, median and mid-point comparison against observed MAT for each study location.

Temperature reconstructed using high resolution $\delta^{18}O_{carb}$ profiles and GISS/extraction line $\delta^{18}O_w$ and mean $\delta^{18}O_w$ from Δ_{47}. Mean Δ_{47} reconstructed temperature comparison against observed MAT for each study location.

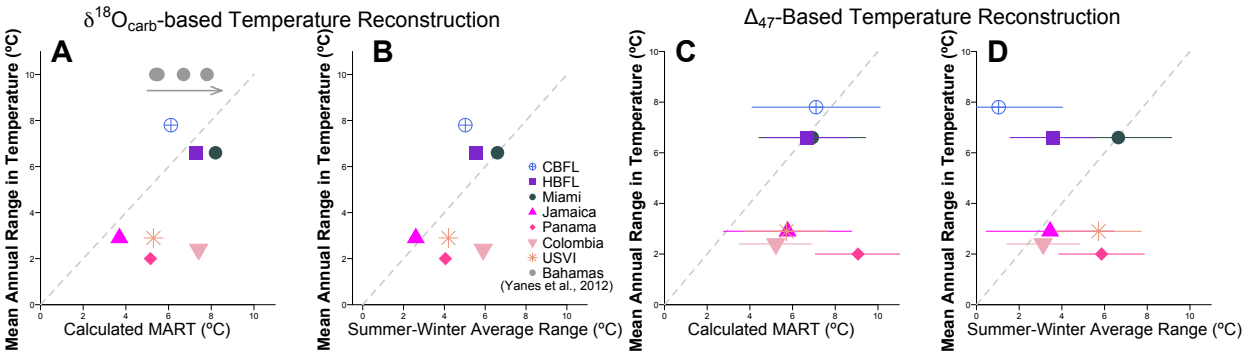

Figure 2.S8. $\delta^{18}O$- and Δ_{47}-based temperature reconstruction compared against modern values.

A, B, Δ_{47}-based temperature range comparison with observed seasonality, and $\delta^{18}O$ data from Yanes et al., 2012. C, D, $\delta^{18}O$-based temperature range comparison with observed seasonality

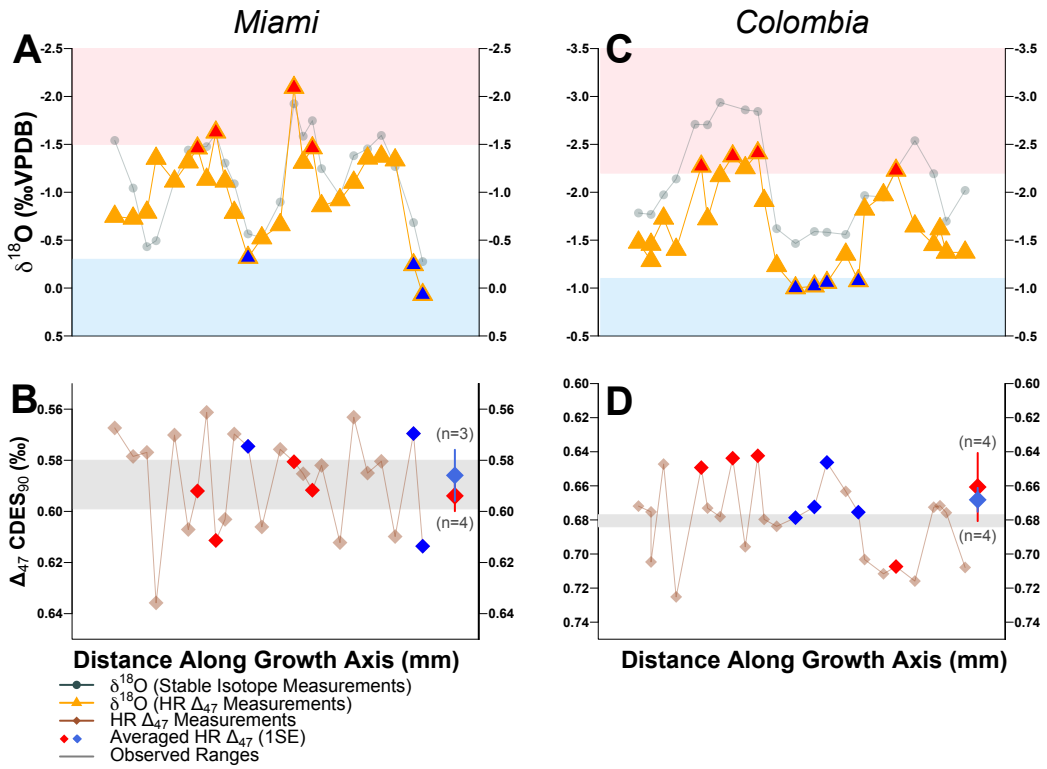

Figure 2.S9. H.R. Δ_{47} measurements (optimization) of shells from Miami and Colombia, (n=3/4).

A, C. $\delta^{18}O$ measurements from stable isotope and H.R. Δ_{47}-based thermometry. Pink and blue shading indicates numbers of datapoints being combined based on data optimization. B, D. H.R. Δ_{47} measurements with red and blue colored datapoints plotted based on categories selected using data optimization.

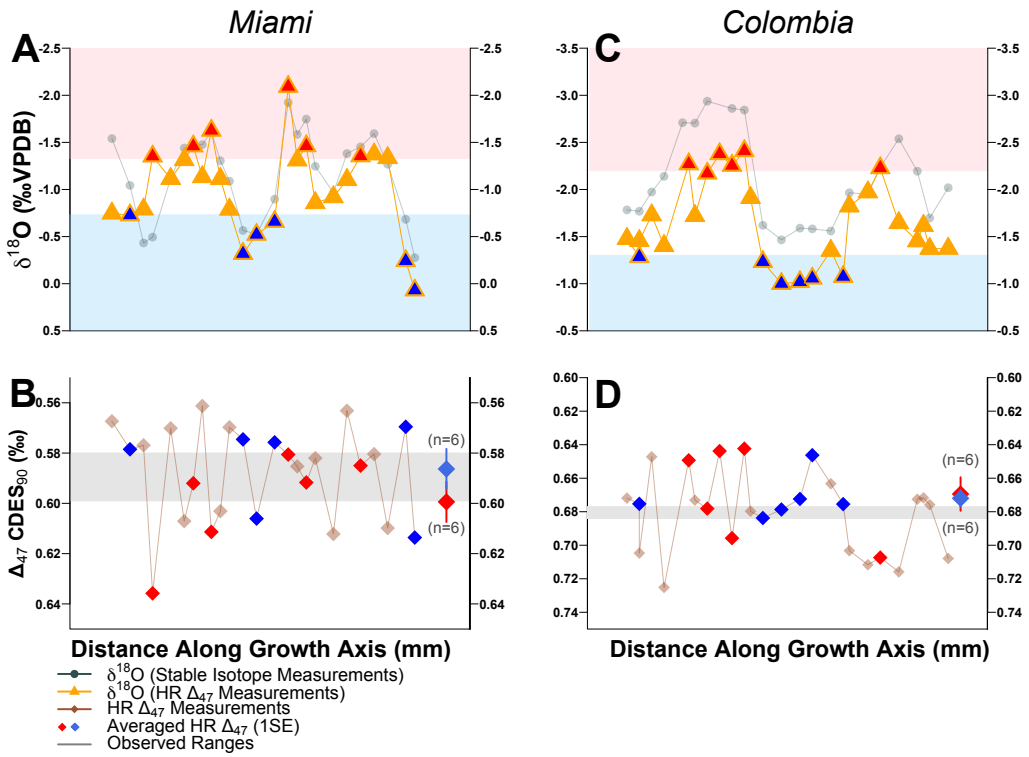

Figure 2.S10. H.R. Δ_{47} measurements (optimization) of shells from Miami and Colombia, (n=6).

A, C. $\delta^{18}O$ measurements from stable isotope and H.R. Δ_{47}-based thermometry. Pink and blue shading indicates numbers of datapoints being combined based on data optimization. B, D. H.R. Δ_{47} measurements with red and blue colored datapoints plotted based on categories selected using data optimization.

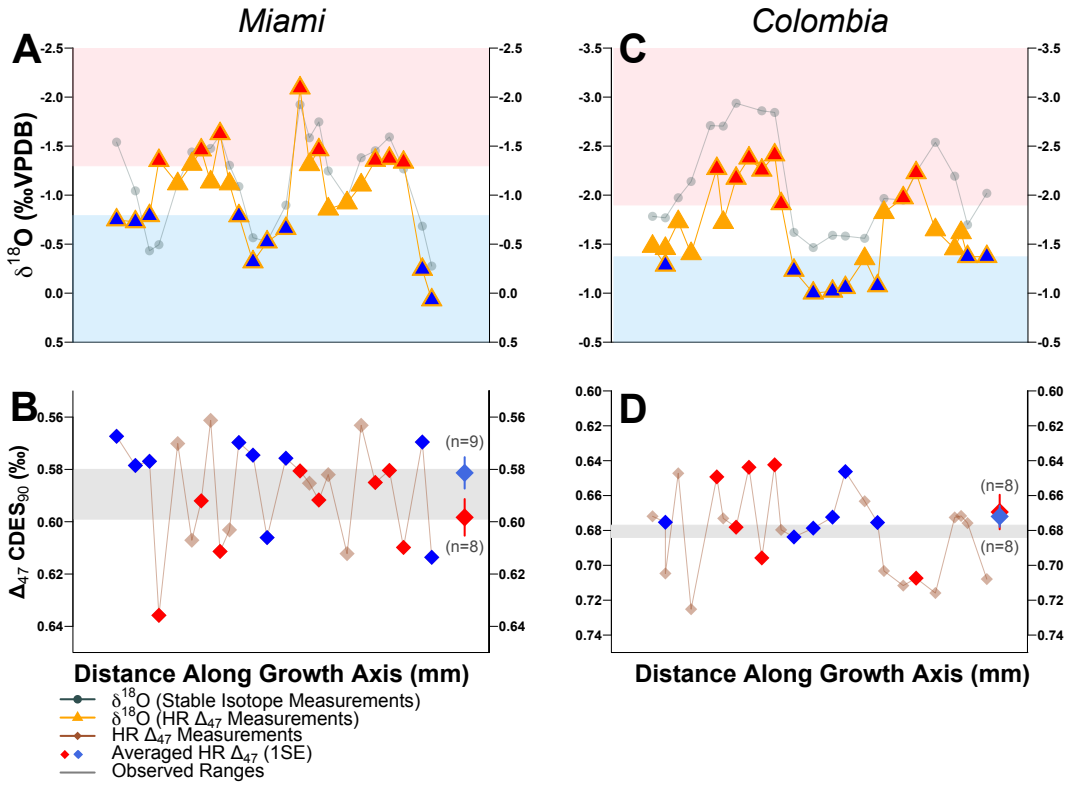

Figure 2.S11. H.R. Δ_{47} measurements (optimization) of shells from Miami and Colombia, (n=8/9).

A, C. $\delta^{18}O$ measurements from stable isotope and H.R. Δ_{47}-based thermometry. Pink and blue shading indicates numbers of datapoints being combined based on data optimization. B, D. H.R. Δ_{47} measurements with red and blue colored datapoints plotted based on categories selected using data optimization.

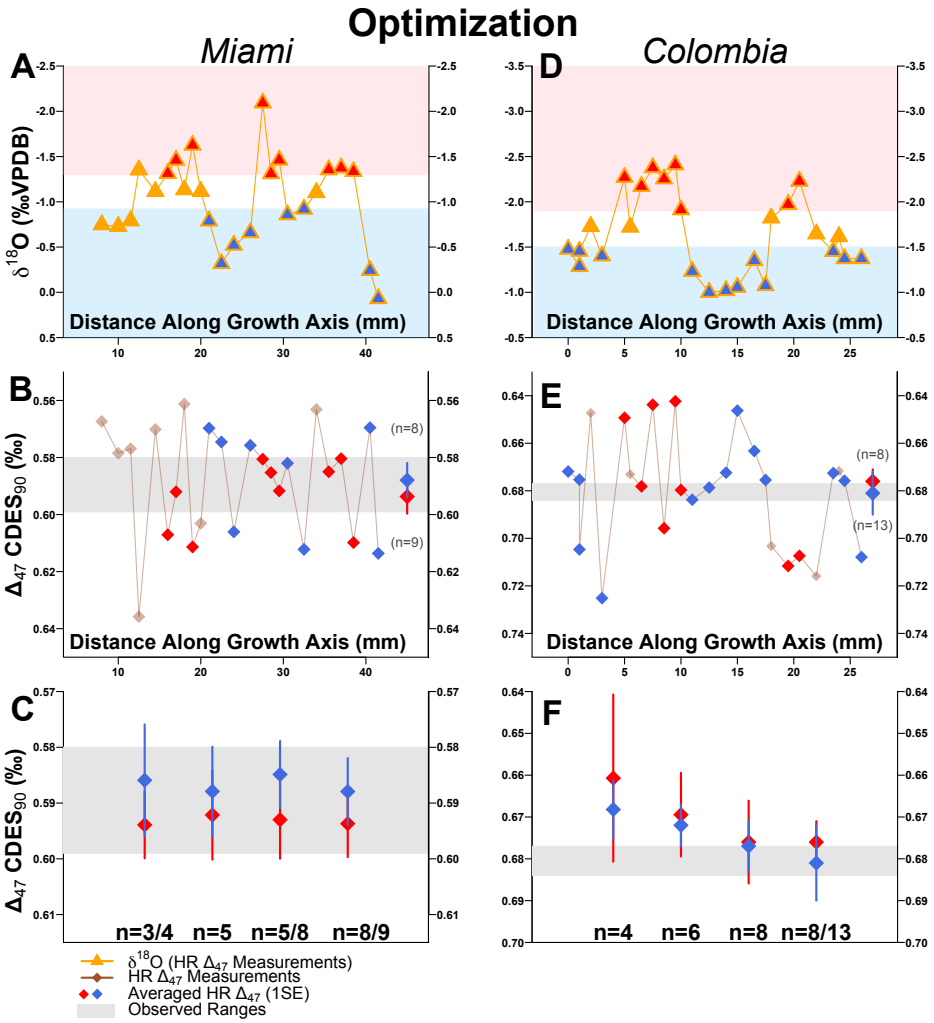

Figure 2.S12. H.R. Δ_{47} measurements (optimization) of shells from Miami and Colombia with first four data points removed from the Miami shell.

A, D. $\delta^{18}O$ measurements from stable isotope and H.R. Δ_{47}-based thermometry. Pink and blue shading indicates warm and cold thresholds defined based on data optimization. B, E. H.R. Δ_{47} measurements with red and blue colored datapoints plotted based on thresholds selected using data optimization. Note that the first four points, where the two $\delta^{18}O$ records clearly misalign, were removed for B. C, F. Averaged Δ_{47} values from each of repeated optimization approaches with different numbers of datapoints combined.

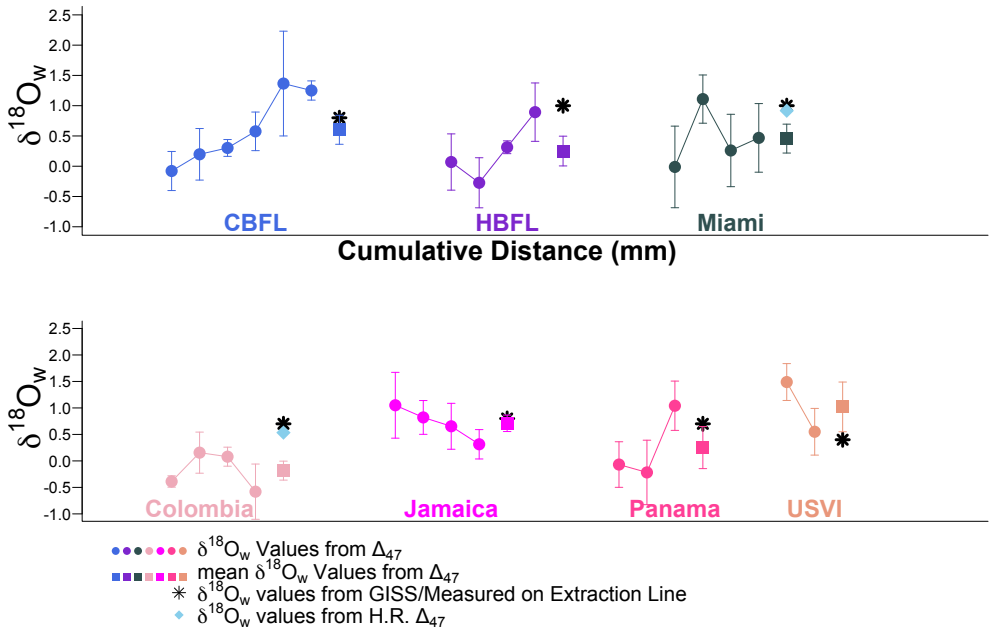

Figure 2.S13. $\delta^{18}O_w$ values and mean measured from Δ_{47}.

Data compared against $\delta^{18}O_w$ values from GISS database or measured from extraction line; and H.R. Δ_{47}.

Table 2.S1. $\delta^{18}O_w$ values used to derive $\delta^{18}O$-based temperature profiles.

Typical uncertainty for Δ_{47}-derived $\delta^{18}O_w$ is ~0.6‰.

Sample Name/Locality	Closest Location of Water Sample	Distance from Locality (Km)	Instrumental $\delta^{18}O_w$ (‰)	Source	Δ_{47}-Derived $\delta^{18}O_w$ (‰)
Cocoa Beach, FL	Near Canaveral	60	0.8	GISS	0.6 (-0.1 to +1.4)
Hollywood Beach, FL	Hollywood Beach, FL	0	1.0±0.1	This Study	0.3 (-0.3 to +0.9)
Miami, FL	Biscayne Bay	34	1.0	GISS	0.5 (0 to +1.1)
Cartagena, Colombia	Western Caribbean	646	0.7	GISS	-0.3 (-0.6 to +0.2)
Montego Bay, Jamaica	Western Caribbean	94	0.8	GISS	0.7 (+0.3 to +1.1)
San Blas Island, Panama	Western Caribbean	700	0.7	GISS	0.3 (-0.2 to +1.0)
St. Thomas, USVI	Near Puerto Rico	125	0.4±0.1	This Study	0.6 (+0.6 to +1.5)

Table 2.S2. All reported $\delta^{18}O$-, Δ_{47}- based isotope analysis data.

Column N shows the number of samples used for analysis with number of total replicates shown in parathesis if applicable

	Analysis Type	N	Minimum Temperature	Maximum Temperature	MART	MAT
Cocoa Beach, FL	**Instrumental**	**NA**	**21.6**	**29.3**	**7.7**	**24.2**
	$\delta^{18}O$-based (GISS $\delta^{18}O_w$)	35	21.2	27.3	6.1	24.3
	$\delta^{18}O$-based ($\delta^{18}O_w$ from Δ_{47})	35	20.2	26.3	6.1	23.3
	S/W Avg-$\delta^{18}O$-based ($\delta^{18}O_w$ from Δ_{47})	7	20.8	25.9	5.1	NA
	Δ_{47}-based	6(19)	21±1.9	28.1±4.0	7.1	24.3
	S/W Avg-Δ_{47}-based	6(19)	23.8	24.8	1.0	NA
Hollywood Beach, FL	**Instrumental**	**NA**	**23.3**	**29.2**	**5.9**	**25.0**
	$\delta^{18}O$-based (GISS $\delta^{18}O_w$)	29	23.6	30.8	7.2	26.8
	$\delta^{18}O$-based ($\delta^{18}O_w$ from Δ_{47})	29	20.1	27.3	7.2	23.3
	S/W Avg-$\delta^{18}O$-based ($\delta^{18}O_w$ from Δ_{47})	6	20.9	25.6	4.7	NA
	Δ_{47}-based	4(12)	18.1±2.2	24.8±0.6	6.7	22.2
	S/W Avg-Δ_{47}-based	4(12)	20.4	24.0	3.6	NA
Miami, FL	**Instrumental**	**NA**	**23.2**	**29.8**	**6.6**	**25.0**
	$\delta^{18}O$-based (GISS $\delta^{18}O_w$)	25	23.5	31.7	8.2	27.8

	$\delta^{18}O$-based ($\delta^{18}O_w$ from Δ_{47})	25	20.9	29.1	8.2	25.3
	S/W Avg-$\delta^{18}O$-based ($\delta^{18}O_w$ from Δ_{47})	6	22.8	27.8	5.0	NA
	Δ_{47}-based	4(20)	21.1±3.1	28.1±2.1	7.0	24.6
	S/W Avg-Δ_{47}-based	4(20)	21.2	27.9	6.7	NA
	Analysis Type	**N**	**Minimum Temperature**	**Maximum Temperature**	**MART**	**MAT**
Miami, FL	Δ_{47}-based (Smoothing)	W=3	21.9	31.9	10.0	27.2
	Δ_{47}-based (Optimization)	25	23.8	28.5	4.7	27.2
Cartagena, Colombia	**Instrumental**	**NA**	**26.5**	**28.9**	**2.4**	**27.5**
	$\delta^{18}O$-based (GISS $\delta^{18}O_w$)	21	27.8	35.2	7.4	31.2
	$\delta^{18}O$-based ($\delta^{18}O_w$ from Δ_{47})	21	22.8	30.2	7.4	25.3
	S/W Avg-$\delta^{18}O$-based ($\delta^{18}O_w$ from Δ_{47})	4	23.7	29.0	5.3	NA
	Δ_{47}-based	4(12)	23.0±2.5	28.3±1.0	5.3	25.3
	S/W Avg-Δ_{47}-based	4(12)	23.8	26.9	3.1	NA
	Δ_{47}-based (Smoothing)	W=4	18.1	33.7	15.6	27.9
		W=5	19.9	32.7	12.8	27.9

		W=6	21.7	33.3	11.6	27.9
	Δ_{47}-based (Optimization)	23	27.6	29.0	1.4	27.9
Montego Bay, Jamaica	**Instrumental**	**NA**	**26.5**	**29.4**	**2.9**	**27.6**
	$\delta^{18}O$-based (GISS $\delta^{18}O_w$)	30	26.4	30.1	3.7	28.3
	$\delta^{18}O$-based ($\delta^{18}O_w$ from Δ_{47})	30	25.9	29.6	3.7	27.8
	S/W Avg-$\delta^{18}O$-based ($\delta^{18}O_w$ from Δ_{47})	4	26.7	29.2	2.5	NA
	Δ_{47}-based	4(22)	24.5±3.0	30.4±3.1	5.9	27.6
	S/W Avg-Δ_{47}-based	4(22)	25.8	29.3	3.5	NA

	Analysis Type	**N**	**Minimum Temperature**	**Maximum Temperature**	**MART**	**MAT**
San Blas Island, Panama	**Instrumental**	**NA**	**26.8**	**28.6**	**1.8**	**27.5**
	$\delta^{18}O$-based (GISS $\delta^{18}O_w$)	25	26.5	31.8	5.3	29.3
	$\delta^{18}O$-based ($\delta^{18}O_w$ from Δ_{47})	25	24.5	29.8	5.3	27.3
	S/W Avg-$\delta^{18}O$-based ($\delta^{18}O_w$ from Δ_{47})	4	26.6	29.2	2.6	NA
	Δ_{47}-based	3(11)	23.4±2.9	32.5±2.3	9.1	27.3

	S/W Avg-Δ_{47}-based	3(11)	23.4	29.3	5.9	NA
St. Thomas, USVI	**Instrumental**	**NA**	**26.0**	**28.9**	**2.9**	**27.5**
	$\delta^{18}O$-based (GISS $\delta^{18}O_w$)	21	24.0	29.3	5.3	26.2
	$\delta^{18}O$-based ($\delta^{18}O_w$ from Δ_{47})	21	25.0	30.3	5.3	27.2
	S/W Avg-$\delta^{18}O$-based ($\delta^{18}O_w$ from Δ_{47})	3	25.3	29.4	4.1	NA
	Δ_{47}-based	2(5)	25.3±1.9	31.1±1.6	5.8	28.2
	S/W Avg-Δ_{47}-based	2(5)	25.3	31.1	5.8	NA

Table 2.S3. Additional $\delta^{18}O_w$ values measured in this study (1SD), organized by decreasing latitude.

Sample Name	Collection Date	Salinity (ppt) (n=3)	Average $\delta^{18}O_w$ (‰) (n=2)
Marginal Way, ME	29-Dec-18	30.4±0.2	-1.1±0.0
Pleasant Bay, MA	2-Jun-19	29.1±0.8	-1.6±0.0
Bald Head Island, NC	27-Jun-19	34.0±0.9	1.0±0.1
Myrtle Beach, SC	21-Aug-21	33.6±0.4	0.5±0.0
Folly Beach, SC	21-Aug-21	32.9±0.4	0.5±0.0
Captiva, FL	6-Jan-22	32.8±0.7	1.2±0.1
Holmes Beach, FL	19-Dec-21	9.9±0.1	1.8±0.1
Hollywood Beach, FL	31-Dec-19	34.4±0.6	1.0±0.0
Hollywood Beach, FL	3-Jan-20	34.1±0.6	1.1±0.1
Hollywood Beach, FL 150ft offshore	26-Dec-21	34.9±0.1	1.0±0.1
Hollywood Beach, FL 50ft from shore	26-Dec-21	34.8±0.3	0.7±0.1
Hollywood Beach, FL wave zone	26-Dec-21	34.8±0.2	0.7±0.2
Islamorada, FL Keys	24-Dec-21	34.2±0.3	1.2±0.1
Isobella, Puerto Rico	21-Dec-21	24.4±0.5	0.4±0.1

2.9 References

Agterhuis T., Ziegler M., de Winter N. J. and Lourens L. J., 2022, Warm deep-sea temperatures across Eocene Thermal Maximum 2 from clumped isotope thermometry. Communications Earth and Environment v. 3, p. 1–9.

Allen J. A., 1958, On the basic form and adaptations to habitat in the Lucinacea (Eulamellibranchia). Royal Society of London v. 241, p. 421–484.

Anderson N. T., Kelson J. R., Kele S., Daëron M., Bonifacie M., Horita J., Mackey T. J., John C. M., Kluge T., Petschnig P., Jost A. B., Huntington K. W., Bernasconi S. M. and Bergmann K. D., 2021, A unified clumped isotope thermometer calibration (0.5–1,100°C) using carbonate-based standardization. Geophysical Research Letters v. 48.

Bernasconi S. M., Daëron M., Bergmann K. D., Bonifacie M., Meckler A. N., Affek H. P., Anderson N., Bajnai D., Barkan E., Beverly E., Blamart D., Burgener L., Calmels D., Chaduteau C., Clog M., Davidheiser-Kroll B., Davies A., Dux F., Eiler J., Elliott B., Fetrow A. C., Fiebig J., Goldberg S., Hermoso M., Huntington K. W., Hyland E., Ingalls M., Jaggi M., John C. M., Jost A. B., Katz S., Kelson J., Kluge T., Kocken I. J., Laskar A., Leutert T. J., Liang D., Lucarelli J., Mackey T. J., Mangenot X., Meinicke N., Modestou S. E., Müller I. A., Murray S., Neary A., Packard N., Passey B. H., Pelletier E., Petersen S., Piasecki A., Schauer A., Snell K. E., Swart P. K., Tripati A., Upadhyay D., Vennemann T., Winkelstern I., Yarian D., Yoshida N., Zhang N. and Ziegler M., 2021, InterCarb: A community effort to improve interlaboratory standardization of the carbonate clumped isotope thermometer using carbonate standards. Geochemistry, Geophysics, Geosystems v. 22. P. 1-25.

Bigatti G., Peharda M. and Taylor J. D., 2004, Size at first maturity, oocyte envelopes and external morphology of sperm in three species of lucinidae (Mollusca: Bivalvia) from Coastal nursery habitats: Patterns and processes of demographic variability in marine fish species along the eastern Adriatic coast View project Sclerochronology as a tool for detecting long-term Adriatic environmental changes-SCOOL View project. Malacologia v. 46, p. 417–426.

Brissac T., Merçot H. and Gros O., 2011, Lucinidae/sulfur-oxidizing bacteria: Ancestral heritage or opportunistic association? Further insights from the Bohol Sea (the Philippines). FEMS Microbiology Ecology v. 75, p. 63–76.

Caldarescu D. E., Sadatzki H., Andersson C., Schäfer P., Fortunato H. and Meckler A. N., 2021, Clumped isotope thermometry in bivalve shells: A tool for reconstructing seasonal upwelling. Geochimica et Cosmochimica Acta v. 294, p. 174–191.

Corrège T., 2006, Sea surface temperature and salinity reconstruction from coral geochemical tracers. Palaeogeography, Palaeoclimatology, Palaeoecology v.232, p.408–428.

Culotta E., 1988, Predators and available prey: naricid predation during a neocene molluscan extinction event.:

Daëron M., Blamart D., Peral M. and Affek H. P., 2016, Absolute isotopic abundance ratios and the accuracy of Δ47 measurements. Chemical Geology v. 442, p. 83–96.

Daëron M., 2021, Full Propagation of Analytical Uncertainties in Δ47 Measurements. Geochemistry, Geophysics, Geosystems v. 22.

Defliese W. F., Hren M. T. and Lohmann K. C., 2015, Compositional and temperature effects of phosphoric acid fractionation on δ47 analysis and implications for discrepant calibrations. Chemical Geology v. 396, p. 51–60.

Eagle R. A., Eiler J. M., Tripati A. K., Ries J. B., Freitas P. S., Hiebenthal C., Wanamaker A. D., Taviani M., Elliot M., Marenssi S., Nakamura K., Ramirez P. and Roy K., 2013, The influence of temperature and seawater carbonate saturation state on ^{13}C-^{18}O bond ordering in bivalve mollusks. Biogeosciences v. 10, p. 4591–4606.

Eiler, J.M., 2007, "Clumped-isotope" geochemistry-The study of naturally-occurring, multiply-substituted isotopologues: Earth and Planetary Science Letters, v. 262, p. 309–327, doi:10.1016/j.epsl.2007.08.020.

Eiler, J.M., 2011, Paleoclimate reconstruction using carbonate clumped isotope thermometry: Quaternary Science Reviews, v. 30, p. 3575–3588, doi:10.1016/j.quascirev.2011.09.001.

Epstein, B.S., Buchsbacm, J., Lowenstam, H.A., and Ukey, H.C., 1953, Revised carbonate-water isotopic temperature scale: Bulletin of the Geological Society of America, v. 64, p. 1315–1326, http://pubs.geoscienceworld.org/gsa/gsabulletin/article-pdf/64/11/1315/3426622/i0016-7606-64-11-1315.pdf.

Ghosh P., Adkins J., Affek H., Balta B., Guo W., Schauble E. A., Schrag D. and Eiler J. M., 2006, ^{13}C-^{18}O bonds in carbonate minerals: A new kind of paleothermometer. Geochimica et Cosmochimica Acta v. 70, p. 1439–1456.

Gillikin D. P., Lorrain A., Navez J., Taylor J. W., André L., Keppens E., Baeyens W. and Dehairs F., 2005, Strong biological controls on Sr/Ca ratios in aragonitic marine bivalve shells. Geochemistry, Geophysics, Geosystems v. 6.

Henkes G. A., Passey B. H., Wanamaker A. D., Grossman E. L., Ambrose W. G. and Carroll M. L., 2013, Carbonate clumped isotope compositions of modern marine mollusk and brachiopod shells. Geochimica et Cosmochimica Acta v. 106, p. 307–325.

Huyghe D., Daëron M., de Rafelis M., Blamart D., Sébilo M., Paulet Y. M. and Lartaud F., 2022, Clumped isotopes in modern marine bivalves. Geochimica et Cosmochimica Acta v. 316, p. 41–58.

Ivany L. C., 2012, Reconstructing paleoseasonality from accretionary skeletal carbonates-challenges and opportunities. The Paleontological Society Papers v. 18, p. 133–165.

Ivany L. C. and Judd E. J., 2021, Deciphering Temperature Seasonality in Earth's Ancient Oceans. Annual Review of Earth and Planetary Sciences, p. 1–30.

Jones D. S., Quitmyer I. R. and Andrus C. F. T., 2005, Oxygen isotopic evidence for greater seasonality in Holocene shells of Donax variabilis from Florida. Palaeogeography, Palaeoclimatology, Palaeoecology, p. 96–108.

Jones M. M., Petersen S. v. and Curley A. N., 2022, A tropically hot mid-Cretaceous North American Western Interior Seaway. Geology, p. 1–27.

Keating-Bitonti C. R., Ivany L. C., Affek H. P., Douglas P. and Samson S. D., 2011, Warm, not super-hot, temperatures in the early Eocene subtropics. Geology v. 39, p. 771–774.

Kelson J. R., Huntington K. W., Schauer A. J., Saenger C. and Lechler A. R., 2017, Toward a universal carbonate clumped isotope calibration: Diverse synthesis and preparatory methods suggest a single temperature relationship. Geochimica et Cosmochimica Acta v. 197, p. 104–131.

Kim S. T., Mucci A. and Taylor B. E., 2007, Phosphoric acid fractionation factors for calcite and aragonite between 25 and 75 °C: Revisited. Chemical Geology v. 246, p. 135–146.

Kocken I. J., Müller I. A. and Ziegler M., 2019, Optimizing the Use of Carbonate Standards to Minimize Uncertainties in Clumped Isotope Data. Geochemistry, Geophysics, Geosystems v. 20, p. 5565–5577.

Leder J. J., Swart P. K., Szmant A. M. and Dodge R. E., 1996, The origin of variations in the isotopic record of scleractinian coral: I. Oxygen. Geochimica et Cosmochimica Acta v. 60, p. 2857–2870.

LeGrande A. N. and Schmidt G. A., 2006, Global gridded data set of the oxygen isotopic composition in seawater. Geophysical Research Letters v. 33.

López-Rocha J. A., Fernández-Rivera Melo F. J., Gastélum-Nava E. and Larios-Castro E., 2021, Abundance and harvest strategy of three species of clam (Bivalvia: Veneridae) located in new fishing banks in the Gulf of California. Aquaculture and Fisheries v. 6, p. 506–512.

Mackey T. J., Jost A. B., Creveling J. R. and Bergmann K. D., 2020, A Decrease to Low Carbonate Clumped Isotope Temperatures in Cryogenian Strata. AGU Advances v. 1.

Negrón J. F. and Cain B., 2019, Mountain pine beetle in colorado: A story of changing forests. Journal of Forestry v. 117, p. 144–151.

Nghiem S. v., Hall D. K., Mote T. L., Tedesco M., Albert M. R., Keegan K., Shuman C. A., DiGirolamo N. E. and Neumann G., 2012, The extreme melt across the Greenland ice sheet in 2012. Geophysical Research Letters v. 39.

O'hora H. E., Sierra B., Petersen V., Vellekoop J., Jones M. M. and Scholz S. R., 2022, Clumped-isotope-derived climate trends leading up to the end-Cretaceous mass extinction in northwest Europe. Climate of the Past, v. 1–28.

Petersen S. v., Defliese W. F., Saenger C., Daëron M., Huntington K. W., John C. M., Kelson J. R., Bernasconi S. M., Colman A. S., Kluge T., Olack G. A., Schauer A. J., Bajnai D., Bonifacie M., Breitenbach S. F. M., Fiebig J., Fernandez A. B., Henkes G. A., Hodell D., Katz A., Kele S., Lohmann K. C., Passey B. H., Peral M. Y., Petrizzo D. A., Rosenheim B. E., Tripati A., Venturelli R., Young E. D. and Winkelstern I. Z., 2019, Effects of improved ^{17}O correction on interlaboratory agreement in clumped isotope calibrations, estimates of mineral-specific offsets, and temperature dependence of acid digestion fractionation. Geochemistry, Geophysics, Geosystems v. 20, p. 3495–3519.

Rosenheim B. E., Swart P. K., Thorrold S. R., Willenz P., Berry L. and Latkoczy C., 2004, High-resolution Sr/Ca records in sclerosponges calibrated to temperature in situ. Geology v. 32, p. 145–148.

Schmid T. W. and Bernasconi S. M., 2010, An automated method for "clumped-isotope" measurements on small carbonate samples. Rapid Communications in Mass Spectrometry v. 24, p. 1955–1963.

Schmidt G. A., 1999, Forward modeling of carbonate proxy data from planktonic foraminifera using oxygen isotope tracers in a global ocean model. Paleoceanography v. 14, p. 482–497.

Schöne B. R., Freyre Castro A. D., Fiebig J., Houk S. D., Oschmann W. and Kröncke I., 2004, Sea surface water temperatures over the period 1884-1983 reconstructed from oxygen isotope ratios of a bivalve mollusk shell (Arctica islandica, southern North Sea). Palaeogeography, Palaeoclimatology, Palaeoecology v. 212, p. 215–232.

Shackleton N. J., 1973, Oxygen isotope analysis as a means of determining season of occupation of prehistoric midden sites. Archaeometry v. 15, p. 133–141.

Spooner P. T., Guo W., Robinson L. F., Thiagarajan N., Hendry K. R., Rosenheim B. E. and Leng M. J., 2016, Clumped isotope composition of cold-water corals: A role for vital effects? Geochimica et Cosmochimica Acta v. 179, p. 123–141.

Taylor J. D., Bigatti G. and David Ball A., 2004, Extraordinary flexible shell sculpture: The structure and formation of calcified periostracal lamellae in Lucina pensylvanica (Bivalvia : Lucinidae) Data in Malacologia · Sclerochronology as a tool for detecting long-term Adriatic environmental changes-SCOOL View project. Malacologia v. 46, p. 277–294.

Taylor J. D. and Glover E. A., 2000, Functional anatomy, chemosymbiosis and evolution of the Lucinidae. The Geological Society of London v. 177, p. 207–225.

Taylor J. D. and Glover E. A., 2006, Lucinidae (Bivalvia)-the most diverse group of chemosymbiotic molluscs. Zoological Journal of the Linnean Society v. 148, p. 421–438.

Thiagarajan N., Adkins J. and Eiler J., 2011, Carbonate clumped isotope thermometry of deep-sea corals and implications for vital effects. Geochimica et Cosmochimica Acta v. 75, p. 4416–4425.

Tierney J. E., Zhu J., King J., Malevich S. B., Hakim G. J. and Poulsen C. J., 2020, Glacial cooling and climate sensitivity revisited. Nature v. 584, p. 569–573.

Tosic M., Restrepo J. D., Lonin S., Izquierdo A. and Martins F., 2019, Water and sediment quality in Cartagena Bay, Colombia: Seasonal variability and potential impacts of pollution. Estuarine, Coastal and Shelf Science v. 216, p. 187–203.

Tripati A. K., Eagle R. A., Thiagarajan N., Gagnon A. C., Bauch H., Halloran P. R. and Eiler J. M., 2010, 13C-18O isotope signatures and "clumped isotope" thermometry in foraminifera and coccoliths. Geochimica et Cosmochimica Acta v. 74, p. 5697–5717.

Trofimova T., Milano S., Andersson C., Bonitz F. G. W. and Schöne B. R., 2018, Oxygen isotope composition of Arctica islandica aragonite in the context of shell architectural organization: implications for paleoclimate reconstructions. Geochemistry, Geophysics, Geosystems v. 19, p. 453–470.

Wacker U., Fiebig J., Tödter J., Schöne B. R., Bahr A., Friedrich O., Tütken T., Gischler E. and Joachimski M. M., 2014, Empirical calibration of the clumped isotope paleothermometer using calcites of various origins. Geochimica et Cosmochimica Acta v. 141, p. 127–144.

Wanamaker A. D., Kreutz K. J., Schöne B. R. and Introne D. S., 2011, Gulf of Maine shells reveal changes in seawater temperature seasonality during the Medieval Climate Anomaly and the Little Ice Age. Palaeogeography, Palaeoclimatology, Palaeoecology v. 302, p. 43–51.

Wanamaker A. D., Kreutz K. J., Schöne B. R., Maasch K. A., Pershing A. J., Borns H. W., Introne D. S. and Feindel S., 2009, A late Holocene paleo-productivity record in the western Gulf of Maine, USA, inferred from growth histories of the long-lived ocean quahog (Arctica islandica). International Journal of Earth Sciences v. 98, p. 19–29.

de Winter N., Agterhuis T. and Ziegler M., 2021, Optimizing sampling strategies in high-resolution paleoclimate records. Climate of the Past , p. 1–52.

Yanes Y., Kowalewski M. and Romanek C. S., 2012, Seasonal variation in ecological and taphonomic processes recorded in shelly death assemblages. Palaios v. 27, p. 373–385.

Zhang J. Z., Petersen S. V., Winkelstern I. Z. and Lohmann K. C., 2021, Seasonally variable aquifer discharge and cooler climate in Bermuda during the last interglacial revealed by subannual clumped isotope analysis. Paleoceanography and Paleoclimatology v. 36, p. 1–19.

Zhou G.-T. and Zheng Y.-F., 2003, An experimental study of oxygen isotope fractionation between inorganically precipitated aragonite and water at low temperatures. Geochimica et Cosmochimica Acta v. 67, p. 387–399.

Chapter 3 Seasonally Variable Aquifer Discharge and Cooler Climate in Bermuda During the Last Interglacial Revealed by Subannual Clumped Isotope Analysis[2]

3.1 Abstract

Faunal analog reconstructions suggest that Last Interglacial (MIS 5e) sea surface temperatures (SSTs) were cooler around Bermuda and in the Caribbean than modern climate. Here we describe new and revised clumped isotope measurements of *Cittarium pica* fossil shells supporting previous findings of cooler than modern temperatures in Bermuda during the Last Interglacial. We resolve temperature and $\delta^{18}O_w$ differences between two closely-located and apparently coeval sites described in Winkelstern et al. (2017) through reprocessing raw isotopic data with the updated Brand/IUPAC parameters. New subannual-resolution clumped isotope data reveal large variations in $\delta^{18}O_w$ out of phase with seasonal temperature changes (i.e. lower $\delta^{18}O_w$ values in winter). Supported by modern $\delta^{18}O_w$ measurements identifying similar processes occurring today, we suggest past variations in coastal $\delta^{18}O_w$ were driven by seasonally variable freshwater discharge from a subterranean aquifer beneath the island. Taken together, our results emphasize the importance of $\delta^{18}O_w$ in controlling carbonate $\delta^{18}O$, and suggest that typical assumptions of constant $\delta^{18}O_w$ should be made cautiously in nearshore settings and can contribute to less accurate reconstructions of paleotemperature.

[2] Zhang, J. Z., Petersen, S. V., Winkelstern, I. Z., & Lohmann, K. C. (2021). Seasonally variable aquifer discharge and cooler climate in Bermuda during the last interglacial revealed by subannual clumped isotope analysis. *Paleoceanography and Paleoclimatology*, *36*(6), 1–19.

3.2 Introduction

The Last Interglacial (Marine Isotope Stage 5e, or MIS 5e) is the most recent time in which global mean surface temperatures exceeded modern values, reaching ~2 °C warmer than present (CLIMAP, 1984; Kukla et al., 2002; Kaspar et al., 2005; Turney and Jones, 2010; Sanchez Goni et al., 2012). Reconstructions of MIS 5e sea surface temperature (SST) as part of the CLIMAP project and subsequent studies found that the oceans were not uniformly warmer during this time (CLIMAP, 1984; Harrison et al., 1994; Turney and Jones, 2010; Brocas et al., 2019). Instead, regional-scale spatial patterns were revealed showing a generally cooler reconstructed Central Atlantic and Caribbean temperatures (with the exception of one study showing warmer than Holocene in the Carribbean; Schmidt et al., 2004) and warmer reconstructed conditions in the North Atlantic and Greenland/Iceland/Nordic Sea (CLIMAP, 1984; Turney and Jones, 2010; Brocas et al., 2019), suggesting differences in meridional heat transport relative to today. The island of Bermuda (32.4ºN, 64.8ºW) sits near this paleo-interface, with cooler-than-modern regions to the south and warmer-than-modern regions to the north.

Today, as a result of the warm Gulf Stream Current that contours along the U.S. East Coast, Bermuda has a warm subtropical climate that defies its latitude and makes it the northern-most Atlantic location where coral reefs grow (Coates et al., 2013). The annual average sea surface temperature (SST) is 23ºC and the throughout the year temperature ranges from 19-29ºC (lowest monthly mean to highest monthly mean - NOAA National Data Buoy Center), compared to 4-28ºC in coastal Charleston, South Carolina at the same latitude (US Climate Data 2019).

Sediments on Bermuda consist of layered eolianites, marine limestones and terra rosa paleosols (Coates et al., 2013). During warm, interglacial periods, carbonates formed across an

expanded platform submerged by higher sea level; during glacial periods, eolianites formed as coastal dunes covered a larger island area exposed by lower sea level (Meischner et al., 1995). Today, marine carbonates exposed ~0-5 meters above the modern water line contain fossil shells and corals that can be dated and used for paleoclimate reconstructions. The stratigraphy of Bermuda has been well characterized, considered and refined over the years (Land et al., 1967; Hearty, 2002; Muhs et al., 2002; Hearty et al., 2004; Hearty and Olson, 2010; Rowe et al., 2014). Geochronological techniques including Amino Acid Racemization, Uranium-Thorium dating, and seismic imaging (Harmon et al., 1983; Vollbrecht, 1990; Hearty et al., 1992; Hearty et al., 1999; Rowe et al., 2014) have led to a robust age model assigning marine deposits to the last several interglacial intervals. Limestone units on the island can now be divided into five main Formations, in ascending order: Walsingham (>700,000 ka, >MIS 13), Town Hill (~400,000 ka, MIS 11), Belmont (~200,000 ka, MIS 7), Rocky Bay (~120,000 ka, MIS 5e) and Southampton Formations (~80,000 ka, MIS 5a). In particular, the Devonshire Marine Member of the Rocky Bay Formation has been dated to the last interglacial (MIS 5e), based on numerous stratigraphic and dating efforts using multiple techniques mentioned above (Land et al., 1967; Hearty, 2002; Muhs et al., 2002; Hearty et al., 2004; Hearty and Olson, 2010; Rowe et al., 2014).

Cittarium pica (*C. pica*), also known as the West Indian top-shell, is a distinct, fast-growing, intertidal gastropod that inhabits crevices and small protected areas of exposed rocky shores (Robertson 2003; Olson and Hearty 2013). This species occurs today in Bermuda, throughout the Caribbean and in Central America. In Bermuda, abundant, well preserved *C. pica* fossils can be found in the marine limestones deposited along past rocky shores during multiple prior interglacial stages, specifically MIS 11, 9, 5e and 1 (Walker 1994; Olson and Hearty 2013).

All fossil *C. pica* mentioned in this study were collected from the Devonshire Marine Member of the Rocky Bay Formation (MIS 5e).

Due to the small size of the island, there are no freshwater lakes or rivers, but freshwater collects in subsurface lenses that discharge directly into the surrounding oceans below the waterline (Vacher, 1978; Rowe, 1984; Figure 3.1). Bermuda has multiple subsurface freshwater lenses, the largest one being the Devonshire Lens or Central Lens under Devonshire, Smith's and Paget parishes. This lens covers an area more than twice that of the other freshwater lenses combined (Rowe, 1984). Large differences in permeability in the hydrostratigraphic units containing the aquifer (hydraulic conductivity of 30-120 m/day in the Langton Aquifer on the north side of the island vs. 1000 m/day in the Brighton Aquifer on the south side of the island) leads to an asymmetrically shaped lens in cross section and impedes the escape of freshwater to the oceans on the north shore vs. the south shore (Vacher and Rowe, 1997).

A previous paleoclimate study reconstructed cooler-than-modern SSTs during MIS 5e at two sites in Bermuda using subannual stable isotopes and bulk clumped isotopes on gastropod fossils of the species *C. pica* (Winkelstern et al., 2017). Reconstructed paleotemperatures differed significantly between the two sites, despite their close proximity (~2 km apart) and apparently equivalent geologic age (based on stratigraphic correlation and limited radiometric age dating). Samples from Grape Bay (GB) recorded significantly cooler temperatures (~10°C cooler than today) compared to samples from Devonshire Bay/Rocky Bay (DB/RB) (~5°C cooler than today). Both the large apparent temperature difference between the two sites and the extreme level of cooling relative to today were difficult to explain. The authors proposed that cool, fresh, isotopically-depleted waters from the melting Greenland Ice Sheet could have

traveled southward and temporarily cooled and lowered the isotopic composition of coastal waters around Bermuda (Winkelstern et al., 2017).

Here, we present new, subannual-scale clumped isotope measurements on five of the ten *C. pica* shells from the original study (1 modern, 2 fossils from DB/RB, 2 fossils from GB) to investigate the seasonal persistence and timing of interglacial cooling and determine whether inter-site differences may have been the result of seasonal sampling bias. Published clumped isotope data from Winkelstern et al. (2017) were recalculated using improved data processing techniques (IUPAC/Brand parameters; see Petersen et al. 2019) for more accuracy and to enable better comparison with new data. Finally, we present $\delta^{18}O$ of modern waters (tap and marine) from 16 locations around the island and compare with reconstructed $\delta^{18}O_w$ based on clumped isotope measurements. Our findings, combining new subannual clumped isotope measurements reprocessed published data, and these modern water data, point to the importance of seasonal variations in $\delta^{18}O_w$ over temperature in controlling carbonate $\delta^{18}O$. They also highlight that typical assumptions of seasonally invariant $\delta^{18}O_w$ should be made cautiously, even in settings like Bermuda that have nearly zero above-ground (riverine) freshwater runoff.

3.3 Materials and Methods

3.3.1 Sample Selection and Sampling Strategy

Carbonate clumped isotope paleothermometry (Δ_{47}) is a thermodynamically-based proxy founded on the temperature dependence of the abundance of ^{13}C-^{18}O bonds in the carbonate mineral lattice (Eiler, 2007; 2011). At colder temperatures, these rare and heavy isotopes clump together at a level higher than expected by the stochastic (random) distribution of these isotopes, denoted as Δ_{47} based on the occurrence of mass-47 CO_2 (containing both heavy isotopes)

produced from acid-digestion of carbonate (Huntington et al., 2009; Affek, 2012). While traditional $\delta^{18}O$-based thermometry requires knowledge of the $\delta^{18}O$ of the precipitating fluid ($\delta^{18}O_w$) to accurately reconstruct past climate, the clumped isotope method has the ability to reconstruct a sample's formation temperature, $\delta^{18}O$, $\delta^{13}C$, and $\delta^{18}O_w$ with a single measurement (Ghosh et al., 2006; Eiler, 2011). In mollusk shells like the gastropod *C. pica*, clumped isotopic sampling along the direction of growth can reveal subannual changes in carbonate $\delta^{18}O$, temperature and $\delta^{18}O_w$ (via Δ_{47}).

Mollusk shells act as high-resolution archives of paleoenvironmental information and the geochemistry of mollusk shells has often been used to reconstruct paleotemperature (Grossman and Ku 1986; Tripati et al., 2001; Wanamaker et al., 2006; Eagle 2013). However, in certain cases, carbonate-secreting organisms (e.g. corals, brachiopods) do not precipitate their skeletons in equilibrium with the ambient environment, leading to inaccurate estimations of paleoenvironmental conditions (Tripati et al., 2010; Eagle et al., 2010; Thiagarajan et al., 2011; Saenger et al., 2012; Bajnai et al., 2018). To date, isotopic vital effects have not been identified in any mollusk species (Eagle et al., 2013; Henkes et al., 2013; Winkelstern et al., 2017).

A total of six well-preserved *C. pica* shells collected, described, and analyzed by Winkelstern et al. (2017) were resampled for this study: two modern specimens from Cooper's Island, two MIS 5e fossil shells each from Devonshire/Rocky Bay and Grape Bay (Figure 3.1). A third modern specimen (BM3), collected alongside the other two modern shells as part of the original study but never analyzed, was added to make a total of seven shells studied. As part of the original study, the first six shells were micro-sampled at high resolution for $\delta^{18}O$ and bulk sampled for clumped isotope (Δ_{47}) analysis at a single point near the aperture. These original Δ_{47} analyses therefore reflected the last shell growth for each organism.

In our current study, additional high resolution $\delta^{18}O$ sampling was conducted on two previously-sampled modern shells (BM1, BM2) to extend the published high-resolution record by 1-2 more years. The third modern shell (BM3) was sliced along the last growth whorl to reveal a cross section of growth using a rock saw, and four years of growth were sampled for high-resolution $\delta^{18}O$. Three or more new clumped isotope measurements were made per fossil shell, targeting the highest and lowest $\delta^{18}O_{carb}$ values, as recorded in published (Winkelstern et al., 2017) and newly-expanded high resolution $\delta^{18}O$ records, with the goal of capturing the full seasonal range in temperature and the oxygen isotopic composition of water ($\delta^{18}O_w$) while further ensuring *C. pica* could accurately record seasonality and serve as a climate proxy for the past. Ten additional Δ_{47} measurements were made on the modern shell BM2.

Winkelstern et al. (2017) used multiple methods to determine these fossil shells were well preserved. As part of the original study, fossil shells were inspected under the microscope, powders were analyzed with X-ray diffraction (XRD), and isotopic analyses of fossils were compared to surrounding bulk material. All fossil samples exhibited excellent preservation, displaying original shell layering and coloration, preserving a 100% aragonitic composition, and retaining contrasting $\delta^{18}O$ and clumped isotope values relative to co-occurring diagenetic cements (Winkelstern et al., 2017). All isotopic samples were taken from the pristine inner shell material from cross section (Figure 3.S1) to avoid the outermost layer that could have been physically abraded, encrusted, or bored by predators. Burial history of these units is negligible – MIS 5e rocks are stranded ~0-5m above modern sea level in their original position and have never been buried or heated, eliminating the possibility of clumped isotopic bond reordering (Henkes et al., 2014, Stolper and Eiler., 2015). All tests mentioned above point to the unlikelihood of diagenetic alteration of the studied fossil shells, and thus no further tests on

diagenesis were deemed necessary for the purpose of this study. Previous work on Bermudan fossil corals also supports excellent preservation and closed-system behavior (e.g. Muhs et al., 2002).

3.3.2 High Resolution Stable Isotope Analytical Methods

High-resolution drilling was carried out with a Merchantek MicroMill computer-controlled drilling stage to collect ~50 μg of powder for each analysis (Figure 3.S1), spaced every ~3mm, resulting in ~20 points per year of growth. Each powder was analyzed for $\delta^{13}C$ and $\delta^{18}O$ using a Kiel IV automated carbonate device attached to a Thermo-Finnegan MAT 253 dual inlet mass spectrometer. Data was standardized by comparison to NBS-18 and NBS-19 with units reported in per mille (‰), relative to the VPDB standard, with a typical uncertainty of ±0.1‰ in both $\delta^{13}C$ and $\delta^{18}O$.

3.3.3 Clumped Isotope Analytical Methods

Seasonal peak and trough points were identified in the high resolution $\delta^{18}O$ data for each shell. Each identified $\delta^{18}O$ maximum or minimum was sampled using a low speed dental drill until a total of 20 mg was collected and homogenized (Figure 3.S1). Individual sample replicates of 4-6mg were reacted in phosphoric acid to produce CO_2 and purified using a custom-built vacuum line described by Defliese et al (2015) with procedures further described in Petersen et al (2016). More details of the procedure can be found in the supplement (Appendix 3.8.2). All samples were replicated three or more times, with most samples replicated four times, spread out over a period of months to accommodate long-term variation in mass spectrometer behavior.

Δ_{47} was calculated from raw voltages using an R-code script applying the updated Brand parameters (Petersen et al., 2019). Δ_{47} values were converted into the absolute reference frame to correct the dependency of the measured Δ_{47} on δ_{47} and mass spectrometer "frame compression/stretching" using heated (1000ºC) and equilibrated (25ºC) gas standards (Dennis et al., 2011). An acid fractionation factor of +0.072‰ corresponding to a reaction temperature of 75°C was applied to account for the isotopic fractionation resulting from loss of one oxygen atom during acid digestion (Petersen et al., 2019). Three in-house carbonate standards (Carrara marble and aragonitic ooids (Defliese et al., 2015), and an aragonitic coral standard CORS (Rosenheim et al., 2013) were monitored and correction windows were adjusted to minimize drift in corrected standard values through time. True values for these standards were separately defined relative to the ETH standards. A secondary transfer function using many replicates of these three standards, plus a handful of replicates of ETH1-4, was applied to bring final Δ_{47} values into alignment with the current best community-wide reference frame (see Appendix 3.8.2).

Individual replicates were determined to be bad if Δ_{48} values were elevated more than 2‰ above pure gas standards indicating contamination. Within each sample, if the standard deviation of all replicates was in excess of the long-term standard deviation of in-house carbonate standards (0.025‰), the most deviant replicate was deemed an outlier and removed, which in most cases corresponded to a single-replicate temperature of >50°C or <-15°C, likely resulting from individual errors during sample preparation. After this screening, only samples with at least three good replicates were included for interpretation.

Δ_{47} values were converted to temperature using the synthetic composite calibration of Petersen et al. (2019) with Brand/IUPAC parameters, updated $\Delta_{47\text{-TE}}$ values and acid digestion

fractionation values ($\Delta_{47\text{-RFAC(Br,P,newAFF)}} = (0.0383 \pm 1.7\ E^{-6}) * (10^6 / T^2) + (0.258 \pm 1.7E^{-5})$). This calibration equation was chosen because it reflects the growing calibration consensus in the clumped isotope community and our modern shell samples presented here produced best results using this calibration.

$\delta^{18}O_{carb}$ values were combined with Δ_{47}-temperatures to calculate $\delta^{18}O_w$ using both the mollusk-specific aragonite-water fractionation factor of Grossman and Ku (1986) and the water-aragonite fractionation factor of Kim et al. (2007) based on synthetic laboratory precipitates. The first equation was chosen because the relationship is defined based on aragonitic mollusks, including gastropods, matching our specimen type (Grossman and Ku, 1986). The second equation of Kim et al. (2007) is a targeted laboratory study on the temperature dependence of mineral-specific acid fractionation factors and is commonly used for many aragonitic taxa. Both equations were explored for our dataset but we chose to present our data in this paper with Grossman and Ku (1986) because this produced the best alignment between our modern shells and modern instrumental temperatures (see Discussion). $\delta^{18}O_w$ values calculated using Kim et al. (2007) can be found in the supplementary material.

3.3.4 Reprocessing of Published Clumped Isotope Data

Original Δ_{47} values and temperatures calculated by Winkelstern et al. (2017) were processed using Santrock/Gonfiantini parameters following Huntington et al. (2009), $\Delta_{47\text{-TE}}$ values from Dennis et al., (2011), and the acid fractionation factor and temperature calibration of Defliese et al., (2015). Since the time of publication, many of these values have been updated (Petersen et al., 2019). Therefore, we reprocessed the Winkelstern et al. (2017) data from raw voltages using the same R-code as new data, this time employing Brand/IUPAC parameters,

updated $\Delta_{47\text{-TE}}$ values and acid fractionation factor from Petersen et al. (2019). It was not possible to apply a secondary transfer function using Carrara and Ooids standards, as was done with new data, due to insufficient standards having been run during the relevant measurement sessions (Appendix 3.8.2). However, the alignment of the reprocessed Winkelstern data points with new data suggest this is not necessary (Figure 3.5). Finally, $\delta^{18}O_w$ was calculated this time using the mollusk-specific fractionation factor of Grossman and Ku (1986).

3.3.5 Modern Water Collection and Isotopic and Salinity Analysis

Modern water samples were collected from around the island over two sampling periods and analyzed for $\delta^{18}O_w$ for comparison with calculated $\delta^{18}O_w$ values from our fossil shells. Eighteen modern water samples were collected from fourteen locations around the island: 17 seawater samples, 1 tapwater sample. Tap water in Bermuda comes from underground cisterns beneath each house that collect rainwater falling on the roof and likely approximates weighted annual average composition of local precipitation. Seven water samples were collected in April 2019 and the other eleven were collected in January/February 2020. All non-tap water samples were collected near shore, except for the sample near Bird Island, which was collected from a kayak away from shore.

All aqueous samples were first equilibrated with tank CO_2 gas for at least 48 hours and pure, dehydrated CO_2 was extracted using a custom-built vacuum extraction line (Figure 3.S2; Appendix 3.8.4). $\delta^{18}O$ of CO_2 was analyzed on the same Thermo-Finnegan MAT 253 dual inlet mass spectrometer used for clumped isotopic measurements and $\delta^{18}O$ of the original waters through calibrated with in-house liquid standards which, in turn, were cross-calibrated using

USGS standards (USGS 45, 46). Details of the procedure and a schematic diagram of the extraction line can be found in supplementary material (Figure 3.S2; Appendix 3.8.4).

All water samples were also measured in duplicate for their total salinity using an Extech EC170 salinity meter (Table 3.1). A third independent salinity measurement was performed using a Leica handheld Temperature Compensated Refractometer for cross-calibration. Basic accuracy for the Extech salinity meter is ±2% and this device reports salinity to 0.1 ppt. The Leica Refractometer has a typical precision of 0.5 ppt. All three measurements were averaged together in Table 3.1. See supplementary Figure 3.S3 and Table 3.S1 for all data.

3.4 Results

3.4.1 Isotopic Analysis of Modern Water Samples

Seawater $\delta^{18}O_w$ values ranged from +0.8 ± 0.1‰ (Hungry Bay) to +1.3 ± 0.1‰ (Bird Island; Hamilton; Grape Bay; Hungry Bay Tide Pool) (Table 3.1). The tap water sample had a $\delta^{18}O_w$ value of -3.9 ± 0.1‰ (Table 3.1), much lower than all seawater samples.

Seawater samples show a salinity range of 34.2-36.8 psu, as expected (Figure 3.S3). However, no clear correlation between salinity and $\delta^{18}O_w$ was observed.

3.4.2 Reprocessing of Published Data using Brand Parameters

Winkelstern et al. (2017) reported Δ_{47}-temperatures from Grape Bay (15-17°C) that were distinct from temperatures calculated for Devonshire Bay/Rocky Bay (19-25°C) (Figure 3.2A). This finding was puzzling given that the deposits at these sites are apparently coeval and only ~2km apart (Winkelstern et al., 2017). After reprocessing using Brand/IUPAC parameters with synthetic calibration, the calculated Δ_{47}-temperature ranges from the two sites overlap (GB = 17

to 24.5°C; DB/RB = 21-29.2°C) (Figure 3.2B). Except for one GB point, the GB temperatures fall within the DB range (GB range with point removed = 23.7 to 24.5°C).

Reprocessing also decreased differences in calculated $\delta^{18}O_w$ values and shifted all $\delta^{18}O_w$ values higher. Prior to reprocessing, $\delta^{18}O_w$ values from Grape Bay were -1 to 0.1‰ and from Devonshire Bay/Rocky Bay were 0.8 to 2.1‰ (Figure 3.2A). After reprocessing, GB $\delta^{18}O_w$ values were -0.3 to 1.8‰ and DB/RB $\delta^{18}O_w$ values were 0.8 to 3.3‰ (Figure 3.2B).

3.4.3 High Resolution Stable Isotope Measurements in the Modern Shell

All three modern shells showed around 3-4 years of growth over the measured interval and demonstrated clear seasonality in $\delta^{18}O_{carb}$ (Figure 3.3). The seasonal cycle is especially clear in shell BM3 and somewhat distorted in the later part of BM1. Drill points are evenly spaced around the last whorl of the shell and the sample spacing of ~10-15 points per year corresponds to roughly monthly resolution. The pseudo-sinusoidal profiles in the modern shells shown in Figure 3.3 show an uneven distribution between warmer and cooler seasons. The larger number of points representing the summer months compared to shorter winters indicates variable growth rates throughout the year (faster in summer, slower in winter).

Using the modern water value of +1.16‰, collected from the same sampling location (Cooper's Island) as the modern *C. pica* shells, we converted the high resolution $\delta^{18}O_{carb}$ values using the mollusk-specific fractionation equation described by Grossman and Ku, 1986 to temperature. Using this $\delta^{18}O_{sw}$ value, our modern shell ranges from 19.8 to 29.7°C for BM1, 20.0 to 29.5°C for BM2, and 20.7 to 30.2°C for BM3 (Figure 3.3), compared to the instrumental range of 19 to 29°C. The ranges seen in the three modern shells (BM1=9.9°C; BM2=9.5°C; BM3=9.5°C) match excellently with the observed instrumental seasonal range of 10°C.

In all three modern shells best alignment with modern instrumental temperatures is achieved using the equation described by Grossman and Ku (1986). Therefore, we choose to use Grossman and Ku (1986) equation going forward when calculating $\delta^{18}O_w$ values for fossil shells using Δ_{47}-based temperatures. A second version of the data calculated using Kim et al. (2007) is available in the supplementary material.

3.4.4 Δ_{47} and $\delta^{18}O_w$ Measurements in the Modern Shell BM2

Previously, the modern shell BM2 had been sampled in a single location for Δ_{47}, near terminal edge of each shell, reflecting a late summer season temperature based on the high-resolution $\delta^{18}O$ profile (Winkelstern et al., 2017). For the current study, ten additional Δ_{47} measurements were made on BM2, targeting the highest and lowest $\delta^{18}O_{carb}$ values to capture the full seasonal range in temperature and $\delta^{18}O_w$ to compare with observed temperature and seawater compositions (Figure 3.S1, 3.4A). The resulting Δ_{47} values correspond to temperatures of 16.1±3.8 to 32.7±4.4°C, matching well with the observed annual seasonal temperature range (Figure 3.4B). The average of all BM2 Δ_{47} measurements is 23.5°C±2.6(1sd) (include the single measurement from Winkelstern et al 2017), combining samples from the ~4 years of life represented by the sampled interval (2008-2011). This shows excellent agreement with the observed mean annual temperature of 23°C over the same interval. This close agreement between the Δ_{47}-based temperatures and reality indicate *C. Pica* shells do not show any "vital effects" (biologically-driven deviations from equilibrium precipitation) in clumped isotope-derived temperatures, or if they do, they are smaller than our measurement error. Fossil *C. pica* shells are therefore likely to be faithful recorders of environmental conditions in Δ_{47} as well, as it

is unlikely that a species has evolved to have a vital effect over 125,000 years without changing any other physical characteristics defining the species.

$\delta^{18}O_w$ values were calculated from Δ_{47}-based temperatures and co-analyzed $\delta^{18}O_{carb}$, and using two different equations (Grossman and Ku, 1986; Kim et al., 2007; Figure 3.4C). Using the Grossman and Ku (1986) equation resulted in a range of -1.4±0.3 to +1.4±0.9‰, and a mean $\delta^{18}O_w$ value of 0.0‰±0.5 (1sd). Using the Kim et al (2007) equation resulted in a range of -0.5±0.3 to +2.2±0.8‰, and a mean $\delta^{18}O_w$ value of 0.9‰±0.5 (1sd). The measured value at Cooper's Island plots within error of the mean $\delta^{18}O_w$ value calculated using the Kim et al (2007) equation, and is within both measured $\delta^{18}O_w$ ranges. The calculated $\delta^{18}O_w$ values from both equations yield greater than expected ranges (2.8‰ for all points included), given the previous (and commonly used) assumption that $\delta^{18}O_w$ is seasonally invariant (Winkelstern et al., 2017). However, modern seawater samples from around the island display a non-zero range in $\delta^{18}O_w$ (+0.8 to +1.3‰ for a range of 0.5‰) (Figure 3.4C, 3.5B).

3.4.5 Δ_{47} and $\delta^{18}O_w$ in Fossil Shells

Fossil shells were sampled in four additional positions for clumped isotopes, selected to target the high and low $\delta^{18}O_{carb}$ values. Δ_{47} values from Grape Bay shells recorded temperatures of 10.1-24.5°C, and a $\delta^{18}O_w$ range of -2.1 to +1.8‰ (Figure 3.5). Δ_{47} in Devonshire Bay/Rocky Bay shells recorded temperatures of 12.7 to 35.2°C, with a $\delta^{18}O_w$ range of -2.03 to +3.3‰ (Figure 3.5). The larger temperature range observed in DB/RB is driven primarily by one sample with a temperature of 35.2°C, 6°C higher than the next closest sample from either fossil site. With this one point removed, temperature range for DB reduces to be 12.7-29.2°C, matching much more closely with GB.

DB/RB and GB shells show minimum temperatures colder than both the modern shell and modern observations, but the overall temperature range is comparable. The fossil shells have a range of 25.2°C (10.1±5.5 to 35.2±7.0°C) or a reduced range of 19°C with the highest points removed. The modern shell has a range of 16.6°C (16.1±3.8 to 32.7±4.4°C) compared to modern instrumental data which records a range of 10°C (from 19 to 29°C, monthly means) (Figure 3.5). Shells from both fossil sites show a wider range in $\delta^{18}O_w$ than the modern shells, potentially due to their proximity to the central lens aquifer (discussed below).

3.5 Discussion

3.5.1 Assessing the Validity of Isotopic Proxies in Cittarium pica Using a Modern Shell

3.5.1.1 Stable Isotope Patterns

$\delta^{18}O_{carb}$ is a function of both temperature and the isotopic composition of water ($\delta^{18}O_w$) (Epstein et al., 1953), both of which have the potential to change on annual timescales. High resolution measurements of $\delta^{18}O_{carb}$ in *C. pica* show sinusoidal, apparently annual cycles, suggesting that shells of this species seemingly can record annual climate fluctuations, albeit with a heavier weighting towards the summer months. When $\delta^{18}O_w$ is assumed to be invariant and equal to the value measured for seawater at the collection locality at Cooper's Island (1.16‰), the calculated $\delta^{18}O_{carb}$-based temperature range using the mollusk-specific fractionation equation described by Grossman and Ku (1986) is 19.8-30.2°C for the three shells combined (Figure 3.3), which matches well with the observed range of 19-29°C from NOAA National Data Buoy Center (https://www.ndbc.noaa.gov/). We do not have year-round water sampling at Cooper's Island to directly confirm low variability in $\delta^{18}O_w$ over the lifespan of the calibration shells, but the close agreement between $\delta^{18}O_{carb}$-based temperature range assuming invariant $\delta^{18}O_w$ and the instrumental temperature range, as well as the sinusoidal shape of the $\delta^{18}O_{carb}$

record, suggests that temperature is the primary driver of the observed variations in $\delta^{18}O_{carb}$ in the modern Cooper's Island shell.

However, this conclusion does not immediately apply to all *C. pica* shells. It is possible that variations in $\delta^{18}O_w$ could occur, now or in the past, at other locations around the island. Modern seawater $\delta^{18}O_w$ measurements indicate variations of ~0.5‰ are possible throughout the year and variations of 0.3‰ are possible from a single location (Hamilton) over a span of weeks (Table 3.1, Figure 3.4C). Instead, this is meant to indicate that no significant vital effects in $\delta^{18}O_{carb}$ are present that would distort environmental signals in *C. pica* shells.

3.5.2 MIS 5e in Bermuda Cooler than Modern

Combining 2-4 new subannual-scale measurements with reprocessed data from Winkelstern et al. (2017) (1/shell) results in 3-5 Δ_{47} samples per fossil shell, selected to cover the full seasonal range in temperature. These samples should, when averaged together, more accurately capture mean annual conditions compared to the single Δ_{47} sample previously published per shell. Shell averages in the DB/RB and GB fossil shells range from 16.6 to 25.6°C, this is colder than the average temperature recorded by Δ_{47} in the modern shell BM2 (23.5°C), which accurately captures modern mean annual temperature of 23°C, indicating temperatures in Bermuda during MIS 5e were cooler than today (Figure 3.5). This result agrees with foraminiferal faunal analog-based regional patterns of reconstructed MIS 5e SSTs that show Bermuda to be cooler than modern by 5°C (CLIMAP, 1984; Turney and Jones, 2010) and is consistent with the major conclusion previously made by Winkelstern et al. (2017).

Other studies have suggested the presence of *C. pica,* a generally warm-water species, in MIS5e deposits indicates climates must have been warmer than modern during the Last

Interglacial, citing the absence of this species in modern Bermuda but its presence in warmer regions to the south (Muhs et al., 2002). However, since collection bans were put in place, populations of *C. pica* have flourished in Bermuda in recent years. For example, *C. pica* shells were live-collected (with a permit) in 2014 for isotope analysis (Winkelstern et al., 2017) and were observed by the authors in abundant numbers on the rocky shores of Hungry Bay in 2019, indicating additional factors beyond temperature likely influence their success. Olson and Hearty (2013), after finding *C. pica* fossils in marine deposits in Bermuda dating to MIS 7, 9, and 11, argue that *C. pica* was expatriated in each glacial period and re-colonized Bermuda four separate times over the past ~200,000 years. This conclusion assumes that *C. pica* could not tolerate the colder temperatures of glacial intervals. However, marine units equivalent to those in which *C. pica* fossils are found are not preserved on the island of Bermuda during glacial times due to much lower sea level and the authors state that no marine gastropods of any kind were found in the terrestrial deposits they searched (Olson and Hearty, 2013), but it is unlikely that all species were wiped out and re-colonized each glacial cycle. Therefore, we conclude that faunal analog arguments are fraught here, as there are no equivalent facies during colder periods in which to observe the presence or absence of fossils, and stronger conclusions can be based on isotopically-derived absolute temperatures like those presented here.

Unlike Winklestern et al. (2017), however, we observed no systematic temperature differences between the two study sites in new data or reprocessed published data (Figure 3.2, 3.5). As originally published, GB temperatures were 10°C cooler and $\delta^{18}O_w$ values 0.7‰ lower than modern, and were hypothesized to record a meltwater event delivering cold and isotopically depleted freshwaters all the way from Greenland. Exact ages of Devonshire Marine Member deposits at GB and DB/RB are overlapping, but not identical (see Winkelstern et al., 2017 Figure

3.5). The potential for Grape Bay deposits to possibly represent the beginning of the cooler phase MIS5d was previously used to explain anomalously cold temperatures from those shells. In the new and reprocessed data, fossil shells from both sites record similar temperatures and $\delta^{18}O_w$ values, eliminating the need for explanations as to why they differed despite being close together and the same age (Figure 3.2, 3.5). Further, since the apparent temperature difference between the two sites is resolved here, this lends additional support to the interpretation of the two deposits as being of the same age. Given the measured age ranges for both (Harmon et al., 1983; Muhs et al., 2002), this suggests the common age range of 120-126 ka, during peak warmth of MIS5e.

3.5.3 Unexpectedly Large Subannual Variations in $\delta^{18}O_w$ Recorded in Fossil Shells

Typical sclerochronology studies convert high-resolution $\delta^{18}O_{carb}$ records into subannual temperature records by assuming a constant $\delta^{18}O_w$ value and calculating a single temperature value for each $\delta^{18}O_{carb}$ data point (Buick and Ivany, 2004; Schöne et al., 2004; Hallmann et al., 2008; Wanamaker Jr et al., 2008; Burchell et al., 2013; Winkelstern et al., 2013). In this scheme, $\delta^{18}O_{carb}$ values increase as temperatures cool, and vice versa, according to the temperature dependence of $\delta^{18}O_{carb}$ established in laboratory calibration studies (e.g., Grossman and Ku, 1986). By measuring Δ_{47}-based temperatures at the subannual scale, $\delta^{18}O_w$ is instead allowed to vary throughout the year and we can establish a subannual record of temperature independent of $\delta^{18}O_w$.

Our subannual clumped isotope measurements on all four fossil shells demonstrated an unexpected, inverse relationship between $\delta^{18}O_{carb}$ and temperature. We find the coldest Δ_{47}-derived temperatures correspond to the lowest, not highest, $\delta^{18}O_{carb}$ values (Figure 3.6). This

inverse relationship necessarily results in calculated $\delta^{18}O_w$ values that vary significantly over the year, in an out-of-phase relationship with temperature. We therefore observe low $\delta^{18}O_w$ values corresponding to the coldest times and high $\delta^{18}O_w$ values during warmer times. The range in $\delta^{18}O_w$ values within one shell is >2‰, indicating unexpectedly large variation in coastal $\delta^{18}O_w$.

Given the sampling resolution (2 pts/year, each averaging ~1-2 months), the >2‰ range in $\delta^{18}O_w$ recorded by the fossil shells reflects seasonal-scale, as opposed to inter-annual, variability. The paleoenvironment in which the MIS 5e shells lived is thought to be very similar to the current South Shore environment seen at Hungry Bay – an unencumbered, rocky shoreline facing out into the Atlantic on a small carbonate platform with no surface rivers, well mixed by wave action. This makes it seemingly difficult to explain such large variations in $\delta^{18}O_w$, as wave action would be expected to dilute away any isotopic anomalies into surrounding seawater. *C. pica* shells live on rocky substrates below the high-tide line, but are often exposed or partially exposed during low tide. Any isotopic gradients produced by the injection of freshwater would therefore need to be maintained only in this extremely near-shore environment and do not necessarily need to extend far offshore.

In the following sections, we explore multiple possible mechanisms that could result in the large changes in coastal seawater $\delta^{18}O_w$ we observed in our fossil data and use modern water samples and modern shell data to distinguish between these mechanisms.

3.5.3.1 Propagation of uncertainty

Modern $\delta^{18}O_w$ around Bermuda only varies over a small range (0.5‰ total, 0.2‰ within a given region excluding south shore), but the modern shell BM2 shows a bigger range in $\delta^{18}O_w$ values calculated from Δ_{47}-based temperatures and $\delta^{18}O_{carb}$ values. No measurements exist

documenting the true range in $\delta^{18}O_w$ at Cooper's island throughout the year, but it's unlikely to be much bigger than the total island variability of 0.5‰. The large range in $\delta^{18}O_w$ values reconstructed from modern shell BM2 might be because of pseudo-propagation of uncertainty - that the relatively large uncertainty in Δ_{47}-based temperatures leads to an amplified range in calculated $\delta^{18}O_w$ values (Note: This is not the same as actual propagation of uncertainty where error on temperature is mathematically transferred through calculation of $\delta^{18}O_w$).

In the case of the modern shells, converting $\delta^{18}O_{carb}$ values to temperature using a fixed $\delta^{18}O_w$ value and the aragonite temperature relationship of Grossman and Ku (1986) correctly captures the seasonal temperature range (Figure 3.3). In BM2, Δ_{47}-based temperatures overestimate the seasonal range, yet still got the mean temperature correct (Figure 3.4B). However, the hottest/coldest temperatures do not always align with the lowest/highest $\delta^{18}O_{carb}$ values, leading to more divergent $\delta^{18}O_w$ values. Supporting this pseudo-uncertainty propagation theory for the expanded range in $\delta^{18}O_w$ in the modern shell, the variability in $\delta^{18}O_w$ does not correlate with $\delta^{18}O_{carb}$ in BM2 (Figure 3.4).

In the fossil shells, the situation is different. The pattern of variability is aligned with $\delta^{18}O_{carb}$ variation, in all four shells with the exception of the middle point on DB48, which we have already identified as an outlier for being higher than reasonable temperature (see *section 3.5*). Therefore, even though the same pseudo-propagation of errors may be artificially amplifying the variation in fossil $\delta^{18}O_w$, the pattern of variation is potentially indicating real environmental variations in $\delta^{18}O_w$ on a seasonal scale.

3.5.3.2 Highly Seasonal Precipitation

One possible source of variation in $\delta^{18}O_w$ is precipitation-driven surface runoff transiently depleting coastal $\delta^{18}O_w$. Bermuda has an average annual precipitation of 1468 mm which is fairly evenly distributed throughout the year, with slightly more rainfall in summertime (Rowe 1984). Monthly average precipitation rates range from 75mm to 172mm (Rowe 1984). Precipitation $\delta^{18}O$ in Bermuda, as elsewhere, is much lower relative to seawater, best indicated by the -3.9‰ tap water sample which approximates the annual average isotopic composition of local precipitation as tap water in Bermuda comes from underground cisterns beneath each house that collect rainwater falling on the roof. Since Bermudian tap water, and therefore precipitation, has a much lower $\delta^{18}O_w$ value than local seawater (average of 1.2‰ for 17 seawater samples), surface runoff of precipitation (or direct rainout on surface waters) could reduce $\delta^{18}O_w$ during times of increased precipitation.

This phenomenon is possibly observable in the modern shell BM2. In the four years the sampled shell lived (2008-2011), there was one month with anomalously high precipitation – June 2009 (LDEO Climate Group Datasets) (Figure 3.S4). This appears to align with a single-point spike in the high resolution $\delta^{18}O_{carb}$ record of shell BM2, slightly before the 2009 summertime peak (Figure 3.S4). However, no anomaly in $\delta^{18}O_{carb}$ is seen in BM1 or BM3, making us hesitant to interpret based on a single (unreplicated) measurement. If real, this offset from the expected temperature-driven sinusoid is on the order of 0.75‰ (Figure 3.S4), and is so transient as to be completely missed in 2 of 3 shells at our ~monthly (to sub-monthly in summer) sampling resolution (Figure 3.3). This constrains the order of magnitude and duration of a potential precipitation-driven change in $\delta^{18}O_w$, and indicates that the extent of influence of precipitation changes on $\delta^{18}O_w$ determined from fossil samples should be minimal. Further,

based on instrumental precipitation records, the month of highest precipitation can occur in different summertime months, and some years have no anomalously high rainfall months at all (e.g. 2008 and 2011). Other less extreme rainy months (e.g. September 2010) were absent in all three modern shells, indicating that for precipitation to impact $\delta^{18}O_w$, rainfall must be significantly above background levels.

In contrast, variations in $\delta^{18}O_w$ seen in fossil shells are greater in magnitude (>2‰ within a single shell, although this may be amplified by an unknown amount) and, more importantly, seem to vary seasonally and in every year measured (excluding the one high point in DB48). We see two single-point spikes in the high resolution $\delta^{18}O$ profile of shell DB48, which could reflect especially rainy periods, but these are very short (Figure 3.5). One of these spikes corresponds to the middle sample that has been potentially identified as an outlier due to its elevated temperature of >35°C. However, the $\delta^{18}O_{carb}$ value measured during clumped isotope analysis was lower and more in line with adjacent points, potentially indicating a measurement error in the original high-resolution profile.

If the observed $\delta^{18}O_w$ variability in our four fossil shells was driven by changes in precipitation-driven surface runoff, it would require rainfall levels potentially more than twice as high as the rainiest months today, occurring every summer season. We would also expect precipitation-driven effects on $\delta^{18}O_w$ to be similar everywhere around the island. Fossil *C. pica* shells are primarily found along the south shore due to their preference for a rocky habitat. Future studies looking at MIS 5e-aged shells (of necessity sampling different species) collected from other locations around the island, would help validate or refute this potential mechanism.

3.5.3.3 Coastal Upwelling

Variability in coastal $\delta^{18}O_w$ could be affected by coastal upwelling. Typically, coastal water show significant variability as depth increases, and upwelling holds extreme importance in mixing water from different depth columns and maintaining productivity (Killingley and Berger, 1979; Tao et al., 2013; Jacob et al., 2016). Further, strong seasonal-wind-driven upwelling could bring cold, ^{18}O-enriched, nutrient-rich water to the surface resulting in higher $\delta^{18}O$ values (Killingley and Berger, 1979; O'Dea et al., 2007; Tao et al., 2013; Jacob et al., 2016). Mainly driven by seasonal wind, its intensity also changes seasonally. There are no measurements of $\delta^{18}O_w$ value of the deep water in order to determine the potential of this mechanism to affect coastal surface $\delta^{18}O_w$ values. However, the size of this effect can be estimated by looking at salinity variation with depth, as salinity and $\delta^{18}O_w$ often correlate strongly within a region due to similar controlling processes. Salinity profiles from Hydrostation S, an offshore long-term monitoring site run by the Bermuda Biological Station, recorded minimal salinity variation from the upper column (0-10m) down to 2000m (36.6 psu to 35 psu, respectively) (https://www.st.nmfs.noaa.gov/copepod/time-series/us-10102/). This salinity profile suggests that deep waters likely have similar $\delta^{18}O_w$ values to surface waters around Bermuda. Therefore, variable contribution of deep water is unlikely to cause large variations in coastal $\delta^{18}O_w$ today. For this mechanism to explain large variations in coastal $\delta^{18}O_w$ in the past, coastal upwelling must have been stronger or deep water off Bermuda must have been more isotopically different than today. Future measurements of the $\delta^{18}O_w$ value of modern deep waters and microfossils from offshore MIS5e sediments would help constrain whether this mechanism could be responsible for coastal $\delta^{18}O_w$ variability during the Last Interglacial.

3.5.3.4 Subsurface Discharge From the Central Freshwater Lens

The proximity of our fossil sites to the largest of four freshwater aquifers in Bermuda (Devonshire lens; Figure 3.1) may provide a potential explanation for the large variations seen in $\delta^{18}O_w$. Freshwater from aquifers is injected into near-coastal waters via the subsurface, with discharge rates controlled by aquifer fill rates (i.e. local precipitation rates), topographic gradients, subsurface porosity, and sea level height at the coast (Vacher, 1978). Freshwater in these aquifers is sourced from local precipitation, which has a composition significantly different than seawater (approximated as -3.9‰ from local tap water, compared to ~0.8-1.3‰ in seawater samples), meaning that increased subsurface aquifer discharge could reduce coastal $\delta^{18}O_w$ values and salinities.

Increased subsurface discharge could be induced by increased recharge into the aquifers (i.e. increased precipitation) or due to a drop in coastal sea surface height. In the case of increased recharge, this would act similarly to the surface runoff mechanism described above. During periods of heavy rain, the subsurface water table height would temporarily rise, leading to more discharge at the coast as the lens returned to equilibrium, decreasing coastal $\delta^{18}O_w$ values. However, as above, this would likely be transient, caused by individual storms or stormy weeks/months, with a possible time lag for the gradient imbalance to travel through the aquifer. In order for this to explain our data, very heavy rainfall would have to occur every winter, unlike today, when peak rainfall typically occurs in summer.

On the other hand, three processes contribute to systematic and predictable changes in coastal sea surface heights: 1) semi-diurnal astronomical tides (~0.7-0.9m); 2) daily to weekly isostatic effects from changes in atmospheric pressure (~0.2m); 3) seasonal thermal expansion (~0.6m), induced by seasonal warming and cooling of North Atlantic ocean temperatures

(Vacher, 1978; Rowe, 1984). During periods of high sea level (either high tide, or late summer after maximum thermal expansion), ocean water would act as a dam, blocking the aquifer from discharging as much freshwater, resulting in higher, more marine $\delta^{18}O_w$ values. When sea surface heights were lower (low tide or end of winter), the topographic gradient between the center of the island/aquifer and coastal waterline would increase, causing increased discharge from the freshwater lens and resulting in lower coastal $\delta^{18}O_w$ values due to an increased component of isotopically-depleted aquifer water (Vacher, 1978; Rowe 1984).

Evidence for tidally-driven subsurface discharge has been observed in Bermuda today. In Green Bay Cave on the north side of the island, daily tidal flow mixes freshwater out into coastal seawater, causing documented changes in salinity (and presumably in $\delta^{18}O_w$ as well, although it hasn't been measured) (van Hengstum and Scott, 2012). Tidally-driven subsurface discharge also occurs in other areas with coastal carbonate aquifers such as the Bahama Bank (Whitaker and Smart, 1990; Vacher and Wallis, 1992; Moore, 1996; Beddows et al., 2007). Δ_{47}-based $\delta^{18}O_w$ values measured in our fossil shells show changes on the seasonal-, not tidal-, scale. This could be achieved through a similar mechanism, driven by thermal expansion instead of daily tides. Thermal expansion causes mean sea level heights to fluctuate at nearly the same magnitude as daily tides, but on the months-to-year timescale suggested by the fossil data. Sea surface heights increase throughout the summer as surface waters warm and expand, peaking in September/October, some of the warmest months (Figure 3.S8). Lowest sea surface heights occur in February/March, aligning with the coldest months of the year (Figure 3.S8). In this way, higher aquifer discharge (and therefore lower $\delta^{18}O_w$ values) could align with the colder months. Slight misalignment between peak temperatures (JAS) and maximum sea surface heights (SON)

may explain the reduced apparent seasonal amplitude in fossil shells compared to modern (Figure 3.5).

This mechanism could potentially apply to any stretch of coastline proximal to one of the four major subsurface aquifers on Bermuda (Figure 3.1), but is perhaps most likely to play a role along the South Shore, where our fossil samples were collected. High permeability in the Belmont Formation outcropping along the South Shore makes this stretch of coast more likely to experience higher levels of freshwater discharge than locations on the north shore equally close to the Devonshire aquifer (Vacher, 1978). Freshwater outflow has not been previously documented in this region, but clumped isotopic measurements of marine cements indicate the presence of isotopically depleted waters in the coastal subsurface. Marine cements from along the South Shore record $\delta^{18}O_w$ values mostly between -3.8 and +3.9‰, with a few even lower than -5‰ (Defliese and Lohmann, 2015).

3.5.4 Present-day Tidal Variability in $\delta^{18}O_w$ as a Proxy for Past Seasonal Variability

In April 2019 and January-February 2020, seawater samples were collected from around the island, spanning multiple tidal heights. Absolute $\delta^{18}O_w$ values differed between regions, but within most regions, measured $\delta^{18}O_w$ values were tightly clustered and inter-regional differences could be explained by geography. Samples from the outer southwest edge of the island were lower (GLB and SLB; 0.9-1.0‰) compared to samples from north shore (TF, PR = 1.1‰) and Great Sound (BI, H1-5, LPP, 1.2-1.3‰) (Table 3.1). High $\delta^{18}O_w$ values found in samples from the Great Sound are consistent with higher evaporative enrichment in this semi-enclosed basin. Unlike all other collection sites which face out to the open Atlantic Ocean, the Great Sound forms a natural harbor within the curve of the island, surrounded on all sides by land except for the northeast, where it is open to a shallower region of the Atlantic Ocean overlying a submerged Bermuda platform. Lower values in other regions may reflect

proximity to freshwater lenses (e.g. SLB and the Somerset Lens) (Figure 3.1). The variability seen within each of these regions is at the level of measurement error (+/- 0.1‰), consistent with regionally homogenous and constant seawater compositions, regardless of tidal height. Particularly, five measurements from the same location in the capital city of Hamilton over a period of 2 months show variability of <0.2‰ despite spanning multiple tidal heights. In contrast, the full magnitude of across-island variability was realized in samples collected from a single region – the South Shore. Here, modern seawater $\delta^{18}O_w$ values ranged from 0.8-1.3‰, and variability was related to tidal height (Figure 3.S10, Table 3.1).

The relationship between $\delta^{18}O_w$ and sea surface height is best demonstrated by two samples from Hungry Bay. There, the seawater samples collected as the tide was rising from its minimum (Table 3.1, Figure 3.S9, 3.S10) recorded a lower value of 0.8‰, while at the same location at the same time, water from a stranded tide pool recorded a value of 1.3‰, likely representing the composition of seawater during the preceding high (and lowering tide: Figure 3.9, 3.10). Water collected at high tide from Devonshire Bay had a $\delta^{18}O_w$ value of 1.1‰, reflecting a higher isotopic value consistent with a lower freshwater contribution (Figure 3.S10B). However, other low-tide samples from both GB and EB (1.3 and 1.2) show high values as well, seemingly in poor agreement with our proposed mechanism. These sites are both located farther away from the Devonshire Lens than DB and HB (Figure 3.1) and rocky cliffs that must have been present during MIS 5e to support *C. pica* shells have been replaced with sandy beaches at these sites, potentially impacting permeability and reducing freshwater discharge. In contrast, both DB and HB still have rocky shorelines and support modern populations of *C. pica*, making these sites more representative of the MIS 5e environment. Regardless of the timing and $\delta^{18}O_w$ values from individual sites, it is clear that the largest variability in $\delta^{18}O_w$ within one region and the lowest absolute value (0.8‰) exists along the South Shore, consistent with freshwater discharge mechanisms.

Additionally, the next lowest values are found in the southwestern region (0.9-1.0‰), which is also close to a freshwater lens (Somerset Lens), and may be similarly influenced by subsurface freshwater.

Our samples were mostly collected from off-peak tidal times, it is possible the true range in $\delta^{18}O_w$ values would increase with a higher sample frequency specially designed to capture both extremes within a tidal cycle. Sea level changes during tidal cycles (0.6 m) compare to the annual, thermal-expansion-driven, cycle (1m), implying a similar magnitude change in $\delta^{18}O_w$ could be expected throughout one year. Future work will be required to track $\delta^{18}O_w$ variability around the island on the annual scale to compare to the timescales recorded in fossil shells.

3.5.5 Implications for MIS5e Bermuda

Overall, our fossil data shows very large changes in $\delta^{18}O_w$, and we present a number of hypotheses to explain this data. Larger-than-expected variation in calculated $\delta^{18}O_w$ in the modern shell indicates that this subannual clumped isotope approach may overestimate the range in $\delta^{18}O_w$ values when temperature extremes do not align with $\delta^{18}O_{carb}$ extremes. However, even if the amplitude of the effect is overestimated, coherent patterns of low/high $\delta^{18}O_w$ values during winter/summer seasons demand explanation.

If precipitation were to drive these anomalies, it would require extreme wintertime precipitation every year, contradictory to the modern climatology which has peak rainfall in summer. If coastal upwelling were to drive observed variability in fossil shells, deep waters during MIS 5e must have been isotopically very different from surface waters, unlike gradients today indicated by salinity. We therefore conclude that a freshwater discharge mechanism, driven by changes in sea surface height, is the most likely explanation, as the isotopic composition of that freshwater is significantly different from seawater (-4‰ vs. +1‰) and the

largest variability in modern coastal $\delta^{18}O_w$ is observed along the South Shore today, proximal to the largest freshwater lens under the island. Thermal expansion changes sea surface heights on seasonal timescales, with peak heights, and therefore most marine $\delta^{18}O_w$ values, occurring in late summer/fall coinciding with some of the warmest months.

This suggests that a freshwater lens likely existed under the island of Bermuda during MIS 5e in a similar location to the central lens today and variably ejected freshwater into the South Shore coast region on an annual scale, leading to measurable annual-scale variations in $\delta^{18}O_w$.

3.6 Conclusions

Previous data reconstructing conditions in Bermuda during the Last Interglacial showed divergent temperatures from two closely-spaced and apparently coeval sites. Reprocessing this published data and combining it with new subannual-resolution clumped isotope measurements bring both sites into alignment and into agreement with established records in showing cooler-than-modern temperatures in Bermuda during MIS 5e. Although the small number of shells studied (4 fossils) should be accompanied by caveats about representativeness of longer-term average climate, the close agreement between absolute temperatures and temperature ranges across these four shells from two localities is encouraging. All four shells have average temperatures cooler than modern.

Additionally, subannual measurements revealed large (>2‰) seasonal variations in $\delta^{18}O_w$, occurring out of phase with seasonal temperature changes. This magnitude may be amplified by misalignment between extrema in $\delta^{18}O_{carb}$ and Δ_{47}-temperatures, propagated through calculations of $\delta^{18}O_w$, as seen in a modern shell. However, systematic alignment of high/low $\delta^{18}O_w$ values with warm/cool seasons implies a real environmental forcing.

We propose that subsurface injection of freshwater from the Central Lens into South Shore coastal waters, driven by changes in sea surface height affecting hydrologic gradients in the subsurface aquifer, cause the ~0.5‰ variations in coastal $\delta^{18}O_w$ seen today on tidal timescales along the South Shore. We suggest this mechanism could have also been operating in the past to drive seasonal variations in $\delta^{18}O_w$ recorded in fossil shells, with changes in sea surface height driven by seasonal thermal expansion. Altogether, our results highlight the importance of variations in $\delta^{18}O_w$ as well as temperature in setting carbonate $\delta^{18}O$. They also suggest that the assumption of constant $\delta^{18}O_w$ fails at this site and common assumptions like this may lead to less accurate reconstructions of paleotemperature at other sites.

3.7 Acknowledgements

We thank Lora Wingate for stable isotope laboratory assistance, Phoebe Aron, Chris Poulsen and the IPL laboratory at the University of Michigan for their discussions, Maria Marcano and Ricardo Anderson for additional modern water sample collection, and Mark Rowe for field assistance. This research was supported by NSF grant 1903237, Univerisity of Michigan ADVANCE Crosby Research Award to S. V. Petersen, and NSF GRFP, Rackham Graduate School Merit Fellowship, University of Michigan Turner Grant and Rackham Graduate School Research Grant to J. Z. Zhang. Coinciding with publication, all raw clumped isotope data (including all sample and standards replicates) will be deposited in the EarthChem ClumpDB database for long-term storage, data DOI: 10.26022/IEDA/111922 (https://doi.org/10.26022/IEDA/111922).

3.8 Appendices

3.8.1 CO_2 Preparation and Δ_{47} Measurements

Seasonal peak and trough points were identified in the high resolution $\delta^{18}O$ data for each shell. Each identified $\delta^{18}O$ maximum or minimum was then sampled using a low speed dental drill until a total of 20 mg was collected and homogenized (Figure 3.3). Approximately 4-6 mg of powder was digested for 15-20 minutes in a common acid bath at a temperature of 75°C using 105 wt. % phosphoric acid (H_3PO_4). Extracted CO_2 was dehydrated through cryogenic separation at -95°C using a mixture of 1-propanol and liquid Nitrogen (LN_2) to remove any water generated during reaction. Dry CO_2 was then purified further by passing through a U-trap filled with PoraPak Q material and topped with silver wool to remove sulfur, chlorine, and other contaminants. Yields were recorded before and after this step using an electric manometer to ensure total sample recovery after the cleaning process. Lastly, purified CO_2 was transferred to a cold finger for temporary storage until analysis on the mass spectrometer was possible. All samples were replicated using the above procedure at least three times, with many samples replicated four times, spread out over a period of months to accommodate for long-term variation in mass spectrometer behavior.

Purified CO_2 was analyzed using a Thermo-Finnigan MAT 253 dual inlet mass spectrometer that has been specially configured to collect masses 44-49 against a reference gas with a composition of $\delta^{13}C$ = -3.69‰ (VPDB) and $\delta^{18}O$ = +34.98‰ (VSMOW). Both bellows were initially compressed to achieve 16 volts on the *m/z* 44 cup. Sample beam intensity for *m/z* 44-49 was measured against reference CO_2 beam intensity for 5 acquisitions of 12 sample-reference cycles for each purified CO_2 sample. All samples were replicated at least three times,

with many samples replicated four times, spread out over a period of months to account for long-term variation in mass spectrometer behavior.

3.8.2 CO_2 Clumped Isotope Data Processing

In order to calculate Δ_{47} from raw mass spectrometer outputs (raw voltages), the absolute abundance of the heavy isotopes in the universal standards (VPDB, VSMOW) needs to be defined first using four parameters: R13_VPDB, R17_VSMOW, R18_VSMOW and λ (Petersen et al., 2019). These values were previously set and established by Santrock and coauthors (Santrock et al., 1985) but have been updated recently (now known as Brand or IUPAC parameters) following improved measurement of the universal standard materials (Brand et al., 2010). Recent studies suggest that use of Brand parameters improves inter-laboratory agreement in clumped isotope calibrations and thus improves the accuracy of Δ_{47} data overall (Kelson et al., 2017; Petersen et al., 2019), making their use desirable and encouraged for all future studies.

Δ_{47} was calculated from raw voltages using an in-house R-code script applying the updated Brand parameters (Petersen et al., 2019). Δ_{47} values were converted into the absolute reference frame to correct the dependency of the measured Δ_{47} on δ_{47} and mass spectrometer "frame compression/stretching" using heated (1000°C) and equilibrated (25°C) gas standards (Dennis et al., 2011). An acid fractionation factor of +0.072‰ corresponding to a reaction temperature of 75°C was applied to account for the isotopic fractionation resulting from loss of one oxygen atom during acid digestion (Petersen et al., 2019). In-house carbonate standards (Carrara marble and aragonitic Ooids (Defliese et al 2015), and CORS coral standard (Rosenheim et al., 2013)) were monitored and correction windows were adjusted to minimize drift in corrected standard values through time. A secondary transfer function using Carrara,

Ooids, CORS, and a handful of replicates of the ETH standards was applied, assigning the true values for in-house standards established independently relative to ETH standards. No secondary transfer function was applied to the Winkelstern et al. (2017) data due to insufficient standards run concurrently with samples during that period of time.

Individual replicates were determined to be bad if Δ_{48} values were elevated more than 2‰ above pure gas standards indicating contamination. Within each sample, if the standard deviation of the combined replicates was greatly in excess of the long-term standard deviation of in-house carbonate standards (0.025‰), the most deviant replicate was removed as an outlier, which in most cases corresponded to a single-replicate temperature of >50C or <-15C, likely representing individual errors during sample preparation. After this screening, only samples with at least 3 good replicates were included for interpretation. A complete version of the raw clumped isotope sample and standard replicates are provided separately.

3.8.3 Modern Water Preparation and Isotope Analysis

All 17 seawater samples and 1 tapwater sample were analyzed for $\delta^{18}O$ in the University of Michigan Stable Isotope Laboratory. All aqueous samples were equilibrated with tank CO_2 before analysis on a Thermo-Finnegan MAT 253 dual inlet mass spectrometer. To prepare samples for equilibration, vials with sealed septa were first pierced with a needle and flushed and filled with dry tank CO_2 to a head-space pressure of 1 atm. 4 ml of an unknown or standard water was injected into each CO_2-containing vial, then left to equilibrate in a 25°C water bath for at least 48 hours. After the equilibration period, pure CO_2 was extracted on a custom-built vacuum extraction line (Figure 3.S3). After all atmosphere remaining above frozen CO_2 was evacuated from the head space, CO_2 was cryogenically drawn out of the sample vial via a needle, then

dehydrated through repeated stages of cryogenic separation at -95°C, achieved through a mixture of 1-propanol and liquid Nitrogen (LN_2), to remove any remaining water carried through the extraction line from equilibration. At this stage, yield of gas was checked using an electric manometer before dividing each sample into 3-6 aliquots. Each aliquot of CO_2 was separately flame sealed into a Pyrex tube for storage until analysis on the mass spectrometer. At least two aliquots of the same sample were measured on the mass spectrometer spread out over weeks to accommodate variation in mass spectrometer behavior, and one aliquot was archived in case a third measurement was needed in the future.

The extracted CO_2 was then analyzed on the same Thermo-Finnigan MAT 253 dual inlet mass spectrometer used for clumped isotope analyses (see Appendix 3.8.3). Unknown CO_2 was measured for at least 2 acquisitions of 12 sample-reference cycles at an m/z 44 beam strength of 16V. All samples were calibrated against in-house liquid standards which, in turn, were cross-calibrated using USGS standards (USGS 45, 46).

3.8.4 Salinity Measurements

Salinity was measured twice on each seawater sample using an Extech EC170 salinity meter and a third time using a Leica handheld Temperature Compensated Refractometer for cross-calibration. Each sample was measured spread out over multiple days with randomized order. Salinity meters were cleaned with DI water in between each sample, and wiped dry followed by further drying with compressed air to ensure they were thoroughly dry before the next measurement. Extech EC170 salinity meter measures conductivity and reports salinity to 0.1 ppt. A seawater sample from Florida (not part of this study) was measured 10 times using the Extech EC170 salinity meter to test reproducibility. This resulted in a salinity of 33.2 ± 0.3 ppt

(1sd). Leica handheld Temperature Compensated Refractometer measures the angle of refraction in order to determine concentration of aqueous solutions, and has a typical precision of 0.5 ppt. Offset between the two methods was 1.2 ppt, with the refractometer typically higher. Reported salinities in the main document represent the mean of all three measurements (combining two methods), since one method was not verified to be better than the other.

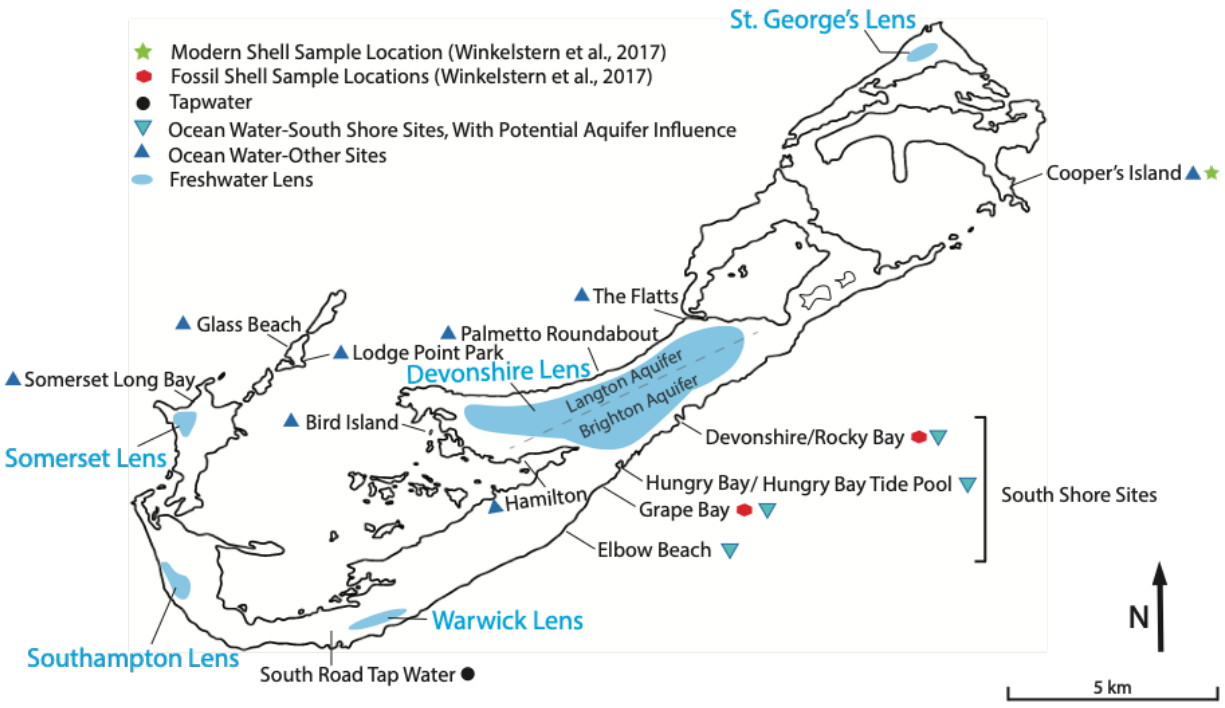

Figure 3.2. Map of Bermuda showing the location of freshwater aquifers, seawater, tap water and lake/pond waters collected across the island.

Fossil and modern shell collection sites also shown for comparison. Freshwater lens locations are from Vacher (1978) and van Hengstum and Scott, (2012).

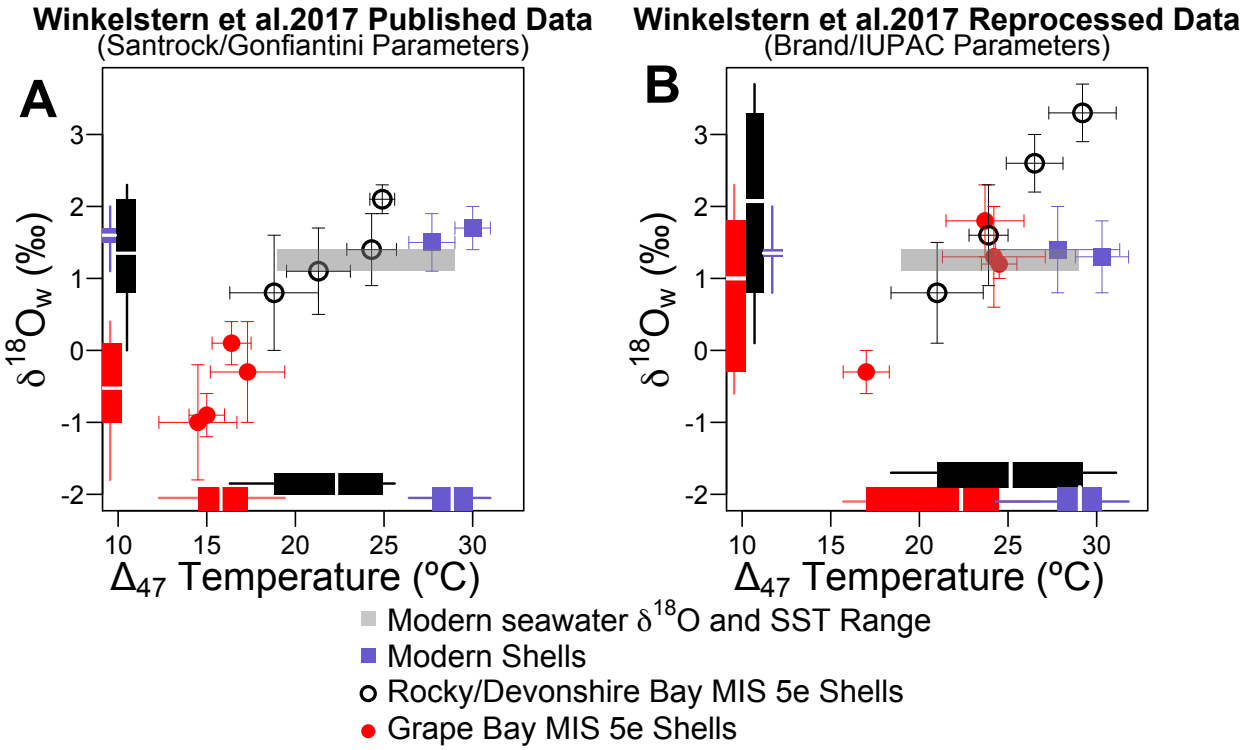

Figure 3.2. Original and reprocessed Δ_{47}-temperatures and $\delta^{18}O_w$ values from Winkelstern et al. (2017).

A, results as originally published (see text), modified from Figure 3.3 of original study with added range bars (Winkelstern et al., 2017). Temperatures calculated using Defliese et al., 2015 calibration equation. B, reprocessed results using updated data processing methods, with temperatures calculated using Brand/IUPAC parameters, synthetic calibration (Petersen et al., 2019) and $\delta^{18}O_w$ values calculated using Grossman and Ku (1986) equation. Errors reported for both Δ_{47}-temperature and $\delta^{18}O_w$ values are based on internal 1 standard error of 3-5 replicates. Gray rectangle denotes modern instrumental variability in temperature (2007-2012 NOAA buoy data) and modern seawater $\delta^{18}O$ values (Global Seawater Oxygen-18 Database), as reported by Winkelstern et al (2017).

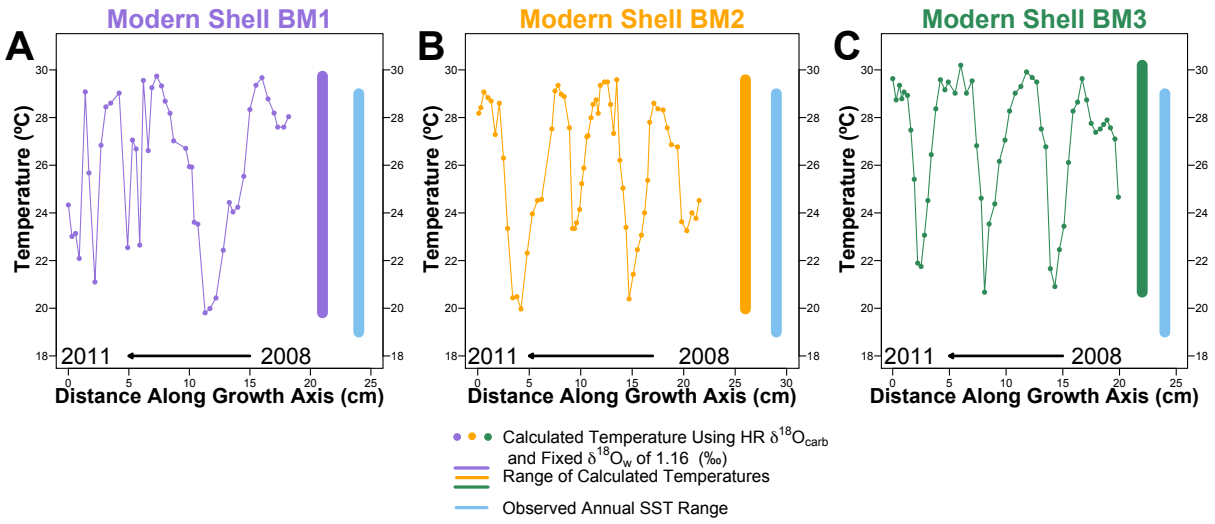

Figure 3.3. Calculated temperatures and range using the mollusk-specific fractionation equation described in Grossman and Ku (1986).

Temperatures calculated from high-resolution $\delta^{18}O_{carb}$ profiles using a single $\delta^{18}O_w$ value of 1.16‰, selected from modern $\delta^{18}O_w$ measurement at collection site, and Blue bars show instrumental temperature range for comparison.

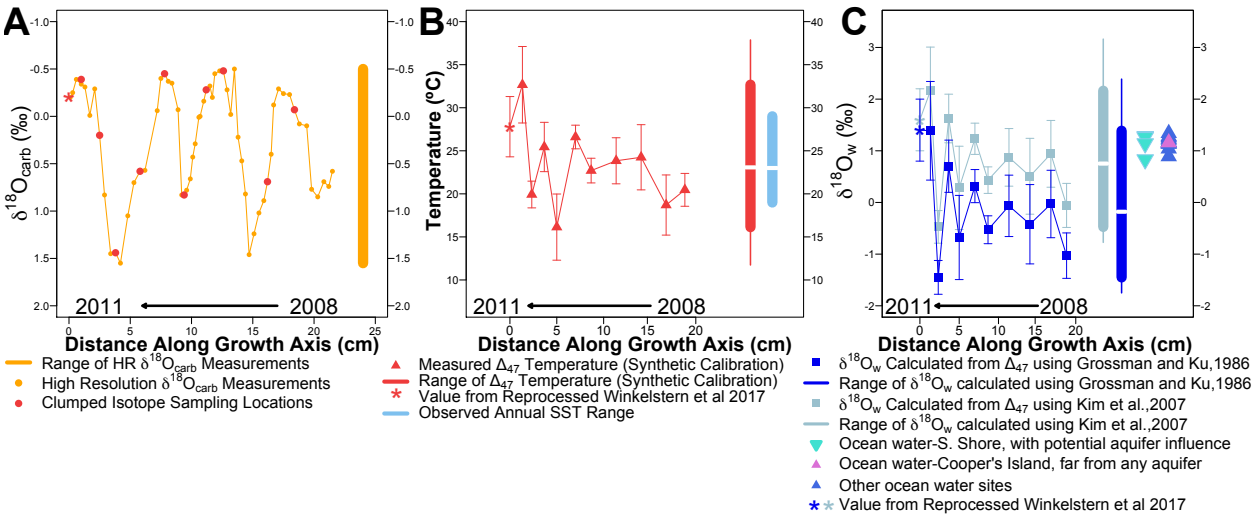

Figure 3.4. $\delta^{18}O_{carb}$, Δ_{47}-based temperature, and $\delta^{18}O_w$ profiles of modern shell BM2.

A, High-resolution $\delta^{18}O_{carb}$ profile from modern shell BM2, with clumped sampling locations shown in red. B, Subannual Δ_{47}-based temperatures from modern specimen BM2. Full measured range is plotted compared to modern instrumental range on the right (blue). C, Subannual $\delta^{18}O_w$ calculated from Δ_{47}-based temperatures and co-analyzed $\delta^{18}O_{carb}$, using two different equations (Grossman and Ku, 1986; Kim et al., 2007). Measured range in $\delta^{18}O_w$ plotted on the right side compared to $\delta^{18}O_w$ values measured on modern waters. Errors reported for both Δ_{47}-temperature and $\delta^{18}O_w$ values are 1 standard error.

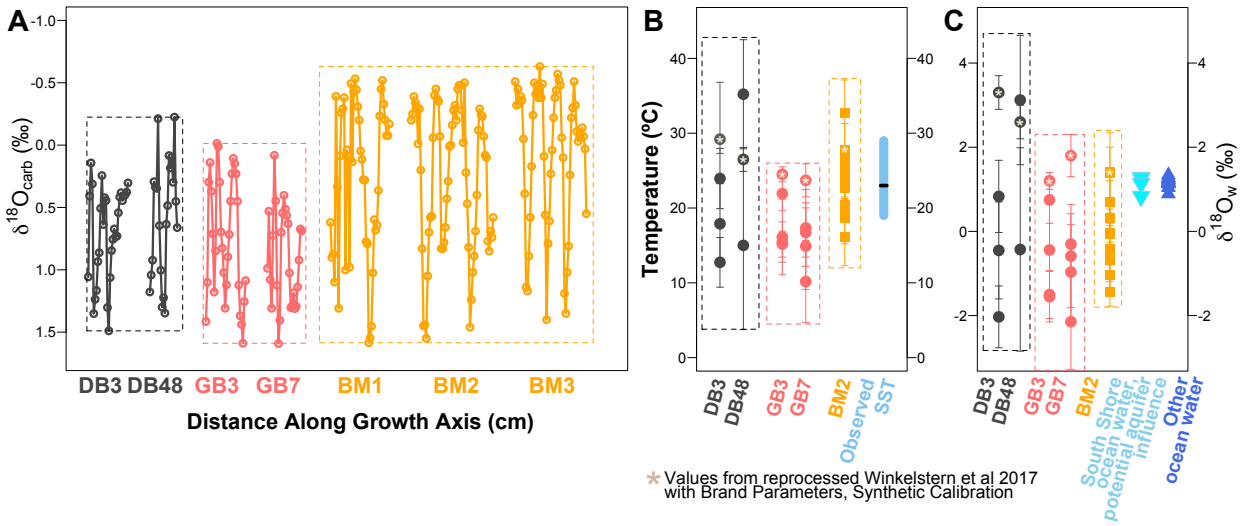

Figure 3.5. $\delta^{18}O_{carb}$, Δ_{47}-based temperature, and $\delta^{18}O_w$ profiles of modern and fossil *C. pica* shells.

A, High Resolution $\delta^{18}O_{carb}$ profiles from fossil and modern shells with ranges indicated by encompassing boxes. B, Δ_{47}-derived temperatures and temperature ranges of fossil and modern shells compared to modern SST. C, $\delta^{18}O_w$ values and ranges of fossil and modern shells, calculated using Grossman and Ku (1986) mollusk-specific fractionation equation, compared to measured modern $\delta^{18}O_w$ values on the right. Errors reported for both Δ_{47}-temperature and $\delta^{18}O_w$ values are based on 1 standard error.

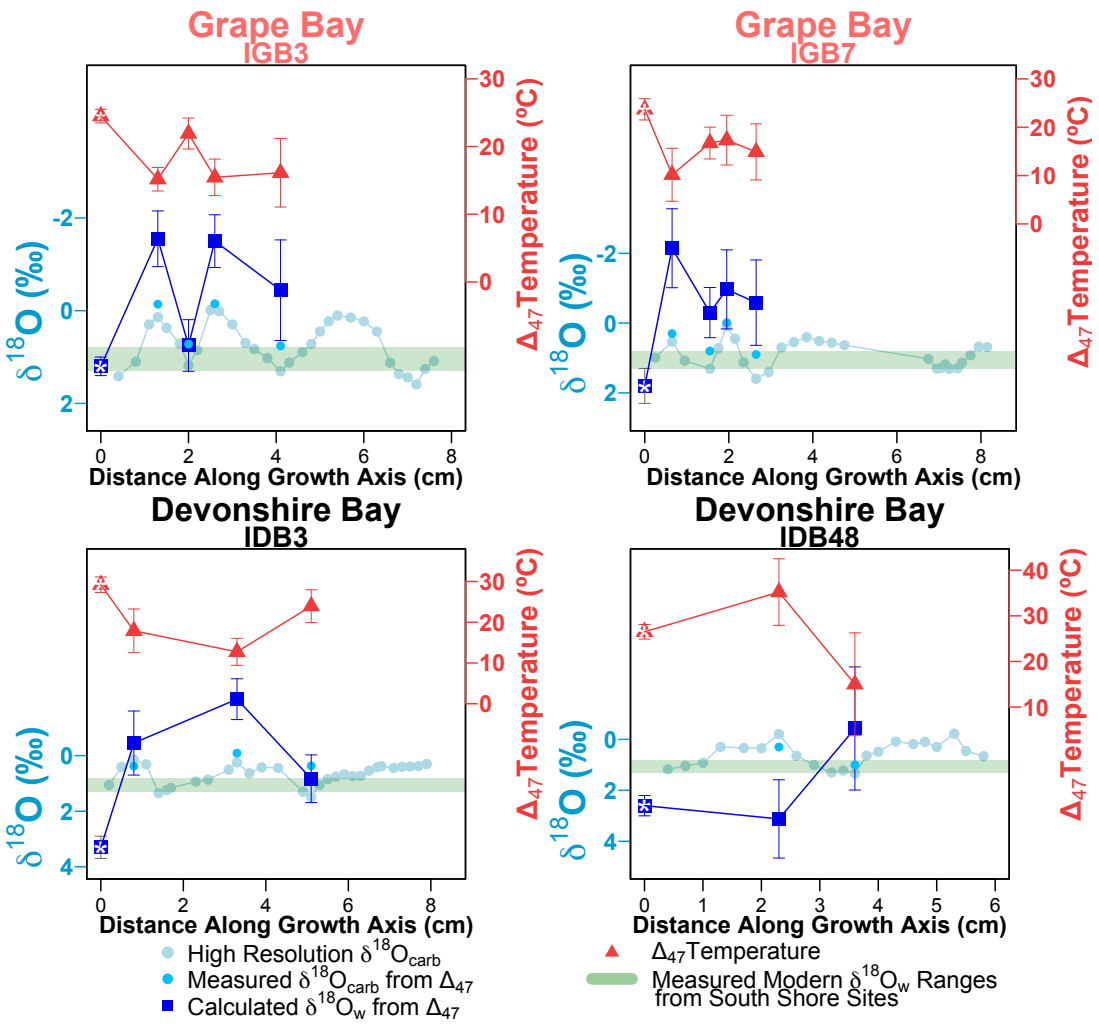

Figure 3.6. Isotope profiles of fossil *C. pica* shells.

High resolution and bulk $\delta^{18}O$ measurements, Δ_{47}-based temperatures and $\delta^{18}O_w$ values, calculated using Grossman and Ku (1986) aragonite-water equilibrium equation, for four fossil shells compared to modern $\delta^{18}O_w$ variability. Note that the y-axes are scaled differently in each plot for best visibility of overlapping data.

Table 3.1. Salinity and isotope analyses data for each water sample collected from Bermuda.

Water Sample	Collection Date	Water Type	Salinity (ppt)[a] (n=3)	$\delta^{18}O$ (‰)[b] (n=2)	Tidal Height
South Road Tap Water	30 April 2019	Tap Water	N/A	-3.9	N/A
Northeast					
Cooper's Island	12 January 2020	Seawater	35.6 ± 0.1	+1.2	High Tide
Great Sound					
Bird Island	01 May 2019	Seawater	34.3 ± 0.6	+1.3	High Tide
Hamilton	11 January 2020	Seawater	35.1 ± 0.2	+1.2	High Tide
	18 January 2020	Seawater	35.3 ± 0.8	+1.2	High Tide
	25 January 2020	Seawater	35.1 ± 0.4	+1.3	High Tide
	01 February 2020	Seawater	35.6 ± 0.4	+1.2	Low Tide
	08 February 2020	Seawater	35.0 ± 1.0	+1.3	High Tide
Lodge Point Park	29 April 2019	Seawater	35.1 ± 0.2	+1.3	Intermediate Tide
Outer Southwest Edge					
Glass Beach	09 February 2020	Seawater	34.5 ± 0.5	+0.9	High Tide
Somerset Long Bay	09 February 2020	Seawater	34.4 ± 0.6	+1.0	High Tide
North Shore					
Palmetto Roundabout	25 January 2020	Seawater	34.7 ± 0.8	+1.1	High Tide
The Flatts	26 January 2020	Seawater	35.1 ± 0.9	+1.1	Intermediate Tide
South Shore					
Devonshire Bay	30 April 2019	Seawater	35.7 ± 0.4	+1.1	High Tide
Elbow Beach	18 January 2020	Seawater	35.7 ± 0.4	+1.2	Low Tide
Grape Bay	29 April 2019	Seawater	35.2 ± 1.0	+1.3	Low Tide
Hungry Bay	29 April 2019	Seawater	35.5 ± 0.6	+0.8	Low Tide
Hungry Bay Tide Pool	29 April 2019	Seawater	35.7 ± 0.3	+1.3	High Tide

[a]Salinity measurements for each sample were replicated at least three times.
[b]Errors for $\delta^{18}O$ values are reported as long term instrument precision of ± 0.1.

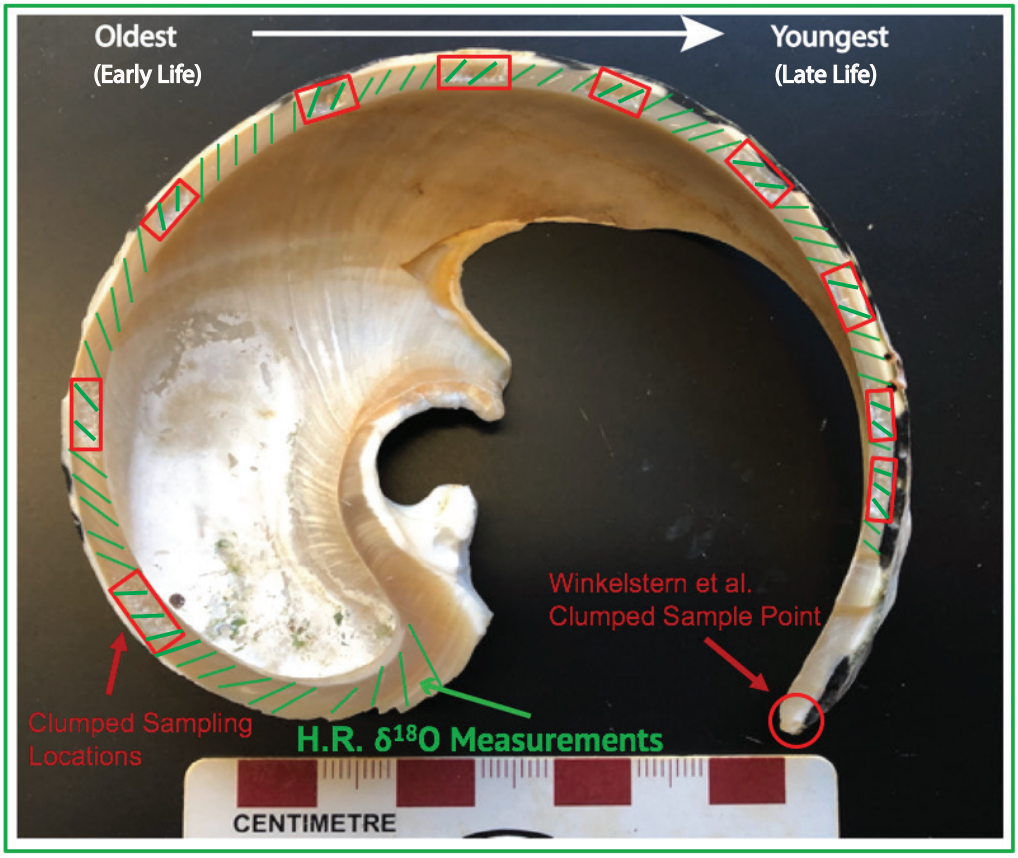

Figure 3.S1. Annotated image of halved modern *C. pica* (BM2) with growth axis facing upwards.

Representative high resolution $\delta^{18}O$ drill lines and larger clumped isotope sampling sites are highlighted in green and red, respectively.

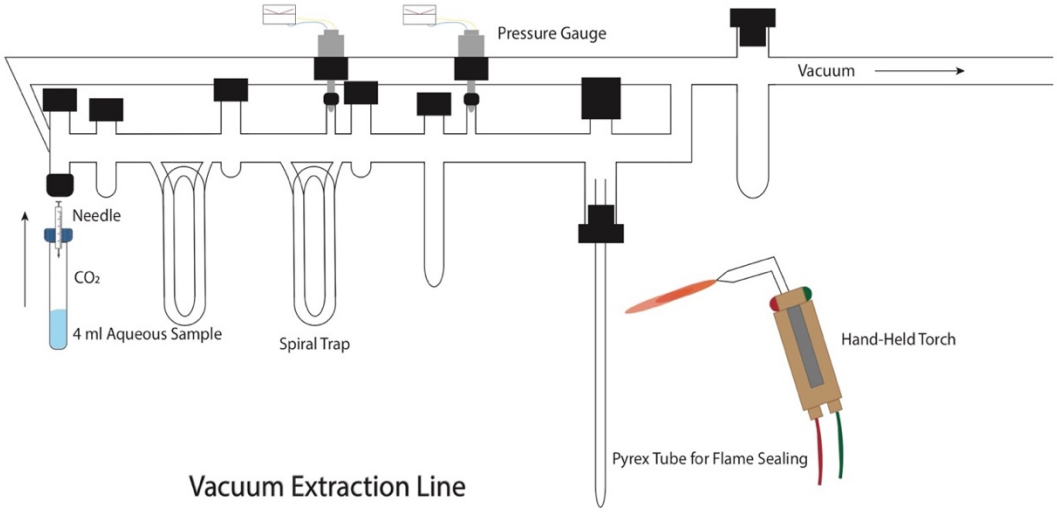

Figure 3.S2. Diagram showing the custom-built vacuum extraction line.

Note that the sample vial is introduced via a needle on the left side. Extracted CO_2 is then sealed in the pyrex tube on the right side.

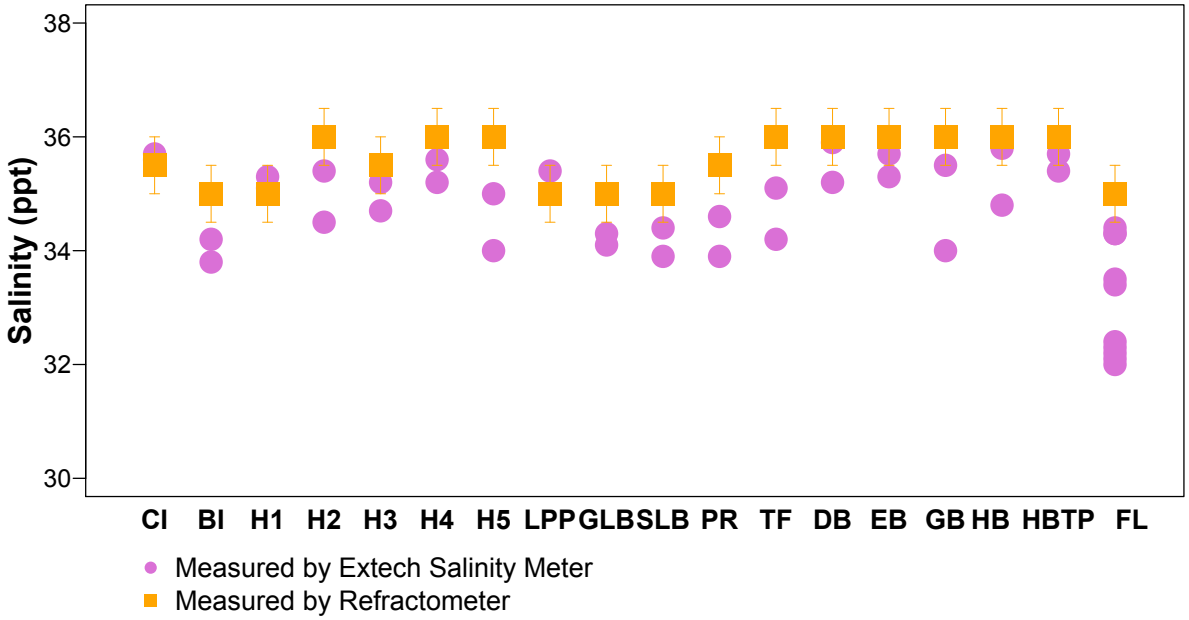

Figure 3.S3. Salinity measurements for each modern water sample.

Salinity was measured in duplicate using Extech EC170 salinity meter and a third time using the Leica handheld Temperature Compensated Refractometer. A randomly-selected sample (FL) was measured 10 times using the Extech EC170 salinity meter to test reproducibility.

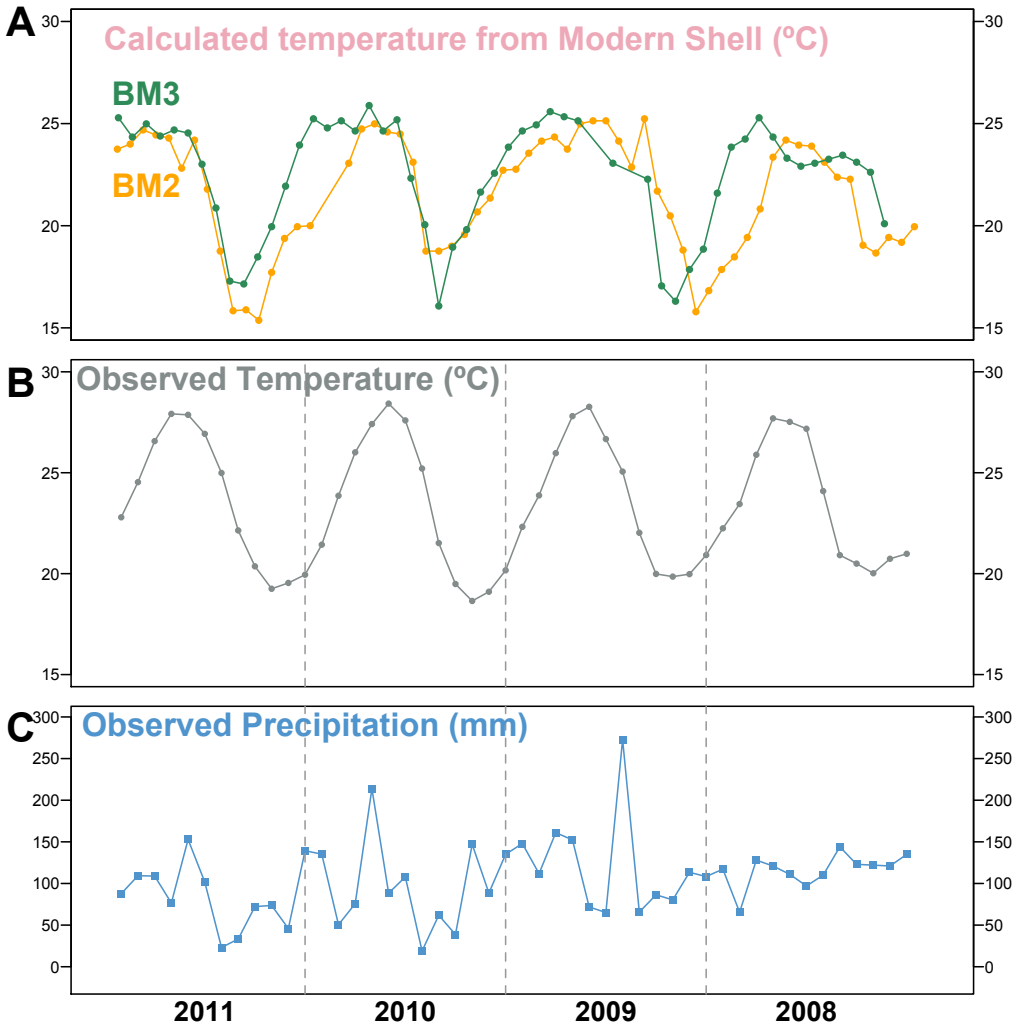

Figure 3.S4. Reconstructed temperature profiles of BM2 and BM3 and their comparison to recorded climate conditions.

A, Calculated temperature, as was done in the original study, from high-resolution $\delta^{18}O_{carb}$ and a single $\delta^{18}O_w$ value of 1.16‰ ($\delta^{18}O_w$ value was selected from modern $\delta^{18}O_w$ measurement of the same site). X-axis is distance along growth axis, and has been stretched to roughly align with the temperature data in B. B, Observed modern (Instrumental) SST from 2008-2011 (NOAA National Data Buoy Center). C, Observed precipitation from 2008-2011 (LDEO Climate Group Datasets).

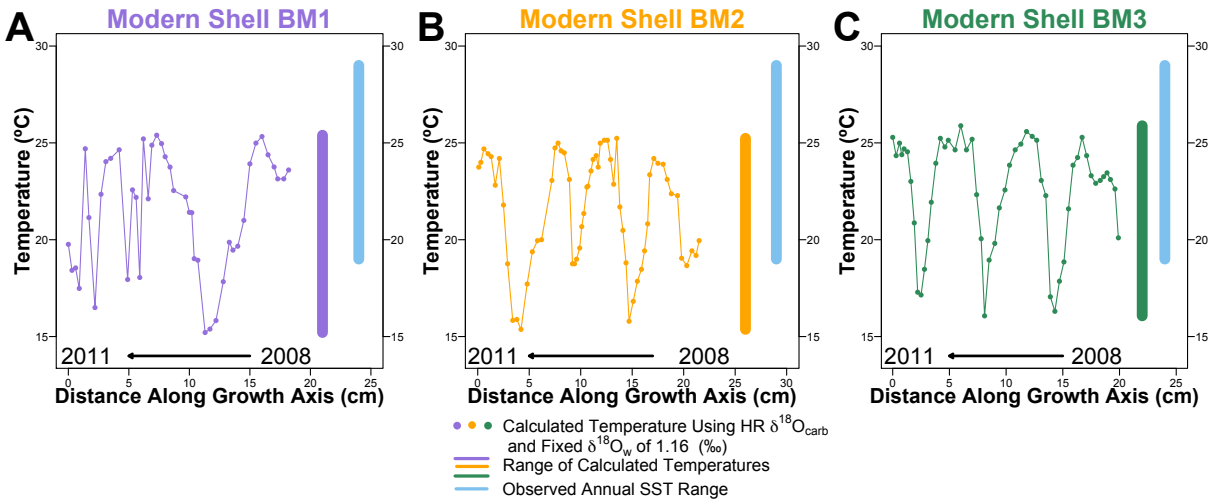

Figure 3.S5. Calculated temperature seasonality and range using the water-aragonite fractionation factor of Kim et al. (2007).

Temperatures calculated from high-resolution $\delta^{18}O_{carb}$ profiles using a single $\delta^{18}O_w$ value of 1.16‰, selected from modern $\delta^{18}O_w$ measurement at collection site, and Blue bars show instrumental temperature range for comparison.

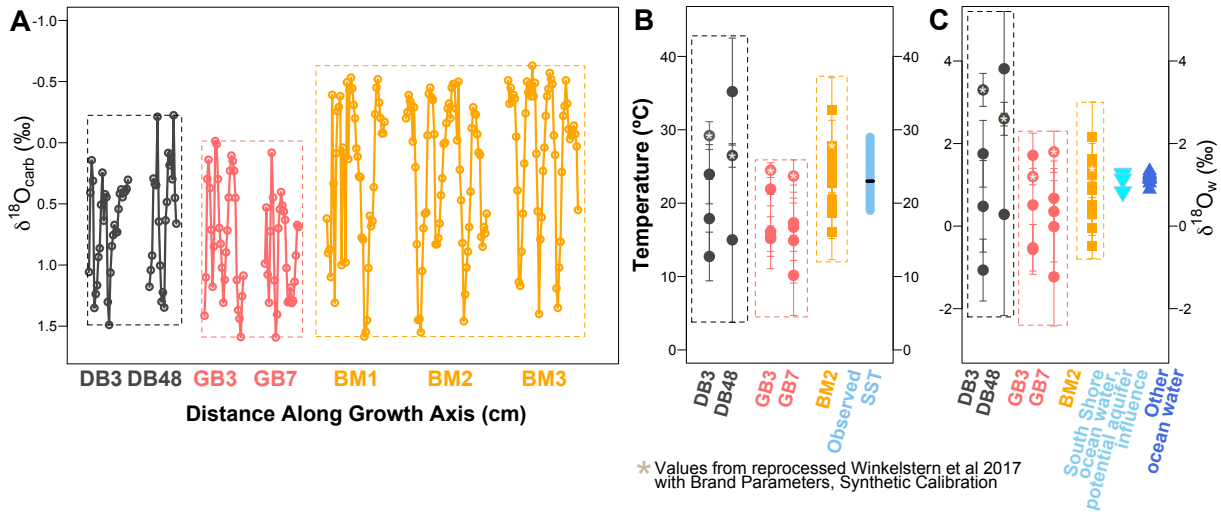

Figure 3.S6. $\delta^{18}O_{carb}$, Δ_{47}-based temperature, and $\delta^{18}O_w$ profiles of modern and fossil *C. pica* shells calculated using the Kim et al., 2007 aragonite-water equilibrium equation.

A, High Resolution $\delta^{18}O_{carb}$ ranges of fossil and modern shells. B, Temperature ranges of fossil and modern shells compared to modern SST on the right. Both DB/RB and GB show minimum temperatures colder than both modern shell and modern observations. C, $\delta^{18}O_w$ ranges of fossil and modern shells, calculated using Kim et al., 2007 aragonite-water equilibrium equation, compared to measured modern $\delta^{18}O_w$ values on the right. Both DB/RB and GB show a wider range in $\delta^{18}O_w$ than the modern shells due to their proximity to the central lens aquifer. Errors reported for both Δ_{47}-temperature and $\delta^{18}O_w$ values are based on 1 standard error.

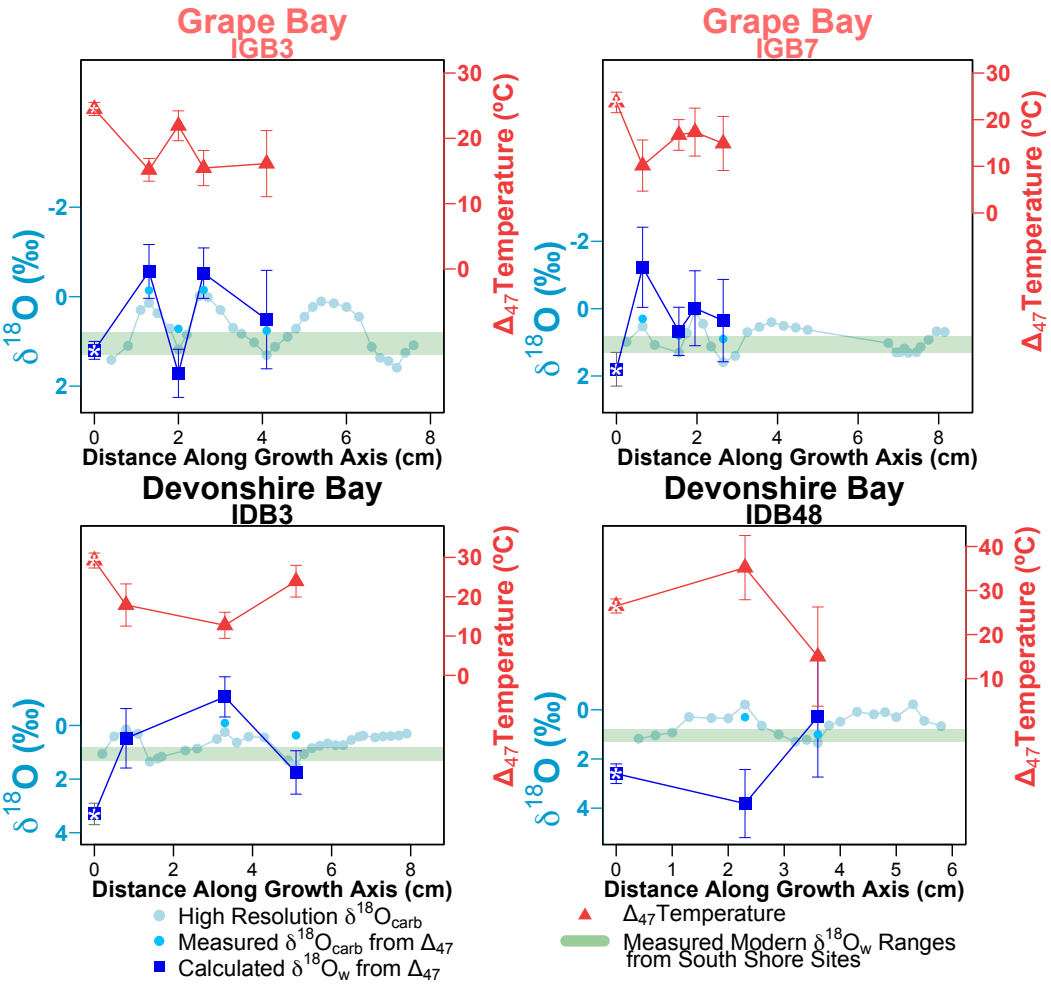

Figure 3.S7. High resolution $\delta^{18}O$ measurements, Δ_{47}-based temperatures and $\delta^{18}O_w$ values, calculated using Kim et al., 2007 aragonite-water equilibrium equation, for four fossil shells.

Note that the y-axes are scaled differently in each plot for best visibility of overlapping data.

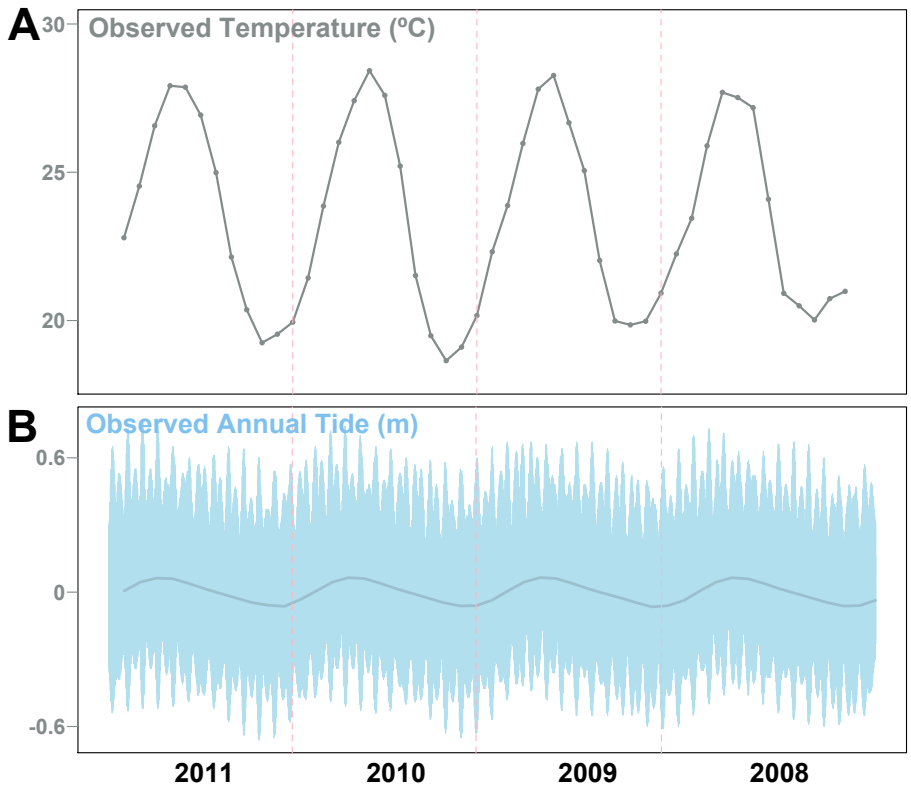

Figure 3.S8. Recorded temperatures and tidal information from Bermuda.

A, Observed modern (Instrumental) SST from 2008-2011 (NOAA National Data Buoy Center). B, Observed annual tide from 2008-2011 (NOAA Tides and Currents).

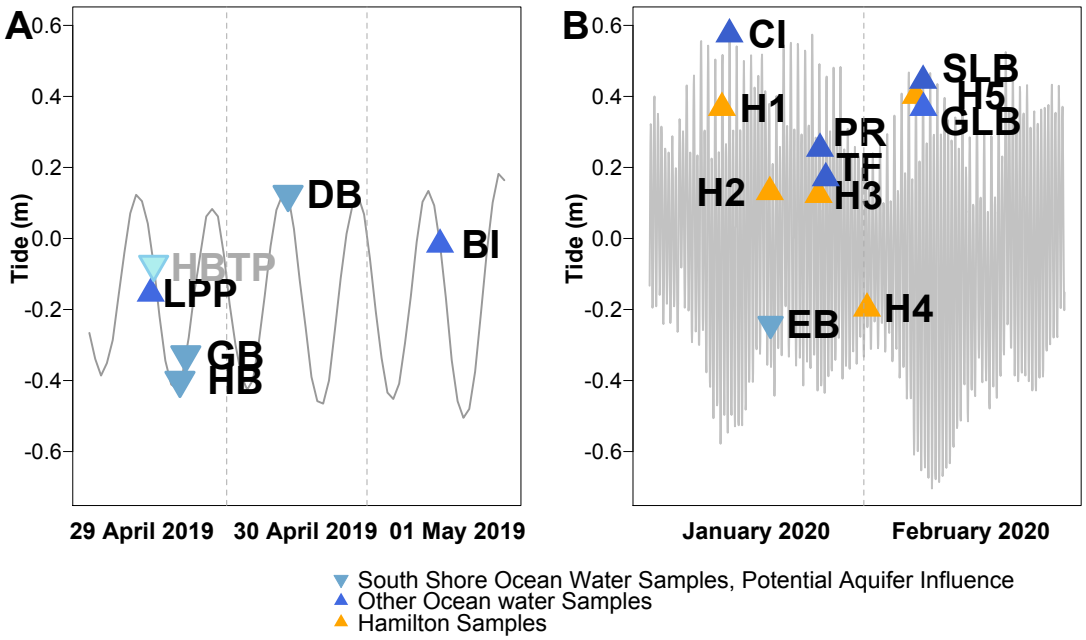

Figure 3.S9. $\delta^{18}O_w$ measurements plotted against tide.

A, Tidal record during 2019 sampling period with each seawater sample plotted according to its collection time. Two letter labels identify collection site, as follows: BI=Bird Island; DB=Devonshire/Rocky Bay; GB=Grape Bay; LPP=Lodge Point Park; HB=Hungry Bay; and HBTP = stranded Tide Pool at Hungry Bay, plotted to represent tidal height of pool above seawater at time of collection. B, Tidal record during 2020 sampling period. Two letter labels identify collection site, as follows: CI=Cooper's Island; EB=Elbow Beach; GLB=Glass Beach; H1-5=Hamilton1-5; PR=Palmetto Roundabout; SLB=Somerset Long Bay, TF=The Flatts. Tide values are from NOAA Tides and Currents (https://tidesandcurrents.noaa.gov/).

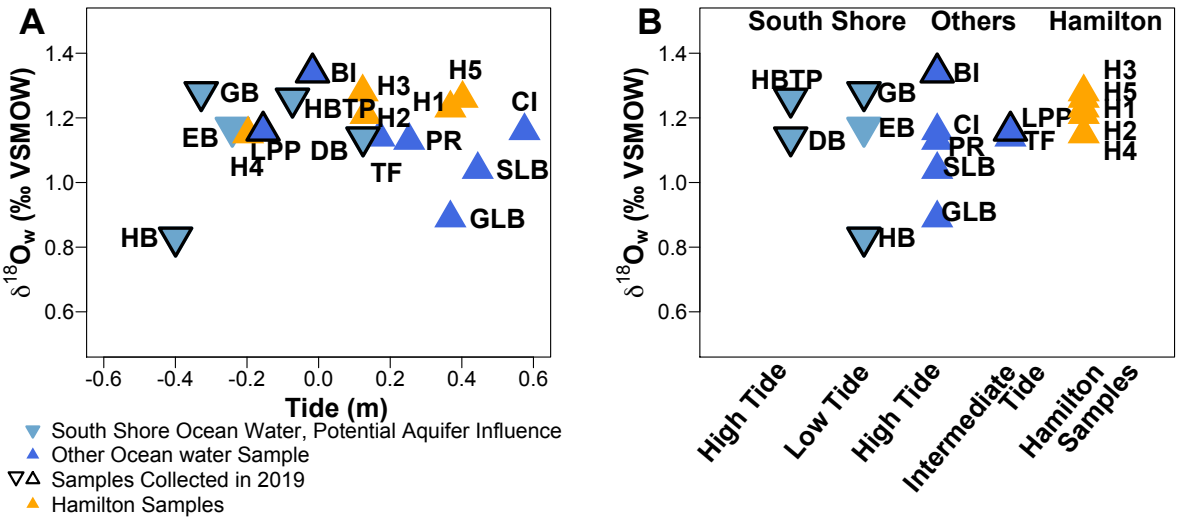

Figure 3.S10. $\delta^{18}O_w$ measurements plotted against tidal height.

A, $\delta^{18}O_w$ values plotted against tidal height for all collected seawater samples. B, $\delta^{18}O_w$ values, with samples separated into tidal height categories (high/intermediate/low tide) and collection site (South Shore sites, non-South Shore sites, Hamilton). Two letter labels correspond to collection locality (see Table 3.1, Figure 3.6). Tide values are from NOAA Tides and Currents (https://tidesandcurrents.noaa.gov/).

3.9 References

Affek, H. P. (2012), Clumped isotope paleothermometry: principles, applications, and challenges, *The Paleontological Society Papers*, *18*, 101–114.

Bajnai, D., J. Fiebig, S. M. Garcia, C. Rollion-Bard, J. Raddatz, C. Primo-Ramos, U. Brand, A. Tomašovych, and N. Löffler (2018), Assessing kinetic fractionation in brachiopod calcite using clumped isotopes, *Scientific Reports*, 1–12, doi:10.1038/s41598-017-17353-7.

Beddows, P. A., P. L. Smart, F. F. Whitaker, and S. L. Smith (2007), Decoupled fresh–saline groundwater circulation of a coastal carbonate aquifer: Spatial patterns of temperature and specific electrical conductivity, *Journal of Hydrology*, *346*(1-2), 18–32, doi:10.1016/j.jhydrol.2007.08.013.

Brand, W. A., S. S. Assonov, and T. B. Coplen (2010), Correction for the ^{17}O interference in $\delta(^{13}C)$ measurements when analyzing CO_2 with stable isotope mass spectrometry (IUPAC Technical Report), *Pure and Applied Chemistry*, *82*(8), 1719–1733, doi:10.1351/PAC-REP-09-01-05.

Brocas, W. M., T. Felis, and M. Mudelsee (2019), Tropical Atlantic Cooling and Freshening in the Middle of the Last Interglacial From Coral Proxy Records, *Geophys. Res. Lett.*, *46*, 8289–8299, doi:10.1029/2019GL083094.

Buick, D. P., and L. C. Ivany (2004), 100 years in the dark: Extreme longevity of Eocene bivalves from Antarctica, *Geology*, *32*(10), 921–4, doi:10.1130/G20796.1.

Burchell, M., A. Cannon, N. Hallmann, H. P. Schwarcz, and B. R. Schöne (2013), Refining estimates for the season of shellfish collection on the pacific northwest coast: applying high-resolution stable oxygen isotope analysis and sclerochronology, *Archaeometry*, *55*(2), 258–276, doi:10.1111/j.1475-4754.2012.00684.x.

CLIMAP (1984), The Last Interglacial Ocean, *Quat. res.*, *21*, 123–224.

Coates, K. A., J. W. Fourqurean, W. J. Kenworthy, A. Logan, S. A. Manuel, and S. R. Smith (2013), Introduction to Bermuda: Geology, Oceanography and Climate, in *Coral Reefs of the United Kingdom Overseas Territories*, vol. 4, edited by C. R. C. Sheppard, pp. 115–133, Springer Netherlands, Dordrecht.

Dansgaard, W. (1964), Stable isotopes in precipitation, *Tellus*, 436–468.

Defliese, W. F., M. T. Hren, and K. C. Lohmann (2015), Compositional and temperature effects of phosphoric acid fractionation on Δ_{47} analysis and implications for discrepant calibrations, *Chemical Geology*, *396*(C), 51–60, doi:10.1016/j.chemgeo.2014.12.018.

Defliese, W. F., and K. C. Lohmann (2016), Evaluation of meteoric calcite cements as a proxy material for mass-47 clumped isotope thermometry, *Geochimica et Cosmochimica Acta*, *173*(C), 126–141, doi:10.1016/j.gca.2015.10.022.

Dennis, K. J., H. P. Affek, B. H. Passey, D. P. Schrag, and J. M. Eiler (2011), Defining an absolute reference frame for "clumped" isotope studies of CO_2, *Geochimica et Cosmochimica Acta*, *75*(22), 7117–7131, doi:10.1016/j.gca.2011.09.025.

Eagle, R. A. et al. (2013), The influence of temperature and seawater carbonate saturation state on 13C-18O bond ordering in bivalve mollusks, *Biogeosciences*, *10*(7), 4591–4606, doi:10.5194/bg-10-4591-2013.

Eagle, R. A., E. A. Schauble, A. K. Tripati, T. Tütken, R. C. Hulbert, and J. M. Eiler (2010), Body temperatures of modern and extinct vertebrates from 13C-18O bond abundances in bioapatite, *PNAS*, *107*(23), 10377–10382, doi:10.1073/pnas.0911115107/-/DCSupplemental.

Eiler, J. M. (2007), "Clumped-isotope" geochemistry—The study of naturally-occurring, multiply-substituted isotopologues, *Earth and Planetary Science Letters*, *262*(3-4), 309–327, doi:10.1016/j.epsl.2007.08.020.

Eiler, J. M. (2011), Paleoclimate reconstruction using carbonate clumped isotope thermometry, *Quaternary Science Reviews*, *30*(25-26), 3575–3588, doi:10.1016/j.quascirev.2011.09.001.

Epstein, S., and T. K. Mayeda (1953), Variation of O^{18} content of water from natural sources, *Geochimica et Cosmochimica Acta*, *4*, 213–224.

Gat, J. R. (1996), Oxygen and hydrogen isotopes in the hydrologic cycle, *Annu. Rev. Earth Planet. Sci.*, *24*, 225–262.

Ghosh, P., J. Adkins, H. Affek, B. Balta, W. Guo, E. A. Schauble, D. Schrag, and J. M. Eiler (2006), ^{13}C–^{18}O bonds in carbonate minerals: A new kind of paleothermometer, *Geochimica et Cosmochimica Acta*, *70*(6), 1439–1456, doi:10.1016/j.gca.2005.11.014.

Grossman, E. L., and T.-L. Ku (1986), Oxygen and carbon isotope fractionation in biogenic aragonite: temperature effects, *Chemical Geology*, 59–74.

Hallmann, N., B. R. Schöne, A. Strom, and J. Fiebig (2008), An intractable climate archive — Sclerochronological and shell oxygen isotope analyses of the Pacific geoduck, Panopea abrupta (bivalve mollusk) from Protection Island (Washington State, USA), *Palaeogeography, Palaeoclimatology, Palaeoecology*, *269*(1-2), 115–126, doi:10.1016/j.palaeo.2008.08.010.

Harmon, R. S., R. M. Mitterer, N. Kriausakul, L. S. Land, H. P. Schwarcz, P. Garrett, G. J. Larson, H. L. Vacher, and M. P. Rowe (1983), U-series and amino-acid racemization geochronology of Bermuda: Implications for eustatic sea-level fluctuation over the past 250,000 years, *Palaeogeography, Palaeoclimatology, Palaeoecology*, *44*, 41–70.

Harrison, S. P., J. E. Kutzbach, I. C. Prentice, P. J. Behling, and M. T. Sykes (1994), The response of Northern Hemisphere extratropical climate and vegetation to orbitally induced changes in insolation during the last interglaciation, *Quat. res.*, *43*, 174–184.

Hearty, P. J., H. L. Vacher, and R. M. Mitterer (1992), Aminostratigraphy and ages of Pleistocene limestones of Bermuda, *Geol Soc America Bull*, 1–10.

Hearty, P. J., Pascal kindler, H. Cheng, and R. L. Edwards (1999), A +20 m middle Pleistocene sea-level highstand (Bermuda and the Bahamas) due to partial collapse of Antarctic ice,, 1–4.

Hearty, P. J. (2002), Revision of the late Pleistocene stratigraphy of Bermuda, *Sedimentary Geology*, *153*, 1–21.

Hearty, P. J., and S. L. Olson (2011), Preservation of trace fossils and molds of terrestrial biota by intense storms in mid-last Interglacial (MIS 5c) dunes on Bermuda, with a model for development of hydrological conduits, *PALAIOS*, *26*(7), 394–405, doi:10.2110/palo.2010.p10-132r.

Hearty, P. J., S. L. Olson, D. S. Kaufman, R. L. Edwards, and H. Cheng (2004), Stratigraphy and geochronology of pitfall accumulations in caves and fissures, Bermuda, *Quaternary Science Reviews*, *23*(9-10), 1151–1171, doi:10.1016/j.quascirev.2003.09.008.

Henkes, G. A., B. H. Passey, A. D. Wanamaker Jr, E. L. Grossman, W. G. Ambrose Jr, and M. L. Carroll (2013), Carbonate clumped isotope compositions of modern marine mollusk and brachiopod shells, *Geochimica et Cosmochimica Acta*, *106*(C), 307–325, doi:10.1016/j.gca.2012.12.020.

Henkes, G. A., B. H. Passey, E. L. Grossman, B. J. Shenton, A. Pérez-Huerta, and T. E. Yancey (2014), Temperature limits for preservation of primary calcite clumped isotope paleotemperatures, *Geochimica et Cosmochimica Acta*, *139*(C), 362–382, doi:10.1016/j.gca.2014.04.040.

Hu, Y. et al. (2018), Using deuterium excess, precipitation and runoff data to determine evaporation and transpiration: A case study from the Shawan Test Site, Puding, Guizhou, China, *Geochimica et Cosmochimica Acta*, *242*, 21–33, doi:10.1016/j.gca.2018.08.049.

Huntington, K. W. et al. (2009), Methods and limitations of "clumped" CO_2 isotope (Δ_{47}) analysis by gas-source isotope ratio mass spectrometry, *J. Mass Spectrom.*, *44*(9), 1318–1329, doi:10.1002/jms.1614.

Jacob, J., P. Ghosh, K. U. A. Jaleel, B. R. Smitha, K. R. Abhilash, and V. N. Sanjeevan (2016), Influence of the upwelling events on the $\delta^{13}C$ and $\delta^{18}O$ of the benthic bivalve shells of the South Western Continental Margin of India, *Environmental Earth Sciences*, *75*(2), 1–8, doi:10.1007/s12665-015-4954-x.

Kaspar, F., N. Kühl, U. Cubasch, and T. Litt (2005), A model-data comparison of European temperatures in the Eemian interglacial, *Geophys. Res. Lett.*, *32*(11), 2362–5, doi:10.1029/2005GL022456.

Kelson, J. R., K. W. Huntington, A. J. Schauer, S. C, and A. R. Lechler (2017), Toward a universal carbonate clumped isotope calibration: Diverse synthesis and preparatory methods suggest a single temperature relationship, *Geochimica et Cosmochimica Acta*, *197*, 104–131.

Killingley, J. S., and W. H. Berger (1979), Stable isotopes in a mollusk shell: detection of upwelling events, *Science*, *205*(4402), 186–188.

Kim, S.-T., A. Mucci, and B. E. Taylor (2007), Phosphoric acid fractionation factors for calcite and aragonite between 25 and 75 °C: Revisited, *Chemical Geology*, *246*(3-4), 135–146, doi:10.1016/j.chemgeo.2007.08.005.

Kukla, G. J., M. L. Bender, J. de Beaulieu, G. C. Bond, and W. S. Broecker (2018), Last Interglacial Climates, *Quat. res.*, *58*, 2–13.

Land, L. S., F. T. Mackenzie, and S. J. Gould (1967), Pleistocene History of Bermuda, *Geol Soc America Bull*, 993–1006.

Meischner, D., R. Vollbrecht, and D. Wehmeyer (1995), Pleistocene sea-level yo-yo recorded in stacked beaches, Bermuda South Shore, *Geological Society Special Publications*, (300), 1–16.

Moore, W. S. (1996), Large groundwater inputs to coastal waters revealed by ^{226}Ra enrichments, *Nature*, *380*, 612–614.

Muhs, D. R., K. R. Simmons, and B. Steinke (2002), Timing and warmth of the Last Interglacial period: new U-series evidence from Hawaii and Bermuda and a new fossil compilation for North America, *Quaternary Science Reviews*, *21*, 1355–1383.

O'Dea, A., J. B. C. Jackson, H. Fortunato, J. T. Smith, L. DCroz, K. G. Johnson, and J. A. Todd (2007), Environmental change preceded Caribbean extinction by 2 million years, *PNAS*, *104*, 5501–5506.

Olson, S. L., and P. J. Hearty (2013), Periodicity of extinction and recolonization of the West Indian topshell Cittarium pica in the Quaternary of Bermuda (Gastropoda: Trochoidea), *Biological Journal of the Linnean Society*, (110), 1–9.

Petersen, S. V., I. Z. Winkelstern, K. C. Lohmann, and K. W. Meyer (2016), The effects of Porapak™ trap temperature on $\delta^{18}O$, $\delta^{13}C$, and Δ_{47}values in preparing samples for clumped isotope analysis, *Rapid Commun. Mass Spectrom.*, *30*(1), 199–208, doi:10.1002/rcm.7438.

Petersen, S. V. et al. (2019), Effects of Improved ^{17}O correction on inter-laboratory agreement in clumped isotope calibrations, estimates of mineral-specific offsets, and acid fractionation factor temperature dependence, *Geochemistry, Geophysics, Geosystems*, 1-33.

Robertson, R. (2003), The edible West Indian “whelk” Cittarium pica (Gastropoda: Trochidae): Natural history with new observations, *Academy of Natural Sciences*, *153*, 27–47.

Rosenheim, B. E., J. Tang, and A. Fernandez (2013), Measurement of multiply substituted isotopologues ("clumped isotopes") of CO_2 using a 5kv compact isotope ratio mass spectrometer: Performance, reference frame, and carbonate paleothermometry, *Rapid Commun. Mass Spectrom.*, *27*, 1847–1857, doi:10.1002/rcm.6634.

Rowe, M. P. (1984), The Fresh Water "Central Lens" of Bermuda, *Journal of Hydrology*, 165–176.

Rowe, M. P., K. A. I. Wainer, C. S. Bristow, and A. L. Thomas (2014), Anomalous MIS 7 sea level recorded on Bermuda, *Quaternary Science Reviews*, *90*(C), 47–59, doi:10.1016/j.quascirev.2014.02.012.

Saenger, C., H. P. Affek, T. Felis, N. Thiagarajan, J. M. Lough, and M. Holcomb (2012), Carbonate clumped isotope variability in shallow water corals: Temperature dependence and growth-related vital effects, *Geochimica et Cosmochimica Acta*, *99*, 224–242, doi:10.1016/j.gca.2012.09.035.

Sanchez Goni, M. F. et al. (2012), European climate optimum and enhanced Greenland melt during the Last Interglacial, *Geology*, *40*(7), 627–630, doi:10.1130/G32908.1.

Santrock, J., S. A. Studley, and J. M. Hayes (1985), Isotopic analyses based on the mass spectra of carbon dioxide, *Anal. Chem.*, *57*(7), 1444–1448, doi:10.1021/ac00284a060.

Schmidt, G. A., G. R. Bigg, and E. J. Rohling (1999), Global Seawater Oxygen-18 Database v1.21.

Schmidt, M. W., H. J. Spero, and D. W. Lea (2004), Links between salinity variation in the Caribbean and North Atlantic thermohaline circulation, *Nature*, *428*, 160–163.

Schöne, B. R., A. D. Freyre Castro, J. Fiebig, S. D. Houk, W. Oschmann, and I. Kröncke (2004), Sea surface water temperatures over the period 1884–1983 reconstructed from oxygen isotope ratios of a bivalve mollusk shell (Arctica islandica, southern North Sea), *Palaeogeography, Palaeoclimatology, Palaeoecology*, *212*(3-4), 215–232, doi:10.1016/j.palaeo.2004.05.024.

Stolper, D., and J. M. Eiler (2015), The kinetics of solid-state isotope-exchange reactions for clumped isotopes: A study of inorganic calcites and apatites from natural and experimental samples, *American Journal of Science*, *315*(5), 1–44, doi:10.2475/05.2015.01.

Tao, K., J. A. Robbins, E. L. Grossman, and A. O'Dea (2013), Quantifying Upwelling and Freshening in Nearshore Tropical American Environments Using Stable Isotopes in Modern Gastropods, *BMS*, *89*(4), 815–835, doi:10.5343/bms.2012.1065.

Thiagarajan, N., J. Adkins, and J. Eiler (2011), Carbonate clumped isotope thermometry of deep-sea corals and implications for vital effects, *Geochimica et Cosmochimica Acta*, *75*(16), 4416–4425, doi:10.1016/j.gca.2011.05.004.

Tripati, A. K., R. A. Eagle, N. Thiagarajan, A. C. Gagnon, H. Bauch, P. R. Halloran, and J. M. Eiler (2010), 13C-18O isotope signatures and "clumped isotope" thermometry in foraminifera and coccoliths, *Geochimica et Cosmochimica Acta*, *74*(20), 5697–5717, doi:10.1016/j.gca.2010.07.006.

Tripati, A., J. Zachos, L. Marincovich Jr, and K. Bice (2001), Late Paleocene Arctic coastal climate inferred from molluscan stable and radiogenic isotope ratios, *Palaeogeography, Palaeoclimatology, Palaeoecology*, *170*, 101–113.

Turney, C. S. M., and R. T. Jones (2010), Does the Agulhas Current amplify global temperatures during super-interglacials? *J. Quaternary Sci.*, *25*(6), 839–843, doi:10.1002/jqs.1423.

Vacher, H. L. (1978), Hydrogeology of Bermuda-Significance of an across-the-island variation in permeability, *Journal of Hydrology*, *39*, 207–226.

Vacher, H. L., and T. N. Wallis (1992), Comparative hydrogeology of fresh-water lenses of Bermuda and Great Exuma Island, Bahamas, *Ground Water*, *30*, 15–20.

Vacher, H. L., and Rowe, M. P (1997), Geology and Hydrogeology of Bermuda, *Developments in Sedimentology*, 54, 35-90.

van Hengstum, P. J., and D. B. Scott (2012), Sea-level rise and coastal circulation controlled Holocene groundwater development in Bermuda and caused a meteoric lens to collapse 1600years ago, *Marine Micropaleontology*, *90-91*, 29–43, doi:10.1016/j.marmicro.2012.02.007.

Vollbrecht, R. (1990), Marine and meteoric diagenesis of submarine pleistocene carbonates from the Bermuda carbonate platform, *Carbonates and Evaporites*, *5*, 1–84.

Walker, S. E. (1994), Biological remaine: Gastropod fossils used by the living terrestrial hermit crab, Coenobita clypeatus, on Bermuda, *PALAIOS*, *9*, 403–412.

Wanamaker, A. D., Jr, K. J. Kreutz, H. W. Borns Jr., D. S. Introne, S. Feindel, and B. J. Barber (2006), An aquaculture-based method for calibrated bivalve isotope paleothermometry, *Geochem. Geophys. Geosyst.*, *7*(9), 1–13, doi:10.1029/2005GC001189.

Wanamaker, A. D., Jr, K. J. Kreutz, B. R. Schöne, N. Pettigrew, H. W. Borns, D. S. Introne, D. Belknap, K. A. Maasch, and S. Feindel (2008), Coupled North Atlantic slope water forcing on Gulf of Maine temperatures over the past millennium, *Clim Dyn*, *31*(2-3), 183–194, doi:10.1007/s00382-007-0344-8.

Whitaker, F. F., and P. L. Smart (1990), Active circulation of saline ground waters in carbonate platforms: Evidence from the Great Bahama Bank, *Geology*, *18*, 200–203.

Winkelstern, I. Z., Surge, D., and Hudley, J (2013), Multiproxy sclerochronological evidence for Plio-Pleistocene regional warmth: United States mid-Atlantic coastal plain, *Palaios*, 28, 649–660.

Winkelstern, I. Z., S. E. Kaczmarek, K. C. Lohmann, and J. D. Humphrey (2016), Calibration of dolomite clumped isotope thermometry, *Chemical Geology*, *443*(C), 32–38, doi:10.1016/j.chemgeo.2016.09.021.

Winkelstern, I. Z., M. P. Rowe, K. C. Lohmann, W. F. Defliese, S. V. Petersen, and A. W. Brewer (2017), Meltwater pulse recorded in Last Interglacial mollusk shells from Bermuda, *Paleoceanography*, *32*(2), 132–145, doi:10.1002/2016PA003014.

Chapter 4 Quantifying Variations in $\delta^{18}O_w$ and Salinity in Modern Bermudan Waters on Hourly to Monthly Timescales

4.1 Abstract

Since the mid-1970s, groundwater resources in Bermuda have been explored to supplement growing potable water demand on the island. Many previous studies have focused on modeling the shape of the freshwater lenses on the island, mainly the Devonshire Lens, and the island's underlying hydrogeology. However, the scale of interaction between aquifer water and the surrounding coastal seawater, such as through submarine groundwater discharge, have not gained as much attention. A pilot study in 2021 (Zhang et al., 2021) found more temporal variation in $\delta^{18}O_w$ in seawater along the island's South Shore (the section of the coast closest to the Devonshire Lens) compared to elsewhere around the island, suggesting that freshwater was discharging from that lens into coastal seawater in quantities sufficient to alter seawater $\delta^{18}O_w$. However, this study had a limited number of samples so could not capture the full variability of $\delta^{18}O_w$ across space and time. Here, we present salinity and $\delta^{18}O_w$ measurements from seawater samples collected around Bermuda and in wells tapping the Devonshire Lens on timescales ranging from hourly to monthly to better visualize the dynamic interaction between coastal seawater and aquifer-sourced freshwater. We find tight correlation between salinity and $\delta^{18}O_w$ in well waters, indicating a simple linear mixing relationship between seawater and aquifer water. We confirm the previous finding of larger variability in $\delta^{18}O_w$ measurements along the South

Shore compared to elsewhere and relate observed changes to tidal height on hourly to monthly timescales. Surprisingly, South Shore seawater salinity does not vary in accordance with the $\delta^{18}O_w$ values, implying additional mechanisms, such as the addition of salt-spray, must be acting to mute salinity changes. The finding that submarine groundwater discharge can act as an "invisible" force changing coastal seawater $\delta^{18}O_w$ values by >1‰ on subannual timescales has implications for paleoclimate studies that often assume constant $\delta^{18}O_w$ through time.

4.2 Introduction

Bermuda is an island with limited freshwater supply, and there are no rivers or freshwater lakes. For over 350 years, the main source of potable water in Bermuda has come from rain collected via specially designed roof catchments. Iconic white, stepped 'Bermuda roofs' made of limestone slow down the flow of rainwater and funnel it via gutters and pipes into underground cisterns beneath each building for storage and use. For example, the majority of Bermudan household tap water comes from this roof-top catchment. Yet despite every building on the island using this effective roof catchment system (Rowe, 2011), this system of rainwater harvesting does not meet all of Bermuda's freshwater needs, especially for high-occupancy buildings like hotels. Rainwater catchment is supplemented by direct extraction of groundwater via ~3000 commercial and domestic wells spread across the island (Vacher and Rowe, 1997). Directly extracted groundwater is typically brackish and can be contaminated by chemicals leached from the ground such as pesticides or nitrates from cesspits (Simmons and Lyons, 1994), making this type of water inappropriate for direct consumption without reverse osmosis or desalination treatments. Increasingly, commercial reverse osmosis plants operate directly on

seawater, particularly to supply high-occupancy buildings like hotels (Andrews and Laker, 2001).

Most extracted groundwater comes from the Devonshire Lens, also called the Central Lens due to its location underlying the central parish (Figure 4.1), which has a total area of approximately 7.2 km^2 and reaches maximum thickness around 10 meters (Vacher and Rowe, 1997). Approximately 200 million gallons per day of water are withdrawn from the Devonshire Lens as supplementary water (Rowe, 2011). There are also smaller lenses elsewhere on the island (Figure 4.1). The Somerset (also known as the Port Royal Lens) and St. Georges Lenses are in the range of 0.5–0.7 km^2 in area each, and other thin lenses that exist in Warwick and Southampton Parishes are not routinely monitored (Vacher and Rowe, 1997).

The shape and hydrogeology of the Devonshire Lens is controlled by the hydraulic conductivity of the two hydrostratigraphic units containing the aquifer: the Langton Aquifer and the Brighton Aquifer (Vacher, 1978) (Figure 4.1, 4.2B). The hydraulic conductivity of the Langton Aquifer is lower (around 30-120m/day) compared to the hydraulic conductivity of the Brighton Aquifer (around 1000m/day), reflecting increased porosity in the lithostratigraphic units on the south side of the island (Vacher and Rowe, 1997; Rowe, 1984). Increased porosity in the Brighton Aquifer leads to more effective mixing of freshwater and saltwater and greater inward penetration of seawater on the south side of the island (Vacher and Ayers, 1980; Vacher and Rowe, 1997). This is further demonstrated by the fact that variations in water table height in wells drilled into the Langton Aquifer are fairly insensitive to variations in sea level, whereas tidally-driven variations in water table height persist much farther inland within the Brighton Aquifer (Vacher and Rowe, 1997). As a result, on the north side of the island (Langton Aquifer) the freshwater nucleus is comparatively much thicker and the seawater-freshwater interface

(50% salinity) is nearly twice as deep compared to the south side of the island (the Brighton Aquifer), and wells tapping the Brighton Aquifer generally provide more brackish water (Figure 4.2).

Previous work defining the extent of underground aquifers in Bermuda have used conductivity (salinity) estimates to define the position of the seawater-freshwater interface (50% contour). The oxygen isotopic composition of water ($\delta^{18}O_w$) can be similarly used to identify and trace seawater-freshwater interactions, as aquifer water (sourced from precipitation) and seawater have very distinct $\delta^{18}O_w$ values (e.g. Povinec et al 2008). One previous study measured the oxygen isotopic composition of a handful of seawater samples collected around Bermuda (Zhang et al., 2021) and found higher variability in $\delta^{18}O_w$ in samples from the South Shore compared to elsewhere. High-resolution clumped isotope measurements in fossil bivalve shells indicated that this variation in South Shore seawater $\delta^{18}O$ also occurred during the Last Interglacial period (~125,000 years ago) on annual timescales. The authors proposed that submarine groundwater discharge from the Devonshire Lens influenced seawater $\delta^{18}O_w$ values along the South Shore, where the lens outcrops closest to the coastline (Figure 4.1A, 4.2), but not elsewhere. They suggested a mechanism - when sea level was lower, the increased topographic gradient between the center of the Lens and the coastal seawater height would lead to increased freshwater discharge out of the Lens into coastal waters and vice versa (Zhang et al., 2021). However, modern seawater samples collected for that study were limited in space and time, preventing direct testing of this hypothesized mechanism or investigation of variability in the timing and magnitude of discharge. Sea levels fluctuations occur on daily timescales due to tidal forces as well as annual timescales due to seasonal thermal expansion, both potentially leading to temporal changes in discharge that were not captured by this early dataset. Further, no water

samples were collected directly from the aquifer to quantify the freshwater $\delta^{18}O_w$ end-member composition.

In this study, we evaluate the variability in salinity and $\delta^{18}O_w$ in seawater around Bermuda and in wells tapping the Devonshire Lens on multiple timescales. We present salinity and $\delta^{18}O_w$ measurements collected bi-weekly over a period of months from sites along the South Shore, as well as hourly measurements from two South Shore sites spanning a full tidal cycle. In addition to constraining the seawater end-member, the freshwater end-member is characterized through rain, tap, and well water samples. A handful of marsh water samples were also analyzed to investigate the connectivity of marshes to the aquifer or ocean.

4.3 Methods

A total of 154 water samples were collected from April 2019 to March 2021, including 17 well water, 124 seawater, 7 inland marsh/pond water, 1 rainwater, and 5 tap water samples. A subset of 18 samples were previously analyzed as part of Zhang et al. (2021) using identical methods, including 17 seawater and 1 tap water and are included here as part of the larger dataset.

4.3.1 Water Collection

4.3.1.1 Well Water

Six wells tapping the Brighton Aquifer portion of the Devonshire Lens were sampled in August 2020, two of which were revisited in March 2021. Sampled wells were located both near the shore and further inland to investigate changes from the center of the lens to the edge (Figure 4.1). Wells close to the middle of the Devonshire Lens (away from the shore) are Brighton Hill

North (BHN), Devonshire Post office (DPO), St. Mark's Road (SMR); and those closer to the South Shore (near the edge of the lens) are Brighton Hill South (BHS), St. Brendan's South (SBS), St. Mark's Church (SMC). Samples were collected using a flow-through, double valve bailer. The bailer was gently lowered into the water column allowing water to move freely through both the top and bottom non-return ball valves until the tube was filled. After each sample was retrieved, it was then transferred into a 50ml sample vial and capped immediately to prevent evaporation. Depending on the location and the depth of the wells, 2-5 samples were taken with increasing depth from 1 to 9.5 meters below water table (Figure 4.3).

Vertical coordinate information is presented in reference to the Ordnance Datum (OD), which approximates the water table height. Surface water height within each well was measured and fell approximately within 0.2 m above or below the OD depending on the well (Figure 4.S1). Previously, Vacher (1978) presented a general cross section of the Devonshire Lens based on converted salinity measurements in multiple wells, which we reproduce here in Figures 4.2 and 4.4B. We used the distance between each of our six well sites and the South Shore coastline to place their position onto this hypothetical cross section (Figure 4.4B).

4.3.1.2 Sea Water

A total of 124 seawater samples were collected with the goal of assessing 1) variation in seawater $\delta^{18}O$ near Devonshire Lens (along the South Shore) over both annual and tidal timescales and 2) establishing baseline variations over annual timescales in sites distal to the Lens.

To capture long term $\delta^{18}O_w$ variability, six sites along South Shore over the period of June 2020 to December 2020 were sampled roughly twice a month. These sites include Devonshire Bay North Beach (DBNB), Rocky Bay East Side (RBES), Cox's Bay, Kent Ave

Shoreline (KAS), Hungry Bay (HB), and Grape Bay (GB). Fewer measurements from another South Shore site of Elbow Beach (EB) were also taken. Away from Devonshire Lens, our baseline site near the city of Hamilton was sampled once per week from January to March 2020 and then again once per month from July to August 2020.

In order to capture $\delta^{18}O_w$ variability during full tidal cycle, hourly measurements were collected from two South Shore sites, Kent Ave Pulpit (KAP) and Devonshire Bay (DB). Fourteen samples were collected from KAP, roughly an hour apart starting from 5:45am until 18:14pm on May 17th 2020; on a separate occasion, ten samples were collected from DB, roughly 1-2 hours apart starting from 5:28am until 18:45pm on January 21st 2021. The site of hourly collection at Kent Avenue (the Pulpit) differed slightly from the site where bi-weekly samples were taken (the Shoreline) because water levels were too low to continually collect from the shoreline site (Figure 4.1C).

Individual samples were collected sporadically from a number of other sites (Cooper's Island, Warwick Long Beach, Devil's Hole within Harrington Sound, and a floating dock near the Bermuda Institute of Ocean Sciences (BIOS)). These data were combined with 17 other published seawater samples from 13 sites (including Cooper's Island), previously published by Zhang et al. (2021) (Figure 4.1).

Additionally, two samples were collected from far offshore to represent baseline marine $\delta^{18}O_w$ values away from the influences of any submarine groundwater discharge. One was collected at the Bermuda Atlantic Time-series Study (BATS) station (47 miles offshore to the southeast), the other was collected roughly 2.1 miles offshore to the southeast from the center of the island (Figure 4.1).

4.3.1.3 Other Water Types

To quantify other aqueous endmembers, rain, tap, marsh, and mangrove pond waters were collected where available (Figure 4.1). A single rainwater sample was collected in July 2020 after a significant storm event. Four tap water samples were collected in households located in Warwick parish from July-September 2020 and combined with data from one additional tapwater sample collected in April 2019, also from Warwick parish (Zhang et al., 2021). Seven samples from island marsh/pond environments were collected, including one sample each from Mangrove Lake and Trott's Pond in May 2019 and five samples from two sites within Devonshire Marsh in January and March 2021.

4.3.2 Salinity

Prior to isotope measurements, all samples were analyzed for their salinity to assess whether this parameter correlated with $\delta^{18}O_w$ and compare traditional methods to new ones. Salinity was measured in duplicate for all water samples using the Extech EC170 salinity meter, which has a typical uncertainty of ±2% (<0.8 ppt). 1 standard deviation (1SD) of the mean was reported as the error bar for individual samples. Salinity measurements from the EC170 were also compared against a third measurement using a Leica handheld temperature compensated refractometer, which has an uncertainty of ±0.5 ppt. Measurements from the Leica refractometer were not included in the final salinity data.

4.3.3 $\delta^{18}O_w$ Measurements

All samples were prepared for $\delta^{18}O_w$ analysis at the University of Michigan, following the CO_2-water equilibration method described in Zhang et al., (2021). Briefly, water samples of

all types were equilibrated with tank CO_2 for at least 48 hours, then CO_2 was analyzed on a Thermo-Finnegan MAT 253 dual inlet mass spectrometer for at least 3 acquisitions of 12 sample-reference cycles at an m/z 44 beam strength of 16 V. At least two aliquots of CO_2 gas from a single water aliquot were measured on the mass spectrometer, spread out over weeks to accommodate variation in mass spectrometer behavior, and the remaining aliquots were archived in case a third measurement was needed in the future. Both in-house liquid standards and USGS standards (USGS 45, 46) were run interspersed with unknowns. Typical measurement uncertainty is ± 0.1‰ based on recurrent analysis of our in-house and USGS water standards.

4.3.4 Tidal Information

Tidal Information used in this study is sourced from NOAA Tide and Current under Bermuda Biological Station number 2695535 (https://tidesandcurrents.noaa.gov/).

4.4 Results

4.4.1 Well water

$\delta^{18}O_w$ values in well waters range from -3.7 to -1.5‰ and salinity varied from 0.2 to 15.2 psu. $\delta^{18}O_w$ and salinity both increase with depth as the contribution of seawater increases (Figure 4.3). Well sites located further inland show gradual increases in both salinity and $\delta^{18}O_w$ values as depth increases compared to sites located close to the South Shore coastline (Figure 4.3-4.4), as expected based on the shape of the lens (Figure 4.2B). Put another way, the increased influence of seawater on salinity and $\delta^{18}O_w$ occurs at a shallower depth near the coastline than further inland.

In addition to following a similar qualitative pattern with depth, salinity and $\delta^{18}O_w$ across all well water samples show a tight quantitative correlation (Figure 4.3C). A linear regression through data from the 17 well water samples (Eqn. 4.1) is statistically indistinguishable from a linear regression though data from the 17 well waters, plus 5 tap waters and 2 offshore seawaters (Eqn. 4.2), suggesting that the majority of variation in well water salinity and $\delta^{18}O_w$ values can be explained by simple mixing between precipitation-derived freshwater and offshore seawater.

$$\delta^{18}O_w = 0.1365 * \text{Salinity} - 3.6039 \quad \text{Eqn. 4.1}$$

$$\delta^{18}O_w = 0.1414 * \text{Salinity} - 3.6446 \quad \text{Eqn. 4.2}$$

The corresponding standard errors on the slope and intercept for Equation 4.1 are 0.0113 and 0.0592, respectively. The corresponding standard errors on the slope and intercept for Equation 4.2 are 0.0047 and 0.0510, respectively.

Following this two-endmember mixing model, the percent contribution of seawater and aquifer water can be estimated using either salinity or $\delta^{18}O_w$ (Figure 4.4A), resulting in similar estimates (Figure 4.S2). Averaging estimates using salinity and $\delta^{18}O_w$, well water samples range from 1% seawater in the surface-most sample from SMR to 42% in the deepest sample from DPO, with the spatial distribution generally following the previously established shape of the Devonshire Lens (Figure 4.4B).

4.4.2 Seawater

Large variations in oxygen isotopic composition and salinity were observed in the seawater sample set, with $\delta^{18}O_w$ values ranging from 0.4‰ up to 3.0‰ and salinity ranging from 31.5 to 38.5psu (Figure 4.5). The majority of this variability occurred in seawater samples collected at 7 sites along the South Shore, located in the center part of the island near the Devonshire Lens ("South Shore samples") (Figure 4.1). With a small number of exceptions, non-South Shore seawater samples produced extremely consistent $\delta^{18}O_w$ values and salinities, essentially invariant given analytical uncertainties.

4.4.2.1 Non-South Shore Seawater

In samples collected from the Great Sound, North Shore, and South Shore areas away from the Devonshire Lens, coastal seawater $\delta^{18}O_w$ values and salinities were generally consistent, ranging from 0.4 ± 0.1‰ to 1.3 ± 0.1‰ and 34.0 ± 0.5psu to 35.7 ± 0.1psu. The primary exceptions to the narrow range in $\delta^{18}O_w$ values seen in non-South Shore samples are the two samples collected from the BIOS floating dock, which have much lower $\delta^{18}O_w$ values of 0.4 and 0.7‰, but similar fully-marine salinities (Figure 4.9B). The floating dock is located along a narrow inner channel near an extensive cave complex, which may affect the exchange of freshwater and seawater. However, with only two measurements, it is difficult to determine the mechanism driving the change in $\delta^{18}O_w$ and lack of change in salinity at this site.

Two samples from the northwest edge of the island (Somerset Long Bay and Glass Beach) record slightly lower $\delta^{18}O_w$ values than the rest of the non-South Shore sites (1.0‰ and 0.9‰, respectively). These sites are located close to the Somerset Lens, the second largest freshwater lens on the island (Vacher and Rowe, 1997), but with only three samples collected near this lens at different times, further systematic study would be needed to evaluate the spatial and temporal variability of seawater conditions in this area.

Excluding samples from the BIOS floating dock and the two sites near the Somerset Lens, remaining non-South Shore seawater samples show a very narrow range in $\delta^{18}O_w$ and salinity (1.1 to 1.3 ± 0.1‰, 34.0-35.7 ± 0.5psu), consistent with the offshore seawater composition, representing baseline seawater compositions away from any terrestrial influence (1.2 ± 0.1‰, 34.5-35.5 psu, Figure 4.5). This holds true through time as well as space. Samples collected over a 6-month period from a dock near the city of Hamilton showed the same narrow range of variability as the offshore samples, equivalent to no variation in composition at all when uncertainty is included.

4.4.2.2 South Shore Seawater

Along the South Shore, $\delta^{18}O_w$ ranged from 0.6 to 3.0‰ and salinity ranged from 31.7 to 38.5 psu (Figure 4.5, 4.10). The wide salinity range is mainly driven by samples from DBNB on the lower end and GB on the higher end. Without these two sites, the South Shore salinity ranges roughly from 34 to 36psu, similar to the temporally invariant non-South Shore site of Hamilton. The range of variability in $\delta^{18}O_w$ is artificially expanded due to one very enriched point from Grape Bay (3.0‰), which was collected in the surf zone, and likely reflects evaporative enrichment. All other samples from Grape Bay were collected in knee-height water. Without this one point, although the total range is reduced, South Shore seawater samples still vary considerably in $\delta^{18}O_w$, ranging from 0.6 to 2.1‰. This variability far exceeds the narrow range in $\delta^{18}O_w$ seen in Hamilton and other non-South Shore sites.

Variation in $\delta^{18}O_w$ in South Shore samples tracked changes in local sea level throughout the year (Figure 4.7). When water levels were higher, $\delta^{18}O_w$ values were higher, closer to or exceeding the offshore seawater value of 1.2‰. When water levels were lower, $\delta^{18}O_w$ values trended downwards. Interestingly, salinity did not vary as clearly with sea level or correlate with

$\delta^{18}O_w$ as closely as in well water samples. For example, at KAS, salinity varied by 7psu while $\delta^{18}O_w$ varied by 1.4‰, while at Cox's Bay, salinity varied by less than 1.5psu while $\delta^{18}O_w$ variation exceeded 1‰.

Samples collected hourly over a 12hr period from Kent Avenue Pulpit (KAP) recorded 1.4‰ variability in $\delta^{18}O_w$, with individual sample values ranging from 0.4 to 2.4‰ (Figure 4.8). Salinity varied in time with $\delta^{18}O_w$, ranging from 33.6 to 36.3psu (Figure 4.8). Both $\delta^{18}O_w$ and salinity showed increasing values near high tide and decreasing values near low tide. Hourly measurements from Devonshire Bay (DB) recorded a similar co-variation of salinity and $\delta^{18}O_w$ with tidal height, although with a much smaller magnitude of variation that barely exceed uncertainty. At this site, over one tidal cycle, $\delta^{18}O_w$ ranged from 1.3 to 1.5‰ and salinity ranged from 33.7 to 34.9psu (Figure 4.8). Although total variation in both parameters approaches detection limits given uncertainty, higher $\delta^{18}O_w$ and salinity values were observed at high tides and lower values were observed at low tides at both sites.

Overall, seawater sampling demonstrates large scale (>1‰) variation in $\delta^{18}O_w$ along the South Shore, correlated with sea level, whether driven by tidal or seasonal sea level changes. Non-South Shore samples demonstrate highly stable $\delta^{18}O_w$ values across space and time, consistent with samples taken far offshore. These findings based on this new large seawater dataset align with those of Zhang et al. (2021) based on a much more limited dataset.

4.4.3 Other Water Types

Two sites within Devonshire Marsh (DM1 and DM2) were each sampled twice on the same day, roughly three hours apart. Site DM1 was revisited two months later and sampled again. Water compositions were very consistent between measurements of the same site, but

sites DM1 and DM2 were significantly different (Figure 4.9). The three measurements from DM1 had $\delta^{18}O_w$ values of -2.5 to -2.3‰ and non-zero salinities of 2.5 to 2.8. The two measurements from DM2 were more depleted in $\delta^{18}O_w$ (-4.4 to -4.1‰) and had salinities indicating nearly pure freshwater (0.35 to 0.38psu). Both of these clusters of data fall off the seawater-aquifer mixing line defined by well waters (Figure 4.9A), indicating water in the marshes is influenced by processes other than direct connection with subterranean aquifers, such as surface evaporation.

Samples collected from inland ponds south of Harrington Sound (Trott's Pond, Mangrove Lake) recorded $\delta^{18}O_w$ values from 0.97 to 1.3‰ and salinities of 27.4 to 27.5psu. These high salinity values suggest a connection with the ocean via the subsurface.

The single rainwater sample recorded a $\delta^{18}O_w$ value of -6.2‰. The tap water samples, representing integrated precipitation with a minor influence of evaporation, had $\delta^{18}O_w$ ranging from -3.9 to -3.2‰. Both tap and rain water samples are completely fresh (salinity = 0 psu).

4.5 Discussion

4.5.1 $\delta^{18}O_w$ and Salinity Define a Slightly Smaller Devonshire Lens Than in 1978

The salinity and $\delta^{18}O_w$ data from the well water samples align with previous depictions of the Devonshire Lens (Figure 4.2B) and freshwater lenses in general. Both salinity and $\delta^{18}O_w$ values increase with depth in the well, transitioning towards the marine end-member as the contribution of seawater increases. Further, the highest-elevation samples taken in wells near the edge of the lens are more saline and enriched in $\delta^{18}O_w$ than the highest-elevation samples taken in wells near the center of the lens (Figure 4.3), reflecting increased interaction between aquifer water and seawater near the edge of the lens.

The size and shape of the Devonshire Lens was previously mapped by estimating the percent seawater with depth in many wells using salinity alone (Vacher, 1978). The fitted Ghyben-Herzberg-Dupuit model of Vacher (1978) is shown in Figures 4.2 and 4.4B. Now, due to the clear distinction between the oxygen isotopic composition of freshwater and seawater, $\delta^{18}O_w$ can similarly be used to estimate the seawater contribution at different points and, through that, define the boundaries of the lens. Using salinity and $\delta^{18}O_w$ produce similar patterns, as shown in Figure 4.S2, and the average of the two methods is shown in Figure 4.4B.

Estimates of the extent of seawater influence in these six wells hint that the Devonshire Lens may have changed shape since it was last characterized in 1978. In the original model reproduced in Figure 4.4 (Vacher, 1978), the depth contours represented a cross section through the thickest part of the Brighton Aquifer, a line running southwest of well DPO. Perhaps unsurprisingly then, new data from DPO closely aligns with the model of Vacher (1978). In contrast to DPO, data from BHS, the closest coastal site to the cross section line, suggests upward motion of the 10% salinity contour.

Wells SMR and SMC also indicate shallower positions of the 10% contour, as well as the 1% contour. Wells SMR and SMC are on the northeastern edge of the lens, so the idealized cross section is not applicable. The previous model suggests the top-of-well samples taken from these two wells should contain between 3% and 10% seawater (Vacher, 1978; Vacher and Ayers, 1980, Figure 4.2). In particular SBS should be closer to 3% while SMC should be closer to 10%. In our new data, the surface-most sample from SBS was 11.5% and SMC was 10.8%, indicating increased seawater penetration at these sites.

Taken together, this data suggests the core of the lens has moved to the southwest (deepening of 50% contour at DPO) and that seawater incursion is greater along the South Shore

(shallowing of 10% contour in BHS, SBS, and SMC). The author of the previous Devonshire Lens characterization raised the possibility that the lens size had already shrunk between the time of characterization and the time of publication due to extractions and droughts (Vacher, 1978). Our data supports this assertion but cannot quantify when that decrease in lens size occurred.

4.5.2 Non-South Shore Seawater Samples Reflect Regional Seawater Compositions

Previous researchers have assumed that seawater $\delta^{18}O_w$ values around the island of Bermuda have been fixed in space and time, based on the lack of riverine inputs and the small land surface area (Winkelstern et al., 2017). The seawater dataset we present here demonstrates that to be true for most coastal areas of Bermuda, but not all. With the exception of samples collected near freshwater lenses (the Somerset Lens or South Shore outcrop of the Devonshire Lens) and/or the BIOS floating dock, all other seawater around the island of Bermuda appears to have a composition of 1.2 ‰ (± 0.1 ‰) and a salinity of 35 psu (± 0.5 psu). Data from Hamilton, a site that was sampled repeatedly over 6 months (Figure 4.6) shows that this stability persists through time as well as across space and occurs irrelevant of tidal height.

The warm, salty water mass bathing Bermuda originates in the Caribbean and travels up the US East Coast as part of the Gulf Stream Current before deviating offshore to intersect Bermuda. Along this pathway, the oxygen isotopic composition and salinity are apparently minimally modified. Long-term monthly observations from BATS record salinity ranges from 36.3 to 36.7 (Griffin et al., 2022). The BATS range is much higher than our single sample collected near BATS (33.1 psu) and our overall non-South Shore salinity range (34.0 to 35.7 psu), which we cannot explain. Additionally, almost all of the South Shore salinity values are lower than the BATS salinity range as well (Figure 4.5). This may suggest a calibration error in

the EC170 digital salinity meter, but all salinity measurements were conducted in random order intermixed with the South Shore samples, so even in the case of a calibration error, some conclusions hold. For example, it is unlikely that the salinity meter recorded a range from 31.7 to 38.5 psu for the South Shore samples and a notably more limited range of 34.0-35.7 for the non-South Shore samples due to a calibration error. Therefore, it is clear that the non-South Shore samples recorded minimally varying salinity compared to South Shore sites, and this agrees with the long-term salinity records from BATS. Further, seawater from the east coast of Florida has a composition of 0.7-1.2‰ and salinity of 34.1-34.9psu (Zhang and Petersen, 2023), similar to baseline Bermuda seawater measured here. Changes in baseline seawater composition around Bermuda may therefore reflect greater regional oceanographic processes.

4.5.3 South Shore $\delta^{18}O_w$ Variability and Its Relation to Sea Level Height

Data from a previous study of Bermudan seawater compositions (Zhang et al., 2021) suggested that variability in seawater $\delta^{18}O$ was greater along the South Shore compared to elsewhere around Bermuda. Our new expanded dataset, collected across more sites and a longer time period, confirms this finding (Figure 4.5, 4.10). The authors of the previous study hypothesized that South Shore seawater, unlike coastal seawater in other areas of the island, may be influenced by submarine groundwater discharge from the nearby Devonshire Lens. Since freshwater lenses are non-saline and their water is sourced from isotopically depleted precipitation, this submarine freshwater discharge should reduce both salinity and $\delta^{18}O_w$ values of affected coastal seawater. Although this large variability in $\delta^{18}O_w$ suggests the discharge mechanism was mainly affecting the South Shore, it does not negate the possibility of discharge along North Shore of the Devonshire Lens. A recent study from Sims et al (2020) showed

groundwater discharge with elevated levels of nitrogen was impacting the reef community on the North Shore. They observed cold, low-salinity water visibly discharging from cracks in the limestone reef in one area termed a “vent site”. Neither that or this study collected systematic samples from North Shore that would be needed to show the magnitude of $\delta^{18}O_w$ variability and make comparisons to our South Shore sites.

Based on the proposed hypothesis, the amount of discharge should be related to local sea level, with increased discharge occurring when sea levels are lower. When sea levels are higher, the topographic gradient from island center to coast is reduced, which would reduce outwards flow of freshwater. The limited dataset in the previous study (Zhang et al, 2021) did not allow testing of the temporal component of this hypothesis or the correlation between sea level and $\delta^{18}O_w$ values. Our new expanded dataset supports this submarine freshwater discharge hypothesis, showing increased $\delta^{18}O_w$ values during periods of elevated sea level (Figure 4.7A, 4.7B). Salinity also varies with sea level, although the relationship is not as clear (Figure 4.7A, 4.7C). Over the sampling interval, daily tidal fluctuations and monthly lunar cycles were superimposed on annual changes in average sea level due to regional thermal expansion and contraction (Figure 4.7A). The relationship between $\delta^{18}O_w$ values and sea level holds true over all three timescales, whereas the relationship between salinity and sea level is most clearly visible on tidal time scales.

4.5.3.1 Tidal Timescales

On tidal timescales, hourly measurements of $\delta^{18}O_w$ and salinity collected at both DB and KAP show increased values at high tides and decreased values at low tides, consistent with the submarine groundwater discharge mechanism (Figure 4.8). Although the patterns are similar at the two sites, the magnitude of variations are very different. Samples from KAP range from 0.4

to 2.4‰ over a single tidal cycle, whereas samples from DB range from only 1.3 to 1.5‰. The latter can barely be distinguished from invariance, given analytical uncertainty, but the pattern is clearer than in the noisier KAP time series. Salinity also varies much more at KAP (33.6 to 36.3 psu) compared to at DB (33.7 to 34.9 psu), although the magnitude of variability is more similar if the single high salinity point from KAP is not included.

This difference in magnitude of variability, and the fact that KAP shows high outliers on both tidal (Figure 4.8) and monthly (Figure 4.7) timescales may be due to the coastal geometry and the time of year of collection. First, the magnitude of the tidal cycle (high tide – low tide) that was sampled in May at KAP was >0.5m, whereas the sampled tidal cycle at DB in January fluctuated only ~0.3m. A greater tidal range would be predicted to correlate to greater variability in salinity and $\delta^{18}O_w$. Second, at KAP, an extended ledge is partially exposed at lower tidal heights, leading to local semi-restriction of coastal waters from the open ocean, potentially making this site more sensitive to both evaporative enrichment and freshwater outflow (Figure 4.1C). The slightly different KAP site was selected for hourly sampling because the established location of biweekly sampling (KAS) was sometimes without water during lowest tides. The hourly sampling at KAP was conducted in May, when low tides reach an annual minimum, enhancing the restriction, whereas the hourly sampling at DB was conducted in January, a time of intermediate sea level. Finally, wind speeds on the day of collection at DB were much higher (8-19 mph) than on the day of collection at KAP (6-8mph). Higher wind speeds would accelerate mixing away of a local salinity or $\delta^{18}O_w$ anomaly, potentially helping explain the lower amplitude of variation at the DB site.

Overall, despite differences in magnitude and noisiness of the time series, both sites show increasing salinities and $\delta^{18}O_w$ values with increasing tidal height (and vice versa), supporting the submarine groundwater discharge mechanism.

4.5.3.2 Lunar and Annual Timescales

Bi-weekly sampling over a period of months also showed the predicted relationship between $\delta^{18}O_w$ and sea level height. Particularly over May-August 2020, $\delta^{18}O_w$ values increased as sea level height increased (Figure 4.7). There is consistency in $\delta^{18}O_w$ values across the six coastal sites through time, indicating a large-scale mechanism at work.

Individual high $\delta^{18}O_w$ outliers at KAP/KAS and GB occur in May, late July, and to a lesser degree, late June. These high $\delta^{18}O_w$ values tend to correspond to higher salinities as well, suggesting evaporative enrichment as the cause. As discussed above, unlike the other rocky shorelines, the KAP/KAS site has a coastal geometry that appears to make it susceptible to restriction and evaporative enrichment. The finding of samples from GB with elevated salinity and $\delta^{18}O_w$ values may be explained by evaporative enrichment as well. GB is a very gently sloping, sandy beach where waves wash over large horizontal distances, promoting evaporative enrichment over subsequent wave cycles. Most GB samples were taken from the surface in knee-depth water. In December 2021, one sample was taken from the surf zone, extremely close to shore in only inches of water. This sample showed significant evaporative enrichment, with a $\delta^{18}O_w$ value of 3.0‰ and a salinity of 36.7 psu. This suggests that evaporative enrichment is happening in the shallowest water, which would have influenced $\delta^{18}O_w$ values and salinity of collected knee-depth waters to a varying degree based on daily conditions such as wind speed, direction, wave height, etc.

The lowest salinities (<34 psu) and $\delta^{18}O_w$ values (<0.75‰) are seen at Devonshire Bay (DB). Of all the South Shore sites, DB is the farthest northeast, closest to the center of the Devonshire Lens. It is also a semi-enclosed bay, so it may trap freshwater discharge more readily than other sites. It is difficult to say whether proximity to the lens or local coastline geometry plays a larger role in producing low salinity and $\delta^{18}O_w$ values at this site.

4.5.4 Mechanisms Controlling Salinity Variation Along South Shore

The submarine discharge mechanism predicts that salinity and $\delta^{18}O_w$ should vary in tandem in coastal waters if discharge of aquifer water mixing with background seawater were the only control on water composition. In both the hourly and bi-weekly sampling, we see a relationship between $\delta^{18}O_w$ values and sea level height that supports the freshwater discharge mechanism. Although in hourly sampling, the salinity changes in concert with $\delta^{18}O_w$, the relationship with salinity is not as apparent in the bi-weekly sampling (Figure 4.7-4.8).

Well-water samples from the transition zone show a clear mixing relationship between salinity and $\delta^{18}O_w$ (Figure 4.9A), defined by Equations 4.1 and 4.2, but South Shore seawater samples do not plot along the same mixing line (Figure 4.9). Excluding high salinity outliers that are likely due to evaporative enrichment (KAP/KAS and GB) and low salinity outliers driven by closest proximity to the lens and/or coastal geometry (DB), the vast majority of other salinity values fall within the stable, narrow range seen at Hamilton (~34.1-35.4 psu) (Figure 4.7), despite these same sites demonstrating >1‰ variability in $\delta^{18}O_w$. Equations 4.1 and 4.2 predict a roughly ~7 psu decrease in salinity for every 1‰ decrease in $\delta^{18}O_w$ due to mixing with pure aquifer water, a magnitude of salinity change that is not seen.

It is difficult to explain the observed low variability in salinity. Variability in $\delta^{18}O_w$ is not inflated due to analytical reasons, as samples from Hamilton and other non-South Shore sites show very stable values. Small variations in salinity may be masked by the precision of the salinity meter (instrument precision = ± 0.1 psu), although even the less precise tool should be able to detect the predicted ~7 psu changes in salinity.

A previous study also found greater variability in $\delta^{18}O_w$ compared to salinity in the Bermuda seawater samples (Epstein and Mayeda, 1953), although they only had a few samples. The authors suggested repeated evaporation and precipitation would remove light oxygen isotopes and transport them away in the vapor phase, while maintaining a similar salinity. This mechanism may be acting but would not apply to very local scale anomalies in $\delta^{18}O_w$ due to freshwater discharge or uniquely target South Shore sites. Another study investigated how sea spray aerosols could deposit salt on land and elevate salinities in interior pools of water (Smith et al., 2021). Surface waters rushing over land may pick up these salt molecules and deliver them to the ocean, or to the aquifer water below as rainwater percolates down beneath the land. However, this mechanism also would not specifically target South Shore areas.

Finally, it is possible that the observed pattern of salinity and $\delta^{18}O_w$ is the result of aliasing due to the low temporal resolution of sampling (once per 2 weeks) vs. tidal timescales and a superposition of influences of daily vs. annual-scale processes. Samples collected in June, a time of lower mean sea level, were also collected from intermediate to low tide. Samples collected in August, a time of higher mean sea level, were collected closer to the daily high tide. It is not clear how this may translate to the observed lower variability in salinity relative to $\delta^{18}O_w$, but we note it in the face of a lack of satisfactory alternative explanations. More work would be needed to resolve this mystery.

The lack of salinity change also raises another point – that the unique hydrological setting of the South Shore would not have been detected by salinity measurements alone. The addition of $\delta^{18}O_w$ provided additional information and shows the benefit of pairing these types of measurements in future hydrology studies like this one. In future work, the further addition of deuterium excess may be helpful in determining the mechanisms behind salinity vs. $\delta^{18}O_w$ changes by helping identify the impacts of evaporation relative to mixing on coastal seawaters.

4.6 Conclusion

Previous studies have modeled and examined aspects of the freshwater lens, mainly the central Devonshire Lens, and the majority of that work was completed in the 1970s. In this study, we present a systematic survey of the hydrologic system through salinity and $\delta^{18}O_w$ measurements of various water types both around and on the island of Bermuda to better understand the dynamic interaction between coastal seawater and freshwater sources. Coastal seawater salinity and $\delta^{18}O$ values are typically considered to be constant, and they are thought to co-vary in many environments. Within the Devonshire Lens, salinity and $\delta^{18}O_w$ measurements from the well samples follow the expected linear mixing relationship between freshwater and seawater, and both transition toward marine endmember as depth increases. The previously hypothesized discharge relationship between $\delta^{18}O_w$ and tidal height is validated through the South Shore samples on multiple timescales. However, salinity measurements from the South Shore samples do not correlate with the $\delta^{18}O_w$ measurements, presenting an area for future study. Due to the discharged freshwater out of the Devonshire Lens, $\delta^{18}O_w$ is observed to vary significantly both on daily and monthly timescales. In contrast, salinity measurements recorded

from these South Shore sites are essentially “non-varying”, revealing a potentially more complex interaction that requires further study to illuminate.

Currently, on the island of Bermuda, potable water supply derived from rainwater collection is exceeded by demand. When precipitation levels decline and/or in high-occupancy buildings like hotels, alternative drinking water sources must be tapped to make up the difference, such as through groundwater extraction. However, unsustainable extraction from the island’s freshwater lenses could result in a reduction of the fresh water nucleus and an increase in saltwater intrusion, reducing the quality of extracted water through salt contamination. Studies like this one are important in order to quantify current aquifer size through multiple metrics, understand freshwater-seawater interaction around the island, and determine a baseline against which future studies can compare.

Global warming is changing global precipitation patterns and melting ice sheets, leading to sea level rise. In Bermuda, sea levels have already risen by >0.2 m since 1930 (NOAA Tide and Current https://tidesandcurrents.noaa.gov/). As sea levels continue to rise, the size of Bermuda’s freshwater lenses will shrink, further exacerbating the issue of insufficient freshwater supply. As extraction plans evolve in the face of these forecasted changes, having a baseline understanding of the processes influencing the island’s valuable freshwater resources is all the more important.

4.7 Acknowledgements

A huge thank you to Ricardo Anderson, Maria Marcano, Bruce Williams, and Shaun Lavis for collecting water samples during COVID-19, which untimely made this research project possible. We thank Ashling Neary and Kyger C. Lohmann for isotope laboratory assistance at

the University of Michigan. This project was supported by National Science Foundation grant 1903237, Alfred P. Sloan Research Fellowship to S.V. Petersen; National Science Foundation GRFP, Rackham Graduate School Merit Fellowship and University of Michigan Turner Grant to J. Z. Zhang.

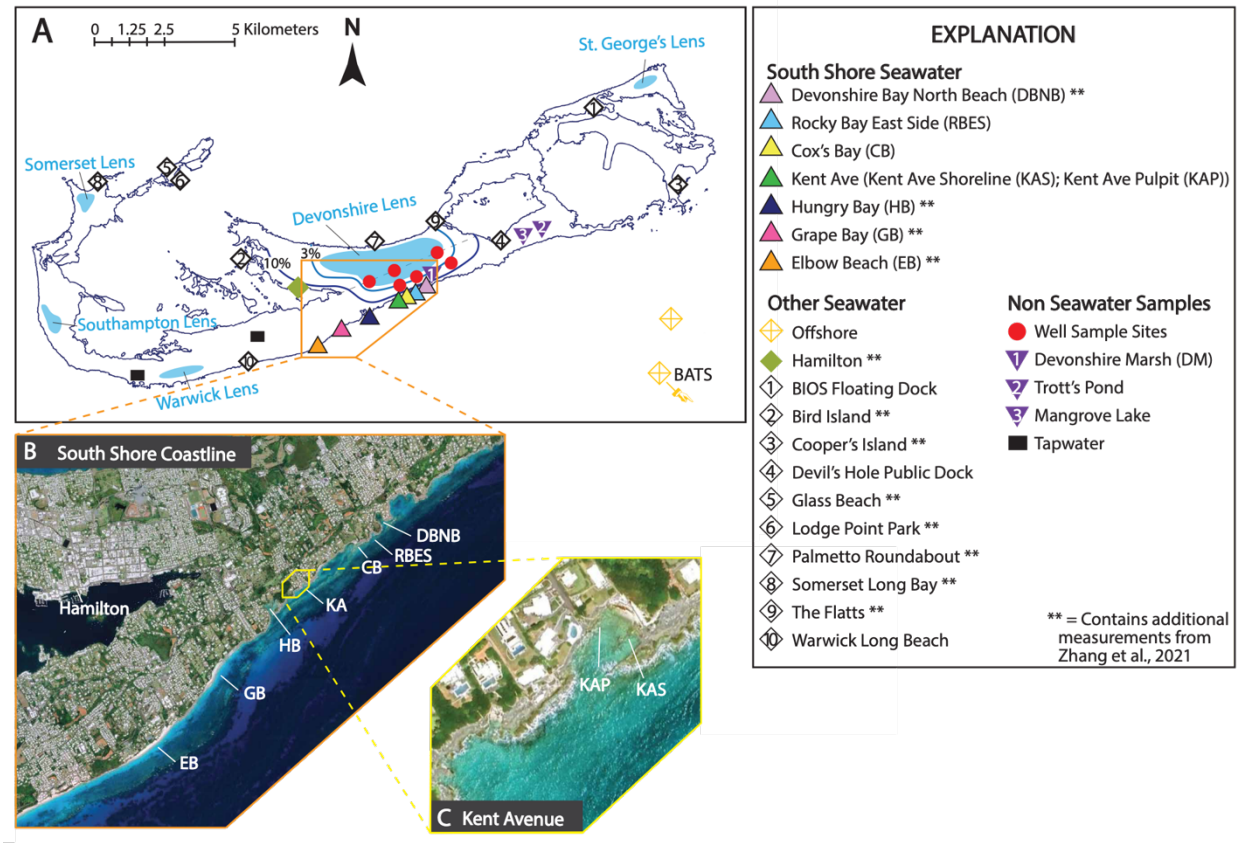

Figure 4.1. Water sampling locations in Bermuda.

A, Map of Bermuda showing water sampling sites. B, Zoomed in satellite image of the south shore coastline. C, Satellite image of Kent avenue showing the locations of Kent Ave Pulpit (KAP) and Kent Ave Shoreline (KAS).

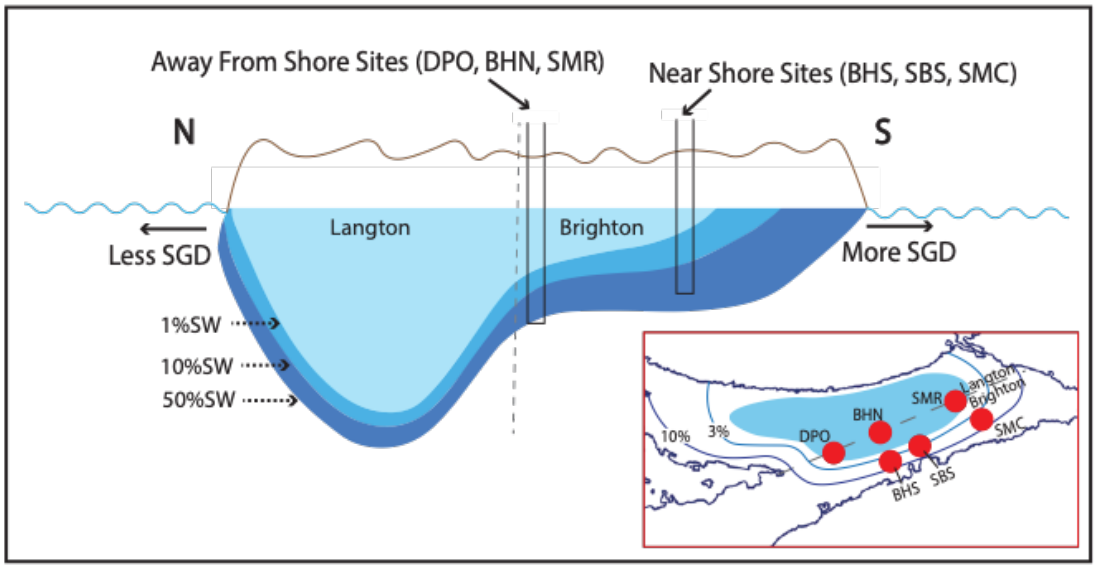

Figure 4.2. Schematic cross section of Devonshire Lens modified from Vacher, 1978.

Isolines representing the amount of mixing based on relative salinity (Vacher, 1978). Six well locations are grouped into either the "away from shore" or the "near shore sites" based on their proximity to the south shore coastline. SGD=submarine groundwater discharge; BHN=Brighton Hill North; BHS=Brighton Hill South; DPO=Devonshire Post Office; SBS=St. Brenden South; SMC=St. March's Church; SMR=St. Mark's Road.

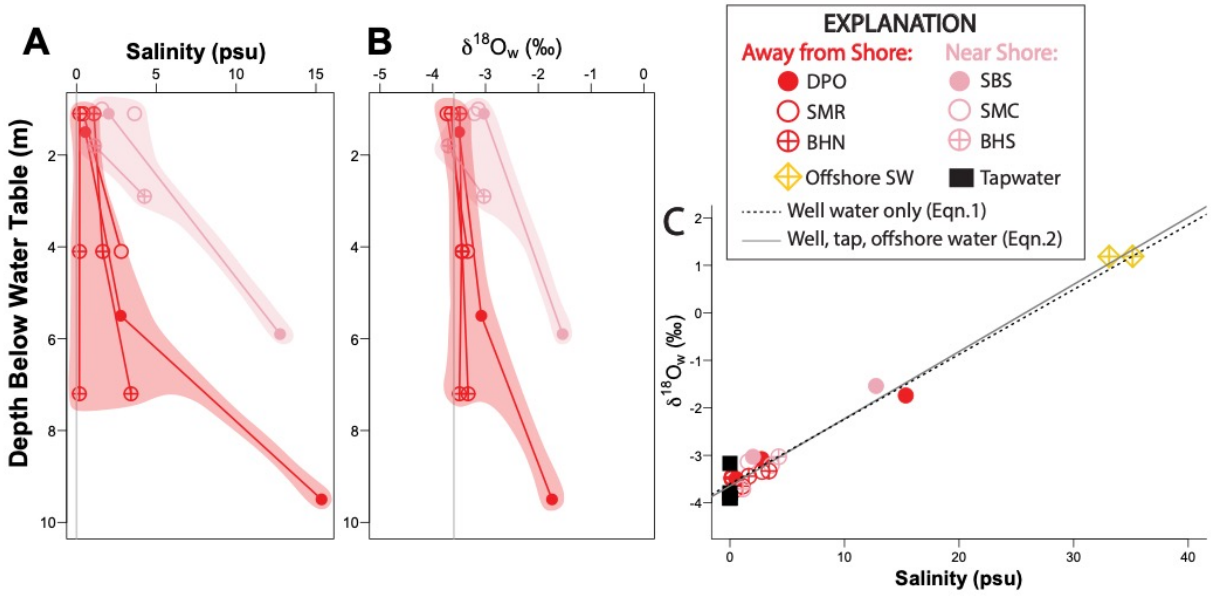

Figure 4.3. Salinity and $\delta^{18}O_w$ measurements of well water samples.

A, Salinity measurements as function of depth at the six well sites. Salinity data are shaded distinguishing the two categories. B, $\delta^{18}O_w$ measurements as function of depth at the six well sites. $\delta^{18}O_w$ data are shaded distinguishing the two categories. C, $\delta^{18}O_w$ and salinity data of the six well sites, offshore and tap water samples. A mixing line fitted through all samples are shown (Eqn. 4.2), and a trendline fitted only through the well samples are also shown (Eqn. 4.1).

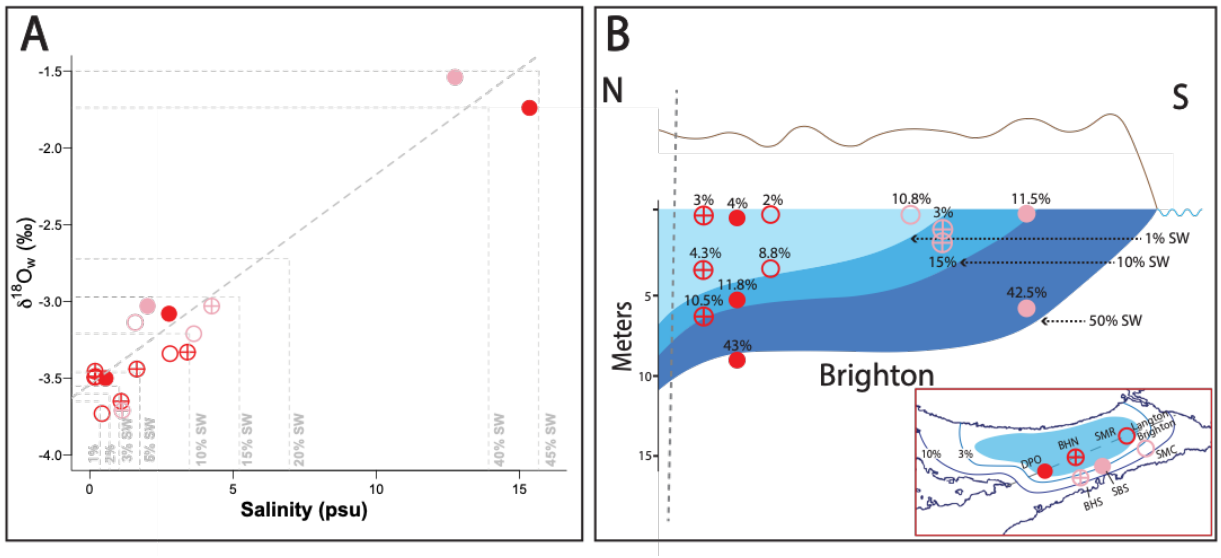

Figure 4.4. Mixing line based on well water salinity and $\delta^{18}O_w$ measurements.

A, $\delta^{18}O_w$ and salinity data of six well sites. Points deviated from the mixing line are estimated using either $\delta^{18}O_w$ or salinity, and an averaged number is shown. B, Schematic cross section of the Devonshire Lens, showing the Brighton Aquifer and isolines representing the amount of mixing based on relative salinity (modified from Vacher, 1978). The six well locations are plotted as function of sample depth, with percentages indicating percent seawater based on the mixing relationship shown in A.

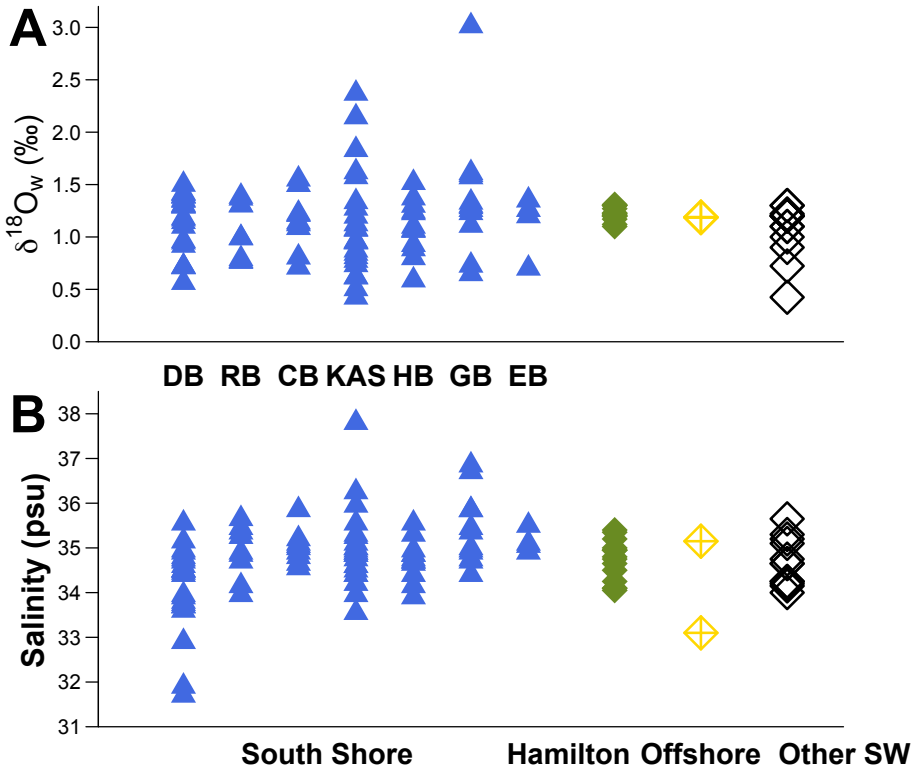

Figure 4.5. $\delta^{18}O_w$ and salinity measurements of all seawater.

Water samples were collected repeatedly throughout 2020. Note the South Shore sites show greater variability in $\delta^{18}O_w$ compared to the Hamilton site.

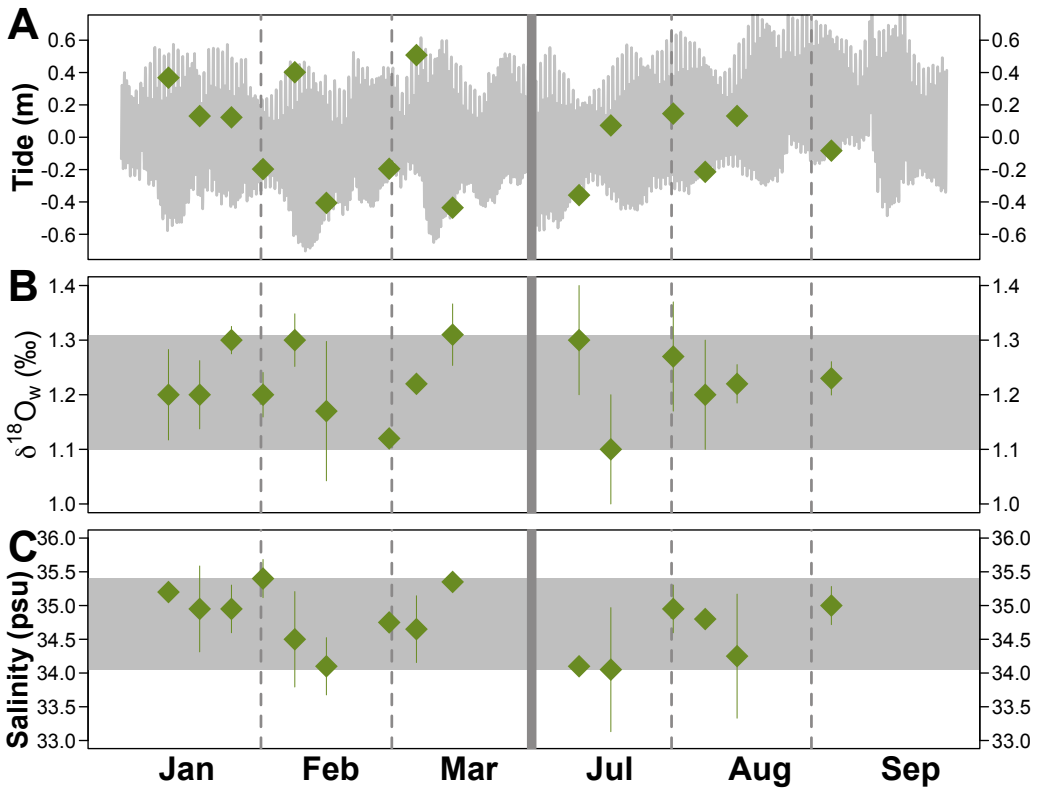

Figure 4.6. Salinity and $\delta^{18}O_w$ measurements of the Hamilton samples.

A, Tidal information over the sampling months in 2020, green points indicate sampling time. B, Hamilton $\delta^{18}O_w$ data. C, Hamilton salinity data. Typical instrument uncertainty is 0.1‰ and 0.1 psu for $\delta^{18}O_w$ and salinity, respectively. Error bars here reflect reproducibility of the measurements, reported as 1SD of the mean.

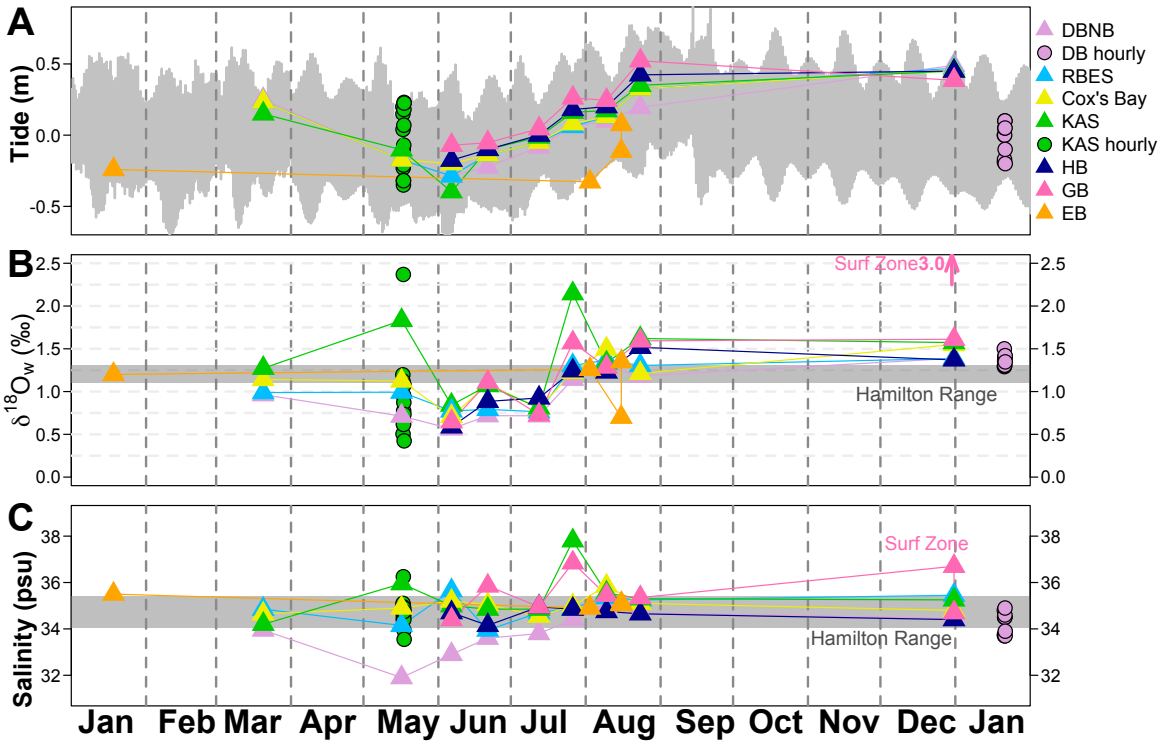

Figure 4.7. Salinity and $\delta^{18}O_w$ measurements of the South Shore samples.

A, Tidal information over the sampling months (January 2020-January 2021), points indicate sampling time. Tide is referenced to mean tide level in meters, 0 represents mean tide/sea level. B, $\delta^{18}O_w$ data of the 6 south shore sites. C, Salinity data of the 6 south shore sites.

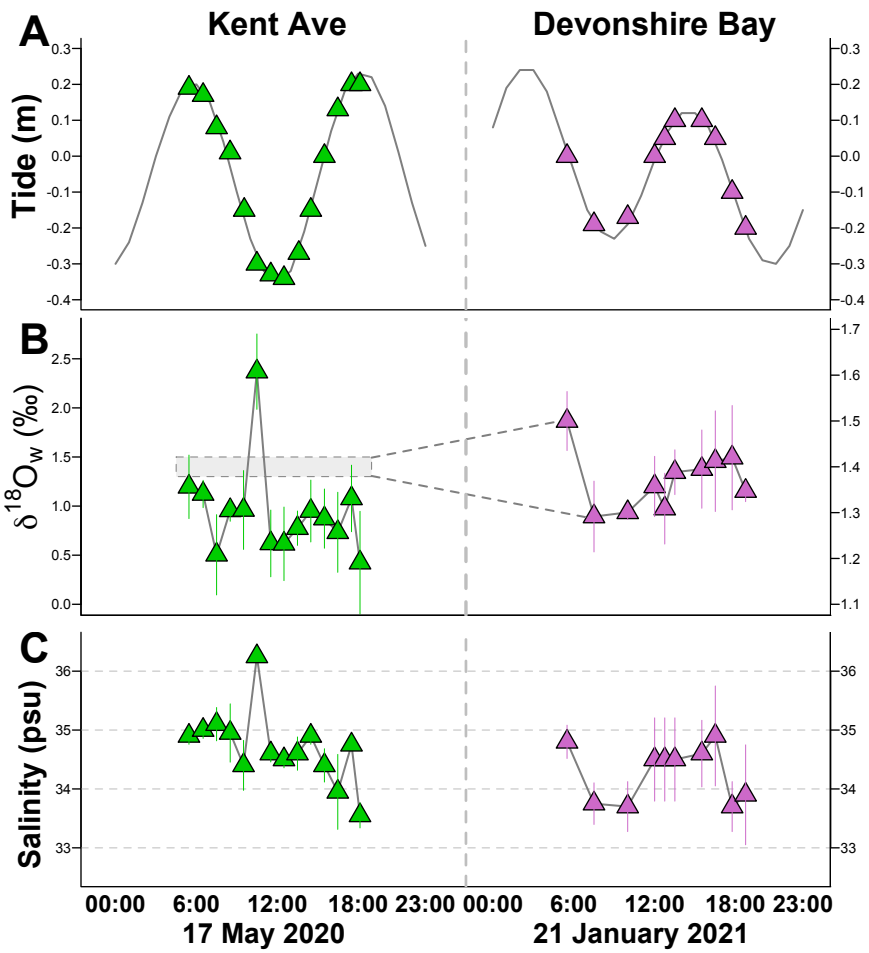

Figure 4.8. Salinity and $\delta^{18}O_w$ data of hourly sampling at Kent Ave and Devonshire Bay.

A, Daily tidal information, with points indicate sampling time. B, $\delta^{18}O_w$ data of hourly sampling at Kent Ave and Devonshire Bay. C, Salinity data of hourly sampling at Kent Ave and Devonshire Bay. Errors reflect reproducibility of the measurements, reported as 1SD of the mean.

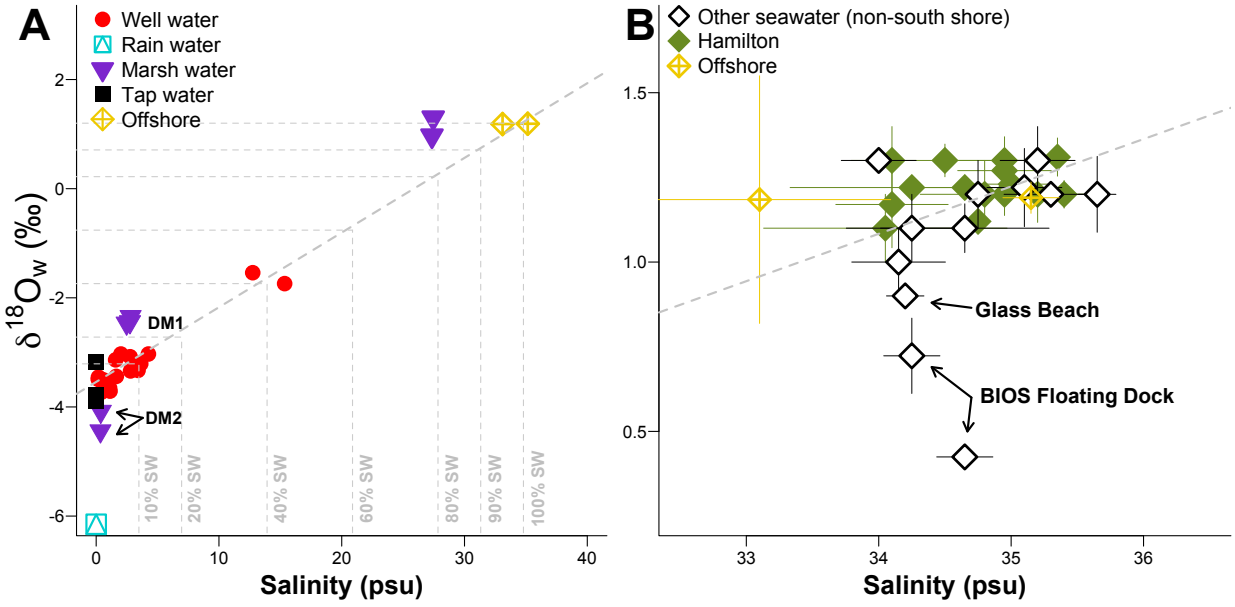

Figure 4.9. Various water types plotted onto the mixing line.

A, $\delta^{18}O_w$ and salinity data of well, rain, marsh, tap and offshore water samples. Trendline indicate mixing relationship. B, $\delta^{18}O_w$ and salinity data of the non-south shore seawater, Hamilton and offshore samples plotted on the mixing relationship. Errors reflect reproducibility of the measurements, reported as 1SD of the mean.

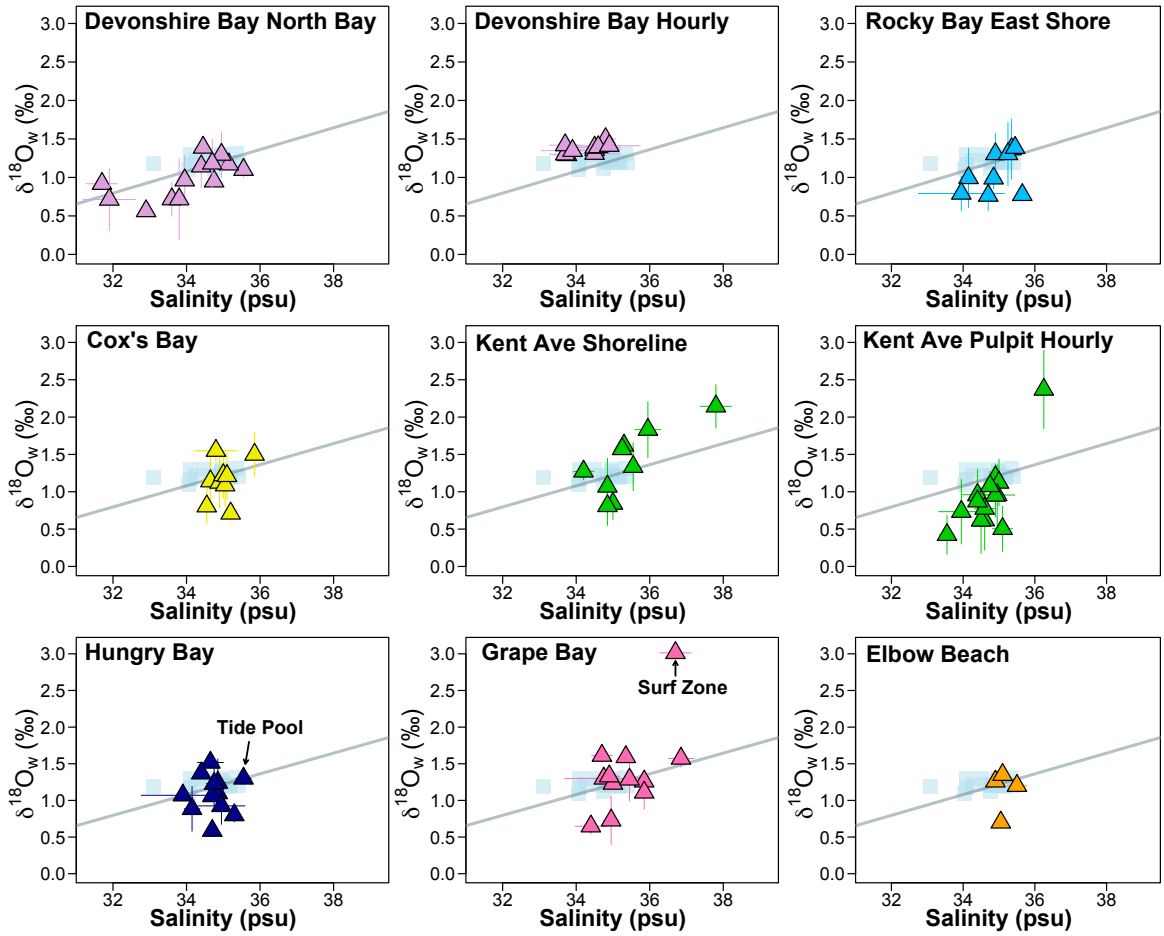

Figure 4.10. $\delta^{18}O_w$ and salinity data of individual south shore sites.

Trendline indicates the mixing line, and background blue cluster represents $\delta^{18}O_w$ and salinity data of Hamilton and offshore samples. Errors reflect reproducibility of the measurements, reported as 1SD of the mean.

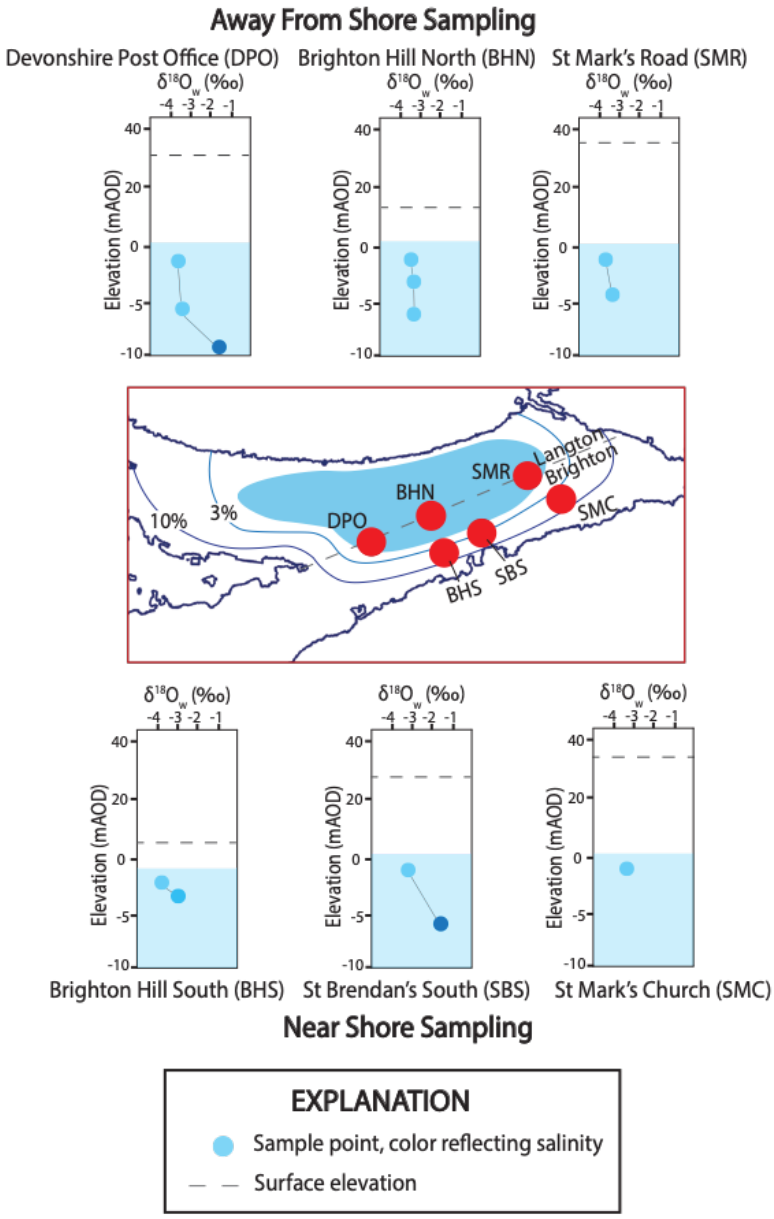

Figure 4.S1. $\delta^{18}O_w$ measurements of the six wells, colored sample points also reflect salinity.

Note the samples collected further inland show gradual increases in $\delta^{18}O_w$ values, whereas samples collected close to the coastline show rapid increases.

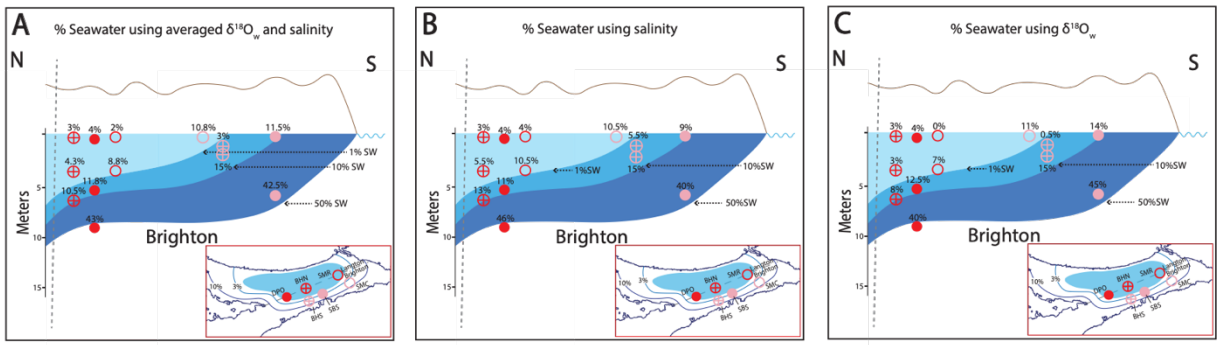

Figure 4.S2. Estimated amount mixing using different methods plotted onto the Schematic cross section of the Devonshire Lens.

A, Schematic cross section of the Brighton Aquifer with six well locations plotted as function of depth. Numbers indicate percent seawater based on the mixing relationship. Points deviated from the mixing line are estimated using either $\delta^{18}O_w$ or salinity, and an averaged number is shown. B, Points deviated from the mixing line are estimated using salinity. C, Points deviated from the mixing line are estimated using $\delta^{18}O_w$.

4.8 References

Andrews, W. T., & Laker, D. S. (2001). A twelve-year history of large scale application of work-exchanger energy recovery technology. *Desalination*, *138*, 201–206. Retrieved from www.elsevier.com/locate/desal

Epstein, S., & Mayeda, T. (1953). variation of O^{18} content of waters from natural sources. *Geochimica et Cosmochimica Acta* , *4*, 213–224.

Griffin, A. J., Anderson, Z., Ballard, J., Bates, N. R., Garley, R., Johnson, R., et al. (2022). Seasonal changes in seawater calcium and alkalinity in the Sargasso Sea and across the Bermuda carbonate platform. *Marine Chemistry*, *238*. https://doi.org/10.1016/j.marchem.2021.104064

Povinec, P. P., de Oliveira, J., Braga, E. S., Comanducci, J. F., Gastaud, J., Groening, M., et al. (2008). Isotopic, trace element and nutrient characterization of coastal waters from Ubatuba inner shelf area, south-eastern Brazil. *Estuarine, Coastal and Shelf Science*, *76*(3), 522–542. https://doi.org/10.1016/j.ecss.2007.07.041

Rowe, M. (1984). The freshwater "central lens" of Bermuda. *Journal of Hydrology*, *73*, 165–176.

Rowe, M. P. (2011). Rain water harvesting in Bermuda. *Journal of the American Water Resources Association*, *47*(6), 1219–1227. https://doi.org/10.1111/j.1752-1688.2011.00563.x

Simmons, J. A. K., & Lyons, W. B. (1994). The ground water flux of nitrogen and phosphorus to Bermuda's coastal waters. *JAWRA Journal of the American Water Resources Association*, *30*(6), 983–991. https://doi.org/10.1111/j.1752-1688.1994.tb03346.x

Sims, Z. C., Cohen, A. L., Luu, V. H., Wang, X. T., & Sigman, D. M. (2020). Uptake of groundwater nitrogen by a near-shore coral reef community on Bermuda. *Coral Reefs*, *39*(1), 215–228. https://doi.org/10.1007/s00338-019-01879-5

Smith, M. E., Wynn, J. G., Scharping, R. J., Moore, E. W., Garey, J. R., & Onac, B. P. (2021). Source of saline groundwater on tidally influenced blue holes on San Salvador Island, Bahamas. *Hydrogeology Journal*, *29*, 429–441.

Vacher, H. L. (1978). Hydrogeology of Bermuda-significance of an across the island variation in permeability. *Journal of Hydrology*, *39*, 207–226.

Vacher, H. L., & Ayers, J. F. (1980). Hydrology of small oceanic islands-utility of an estimate of recharge inferred from the chloride concentration of the freshwater lenses. *Journal of Hydrology*, *45*, 21–37.

Vacher, H. L., & Rowe, M. P. (1997). Geology and Hydrogeology of Carbonate Islands. *Developments in Sedimentology*, *54*.

Winkelstern, I. Z., Rowe, M. P., Lohmann, K. C., Defliese, W. F., Petersen, S. V., & Brewer, A. W. (2017). Meltwater pulse recorded in Last Interglacial mollusk shells from Bermuda. *Paleoceanography*, *32*(2), 132–145. https://doi.org/10.1002/2016PA003014

Zhang, J. Z., & Petersen, S. V. (2023). Clumped and oxygen isotope sclerochronology methods tested in the bivalve *Lucina pensylvanica*. *Chemical Geology*, *620*, 121346. https://doi.org/10.1016/j.chemgeo.2023.121346

Zhang, J. Z., Petersen, S. V., Winkelstern, I. Z., & Lohmann, K. C. (2021). Seasonally variable aquifer discharge and cooler climate in Bermuda during the last interglacial revealed by subannual clumped isotope analysis. *Paleoceanography and Paleoclimatology*, *36*(6), 1–19. https://doi.org/10.1029/2020PA004145

Chapter 5 The Cooling of the Last Interglacial Climate and the Rapid Sea Level Changes in Bermuda

5.1 Abstract

The warmer Last Interglacial period is often considered as a potential analogue for future climate change, and it was the most recent time in which the global temperatures exceeded modern values. Locally, in Bermuda, paleoclimate reconstructions over the recent years disagreed on whether it was warmer or cooler during the Last Interglacial. Here, we present new oxygen and clumped isotope measurements on fossil bivalves *Lucina pensylvanica* and *Glycymeris americana* from 3 new sites, along with detailed stratigraphy, previously published climate and Amino Acid Racemization data to depict a fuller picture of climate and paleoenvironmental evolution through the Last Interglacial. We find that the previous disagreement on temperatures could be explained by different time intervals within MIS 5e. The composite stratigraphy shows a trend of cooling temperature as sea level rises, observed in both Great Sound and South Shore sites. This indicates that peak MIS 5e warming occurred early in the Last Interglacial, initiated the rise in sea level, and as sea level continued to rise, temperature began to decline, consistent with sea level modeling studies. The observed decrease in $\delta^{18}O_w$ over the same interval provides further evidence of the arrival of meltwater from the Greenland icesheet and the high latitude ice fields. The findings in this study emphasize that MIS 5e is not a

single moment in time with static climate conditions, but, it rather represents a period of change in climate and paleoenvironment.

5.2 Introduction

The Last Interglacial, Marine Isotope Stage 5e (MIS 5e), was an interval with climate as warm or slightly warmer than today. Global mean sea surface temperature was reconstructed as ~2°C warmer than present, accompanied by a ~6-9m increase in the sea level (CLIMAP, 1984; Kukla et al., 2002; Turney and Jones, 2010). While overall, Last Interglacial climate was reconstructed as warm, there was regional-scale temperature variation between the Central and North Atlantic. Studies suggested generally cooler-than-modern temperatures from the Central Atlantic and Caribbean region, and warm temperatures from the North Atlantic region (CLIMAP, 1984; Harrison et al., 1995; Turney and Jones, 2010). Bermuda (32.4°N, 64.8°W) is located in between the regions with temperature dichotomy, and could potentially provide additional insights on the Last Interglacial climate and aid in the understanding of temperature inconsistencies between the oceans.

On the island of Bermuda, sediments mainly consist of marine limestones, aeolian sands and terra rosa paleosols. The marine limestones can be divided into five main formations, with age ranges from older than MIS 13 to MIS 5a (Harmon et al., 1983; Hearty et al., 1992; 1999; Rowe et al., 2014). Typically, the youngest sediments from these formations can be readily distinguished from the oldest through the level of cementation and weathering, but it gets increasingly difficult to distinguish formations from sequential interglacials that are closer in age. Further, stratigraphic layers are not commonly laterally traceable, and outcrops are often interrupted by anthropogenic development and natural features of the coastline that prevent

access, increasing the level of difficulty correlating outcrops across the island. Absolute ages determined from Uranium-Thorium (U/Th) radiometric dating are limited to a handful of sites along the South Shore and the Northernmost tip of the island (Harmon et al., 1978; 1983, Hearty, 2002; Rowe et al., 2014; Muhs et al., 2002). Additional age determination across the island come from relative dating technique, known as Amino Acid Racemization (AAR) or allostratigraphy.

Difficulties in absolute dating have led to controversy about the island-wide stratigraphy over the years. For example, there has been disagreement over the age of the Belmont Formation (MIS 5 vs. MIS 7) (Hearty, 2002; Rowe et al., 2014). Additionally, within MIS 5e, discussions continue over whether MIS 5e deposition occurred in one episode during peak sea level or in two episodes reflecting two intervals of peak sea level (Harmon et al., 1983; Muhs et al., 2002; Hearty et al., 2002, Rowe et al., 2014).

MIS 5e paleoclimate reconstruction efforts have focused on two well dated sites from the South Shore, Devonshire/Rocky Bay and Grape Bay (Winkelstern et al., 2017; Zhang et al., 2021). Clumped and oxygen isotope analyses on marine gastropods of the species *Cittarium pica* reconstructed cooler-than-modern temperatures from these sites. In addition, although both sites were dated to MIS 5e using U/Th dating (Harmon et al., 1983; Muhs et al., 2002), previous studies found temperature differences between the two sites, with samples from Grape Bay (GB) recording ~8 °C cooler than modern mean annual temperatures and samples from Devonshire/Rocky Bay (DB/RB) recorded ~2 °C cooler than modern mean annual temperatures (Winkelstern et al., 2017; Zhang et al., 2021). Differences in mean U-Th age of each outcrop suggest that the two sites may represent different time intervals within MIS 5e. U-Th dates indicate the Grape Bay outcrop is ~ 112-126 ka and the RB/DB outcrop is ~120-128 ka (Harmon et al., 1983; Muhs et al., 2002; Winkelstern et al., 2017). However, the multi-thousand-year

uncertainties have led previous authors to treat these two sites as coeval (Winkelstern et al., 2017; Zhang et al., 2021).

A recent study identified additional MIS 5e localities on islands in Bermuda's Great Sound using amino acid racemization (Minnebo et al., *in prep*). The Great Sound islands have been understudied to date but have abundant and well-preserved shell beds and the potential to contribute to paleoclimate interpretations for Bermuda. Through clumped and oxygen isotope analyses on the oyster *Dendostrea frons* from Verrill Island, Minnebo et al. (*in prep*) found mean temperature and seasonality very similar to the modern range, in contrast to cooler-than-modern temperatures recorded in gastropods from the South Shore (Zhang et al., 2021). Examination of additional Great Sound Island sites is needed in order to shed light on local paleoenvironment and potentially explain across-island differences in temperatures recorded in MIS 5e outcrops.

Here, we conduct clumped and oxygen isotope analyses on fossil bivalves from Bird Island, Long Island East and Lodge Point Park (*Lucina pensylvanica*) or from Grape Bay and Bird Island (*Glycymeris americana*) to understand changes in local paleoenvironment during the Last Interglacial. We compare our findings with the previously published data reconstructed using other genera from Bermuda (Winkelstern et al., 2017; Zhang et al., 2021; Minnebo et al., *in prep*). Combined with the AAR dates and stratigraphy from Minnebo et al. (*in prep*), we attempt to gain a broader understanding of climate evolution in Bermuda during the Last Interglacial.

5.3 Geologic Setting

5.3.1 Site Description

Bird Island (BI)

Located in the Great Sound, Bird Island (BI) has multiple well preserved beds of fossil bivalves. Underlain by a ~1 m thick aeolian bed, these fossil beds can be separated into four distinct stacked shell layers which we label A-D (layer A = top) that can be distinguished by shell abundance and preservation (Figure 5.2). The basal shell layer (D) at BI is exposed ~0.3m above the present-day high tide level. When this site was visited, an additional meter of outcrop below layer D was exposed but difficult to access or view. No clearly visible shell-rich layers were observed below layer D. BI-D contains disarticulated and whole and fragmented shells. Similar to BI-D, BI-C also has fragmented, more poorly preserved shells, but at lower abundance, with the layer itself sometimes pinching in and out laterally over ~10-20m of exposure. There is a clear increase in shell abundance between the lower shell layers (D/C) and upper shell layers (A/B). BI-A and BI-B both have more abundant, better preserved shells, including some articulated shells.

Since there is no evidence of tectonics at BI or anywhere on Bermuda, the observed stacking of layers here can be interpreted as representing their original, sequential order of deposition. Therefore, layer D would represent the oldest time interval and layer A would represent the youngest. The presence of fragmented, abraded shells in layers D and C suggest time spent in a higher-energy wave-influenced environment, whereas the minimal wear on valves from layers A and B suggests a shorter transport distance and rapid burial after death. We interpret these layers to have been deposited sequentially during a transgression.

Mollusk samples were collected from all four layers for AAR dating by Minnebo et al. (*in prep*). The reported mean A/I ratio for samples from all four layers combined was 0.529 ± 0.020 (1sd) (Minnebo et al., in prep), placing this outcrop within MIS 5e based on previously calibrated A/I ratio ranges (Harmon et al., 1983; Muhs et al., 2002).

In this study, valves of *L. pensylvanica* were analyzed from layers A through D as follows: 4 from layer A, 3 from layer B, 1 from layer C, 2 from layer D. Additionally, a single valve of *G. americana* was analyzed from layer B.

Long Island East (LIE)

At Long Island East (LIE), a single shell lens about 20cm in thickness is exposed around 0.5m above the present-day high tide level (Figure 5.2). This narrow shell lens consists of more poorly preserved, fragmented and disarticulated shells. The general shell assemblage and appearance of the LIE shell layer resembles that of layers BI-C and BI-D. Unlike at BI, overlaying the narrow shell bed is an interval of distinctive, large scale rip-up clasts consisting of limestone cobbles and rounded boulders ranging in size up to around 0.6 meter. Large rip-up clasts are interpreted to reflect a major storm event, potentially a hurricane, that possibly removed material equivalent to BI-A and BI-B.

Mollusk samples were collected from this shell lens for AAR dating, and the reported A/I ratio for LIE was 0.523 ± 0.021 (1sd) (Minnebo et al., *in prep*), also placing it within previously described MIS 5e A/I ranges (Harmon et al., 1983; Muhs et al., 2002). In this study, two single valves of *L. pensylvanica* were analyzed from this site.

Lodge Point Park (LPP)

At Lodge Point Park (LPP), one thick shell-containing unit begins around 0.2m above the high tide line (Figure 5.2). This full exposure is close to 3m in thickness. Similar to BI, there is an increase in shell abundance with stratigraphic height at LPP but shells are spread throughout as opposed to being concentrated in clear shelly horizons. Abundant, well preserved shells

including many articulated bivalves and a whole sand dollar were observed near the top of the outcrop. The abundant articulated shells here suggest they were rapidly buried soon after death. In general, the upper portion of the marine deposits here greatly resemble those from BI-A/B. The lower portion of the section was less exposed and harder to study.

Mollusk samples collected near the top of the section were used for AAR dating, and the reported A/I ratio for LPP was 0.516 ± 0.037 (1sd) (Minnebo et al., *in prep*). Two *L. pensylvanica* shells were analyzed from this site.

Verrill Island (VI)

Previous paleoclimate work in the Great Sound was conducted at Verrill Island, located between Bird Island and Long Island (Minnebo et al, *in prep*). At Verrill Island (VI), a distinct layer of oysters about 0.5m in thickness is exposed at the base of the outcrop, just above the present-day high tide level. Above the oyster bed, a shell bed about 0.5m in thickness is observed, followed by an interval with few shells, contained in isolated lenses. Above this interval, a ~1m thick shelly layer occurs. The total thickness of sediments above the oyster bed yet below the aeolian sand deposits is nearly equivalent to the total thickness of the shell layers and intervening shell-poor sediments at BI (BI-D to BI-A) (Figure 5.2). A small coral fragment was found just above the oyster bed. In the shell-rich layers, articulated shells and a sand dollar were observed.

Mollusk samples collected right above the oyster bed were used for AAR dating, and the resulting A/I ratio was 0.614 ± 0.015 (1sd), the oldest relative to other measured A/I ratios within MIS 5e in the Great Sound and around Bermuda. Minnebo et al. (*in prep*) estimated temperatures and $\delta^{18}O_w$ from oysters collected from the basal layer of the outcrop. They found temperatures

range from 17.7 °C to 28.3 °C and $\delta^{18}O_w$ values range from 0.4 ‰ to 2.3 ‰ with a mean of 1.6 ‰, similar to modern conditions in the Great Sound (Zhang et al., in prep – Chapter 4). No new shells from this site were sampled for this study.

Grape Bay (GB) and Rocky Bay (RB)

Previous paleoclimate work from the South Shore sampled *C. pica* shells from Grape Bay and Rocky Bay, two coves roughly ~2 km apart. The outcrops at both sites have been previously described (Land et al., 1967; Muhs et al., 2002; Hearty and Olson, 2010; Winkelstern et al., 2017) and include the highly cemented, MIS 7 aged Belmont Formation overlain by the poorly cemented MIS 5e aged Rocky Bay Formation, containing the shell-rich Devonshire Marine member. Muhs et al (2002) represent the MIS 5e formation at Grape Bay to occur 2.5-3.5m above modern sea level, which would translate to slightly less (maybe ~1.5-2.5m) above a supposed high tide line, although the deposits are dipping upwards away from the sea.

At Grape Bay, the MIS 5e marine unit has been absolutely dated to ~112-126 ka using U/Th (Muhs et al., 2002) and relatively dated using AAR, producing a value of 0.44 ± 0.04 (1sd) (Hearty et al., 1992). At Rocky Bay, U-Th dates range from ~120-128 ka (Muhs et al., 2002) and AAR values average to 0.57 ± 0.03 (1sd) (Hearty et al., 1992). Both methods suggest the RB site is slightly older within MIS 5e than the Grape Bay site. Due to this extensive previous dating work, no additional AAR dates were conducted at this site by Minnebo et al. (*in prep*).

Previous paleoclimate work at these sites was conducted by Winkelstern et al. (2017) and extended by Zhang et al. (2021). Clumped isotope temperatures from the gastropod *C. pica* indicated Grape Bay deposits were laid down under ocean temperatures ~8 °C cooler than modern on average, in seawater with a mean $\delta^{18}O_w$ value of -0.5 ‰. Rocky Bay deposits suggest

ocean temperatures ~2 °C cooler than modern on average and seawater with a mean $\delta^{18}O_w$ value of 0.9 ‰. One *G. americana* shell from Grape Bay was analyzed in this study for comparison to Great Sound bivalves and the *G. americana* from Bird Island in particular.

5.3.2 Site-to-site Correlation in the Great Sound Based on Stratigraphic Information

Within the Great Sound, deposits of shell-rich sediments (massive or containing discrete layers) roughly 2-3m thick have been identified as MIS 5e in age using AAR (Minnebo et al., in prep). Similarities in sedimentology, fossil abundance and preservation, combined with stratigraphic height relative to the high tide line allowed correlation between sites, reinforced by AAR dating.

Closest to the high tide line (0-0.5m above) we find the oyster bed at Verrill Island. This lowest layer is not seen at other sites, but above this, stratigraphy becomes more similar across islands. Roughly 1-2m above the high tide line, sediments containing fewer, often poorly-preserved single valves are found at LIE, VI, and BI. In particular, a shellier layer BI-D overlain by a thinner, spotty BI-C can be linked to nearby Verrill Island where a shell-rich layer overlies the oyster bed, followed by a shell-poor layer containing only lenses of shells. This low interval was harder to observe at LPP, so we cannot rule out similar presentation there. From ~1.5-3m above the high tide line at LPP, VI, and BI, more abundant, sometimes articulated shells showing better preservation were observed. At LIE this portion of the section has been replaced with a massive storm deposit.

This correlation is supported by AAR dating, with very similar average values occurring at LIE, LPP, and BI (Minnebo et al., in prep). If the lower shell-poor units are combined (LIE, VI (lower shell bed), BI-C, BI-D) they have an average AAR value of 0.56. This can be

distinguished from the upper shell-rich units (LPP (upper portion), BI-A, BI-B), which have an average AAR value of 0.52. Although not directly dated, stratigraphy places the oyster layer as older than either of these units.

The lack of tectonic activity in Bermuda allows us to infer that these layers are found in their original position and were deposited during a period of sea level rise. This fits with the preservation and paleoenvironmental interpretations as well. The oyster bed would have been deposited in the shallowest water. The highly worn shells of the lower shell-poor unit were deposited in intermediate depth waters where wave action would move them around and wear down valves. The upper shell unit was deposited under deeper, calmer water condition, allowing the preservation of articulated shells and whole sand dollars. Following this interpretation, isotopic paleotemperatures from these layers should record the evolution of climate and environment in the Great Sound during a sea level rise.

5.3.3 Site-to-Site Comparison Between the Great Sound and South Shore

Dating of Grape Bay and Rocky Bay described above indicate that Grape Bay is younger than Rocky Bay. AAR dating suggests RB (A/I = 0.57 ± 0.03 (1sd)) is roughly similar to the lower shell unit in the Great Sound (LIE/BI-C/D/VI average = 0.56 ± 0.05 (1sd)) whereas GB (A/I = 0.44 ± 0.04 (1sd)) is younger than the upper shell unit (LPP/BI-A/B average A/I = 0.52 ± 0.01 (1sd)). Although this AAR data was analyzed many years apart from the new data of Minnebo et al. (*in prep*), similarity in techniques warrants this cautions correlation. Regardless of the cross-region correlation, within the South Shore sites, the relative ages are clear, with RB older and GB younger.

5.4 Methods

5.4.1 Sample Selection and Preservation Assessment

A total of 14 *L. pensylvanica* were sampled for $\delta^{18}O$ sclerochronology: 4 were from Bird Island layer A (BI-A), 3 were from BI-B, 1 was from BI-C, 2 were from BI-D, 2 were from Long Island East (LIE), and 2 were from Lodge Point Park (LPP) (Figure 5.1). 10 out of the 13 shells were resampled for seasonally-targeted Δ_{47} measurements: 2 of 4 from BI-A, 2 of 3 from BI-B, 1 of 1 from BI-C, 2 of 2 from BI-D, 1 of 2 from LIE, and 1 of 2 from LPP. Two *G. americana* shells were sampled for both $\delta^{18}O$ sclerochronology and seasonally-targeted Δ_{47}: 1 from Grape Bay and 1 from BI-B.

The selected samples exhibit clear growth lines and coloration, indicating excellent preservation of original shell material. Where shell preservation was previously described as "poorly preserved" (e.g. BI-C), this indicated a higher level of boring, wear, and encrustations on the outside. Even on these "poorly preserved" shells, original material is accessible in cross section where boring holes can be avoided. There is no evidence for recrystallization of the original shell material in the shell interior – all this wear and tear is restricted to the outside of the shells.

A subset of the shells were further assessed for diagenetic alteration through scanning electron microscopy (SEM). The SEM showed that imaged shells still retained crossed-lamellar aragonite structures and a visible pallial myostracum, confirming the lack of post-deposition recrystallization and the presence of the original aragonitic material. The position of these shells above sea level in their approximate position of deposition, as well as the lack of tectonic activity on Bermuda, indicate that there has been no opportunity for heating or thermal resetting of the isotopic signals.

5.4.2 Oxygen Isotope Sclerochronology

A total of 14 *L. pensylvanica* and 2 *G. americana* were sampled serially from umbo to ventral margin at a resolution of ~1 drill point per 1-2mm, following the sampling methods from Zhang and Petersen (2023). If outer encrusting was present, this was drilled off before the original shell below was sampled. Drill holes were kept very shallow (1-2mm) to only sample the outer shell layer.

Sclerochronology samples were analyzed for $\delta^{13}C$ and $\delta^{18}O$ by a Kiel IV automated carbonate device attached to a Thermo-Finnegan MAT 253 dual inlet mass spectrometer at the University of Michigan. The data were standardized by comparison with NBS-18 and NBS-19, units in per mille (‰) relative to VPDB standard, with an uncertainty of ± 0.1‰ for both $\delta^{13}C$ and $\delta^{18}O$. Assuming a constant $\delta^{18}O_w$ value, each $\delta^{18}O_c$ was converted to temperature using the water-aragonite fractionation factor of Kim et al. (2007). The chosen $\delta^{18}O_w$ value was calculated by averaging 2-10 $\delta^{18}O_w$ measurements from that same shell, derived from seasonally-targeted Δ_{47}measurements. Use of the shell mean $\delta^{18}O_w$ value from Δ_{47} was shown to best reconstruct seasonality in a modern calibration study on *L. pensylvanica* (Zhang and Petersen, 2023). For shells that were only measured for oxygen isotope sclerochronology and had no Δ_{47} data (N=5), $\delta^{18}O_w$ was chosen as a mean of all $\delta^{18}O_w$ values from all shells from that site/layer.

5.4.3 Seasonally-targeted Clumped Isotope

10 of 13 *L. pensylvanica* and 2 of 2 *G. americana* shells were analyzed for seasonally targeted Δ_{47}. Maxima and minima from each $\delta^{18}O$ profile were redrilled to collect ~20mg of homogenized calcium carbonate powder, following sampling methods described by Zhang and

Petersen (2023). The samples were analyzed on a Nu Instruments Perspective isotope ratio mass spectrometer connected to a NuCarb automated carbonate sample preparation device at the University of Michigan. All samples were run under "Bellows mode" (Jones et al., 2022; O'hora et al., 2022).

Δ_{47} values were calculated from raw voltages using an R-code script and Brand/IUPAC ^{17}O parameters, as described in Petersen et al. (2019). Δ_{47} values were projected into the I-CDES90 reference frame by fitting one line through ETH 1 and ETH2 in δ_{47} vs Δ_{47} space with a +0.003‰ adjustment for the difference between ETH1/2, then using all four ETH standards and defined I-CDES90 Intercarb values (Bernasconi et al., 2021) to create the empirical transfer function. Five in-house standards (calcitic Carrara marble "CM", aragonitic ooids from Joulter's Cay Bahamas "Ooids", an aragonitic coral mixture "CORS", an aragonitic gastropod *Cittarium pica* "Pica", and a cold-water aragonitic bivalve *Arctica islandica* "Ice") were run periodically to monitor for drift in corrected values through time. Final Δ_{47} values were converted to temperature using the temperature relationship of Anderson et al. (2021). Uncertainty on the Δ_{47} measurements were calculated as 1 standard error.

5.5 Results

5.5.1 $\delta^{18}O_{carb}$ Profiles

Figure 5.S1 shows $\delta^{18}O_{carb}$ profiles of each shell. The $\delta^{18}O_{carb}$ profiles of *L. pensylvanica* show semi-sinusoidal profiles, with slightly wider peaks on the light/warm end and spikier peaks on the heavy/cold end, indicating faster growth rates in summer and slower growth in winter. Growth rates are slower than modern *L. pensylvanica* from Florida and the Caribbean, in line with cooler mean temperatures at this higher latitude location. Profiles from LPP show more

variability between years, with some years capturing the full winter $\delta^{18}O$ maxima and others only capturing half the seasonal range. This is found in both shells from LPP, although the overall range is similar to other sites.

G. americana shells show much spikier profiles, with faster oscillations, indicating a much slower growth rate and longer lifetime than *L. pensylvanica*. Although the sampling resolution was insufficient to capture smooth sinusoids in each year of growth, the total range in $\delta^{18}O_c$ is similar in shells of the two species taken from the same layer (BI-B). The range in $\delta^{18}O_c$ is also similar between *G. americana* and the gastropod *C. pica* analyzed from Grape Bay when a single-point outlier is excluded. Figure 5.4C shows the full temperature range derived from $\delta^{18}O_c$ for the Grape Bay *G. americana* (8.5-20.6 °C), which appears much greater than the temperature range defined by the four *C. pica* shells. The upper end of this larger seasonal range in *G. americana* is reduced to 8.5-16.9 °C when the single-point outlier is removed (Figure 5.S1). Overall, this indicates that despite the slower growth rate in *G. americana*, a sampling profile covering many years manages to capture the full seasonal range in this species.

5.5.2 Site-by-site Isotopic-based Temperature and $\delta^{18}O_w$ Estimates

Seasonally-targeted Δ_{47} values measured on two *L. pensylvanica* from LPP produce Δ_{47} temperatures ranging from 14.7 °C to 23.1 °C, with a mean of 19.4 °C ± 3.9 °C (1SD). Calculated $\delta^{18}O_w$ values ranged from -1.4 to 0.2 ‰, with a mean of -0.4‰ ± 0.7‰ VSMOW (1SD). Using individual shell mean $\delta^{18}O_w$ values, the site-wide $\delta^{18}O_{carb}$ range of -1.4 to 1.1 ‰ (VPDB) becomes a temperature range of 10.3°C to 22.1°C, slightly colder than the range produced by Δ_{47}, and with wider mean annual range. Both the upper and lower end estimates from Δ_{47} are within error of the upper and lower end estimates from $\delta^{18}O_{carb}$.

L. pensylvanica from all four layers at BI produce a site-wide Δ_{47} temperature range of 11.5 to 27.0 °C, with a mean temperature of 19.8 °C ± 3.5 °C (1SD) (Figure 5.3). The mean temperature from layers BI-A and BI-B is 18.8 ± 3.1 °C, and the mean from layers BI-C and BI-D is 18.8 ± 3.6 °C, identical within error. Using individual shell layer $\delta^{18}O_w$ values, $\delta^{18}O_{carb}$ values from all layers translate to temperatures ranging from 10.0 to 24.3 °C, with a mean of 18.0 ± 2.6 °C. The mean temperature from layers BI-A and BI-B is 17.9 ± 2.4 °C, and the mean from layers BI-C and BI-D is 18.2 ± 2.9 °C, again identical within error. Combined, all four layers produce $\delta^{18}O_w$ values from -1.4 to +1.4 ‰, with a mean of 0.1‰ ± 0.7‰ (1SD) VSMOW (Figure 5.3). The mean $\delta^{18}O_w$ value for layers BI-A and BI-B is 0.0 ± 0.7 ‰ and for layers BI-C and BI-D is 0.0 ± 0.6 ‰, identical within error.

A single *G. americana* from BI-B shows Δ_{47} temperatures of 18.1-19.8°C, similar to *L. pensylvanica* on average but with significantly reduced range. This may be the result of mixing of shell material representing adjacent seasons in sampling for Δ_{47}. The temperature range derived from $\delta^{18}O_{carb}$ is 11.5-22.0 °C, much closer to the range observed in *L. pensylvanica* (10.0 to 24.3 °C).

Shells of *L. pensylvanica* from LIE recorded a Δ_{47} temperature range from 17.7 to 29.1°C, with a mean of 22.3 °C ± 2.8 °C (1SD), the warmest of any of the newly studied sites. Reconstructed $\delta^{18}O_w$ values from LIE ranged from -0.7 to 2.0 ‰, with a mean of 0.4‰ ± 0.7‰ (1SD).

In general, all Great Sound sites reported seasonal ranges similar to Bermuda's modern mean annual temperature range, although the absolute maximum and minimum temperature extremes vary by site. Out of all the Great Sound sites, the warmest temperatures come from LIE (17.7 to 29.1°C), closest to the modern Bermuda range of 19-29 °C. Temperatures from both

LPP and BI are slightly cooler than modern. The overall estimated $\delta^{18}O_w$ values are much lighter than modern $\delta^{18}O_w$ values measured around Bermuda. Modern LPP and BI $\delta^{18}O_w$ values are both reported to be 1.3‰ (Zhang et al., 2021).

5.5.3 $\delta^{18}O$ Sclerochronology vs. Seasonally-targeted Δ_{47} Measurements

Generally, both $\delta^{18}O$ sclerochronology and Δ_{47} reconstructed similar overall temperature ranges and captured the cooler-than-modern trend (Figure 5.3). Specifically, both methods show warmest ranges from LIE and coolest ranges from BI. Although $\delta^{18}O$ sclerochronology calculated temperatures are consistent within each site or layer, this method could mask the possible variability in temperature when it assumed a constant $\delta^{18}O_w$ value throughout the life span of the shell. Previous study has already demonstrated the possibility of varying $\delta^{18}O_w$ from Bermuda (Zhang et al., 2021). Thus, it is very likely that $\delta^{18}O_w$ was varying and by assuming a constant $\delta^{18}O_w$ value at each site, the resultant temperature ranges could be too conservative to reflect the real changes.

On the other hand, temperature ranges estimated from Δ_{47} could fail to capture the absolute max-and-min temperatures. This is possibly due to drilling into a deeper layer during sampling. Since each clumped isotope sample requires a much larger sample material, and it was typically re-sampled over the previous $\delta^{18}O$ sampling site, it is possible the drilling had gone deeper than intended. This could possibly occur here. When comparing the reported $\delta^{18}O_{carb}$ values between the two methods, most of the Δ_{47} reconstructed $\delta^{18}O_{carb}$ values misalign with the $\delta^{18}O_{carb}$ values reconstructed from $\delta^{18}O$ sclerochronology (Figure 5.S1). While $\delta^{18}O_{carb}$ summer/minima values mostly align between the two methods, $\delta^{18}O_{carb}$ winter/maxima values are much lighter from Δ_{47}. This could suggest the resulting temperature ranges potentially do not

capture the absolute coldest times. Additionally, this would also indicate that the already apparent cooler-than-modern trend could be even greater if the winter maxima were fully captured.

Even though Δ_{47} reconstructed temperatures could be missing wintertime lows, the overall reconstructed temperature ranges and mean values from BI, LIE and LPP are similar between the two methods (Figure 5.3A, C). Both methods record warmest ranges and mean from LIE, while BI records the coolest ranges and mean of the three sites. Additionally, there are 4-10 sampled points from each *L. pensylvanica*, and multiple shells from each site to achieve a general understanding on the seasonal variability from each site. Altogether, it is less important to be able to distinguish a particular season than understanding the overall range and seasonal variability. In addition, Δ_{47} also reconstructs $\delta^{18}O_w$, which allows for important understanding of the paleoenvironment at different sites. Therefore, Δ_{47} is preferred over the two methods for temperature estimates, but temperature results from $\delta^{18}O$ sclerochronology are also helpful for comparison purposes, with the caveat that the converted temperature ranges could be artificially changed with a different $\delta^{18}O_w$ value and there is ambiguity on the paleo $\delta^{18}O_w$ values.

5.6 Discussion

5.6.1 The Decreasing Temperature Trend Within MIS 5e

Two previous paleoclimate reconstruction using *C. pica* samples from the South Shore found cooler-than-modern temperatures (Winkelstern et al., 2017; Zhang et al., 2021), while a more recent study found close-to-modern temperatures using *D. frons* from Verrill Island, located in the Great Sound (Minnebo et al., *in prep*). From these studies alone, it was difficult to decipher the cause of this inconsistency in reconstructed temperatures because the two sets of

studies used different taxa collected from study locations representing different paleoenvironments (rocky shoreline vs. sandy bay).

Using published AAR dates (Hearty et al., 1992; Minnebo et al., *in prep*) and stratigraphic observations, we now align these previous study sites into a chronology that reconciles the apparent disagreement between the early studies. When temperature data from multiple sites are arranged in chronological order based on ages and stratigraphic relationships, we observe a decreasing trend in temperature through time, captured by both $\delta^{18}O$-based and seasonally-targeted Δ_{47} temperature reconstruction (Figure 5.4, 5.5). In the Great Sound, *D. frons*, *G. americana,* and *L. pensylvanica* samples reconstruct a decrease in mean temperature from 23.9°C (VI) to 19.7°C (LIE/ BI/LPP) based on Δ_{47} or from 27.5°C (VI) to 18.6°C (LIE/ BI/LPP) based on $\delta^{18}O$ (Figure 5.4). A similar degree of cooling is also reproduced in the South Shore *C. pica* and *G. americana* samples (22.5°C (RB) to 17.1°C (GB) from Δ_{47} or 18.0 °C (RB) to 11.7 °C (GB) from $\delta^{18}O$) (Figure 5.4), reinforcing the observed temperature pattern.

The coherency of the resulting temperature pattern now illuminates that the previously discordant results were actually representing two different time periods in an interval of variable climate. Additionally, this observed temporal temperature trend can explain the significant temperature differences found between RB and GB in the previous studies (Winkelstern et al., 2017; Zhang et al., 2021), which were previously difficult to explain as today, these two closely located study sites have no difference in seawater temperature between them. Now, it becomes apparent that the slight difference in age within MIS 5e is important. RB represents an earlier, warmer interval and GB represents a later cooler interval. MIS 5e is not a single moment in time, but rather a ~10-15 kyr interval of time during which climate varied in Bermuda. Considering all MIS 5e deposits to be contemporaneous leads to incorrect interpretations of spatial variability.

Using the relative dating technique of AAR, we were able to observed that, as time progressed within MIS 5e, temperature decreased (Figure 5.4, 5.5). Only two sites (GB, RB) have absolute dates using U-Th, and these dates themselves have uncertainty on the scale of thousands of years. However, we can say that the earlier of these two dated sites, RB, (120-128 ka, mean=125ka) (Muhs et al., 2002) already represents cooler-than-modern temperatures, with temperatures only declining further as time progressed. Only VI, which is placed earliest in the stratigraphy (pre RB), contains near-modern temperatures. Therefore, assuming warm conditions did not appear until the typically-assumed onset of MIS 5e (130ka) it is possible to constrain the duration of peak warmth in Bermuda to be ~5000 years or less. Alternatively, Bermuda could never have been as warm as today during the LIG and VI could represent a small locally-warmer environment created by shallower water conditions and solar heating.

5.6.2 The Decreasing $\delta^{18}O_w$ Trend Within MIS 5e

Correlating with the decreasing temperature trend is the consistent decrease in $\delta^{18}O_w$. Similar to the decreasing temperature pattern observed from both groups, the decreasing $\delta^{18}O_w$ trend is also observed from the Great Sound sites and the South Shore sites (Figure 5.4B). Mean $\delta^{18}O_w$ value decreased from 1.6‰ to 0.1‰ in the Great Sound sites and decreased from 0.9‰ to -0.5‰ in the South Shore sites. Once again, the magnitude of this decrease in $\delta^{18}O_w$ is similar between the two regions. When viewing it as a whole, $\delta^{18}O_w$ is observed to be consistently decreasing through time (Figure 5.5). Here, warm temperatures are observed to be correlated with higher $\delta^{18}O_w$ values, and as temperatures decline, $\delta^{18}O_w$ becomes lighter.

From this dataset, it cannot be determined whether this is a local signal reflecting changes in hydrology in Bermuda or whether this reflects a basin-wide decreases in $\delta^{18}O_w$. Local changes

in $\delta^{18}O_w$ could have been caused by increased rainfall, or increased freshwater discharge from underground aquifers, although higher sea levels during the LIG would actually have reduced the size of these aquifers. Basin-wide changes may have been due to increased precipitation, decreased evaporation in cooler climates, and/or melting of the Greenland and Laurentide ice sheets as well as other smaller ice sheets in Europe and Scandinavia (Cuffey and Marshall, 2000; Kopp et al., 2009; Turney and Jones, 2010; Stone et al., 2013; Dutton et al., 2015). Isotopically depleted meltwater deposited in the northern Atlantic could have traveled down the US East Coast and then up to Bermuda via the Gulf Stream current.

Sea level reconstructions for Bermuda suggest that sea levels reached modern levels around 125-130 ka and continued to rise for the next ~10-15 kyr due to glacial isostatic adjustment (GIA) (Dutton and Lambeck, 2012). This is consistent with our observed stratigraphy, which indicates successive horizons on the Great Sound islands were deposited under conditions of rising sea level and increasing water depths. Dutton and Lambeck (2012) and other studies suggest the possibility of more ice melt during the latter part of MIS 5e, but cannot separate the influences of additional melting from GIA. If our observed pattern of decreasing $\delta^{18}O_w$ is due to melting ice sheets, it suggests ice sheets continued to melt even after peak temperatures were over and the region began to cool towards MIS 5d.

Overall, the decreasing $\delta^{18}O_w$ trend correlates with the decreasing temperature trend. This suggests the occurrence of the peak sea level offsets from the occurrence of the peak temperature. Whether this was a basin-wide signal or a local hydrologic effect, a drastic decrease in $\delta^{18}O_w$ is observed during the period of rising sea level.

5.7 Conclusions

Two previous paleoclimate reconstruction studies, one focusing on an island in the Great Sound and another from the South Shore of Bermuda, disagreed on whether Bermudan waters were warmer than, similar to, or cooler than today. In this study, we combine the previously published paleoclimate, AAR and stratigraphy data with new temperature and $\delta^{18}O_w$ measurements from multiple sites in the Great Sound using multiple taxa. We find peak temperatures and peak sea levels did not coincide. Warm temperatures and high $\delta^{18}O_w$ were observed at the onset of MIS 5e, possibly lasting ~5000 years or less. Following peak warming, sea level continued to rise due to glacial isostatic adjustment and possible additional ice sheet melting, while temperatures began to cool. This coincides with a decline in $\delta^{18}O_w$, potentially reflecting increased meltwater being delivered to the Atlantic.

Previous paleo-temperature reconstruction studies have considered MIS 5e outcrops in Bermuda to represent a single time slice, categorizing the MIS 5e climate into either cooler or warmer depending on the region. However, we show that during MIS 5e, local climate changed measurably. Both the cooler-than-modern and warmer-than-modern conditions existed during MIS 5e in Bermuda. Our results emphasize that MIS 5e in Bermuda is a dynamic time period, and suggests that other sites may have experienced similarly large climate change, which should be considered in any site-to-site time-slice comparisons like the CLIMAP project.

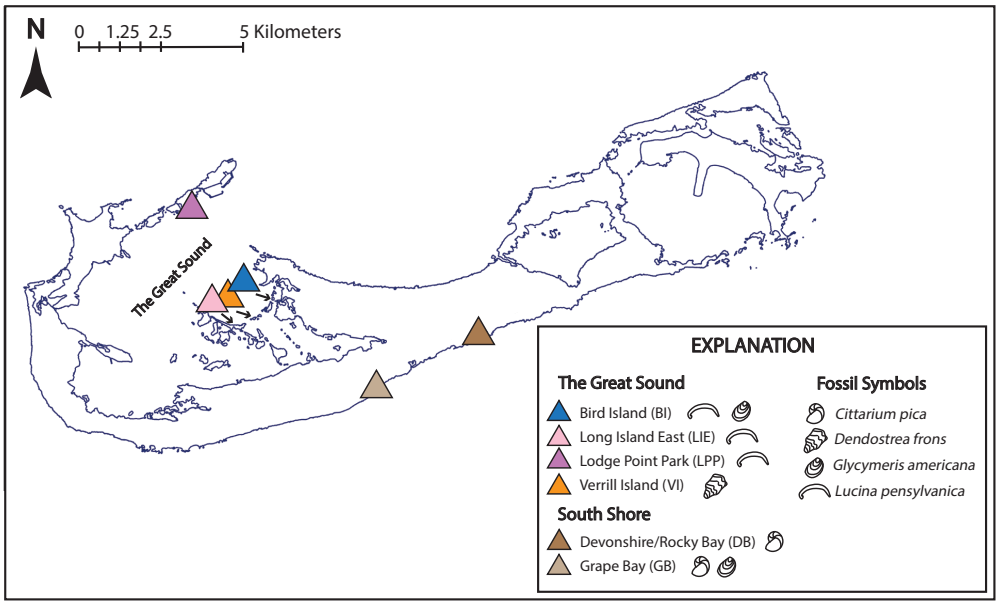

Figure 5.1. Map of Bermuda showing sampling locations.

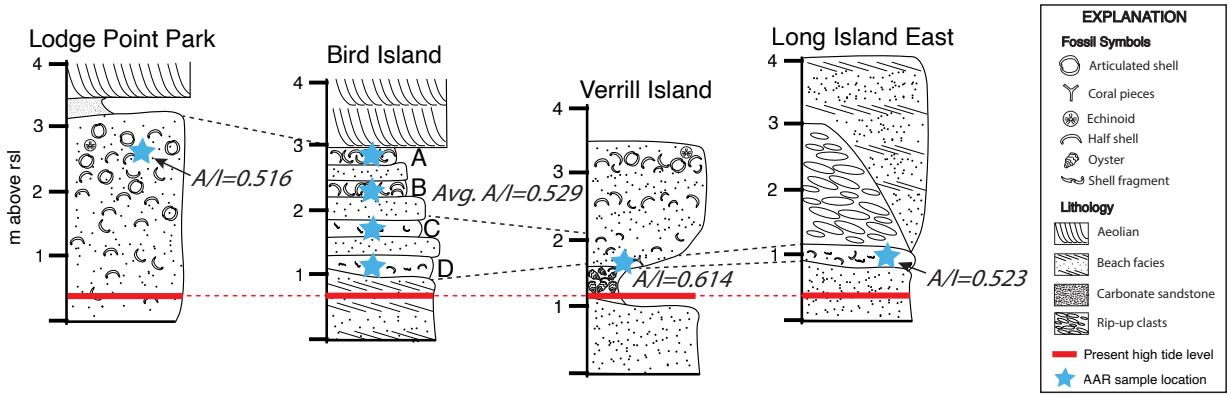

Figure 5.2. Stratigraphic columns of the Great Sound sites.

Sites are correlated by the high tide level (red line) observed in the field. Above the high tide level, sediments show similarities in sedimentology, fossil abundance and preservation.

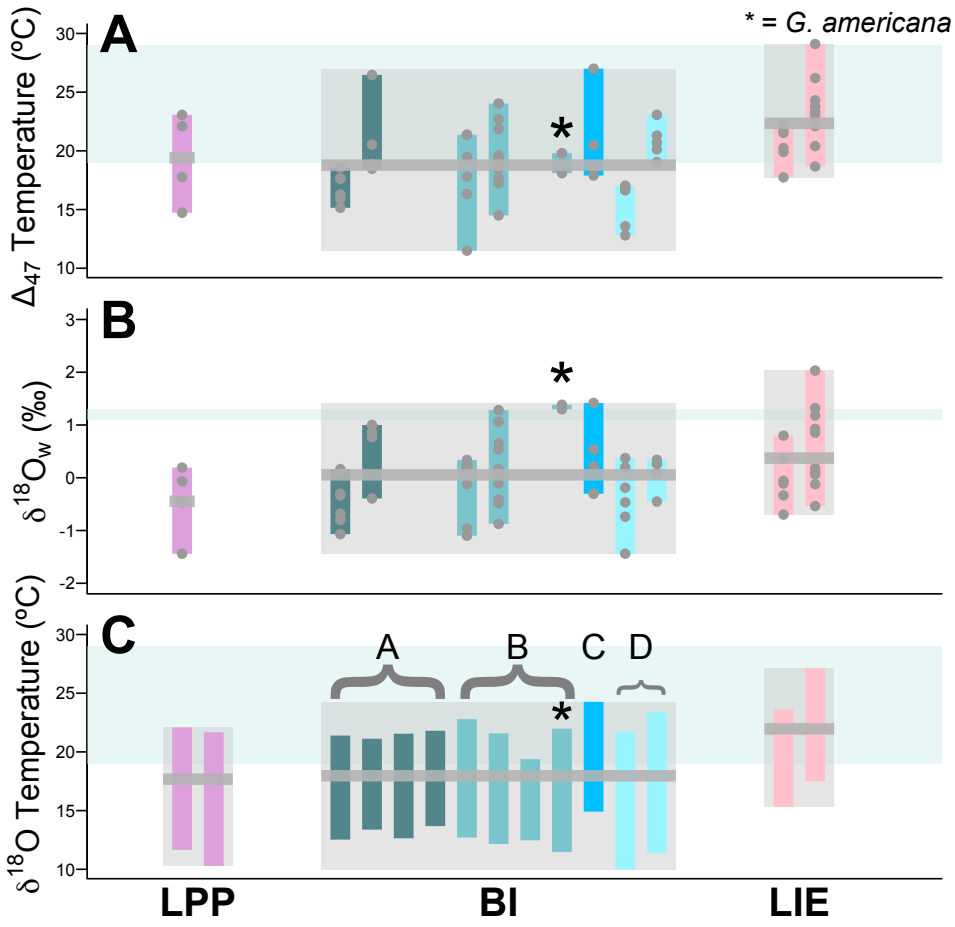

Figure 5.3. $\delta^{18}O$ and Δ_{47}-based temperature and $\delta^{18}O_w$ reconstructions and their range comparison against modern climate record.

Both Δ_{47}-based and $\delta^{18}O$-based temperature ranges show similar degrees of seasonal range (~10 °C) when compared to the modern Bermuda record. Blue shaded regions indicate modern Bermuda records. Grey bars indicate mean values.

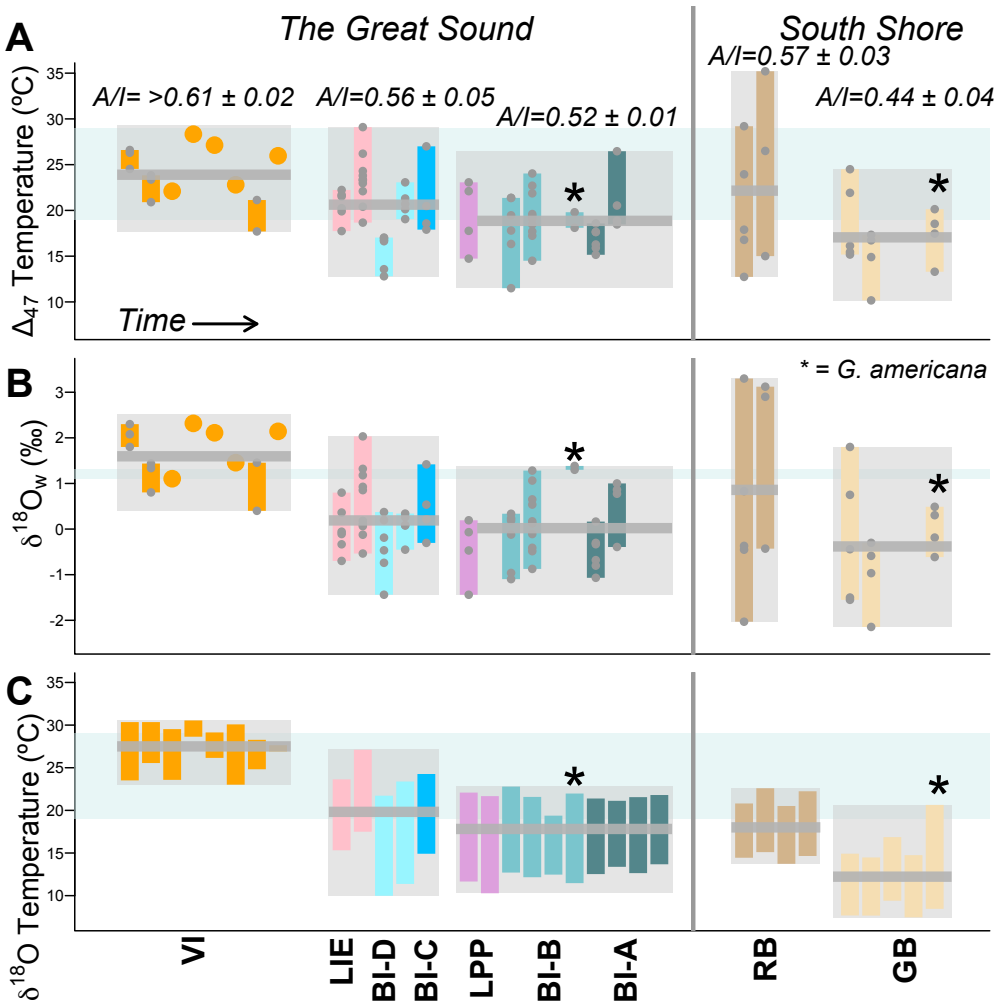

Figure 5.4. $\delta^{18}O$ and Δ_{47}-based temperature and $\delta^{18}O_w$ reconstructions from *C. pica*, *D. frons*, *G. americana*, and *L. pensylvanica,* arranged by regions.

Both reconstructed temperatures and $\delta^{18}O_w$ show a decreasing trend through MIS 5e. Additionally, both the Great Sound and the South Shore sites record this decreasing pattern. Blue shaded regions indicate modern Bermuda records. Grey bars indicate mean values. *C. pica* measurements are compiled from Winkelstern et al. (2017) and Zhang et al. (2021), *D. frons* measurements are compiled from Minnebo et al. (*in prep*).

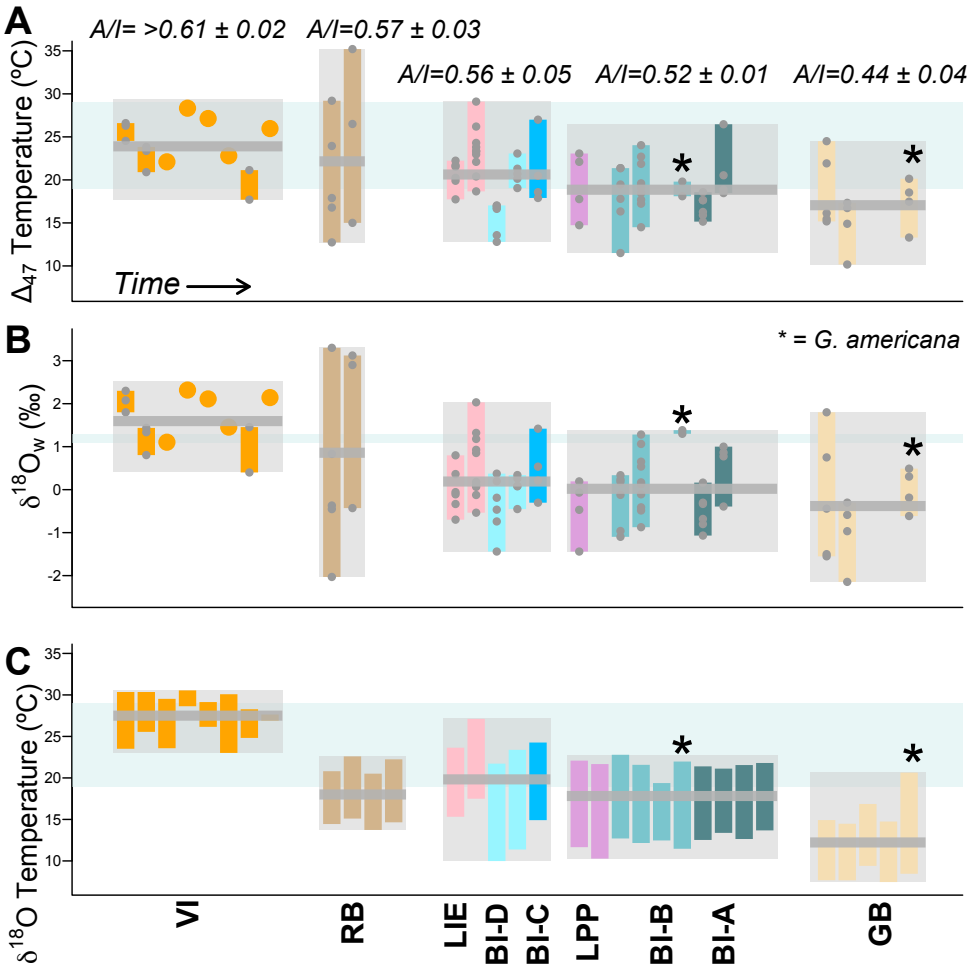

Figure 5.5. $\delta^{18}O$ and Δ_{47}-based temperature and $\delta^{18}O_w$ reconstructions from *C. pica*, *D. frons*, *G. americana*, and *L. pensylvanica,* arranged by stratigraphic information and A/I ratios.

When organized by A/I ratios, reconstructed temperatures and $\delta^{18}O_w$ transition from close-to-modern conditions to cooler-than-modern conditions through MIS 5e. Blue shaded regions indicate modern Bermuda records. Grey bars indicate mean values. *C. pica* measurements are compiled from Winkelstern et al. (2017), *D. frons* measurements are compiled from Minnebo et al. (*in prep*).

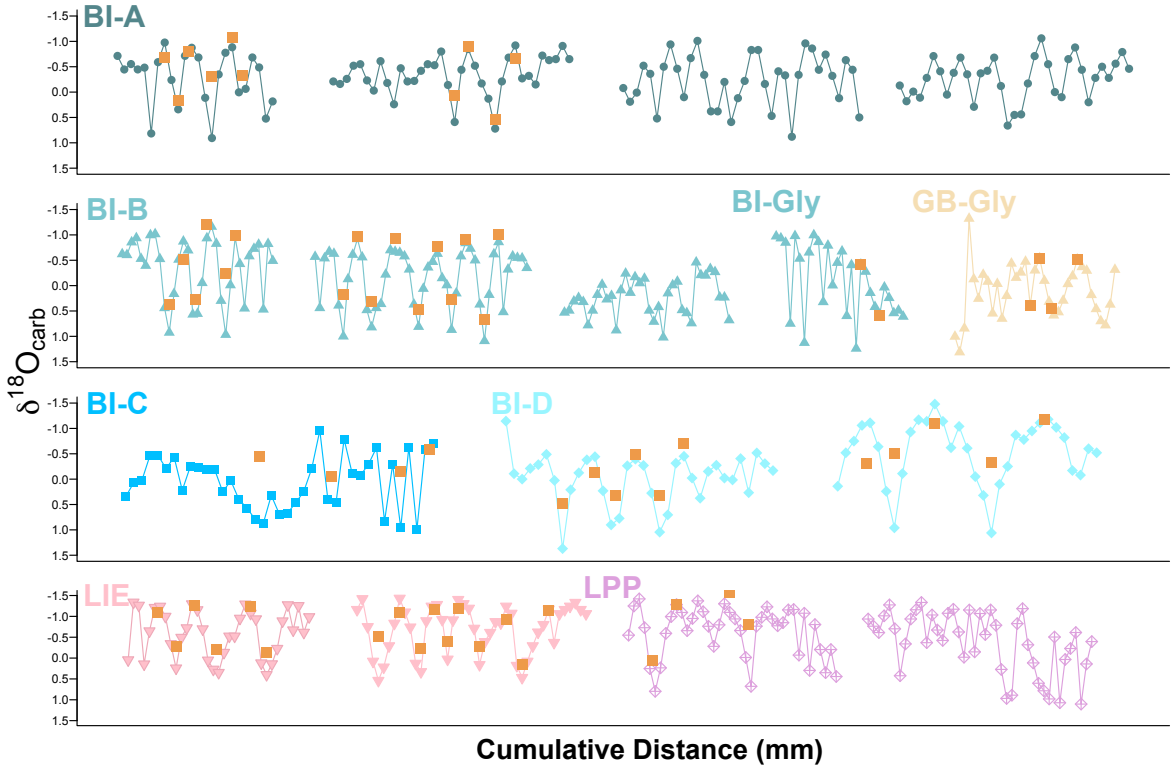

Figure 5.S1. $\delta^{18}O_{carb}$ measurements from *G. americana*, and *L. pensylvanica.*

Orange points indicate $\delta^{18}O_{carb}$ measurements reconstructed from Δ_{47}. Note that the higher $\delta^{18}O_{carb}$ measurements reconstructed from Δ_{47} are mostly misaligned with the $\delta^{18}O_{carb}$ measurements from $\delta^{18}O$-based sclerochronology.

5.8 References

Anderson, N.T. et al., 2021, A unified clumped isotope thermometer calibration (0.5–1,100°C) using carbonate-based standardization: Geophysical Research Letters, v. 48, doi:10.1029/2020GL092069.

Bernasconi, S.M. et al., 2021, InterCarb: A community effort to improve interlaboratory standardization of the carbonate clumped isotope thermometer using carbonate standards: Geochemistry, Geophysics, Geosystems, v. 22, p. 1–25, doi:10.1029/2020GC009588.

CLIMAP (1984), The Last Interglacial Ocean, Quaternary Research, v. 21, 123–224.

Cuffey, K.M., and Marshall, S.J., 2000, Substantial contribution to sea-level rise during the last interglacial from the Greenland ice sheet: Nature, v. 404, www.nature.com.

Dutton, A., and Lambeck, K., 2012, Ice Volume and Sea Level During the Last Interglacial: Science, v. 337, p. 216–219.

Dutton, A., Carlson, A.E., Long, A.J., Milne, G.A., Clark, P.U., DeConto, R., Horton, B.P., Rahmstorf, S., and Raymo, M.E., 2015, Sea-level rise due to polar ice-sheet mass loss during past warm periods: Science, v. 349, doi:10.1126/science.aaa4019.

Harmon, R.S., Mitterer, R.M., Kriausakul, N., Land, L.S., Schwarcz, H.P., Garrett, P., Larson, G.J., Leonard Vacher, H., and Rowe, M., 1983, U-series and amino-acid racemization geochronology of Bermuda: Implications for eustatic sea-level fluctuation over the past 250,000 years: Palaeogeography, Palaeoclimatology, Palaeoecology, v. 44, p. 41–70, doi:10.1016/0031-0182(83)90004-4.

Harmon, R.S., Schwarcz, H.P., and Ford, D.C., 1978, Late Pleistocene sea level history of Bermuda: Quaternary Research, v. 9, p. 205–218, doi:10.1016/0033-5894(78)90068-6.

Harrison, S.P., Kutzbach, J.E., Prentice, I.C., Behling, P.J., and Sykes, M.T., 1995, The response of northern hemisphere extratropical climate and vegetation to orbitally induced changes in insolation during the Last Interglacial: Quaternary Research, v. 43, p. 174–184.

Hearty, P.J., 2002, Revision of the late Pleistocene stratigraphy of Bermuda: Sedimentary Geology, v. 153, p. 1–21, www.elsevier.com/locate/sedgeo.

Hearty, P.J., Kindler, P., Cheng, H., and Edwards, R.L., 1999, A +20m middle Pleistocene sea-level highstand (Bermuda and the Bahamas) due to partial collapse of Antarctic ice: Geology, v. 27, p. 375–378.

Hearty, P.J., and Olson, S.L., 2010, Geochronology, biostratigraphy, and changing shell morphology in the land snail subgenus Poecilozonites during the Quaternary of Bermuda: Palaeogeography, Palaeoclimatology, Palaeoecology, v. 293, p. 9–29, doi:10.1016/j.palaeo.2010.04.026.

Hearty, P.J., Vacher, H.L., and Mitterer, R.M., 1992, Aminostratigraphy and ages of Pleistocene limestones of Bermuda: Geological Society of America Bulletin , v. 104, p. 471–480, http://pubs.geoscienceworld.org/gsa/gsabulletin/article-pdf/104/4/471/3381525/i0016-7606-104-4-471.pdf?casa_token=Ft-nv8fw9vIAAAAA:Ax7Z7qJpOfSaJ0Flmlw3fUtut7u3PqdcQOwqWurrD-0_BuOoLum.

Jones, M.M., Petersen, S. V., and Curley, A.N., 2022, A tropically hot mid-Cretaceous North American Western Interior Seaway: Geology, p. 1–27, doi:10.1130/g49998.1.

Kim, S.T., Mucci, A., and Taylor, B.E., 2007, Phosphoric acid fractionation factors for calcite and aragonite between 25 and 75 °C: Revisited: Chemical Geology, v. 246, p. 135–146, doi:10.1016/j.chemgeo.2007.08.005.

Kopp, R.E., Simons, F.J., Mitrovica, J.X., Maloof, A.C., and Oppenheimer, M., 2009, Probabilistic assessment of sea level during the last interglacial stage: Nature, v. 462, p. 863–867, doi:10.1038/nature08686.

Kukla, G.J. et al., 2002, Last interglacial climates: Quaternary Research, v. 58, p. 2–13, doi:10.1006/qres.2001.2316.

Land, L.S., Mackenzie, F.T., and Gould, S.J., 1967, Pleistocene history of Bermuda: Geological Society of America Bulletin, v. 78, p. 993–1006.

Minnebo, L., Winkelstern, I. Z., Zhang, J. Z., Petersen, S. V., Highly local variability in coastal last interglacial temperature and seawater $\delta^{18}O$ in Bermuda revealed by clumped isotope sclerochronology, Manuscript in preparation.

Muhs, D.R., Simmons, K.R., and Steinke, B., 2002, Timing and warmth of the Last Interglacial period: new U-series evidence from Hawaii and Bermuda and a new fossil compilation for North America: Quaternary Science Reviews, v. 21, p. 1355–1383.

O'hora, H.E., Sierra, B., Petersen, V., Vellekoop, J., Jones, M.M., and Scholz, S.R., 2022, Clumped-isotope-derived climate trends leading up to the end-Cretaceous mass extinction in northwest Europe: Climate of the Past, p. 1–28, doi:10.5194/cp-2021-104.

Petersen, S. V. et al., 2019, Effects of improved ^{17}O correction on interlaboratory agreement in clumped isotope calibrations, estimates of mineral-specific offsets, and temperature dependence of acid digestion fractionation: Geochemistry, Geophysics, Geosystems, v. 20, p. 3495–3519, doi:10.1029/2018GC008127.

Rowe, M.P., Wainer, K.A.I., Bristow, C.S., and Thomas, A.L., 2014, Anomalous MIS 7 sea level recorded on Bermuda: Quaternary Science Reviews, v. 90, p. 47–59, doi:10.1016/j.quascirev.2014.02.012.

Stone, E.J., Lunt, D.J., Annan, J.D., and Hargreaves, J.C., 2013, Quantification of the Greenland ice sheet contribution to Last Interglacial sea level rise: Climate of the Past, v. 9, p. 621–639, doi:10.5194/cp-9-621-2013.

Turney, C.S.M., and Jones, R.T., 2010, Does the Agulhas Current amplify global temperatures during super-interglacials? Journal of Quaternary Science, v. 25, p. 839–843, doi:10.1002/jqs.1423.

Winkelstern, I.Z., Rowe, M.P., Lohmann, K.C., Defliese, W.F., Petersen, S. V., and Brewer, A.W., 2017, Meltwater pulse recorded in Last Interglacial mollusk shells from Bermuda: Paleoceanography, v. 32, p. 132–145, doi:10.1002/2016PA003014.

Zhang, J.Z., and Petersen, S. V., 2023, Clumped and oxygen isotope sclerochronology methods tested in the bivalve Lucina pensylvanica: Chemical Geology, v. 620, p. 121346, doi:10.1016/j.chemgeo.2023.121346.

Zhang, J.Z., Petersen, S. V., Winkelstern, I.Z., and Lohmann, K.C., 2021, Seasonally variable aquifer discharge and cooler climate in Bermuda during the last interglacial revealed by subannual clumped isotope analysis: Paleoceanography and Paleoclimatology, v. 36, p. 1–19, doi:10.1029/2020PA004145.

Zhang, J.Z., Petersen, S. V., Lavis, S., Williams, B., Quantifying variations in $\delta^{18}O_w$ and salinity in modern Bermudan waters on hourly to monthly timescales, Manuscript in preparation.

Chapter 6 Conclusion

This dissertation consists of four content chapters that use oxygen and clumped isotope analyses to improve knowledge of Last Interglacial climate and modern hydrology in Bermuda. This concluding chapter highlights the most important findings and implications from each of the body chapters and offers a discussion of future research directions.

6.1 How accurately does H.R. Δ_{47} thermometry reconstruct seasonal temperatures compared to other isotopic sampling approaches? (Chapter 2)

In Chapter 2, we assessed the performance of multiple isotopic sampling techniques including subannual $\delta^{18}O$-based, subannual/seasonally-targeted and subannual/continuous H.R. Δ_{47} thermometry, and tested their ability to accurately reconstruct mean annual temperatures and seasonality in a modern setting. We compared these geochemical methods to determine the best measurement and analysis approaches for future use.

Through testing the different isotope techniques, we demonstrated the importance of considering species growth rate when selecting a sampling method. For our chosen mid-sized bivalve species *Lucina pensylvanica* (*L. pensylvanica*) which has an intermediate growth rate, a combination of subannual $\delta^{18}O$ and seasonally-targeted Δ_{47} analysis resulted in the closest alignment with modern climate conditions. Specifically, we showed that seasonality is best matched through $\delta^{18}O$-based thermometry while seasonally-targeted Δ_{47} measurements reconstructed annual mean temperatures the best. Through close examination, we also showed

that H.R. Δ_{47} does not work to its full potential on *L. pensylvanica*, mainly due to the shell's smaller size and slower growth rate. Lastly, we presented a framework for balancing growth rate, sample size, sampling resolution and analytical uncertainty that can be generalized to other species.

Altogether, Chapter 2 helps determine the most accurate isotopic sampling approach for estimating temperature seasonality and highlights the importance of balancing sampling resolution and growth rate. Even though H.R. Δ_{47} does not work effectively on slow growing specimens like *L. pensylvanica*, this Chapter generates understanding toward its applicability in faster growing species.

6.2 What was the seasonality in temperature in Bermuda during MIS 5e? (Chapter 3)

In Chapter 3, we explored paleoseasonality in Bermuda through subannual-scale clumped isotope measurements on the large gastropod (*Cittarium pica*). We sampled shells for Δ_{47} at subannual resolution, aiming to resolve temperature and $\delta^{18}O_w$ differences observed between two closely located study sites in a previously published study. We also analyzed modern seawater $\delta^{18}O_w$ from several sites to understand its variability and the processes driving these changes in the modern setting.

We found that our subannual clumped isotope results align with previously-described cooler-than-modern conditions in Bermuda derived from bulk (single point per shell) Δ_{47} analysis. Reprocessing the previously published data combined with new analyses from this study reduced the temperature and $\delta^{18}O_w$ differences between the two study sites, although a differences between the sites persists. We found unexpectedly large variation in $\delta^{18}O_w$ at the subannual scale in paleo-$\delta^{18}O_w$ reconstructed from Δ_{47}, which was supported by spot

measurements of modern $\delta^{18}O_w$ from near the fossil sites. Modern seawater $\delta^{18}O$ measurements demonstrated higher variation along the South Shore relative to the rest of the island, potentially caused by subsurface injection of freshwater from the Central Devonshire lens into the South Shore coastal water. This mechanism was hypothesized to be driven by changes in sea surface height, potentially causing ~0.5‰ variation in modern coastal $\delta^{18}O_w$ along the South Shore. A similar process was speculated to occur during MIS 5e, causing the observed >2‰ seasonal variation in $\delta^{18}O_w$ reconstructed by Δ_{47} in the fossil samples.

Altogether, Chapter 3 supports cooler-than-modern conditions in Bermuda during the Last Interglacial and challenges the common assumption of invariant $\delta^{18}O_w$ at a coastal setting like Bermuda.

6.3 What are the magnitudes of $\delta^{18}O_w$ variability in different types of water in modern Bermuda? (Chapter 4)

The previous chapter (Chapter 3) demonstrated temporal variation in seawater $\delta^{18}O$ along South Shore due to a speculated interaction between aquifer and coastal seawater. Chapter 4 built upon previous insights from Chapter 3 and quantified variations in $\delta^{18}O_w$ and salinity through an expanded dataset of modern Bermudan waters including sea, well, tap, marsh, and rain waters. We established baseline behavior of the multiple aqueous endmembers on hourly to monthly timescales.

We found that $\delta^{18}O_w$ and salinity measurements from samples collected in wells tapping the Devonshire Lens are tightly correlated, following a simple linear mixing relationship. Profiles with depth depict a slightly smaller Devonshire Lens compared to the last assessment of lens size performed in 1978. With our expanded dataset, we demonstrated significant ~2.4‰

variation in seawater $\delta^{18}O$ on monthly timescales, and up to 1.4‰ variation on hourly timescales. Lastly, we discovered that South Shore seawater salinity varies much less than expected given variation in $\delta^{18}O_w$ values and the quantified linear mixing relationship between seawater and aquifer water, which suggested the presence of additional processes at play defining salinity in these coastal settings.

Overall, these findings from Chapter 4 more completely visualize the dynamic interaction between coastal seawater and aquifer-sourced freshwater in Bermuda. This newly generated understanding provides a baseline for future, long-term sustainable freshwater extraction practices on the island. Further, Chapter 4 illustrates the risk of assuming a $\delta^{18}O_w$ value in an unknown paleo-hydrologic environment and contributes valuable insights into submarine groundwater discharge processes both in the modern setting and in the past.

6.4 Was seasonality in temperature and $\delta^{18}O_w$ in the Great Sound similar to or different from variability along the South Shore? (Chapter 5)

In Chapter 5, we estimated seasonality in temperature and $\delta^{18}O_w$ from fossil *L. pensylvanica* collected from multiple sites in the Great Sound, all dated to MIS 5e. We compiled previously published climate, stratigraphy and amino acid racemization (AAR) data from the Great Sound and South Shore sites to refine understanding of Last Interglacial climate, specifically local variability in temperature and $\delta^{18}O_w$ through time in Bermuda.

Through synthesizing newly measured and published isotope data as well as stratigraphy and AAR dates, we found a consistently decreasing trend in both temperature and $\delta^{18}O_w$ through MIS 5e. As time progressed within MIS 5e, temperature and $\delta^{18}O_w$ transitioned from close-to-modern conditions to cooler-than-modern conditions. We found corresponding change in

paleoenvironment from the Great Sound sites, transitioning from high energy environment to low energy environment with increasing water depth.

Overall, our findings demonstrate that MIS 5e is not a single moment in time with static climate conditions. Instead, it should be viewed as an interval containing changing conditions, which we capture in the transition in temperature and $\delta^{18}O_w$ through time in Bermuda. Altogether, the large dataset from Chapter 5 robustly depicts climate and paleoenvironmental evolution through the Last Interglacial in Bermuda, a finding which has implications for possible changes in the ocean circulation or heat transport during the Last Interglacial interval.

6.5 Future Directions

The conclusions and implications from this dissertation enable a robust understanding of Last Interglacial climate and hydrologic processes between coastal seawater and aquifer-sourced freshwater in Bermuda. Taken together, the four content chapters document a wide range of applications of isotopic geochemistry to fields such as paleoclimatology, paleoceanography, and hydrology.

Throughout this dissertation, we demonstrated the importance of understanding the mechanism behind submarine groundwater discharge (SGD) and the delicate balance between sea level and the volume of freshwater stored in coastal aquifers and in Bermuda. Similar to understanding the aquifer discharge to coastal seawater, monitoring and quantifying seawater infiltration into the freshwater aquifers is equally crucial. For example, in southeastern Florida, increased groundwater withdrawals, periodic droughts, and extreme storm events alter the balance between the sea level and the fresh groundwater level in the Biscayne aquifer, which provides 98% of the public water supply in south Florida. These practices and natural events

allow saltwater from the ocean to intrude into this surficial aquifer, leaving the water non-potable. A similar process is also known to occur in several aquifers in Florida and Puerto Rico. The isotope analytical approaches used in this study and the accumulated understanding of SGD in Bermuda could be applied towards understanding saltwater intrusion in many other coastal regions, with great implications for citizens in these areas. As a next step, I plan on continue to understand these hydrologic processes both in the modern setting and in the past.